Masked Projection Stereolithography:

Improvement of the Limaye Model for Curing Single Layer Medium Sized Parts

A THESIS PRESENTED IN PARTIAL FULFILLMENT OF THE

REQUIREMENTS FOR THE DEGREE OF

DOCTOR OF PHILOSOPHY

IN

ENGINEERING
(School of Engineering and Advanced Technology)

AT MASSEY UNIVERSITY, ALBANY,
NEW ZEALAND

Jonathan Richard Zyzalo

June 2008

PREFACE

The author declares that this is his own work except where due acknowledgement has been given. It is being submitted for the PhD in Engineering, majoring in Mechatronics to the Massey University, Albany, New Zealand.

This thesis describes the research carried out by the author at the School of Engineering and Advanced Technology, Massey University, Albany, New Zealand from February 2004 to March 2008, supervised by Dr. J. Potgieter.

ACKNOWLEDGMENTS

The author wishes to thank the following people for their contributions:

- All glory to the Lord for guiding my life to the point where I can submit a thesis to qualify for a PhD. He has guided all my steps and placed the right people in my path. He has been my inspiration to research the sciences in order to understand His great and wonderful creation. All wisdom, knowledge and understand are His to give to whom He desires.
- Doctor J. Potgieter for his guidance and assistance during the project. Thank you for your willingness and enthusiasm that you have showed in helping me develop in my understanding of the project. Also, for your assistance with research funding for the project.
- Dick and Mary Earle who substantially funded the project for the first two years of the research by providing the Dick and Mary Earle Scholarship in Technology. Thank you both for your helpful insights into the chemistry of photopolymers. You have been a great encouragement to my research.
- Brien O'Brien and the staff at Plastic Design Technologies who have aided in the construction of the project. Thank you, Brien, for help with funding and your support which has been essential for me to be able to hand in this dissertation.
- Dr. O. Diegel for his guidance and assistance during the project with the design considerations, software programming and paper submissions.
- Gordon Warren for all is technical assistance and being a very good friend.
- Professor G. Bright for his help with the project.
- The staff from the Institute of Engineering and Technology, especially, Ray-ray and Eddie in the workshop and Jenny in admin.
- Fellow students Matthew Reed, Lim Kang, Badon Ryle and Terry for their support and assistance in the early stages of development.
- The Christians family, David, Joslyn, Jody, Sharee, and Renski for all their love and support. Thanks for all the amazing family times and all the dinners. You have been a big part of my life and the major influence during my years of study. Thank you for so much for treating me just like your own son.

- My family for their love and support and financial assistance throughout this thesis work. Much of my gratitude belongs to my mum, Annette, for always promoting my education and giving me the opportunity in life to be all that I can be. Thanks heaps for all you help with developing whanau links and scholarship applications.
- Thanks to my extended whanau. Tony Tapp for his help in raising awareness within my hapu Ngati Matepu and writing supporting letters for scholarship and funding applications.
- Thanks to Clay Hawke, the Maori student liaison at Massey University (Albany Campus), and Robyn Borne for allowing me to talk to young people about having goals in life and what it takes to succeed at university level.
- My sweetheart Natasha. You have been my inspiration to finish this thesis. Thank you for all your love and cuddles. All the late nights are worth it. I love you so much more than words can ever express!
- My flatmates Jason and Daniel Laird. Thanks for all the great times and teaching me the "divide by two and add seven" rule. Go Tongan power.
- The guys of the band Lieutenant Funk. Gigging with you guys has been a major stress relief during the years of my thesis. Thanks for all the fun and laughs and the great musicianship.
- A special thanks to the Page family, Brian, Karen, Jonathon, Kristen, Kelsey, and Katelyn for being so kind to me always. Thanks for all the food, bread and coffee!
- A big thank you to Mark, Haley and Harriett. Staying at your place in Raglan really helped me relax. Thanks for all your encouragement. You guys are awesome!
- And lastly, I'm grateful to all my close friends that have always been an encouragement. Thanks for all your support and great times Jody and Sharee, Ricky and Cassie, Buddah (Adrian), Jono, Nick, Tarnz and Nicky, Muzzy and Caroline, and Part. It's all about the memories. How meke? Too meke! Arohanui whanau.

Table of Contents

Table of Figures

List of Tables

Executive Summary

Modern Rapid Prototyping (RP) technology has been available for more than a decade and has aided in shortening product development times and costs in the manufacturing sector. Stereolithography (SL), the most mature of RP technology, has primarily been used to build small to medium sized parts although there are large-scale applications i.e. the automotive industry that uses “mammoth SLA”. Recent developments in SL have been aimed at increasing the speed of the additive process of most SL apparatus (SLA). Developments include the chemistry of photopolymer resins, integral-curing processes as opposed to vector-by-vector processes, and what is now called microstereolithography.

Integral curing has been made possible by the advent of dynamic masking generators such as liquid crystal displays (LCDs) and digital micromirror devices (DMDs). Much of the theory for this new layering process has been applied to the micro-scale and awaits application for medium to large sized parts. The Limaye Model was applied to a microstereolithography apparatus (μSLA) and used as a process planning method for curing dimensionally accurate micro parts. Examination of the results of this mathematical model shows an irradiance map simulating the irradiances on the resin surface. The light is expected to attenuate from the central axis according to a measured irradiance curve. Improvements can be made to the Limaye Model to make it applicable for the process planning of medium to large parts. It is the aim of this research to present an improved mathematical model of the Limaye Model, so that a given irradiance map will produce an evenly distributed irradiance and account for errors in the optical imaging system. It is hoped that the field of exposure of 200mm x 270mm or larger will be achieved.

1 Introduction

1.1 The Topic of this Thesis

The majority of the research conducted for this thesis took place at the Institute of Technology and Engineering, Massey University, Auckland, New Zealand. Design and development work continued at New Zealand's only laser-based SLA (stereolithography apparatus) rapid prototyping installation, Plastic Design Technologies Ltd, Silverdale, Auckland, New Zealand. The Dick and Mary Earle Scholarship in Technology substantially aided funding for the first two years of the research. The primary objective of this PhD research was to present an improved mathematical model for integral ultraviolet (UV) stereolithography that predicts the dimensional cure of a layer and provides layer thickness compensation. Review of current literature on rapid prototyping and experience at Plastic Design Technologies Ltd helped reach the objective. The thesis has two main components, namely, development of the mathematical model, followed by design and implementation of an SLA to test the model. The thesis concludes with a discussion on experimental results and findings and conclusions.

The major disadvantage of current SLA technology is that it is expensive. The setup cost involved for a Viper SLA-250 by 3D Systems is in the range of $NZ200,000 - $NZ250,000 depending on optional extras. The cost of the laser is considered to be a significant factor. Then there are the different costs of maintenance (i.e. software updates, calibration, and laser replacement) and consumables (i.e. resin and cleaning equipment). Resin costs range from $US150-$US350 per kilogram depending on the resin composition and supplier. Another major disadvantage is the build time due to the raster with which the laser cures the profile of a layer. Although this disadvantage is common to most rapid prototyping (RP) technologies, the lead-time of rapid prototyping should ideally be minimal or immediate.

Recent developments in stereolithography (SL) have aimed to increase the speed of the additive process of SLA. There has been a shift from the vector-by-vector processes to flashing or integral processes. In a vector-by-vector process, a layer is drawn using finite-sized lines whereas an integral process cures an entire layer in one exposure to irradiation. Integral curing, also known as projection-based curing, has been made possible by the advent of dynamic pattern generators such as LCD and

DMD. Dynamic pattern generators do away with the lasers that reduce the cost of SLA.

Modelling the integral process is of interest to rapid prototyping (RP) so as to understand the physical and chemical factors affecting the parts produced. A model aids in process planning of the new technique and design of the SLA.

The primary object of this thesis is broken down into the following sub-objectives:

- The cost of the SLA is restricted to a limited project budget of $NZ10,000. Most companies are reluctant to purchase expensive technology that requires a large initial setup along with potentially high ongoing maintenance costs.
- The SLA must accomplish the integral process for fabrication of parts. A projector utilizing DMD technology has been donated to the research project by the College of Sciences at Massey University.
- The SLA must use UV light to cure an epoxy-based photopolymer resin. This objective sets the research apart from SLA that fabricate parts using the visible light spectrum and acrylic-based resins.
- The SLA is expected to cure a reasonably large area. Medium to large sized parts should be built. A field of exposure of 200mm x 270mm or larger is expected. This objective was chosen by general observations of commercial SLA build envelopes.
- A mathematical model must be found or created to model the SLA design proposed. The mathematical model is expected to account for the particular design of the SLA. The model proposes to give an understanding of what curing characteristics to expect over an integrally cured layer.

The sub-objectives above gave a general guideline for the development of the research work. Refinement of the objectives was a continuous part of the research methodology and design process.

This thesis is written for anyone with an interest in and knowledge of engineering, science and mathematics. Knowledge of chemistry fundamentals is helpful but not essential for the reader. The thesis is written so that a reader with little knowledge of rapid prototyping will be able to understand the basics and what is trying to be achieved by this research. The thesis is written with future development of the theory and experimental tests in mind. In this way, the thesis can be consulted by researchers around the world.

1.2 The Need to Model the Integral Process

SLA technology has established itself as a rapid prototyping technology that offers designers increased resolution of prototyped models. With SLA technology, the slice thickness ranges from around 0.01mm to 0.25mm per slice, and this determines the resolution (quality/ surface finish) of models.

As all of the RP systems available can produce physical objects, there are many overlapping strengths and limitations. Some are faster and better at certain aspects of prototype creation than others are. Therefore, to determine which process is best is dependent on what outcome is required. For example, designers may use an Fused Deposition Modelling (FDM) RP machine purely for aesthetics of small to medium size parts, while the use of SLA is better for more detailed aesthetics and functional testing.

One problem with the SLA process happens at the layering stage. Prototypes require relatively long production times, which have only been reduced by minimal amounts with the use of efficient lithography tracing algorithms (Yang et al, 2001). Often prototypes are set up and left to run during the day when the operator is present in the factory. The operator can monitor the model's 'build' progress throughout the day. However, for parts that require longer build times, say more than 12 hours, the operator needs to be able to leave the SLA machine running unattended, i.e. overnight. Problems can occur during this time that may compromise or ruin the part, requiring a completely new part to be built from scratch. It is important to note that this problem does not make the overall process of rapid prototyping slow. The overall process is indeed quite fast in terms of 'product idea', right through to time-to-market.

One way to build parts efficiently is by processing many parts on the 'build' platform at the same time. This is faster and more efficient than building parts individually in a one-at-time process like CNC machining.

Another problem arises where some parts may not have enough supports to be built correctly and delamination occurs. Delamination occurs when a small section of a layer (usually on edges such as points or overhangs) does not bond to the previous layer and so floats freely in the resin. The result is that delaminated fragments float into neighbouring parts, which in turn ruins those parts.

One disadvantage of laser-based SLA is the build time due to the laying process. There are several steps that determine how much time is used to effectively build a

layer. These steps include the raster time with which the laser cures the profile of a layer (the layer thickness and laser power effect this time), the time it takes to move the elevator to the next layer position, and the levelling time to allow for the resin to settle before the next layer begins. These steps all take time and require more efficient, innovative techniques to improve the overall lead-time to build parts.

An analysis of the above issues with a mathematical model helps to find and provide solutions. Modelling the layering process can provide an understanding of several factors or process parameters. Temperature effects, light flux density, resin chemistry, layer thickness, and material tensile and shear strength are all parameters that can be modeled to understand the effects that each have on the end product. Parameters can be subdivided into fixed and variable process parameters. Knowing what process parameters are available allows for more informed control of the overall system. The primary objective of this research aims to use a mathematical model to predict the required control of a dynamic pattern generator, which cures geometric profiles with a photopolymer resin.

1.3 What is Rapid Prototyping?

The manufacturing companies of today are faced with the challenge of unpredictable, high frequency market changes in both local and international markets. These are results of shorter product development times, changes to existing products, fluctuations in product demand, and changes in processes and technology. To be successful, rapid time-to-market of new products is critical in the midst of highly competitive markets (Krar and Gill, 2003).

Rapid Prototyping (RP) is one technology that has aided in shortening product development times and costs. RP is a relatively recent technology that allows the creation of complex three-dimensional parts or models. These models are created on computer using computer-aided design (CAD) packages. Then the RP machine's software package takes the CAD model data, carves it up into thin slices, and then builds the model, one slice at a time into a physical model.

A prototype is a common term used in any engineering design process. Dictionary.com defines the word “prototype” as the following (Lexico Publishing Group, 2000):

"**pro·to·type** (prō'tə-tīp') *n.* An original type, form, or instance serving as a basis or standard for later stages; an original, full-scale, and usually working model of a new product or new version of an existing product."

In engineering terms, a prototype usually means more than this. The following definition covers most definitions of a prototype as applied to engineering design:

"An approximation of a product (or system) or its components in some form for a definite purpose in its implementation." (Chua et al, 2003)

It is important to note the difference between a prototype and a model. A model is a representation of a device or a thing whereas a prototype is the first of its kind. The difference between the two is discernable by knowing the intent behind their creation and the environments in which they are to be tested. Designers testing parts in controlled environments allow for a better understanding and control of the parameters tested. Prototypes are used to verify that a product will function as designed for their real-world environment (Dym and Little, 2004). However, there are limits to a rapid prototyped part. A functional test performed on a prototyped part should be within the physical limits of the build material. The build orientation of a prototyped part greatly affects the physical limits of the build material.

RP aids product development and engineering design in several ways. First, there is visualization. Prototypes can be purely for aesthetic reasons. No matter how good a computer aided design (CAD) image looks, there is something comforting about having the actual part in your hands. The complex geometries of a part can often lead to confusion and misinterpretation if read purely from blueprints and drawings. The physical visualization of a part reduces these types of errors.

One of the main advantages of RP is that it speeds up product design verification. Through quick design and error debugging and elimination, rapidly prototyping parts show great cost savings over traditional methods in the total product life cycle (Wohlers, 1999). Rapid Prototyping enables designers to test out their ideas and concepts before making tooling for moulds and fixtures. Having parts rapid prototyped certainly reduces the costs involved in designing products and it reduces product time-to-market. Supplying complete parts and assemblies within a 24-hour period is very common.

An example of how verification works is through design iteration. Several designs can be rapidly prototyped and tested within a week. This represents considerable time saving over traditional methods which may take months. For example, flow tests performed on an impeller or pump may find problems or inefficiencies in the flow pattern. Then modification of the impeller design is performed and rapid prototyping a new part for retesting. All this development is accomplished in a day or two.

RP also works well for rapid fabrication. The ultimate aim is to manufacture 'real parts'. The materials available for RP machines are ever expanding. So far, the range of materials available includes metals, silicones, ceramics, plastics and rubber. Rapid prototyped parts are useful as patterns or moulds for investment castings. In this way a real casting of the prototype can be made without the need for creating expensive dies and tooling (Jacobs, 1992).

Rapid prototyping can be divided into four main areas: input, method, material and applications. These are shown in the Rapid Prototyping Wheel in Figure 1.1. Input - refers to the data format that represents a computer model. This is usually in the form of CAD files. It also includes the way a physical model is input transposed into digital form by reverse engineering technology, i.e. CMM (coordinate measuring machine). Method - refers to the way in which parts are created in the RP machine. This includes all the techniques that various machines employ. Material - encompasses all substances (solid, liquid or powder states) that are used in the creation of parts. Applications of RP are divided into three main industries. But there are always new application areas being found for RP (Chua et al, 2003).

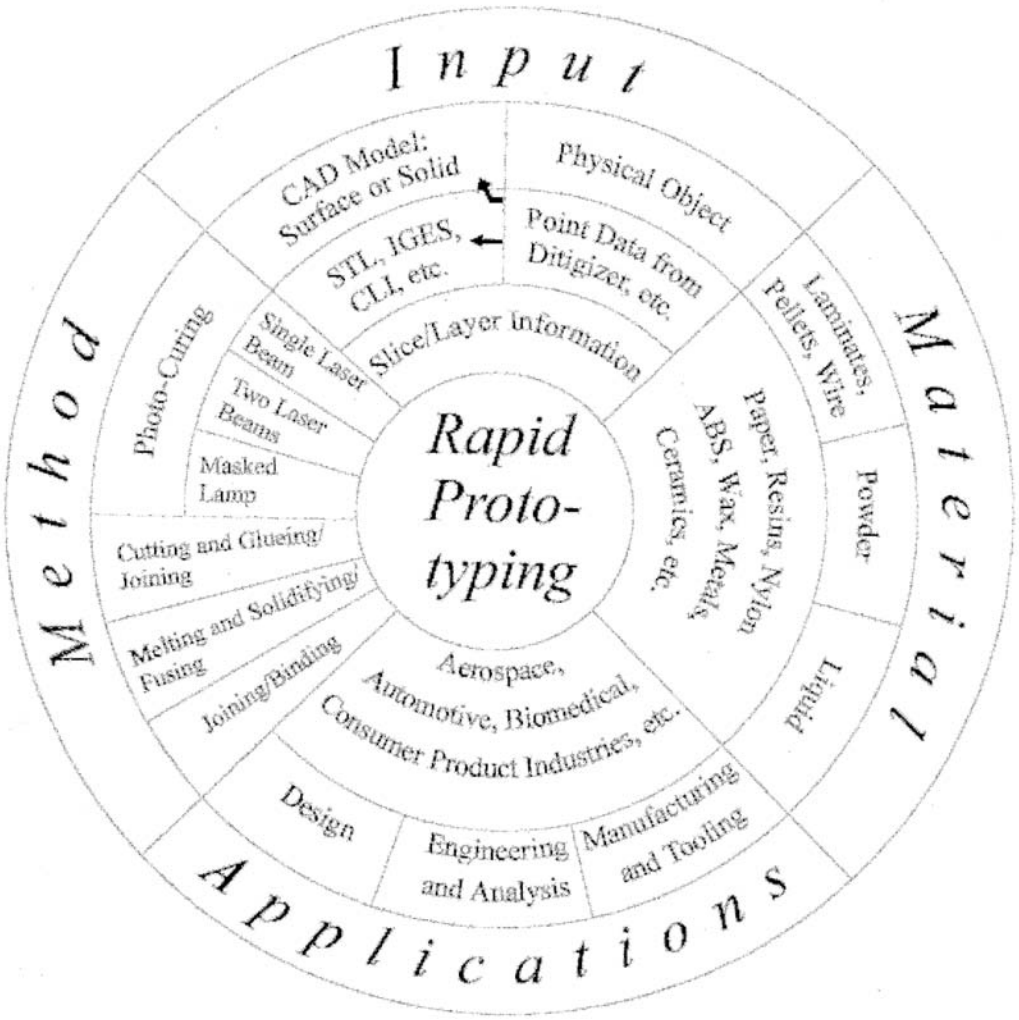

Figure 1.1 Rapid Prototyping Wheel (Chua et al, 2003)

The area of interest for this thesis work is mainly concerned with the Method section of the Rapid Prototyping Wheel (Figure 1.1). RP is important because of its ability to produce parts rapidly in time to meet market demands. The methods with which prototyped parts are created have a significant impact on delivery and cost of the part.

Another important criterion for rapid prototyped parts is dimensional accuracy. Dimensional accuracy depends on what RP technology is used to create the part. Some technologies use melting and solidifying of material in discrete amounts. Others may use bonding or lamination of layers followed by machining. Stereolithography (SL) is perhaps the most popular RP technology in the industry as it achieves the best dimensional accuracy for the price. Dimensional accuracy down to 0.01mm is reliably achievable. In general, an accuracy of ±0.1mm is acceptable for finely detailed parts as this offers the best time, cost and detail of a part's features.

SLA, (stereolithography apparatus) has historically been associated with liquid based RP technology. RP machines that use lasers to achieve the SL process are particularly known as SLA. However, the definition of the term SLA refers to any RP technology that achieves a layered manufacture of parts. For clarity in this thesis, the term SLA refers to liquid based RP machines.

The major disadvantage of current SLA technology, as mentioned at the start of this introduction, is the cost. Another major disadvantage is the build time due to the raster with which the laser cures the profile of a layer.

Integral processes are one of the recent developments in SL prototyping. Integral or projection-based curing has been enabled through the implementation of dynamic masking generators such as LCD (liquid crystal display) and DMD (digital micromirror device). Masking generators do away with the lasers, which reduces the cost of SLA. Also, the integral process of part fabrication reduces the build time of parts because the build time is independent of build area.

Modelling the integral process has benefits in providing an understanding of process parameters. A projector utilizing DMD technology has been provided for the research project by the College of Sciences at Massey University. The research uses a mathematical model for the curing of parts using the projector as a light source and dynamic pattern generator. The outcome of the research is expected to show some useful ways of applying the projector to cure parts in agreement with the mathematical model devised.

2 Overview of Rapid Prototyping

This chapter discusses the various forms of Rapid Prototyping in order to show how this thesis research fits within the Rapid Prototyping field. Section 2.1 begins with an overview of the current RP technologies available. Then section 2.2 describes the history of SLA and how a conventional SLA works. Section 2.3 reviews basic SLA fundamentals.

2.1 Overview of Other Commercial Rapid Prototyping Technologies

There are numerous RP systems available on the market. As seen in the Rapid Prototyping Wheel (Figure 1.1), they can be broadly categorised by the initial form of their build material, i.e. the initial material from which a prototype is formed. These categories are solid-based, powder-based, and liquid-based. Within these categories, the RP machines differ in the fabrication method of parts.

There are three fundamental fabrication methods (see Figure 2.1). Subtractive methods start with a solid block of build material larger than the final part. The desired shape is achieved by removal of material. Additive methods are the opposite of subtractive methods. Build material is added to the successive layers in order to build a part. Finally, formative methods use moulds or dies to form parts.

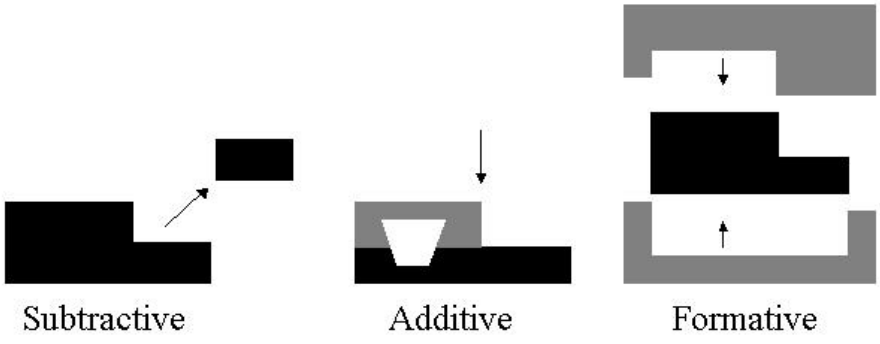

Figure 2.1 Three Fundamental Fabrication Methods (Chua et al, 2003)**.**

2.1.1 Solid-based Rapid Prototyping

2.1.1.1 Fused Deposition Modelling (FDM)

One solid-based technology is Fused Deposition Modelling (FDM). FDM is an additive process and employs the extrusion of a thermoplastic material through a nozzle. It works much like a MIG welder system where the extruded material is on a spool. The FDM machine builds each layer by essentially drawing the shape with the nozzle whilst extruding plastic for that layer. The nozzle heats the thermoplastic so

that thermoplastic is just above its melting point. The plastic cools down and hardens immediately after extrusion from the nozzle and bonds to the layer below.

Stratasys Inc., founded in 1989, is the manufacturer of FDM machines. Stratasys released their first machine in 1992. Currently there are seven FDM systems available ranging from small machines with build envelopes of 203mm(w) x 203mm(l) x 305mm(d) to very large envelopes with a 600mm(w) x 500mm(l) x 600mm(d) build envelope.

The FDM machine uses two types of build material. The extrusion head is fitted with two nozzles. One is for the model; the other is for support material. Support material acts as a scaffolding structure that allows the model material to build on top of the support material, for example, where a part has overhangs. There are differing chemical properties between the two build materials that prevent them bonding to each other. This allows for easy separation of the part from the support material. Support material is also available in a water-soluble form. These supports dissolve in water and separation of supports from parts becomes much easier.

The FDM method results in a reasonable surface finish and dimensional stability. The resolution of layers that can be made range from 0.178mm to 0.356mm and the horizontal width of the extruded material vary between 0.25mm to 0.965mm (Chua et al, 2003; Stratasys, 2005). The final part has properties similar to that of ABS plastic. Other materials available for this process include wax for investment casting models.

There are several advantages of FDM. The option of water-soluble supports is available which reduces the time for post processing of parts. FDM is a clean process and does not use toxic chemicals. An FDM system is capable of running in an office environment for this reason. Parts are functional once the supports are removed and suitable for testing.

Disadvantages include slow processing due to raster of layers, restricted accuracy and unpredictable shrinkage. The process is slow because each layer is dependent on the amount of solid area filled by build material. The nozzle size limits the accuracy of parts. Some part features may be too small to manufacture.

2.1.1.2 Laminated Object Manufacturing (LOM)

Laminated Object Manufacturing (LOM) is another additive solid-based RP technology. Michael Feygin developed the LOM process in 1985 making it one of the older methods. His company Helisys Inc sold LOM machines, but the demand for the

LOM machine was less than expected and Helisys Inc. closed down in November 2000. In December 2000, Feygin established Cubic Technologies to manufacture LOM systems based in Carson, California.

The LOM system is supported with a software package called LOMSlice. LOMSlice performs the slicing up of STL CAD files into cross sections. It manages the slicing algorithm for the CAD file that divides it into layers and also controls the motion of LOM system to laser-cut 2D profiles for each layer. A range of materials is available such as paper, plastic film, ceramic and composite sheets. These materials are supplied to the machine in roll form. The LOM system has an X-Y positioning system that carries two mirrors that reflect the beam of a CO_2 laser onto the surface of the build material. The positioning system has an accuracy of ±0.127mm in the X- and Y-axes. The laser is finely focused to only cut through one layer thickness. The computer generates the motion paths of the laser. The laser burns out the part's profile and creates a crosshatch pattern with the unwanted areas of build material. The excess build material is used as support material and is later removed from the part due to the crosshatch pattern. The build material contains heat-activated glue on the top of each layer. Once a layer is complete, the build platform is lowered and a fresh layer of build materials is advanced from the roll. The platform is then raised and a thermal roller binds the new layer to the previous layer.

The main advantages of LOM are reduced product development and cost. Advantage is the part size. The maximum build size is 813mm(w) x 559mm(l) with a height of 508mm. Parts of this size can weigh up to 204kg. Other advantages include a variety of inexpensive materials, dimensionally accurate parts and virtually no internal stresses. LOM has a fast build time compared with other RP technologies. The laser does not have to scan the entire surface area of a layer. It only cuts the perimeter of the profile for each cross-section and the crosshatch pattern.

LOM is not suitable for thin walled parts especially in the Z-axis. This is because the part is not rigid enough in the Z-axis to withstand post processing. When the crosshatched material is removed, thin walled features are often easily broken. Removal of support material can be very time consuming and is usually done with the use of wood working tools. Often a person removing supports must be aware of the delicate parts of the part. Another disadvantage of LOM is that parts are not suitable for vigorous functional testing. The bonding adhesive and not the build material limit the strength of the part. In addition, parts are usually coated with urethane, epoxy, or

silicon spray to prevent the absorption of moisture, which results in expansion and warping of the part.

The finish is similar to that of wood, and the part can then be worked on as if it were wooden. LOM is still often used to produce patterns for sand-casting, investment casting and rubber moulding. It is also used for concept models and vacuum forms.

2.1.2 Powder-based Rapid Prototyping

2.1.2.1 Selective Laser Sintering (SLS)

Powder-based build material is often considered as solid state. However, it has its own category, as build material has intentionally been made into a powdered form (Chua et al, 2003). One powder-based rapid prototyping is known as Selective Laser Sintering (SLS) and is based on research at the University of Texas. The SLS system was developed under the DTM Corporation established in 1987. The first commercialised systems were available in 1992. DTM was taken over by 3D Systems in August 2001. Since then, SLS technology has gone through five generations of products. Improvements have been in part accuracy, speed, smoother surface finish and finer resolution. There are two SLS systems supplied by 3D Systems called Sinterstation HiQ and Sinterstation Pro series. Sinterstation Pro has the largest part size available with SLS technology with parts sizes up to 550mm x 550mm and 750mm in height. However, Sinterstation Pro is only designed to produce plastic parts. The Sinterstaion HiQ works with a variety of materials such as thermoplastics and composites, metals and ceramics. It can produce parts up to 381mm(w) x 330mm(l) and 457mm in height. Both systems have a layer thickness that can be 0.1mm or 0.15mm. In the XY-axes, the resolution is limited by the diameter of the laser beam, which is 0.4mm and 0.5mm for the HiQ and Pro systems respectively.

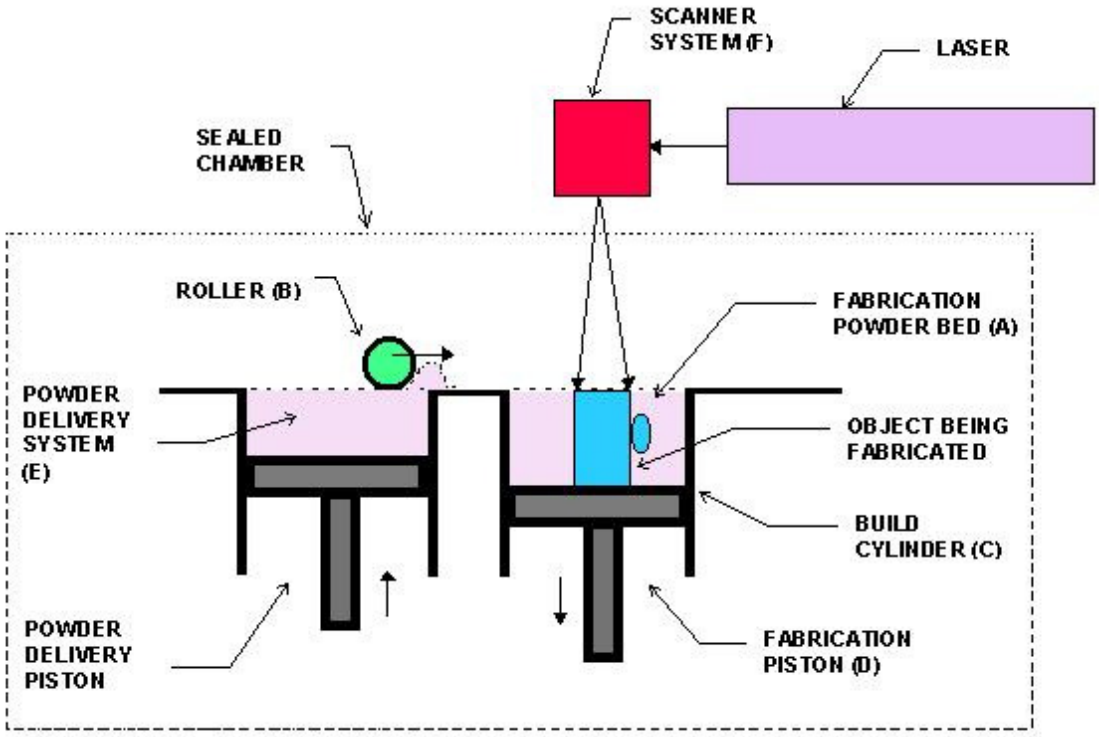

Figure 2.2 Selective Laser Sintering (SLS) Layout (Castle Island Co, 2007).

SLS uses material made up of micro particles to form a powder. A layer of powder is spread in the desired thickness from reservoirs on either side of the SLS machine. Spreading is done with a roller mechanism that passes over the powder bed as shown in Figure 2.2. The cross-sectional layer of the part is then scanned or drawn by the infrared heat-generating CO_2 laser. Where the laser strikes the powder, the powder temperature is raised to the melting point. The powder particles fuse together and form a solid mass. Successive layers also fuse with previous layers. Once the cross-section is scanned the powder bed is lowered one layer thickness and the process repeats until the part is completed.

SLS results in a good surface finish and excellent dimensional stability. Little post post-processing is required. If necessary, particle or sand blasting is done to smooth surface finishes. SLS parts are porous due to the sintering process. Usually post curing of parts is not necessary, but to improve the mechanical properties of the part, parts can be infiltrated with another material. SLS can produce parts for both aesthetic and functional testing. The main advantage of this technology is that it can work with a variety of materials provided that they are in powered form. No supports are needed as the unsintered powder acts to support the part as it is made.

A major disadvantage of SLS is the cost. SLS is the most expensive rapid prototyping system available at over $750,000 per SLS. Another disadvantage is the high power consumption due to the high wattage laser used. Often the powder bed is heated to reduce the amount of energy required from the laser to bring the powder to the glass-transition state.

2.1.2.2 3D Printing

3D printing is one of the more recent solid-based technologies. The idea of 3D printing was developed at the MIT, Massachusetts in the mid 1990s. The MIT now licenses out its patents to several companies.

3D printing uses standard inkjet technology to print each slice of the model, one layer on top of the other until the model finishes. The build process starts by depositing a thin layer of fine starch powder on the fabrication piston as shown in Figure 2.3. Using the Z-Corp Spectrum Z510 as an example (Z Corporation, 2008), layer thickness can range from 0.089mm – 0.203mm. The build platform of the Z510 is 254mm(w) x 356mm(l) x 203mm(d). The inkjet head puts down 50-100µm diameter droplets in the profile of the slice required. The droplets act as glue binding the powder together. The XY resolution is usually given in dots per square inch (dpi). The Z510 provides a resolution of 600 x 540dpi and uses four printheads. The last step in the process moves the fabrication down one layer thickness before the process begins all over again.

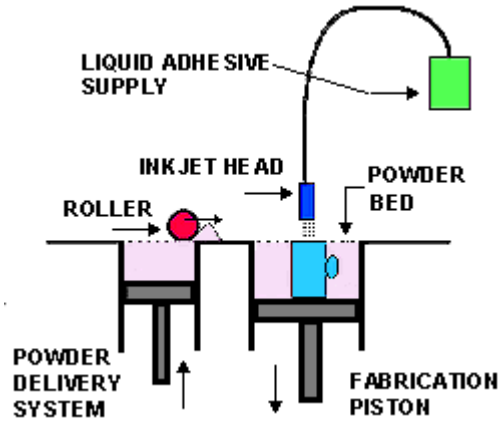

Figure 2.3 3D printing process (ESG Associates Corporation, 2003).

3D printing has several advantages. The process is relatively fast when compared with the other RP technologies. The print heads are often multi-head like the Z-corp machine, which cover a greater area of the layer to be printed. Another advantage is

that parts can be printed in colour. In addition, the cost of buying a 3D printer is very cost effective and cheap to run and maintain.

The 3D printing method results in a reasonable surface finish and reasonable dimensional stability. The most commonly used materials are starch or plaster, so the models are not very strong or durable. This property of the materials used in 3D printing is the biggest disadvantage. However, parts can be further strengthened by infusing them with wax or epoxy. In general, parts made using 3D printing are only used as aesthetic models and are not suitable of functional testing.

2.1.3 Liquid-based Rapid Prototyping

SLA is a form of liquid-based rapid prototyping. SLA is an abbreviation for Stereolithography Apparatus. SLA build objects a layer at a time by tracing a laser beam on the surface of a vat of liquid resin. The resin is of a class of materials, which was originally developed for the printing and packaging industries. The resin quickly solidifies wherever the laser strikes the surface of the liquid. The SLA controls the laser beam and draws one model slice or layer at a time. Once one layer is completely traced, the build platform is lowered a small distance into the vat and a second layer is traced right on top of the first. The self-adhesive property of the material causes the layers to bond to one another and eventually form a complete, three-dimensional object after many layers are formed.

Support structures, in the form of a fine lattice structure of cured resin, are needed to maintain the structural integrity of a part. They support overhangs, as well as provide a starting point for the overhangs and for successive layers on which to be built. After the part is fully built, the support structures are removed and the part is cleaned in a bath of solvent and air-dried (De Laurentis et al, 2004).

This method can produce parts for both aesthetic and functional testing. SLA is generally considered to provide the greatest accuracy and best surface finish of any rapid prototyping technology. The technology is also notable for the large object sizes that are possible with the use of “mammoth” SLA machines.

On the negative side, working with liquid materials can be messy and parts often require post-processing to remove support material and post-curing operation in a separate oven-like apparatus for complete cure and stability.

2.2 History of SLA

Rapid prototyping is a result of several important technologies. The increased power and capability of computers has lead to the development of more and more advanced manufacturing technology. These include Computed-Aided Design (CAD), Computer-Aided Manufacturing (CAM), and Computer Numerical Control (CNC) machine tools. The complex geometries that RP can create would not have been possible without the development of CAD (Chua et al, 2003). Other technologies that have lead to RP are mechanization, commercial lasers and commercial robots.

In order to understand how far rapid prototyping systems have come in the past decade, it is important to look back at the first systems developed. Stereolithography was the first type of rapid prototyping systems to appear. Research into the concept of rapid prototyping began as far back as the late 1970s. Three researchers, A. Herbert of 3M in Minneapolis, H. Kodama of the Nagoya Prefecture Research Institute in Japan, and C. Hull of Ultra Violet Products Inc. (UVP) were separate researchers that began development of their own concepts for rapid prototyping. Herbert and Kodama faced problems with support for their research. Hull, backed by UVP, continued his research and was able to develop a complete system. In 1986, his system was patented and 3D Systems Inc. was founded to develop a commercial machine. The first machine was released at the AUTOFACT Show in Detroit in 1987. This machine was called the SLA-1 and was superseded by the SLA-250 in 1989. Now named the Viper SLA-250, it has been one of the most popular systems used around the world (Jacobs, 1992). 3D Systems now supply a range of the SLA equipment such as the SLA-5000, SLA-7000, Viper SLA, and Viper HA SLA (3D Systems, 2007).

Typical composition of an SLA is shown in Figure 2.4. The layout includes a light source, optics and an X-Y positioning device, a vat of resin, build platform, a recoating system, and a high accuracy motion control system.

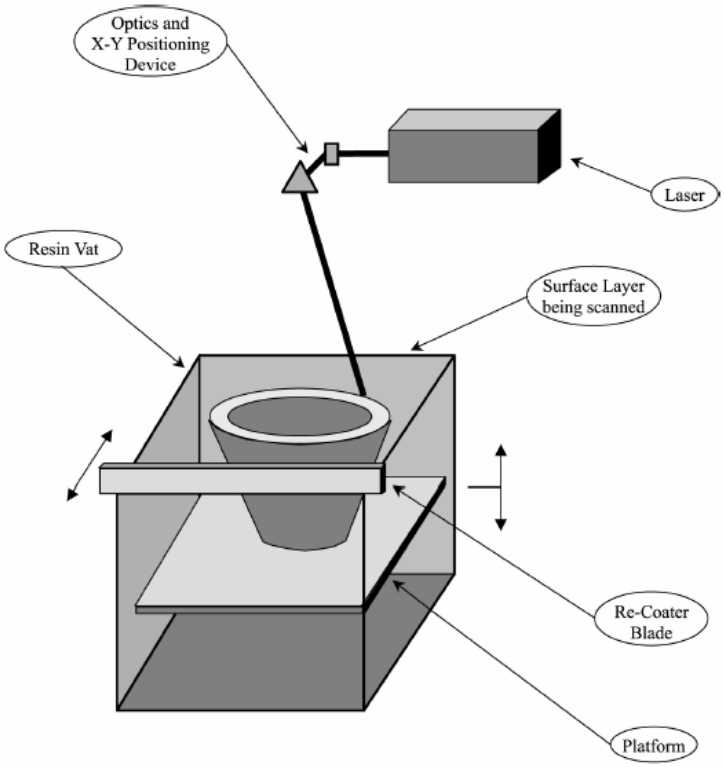

Figure 2.4 Typical composition of SLA (Upcraft and Fletcher, 2003).

The Viper SLA-250 has one of the highest resolutions among the RP technologies. The light source used is a solid state Nd:YVO_4 (Neodymium Doped Yttrium Orthvanadate) laser. The laser produces a 100mW ultraviolet beam with a wavelength of 354.7nm. The beam width is 0.25mm in standard mode and 0.075mm in high resolution mode (3D Systems, 2007). The laser passes through collimation lenses onto two galvo mirrors (see Figure 2.5). A galvo mirror is essentially a stepper or servo motor with a mirror attached to the axle. Galvo mirrors guide the laser beam in the X and Y axis. There is a trade off between the accuracy and speed of the galvo mirrors. The faster the speed the less accurate the position of the mirrors becomes. The performance of the galvo mirrors is 5m/sec with an accuracy of ±50μm on the SLA-250 (Sachs, 1997).

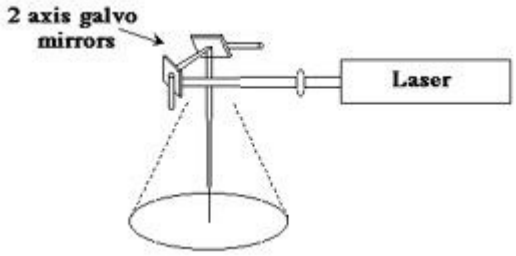

Figure 2.5 The setup of two galvo mirrors (Sachs, 1997).

The build platform has a build area of 250mm (width) x 250mm (length). The build platform rests on an elevator mechanism that has high enough resolution to

move the build platform in very fine steps of 0.0025mm. The elevator is capable of moving at up to 5mm/sec. The vat holds a volume of 32lt of photopolymer resin which is temperature controlled between 25-27°C. 3D Systems have a patented recoating system called the Zephyr™ recoating system that is able to spread a precise layer thickness over a previously cured layer. The Zephyr blade is equipped with a vacuum pump that sucks resin from the sides of the vat into a reservoir inside the Zephyr blade thus being able to spread an even recoated layer.

The major disadvantage of current SLA technology is the cost. The setup cost of a Viper SLA-250 is in the range of $200,000 - $250,000NZD depending on optional extras. Then there are the costs of maintenance (i.e. software updates and lasers) and consumables (i.e. resin). Another major disadvantage is the build time due to the raster with which the laser cures the profile of a layer. Although this disadvantage is common to most RP technologies, the lead time of rapid prototyping is always wanted to be minimal or even instant.

2.3 SLA Fundamentals

Conventional SLA use lasers to cure a photopolymer resin. The levelling system controls the layer thickness of resin cured by the laser. The levelling system is a combination of an elevator mechanism, recoating blade and a level sensor. The layer thickness to be polymerised is governed by the amount of resin recoated onto the previous layer. As the laser scans across the surface of the new layer, excess laser radiation penetrates the previous layer slightly, increasing the cure in the previous layer. Where a layer is part of an overhang or the very first layer, the laser irradiation penetrates down into the vat and attenuates by the initiator absorption according to the Beer-Lambert law of absorption. The Beer-Lambert law states that the intensity of light transmitted by an absorbing material decreases exponentially with the part length through the material (Atkins & de Paula, 2005). According to the Beer-Lambert law, the laser irradiation, E (mJ/cm^2), decreases exponentially with depth, z, and is expressed by (2.1.

$$E(z) = E_0 e^{-z/D_p} \tag{2.1}$$

where D_p is the resin's penetration depth at the laser wavelength and E_0 is the laser irradiance at the resin surface.

Deviations from the Beer-Lambert law can occur depending on the photopolymer composition and photoinitiator characteristics. Deviations are predominant when the initiator shows "photobleaching" or when the whole formulation is optically inhomogeneous and scatters the laser beam. Photobleaching is the overexposure of excitatory light by a photopolymer that results in the extinction of fluorescence and loss of light absorption. Photobleaching leads to larger cure depth than predicted.

2.3.1 Penetration Depth, Critical Exposure and Cure Depth

Penetration depth (D_p), critical exposure (E_c) and cure depth (C_d) are three parameters of a photopolymer that describe the behaviour of the photopolymer when it is exposed to actinic light. Penetration depth is the distance at which the light intensity is reduced to about 1/e times its value on the resin surface. This is not to be confused with C_d, which is the distance to which the resin transforms from liquid to solid. E_c is the amount of energy required for the resin to reach its gel point (the state between liquid and solid). E_c is the threshold value that is required for polymerisation of the resin to proceed. This threshold is primarily caused by oxygen inhibition. All three parameters are related by the cure depth equation (Jacobs, 1992).

$$C_d = D_p \ln\left(E_{max} / E_c\right) \tag{2.2}$$

The cure depth equation is found by insertion of the manufacturer's test data that characterizes the photopolymer resin (usually given on the resin datasheet), into (2.2. When the C_d is plotted against the UV exposure (E in mJ/cm^2) using a semi-log plot the result is a line known as the resin's working curve as seen in the example in Figure 2.6. From the working curve, the penetration depth (D_p) and the critical exposure (E_c) can be found. D_p is the slope of the line and the E_c is where the line intercepts the x-axis. E_{max} is the maxium exposure incident on the resin surface.

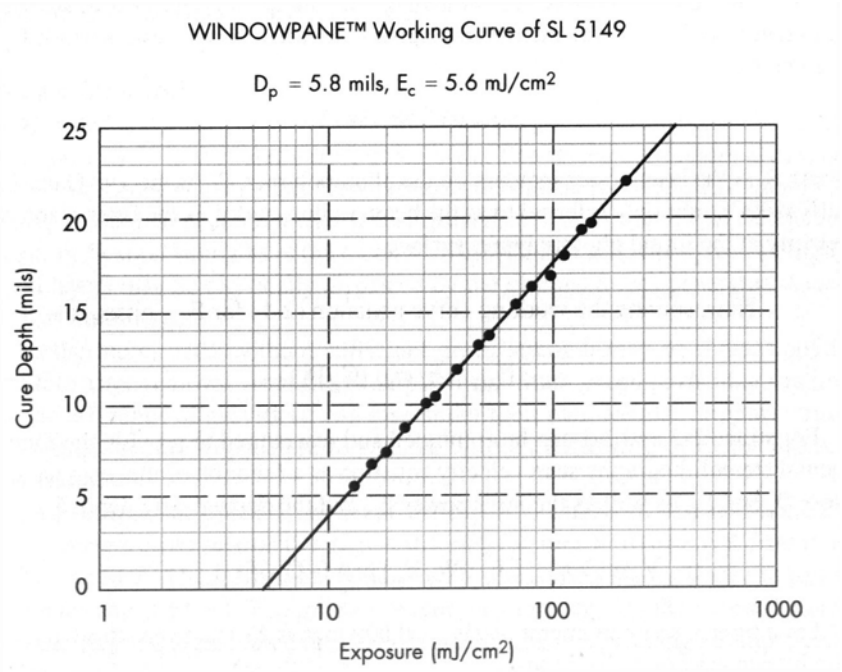

Figure 2.6 Working curve of SL5149 photopolymer (Jacobs, 1992).

2.3.2 Laser Exposure

One reason that lasers are preferred over incandescent or arc lamps is because the irradiance time required to achieve photopolymerisation is in milliseconds as opposed to several seconds with arc lamps. Arc lamps are limited by the photon flux reaching the exposed area, however, the exposure is independent of the area. Lasers are dependent on the area to scan and have to incorporate a scanning velocity parameter in exposure calculations.

The solid state laser capitalizes on the unique properties of certain elemental crystals to generate an ultraviolet laser beam. At the heart of the laser cavity is a Neodymium-doped Yttrium Vanadate crystal (Nd:YVO_4). The Nd:YVO_4 laser then emits a different frequency of infrared light.

The Nd:YVO_4 laser has another crystal known as the Q Switch. This crystal acts as a light diffracting device. When light is allowed to pass straight through, a short pulse of high-intensity infrared laser light is released. These pulses last 10 billionths of a second.

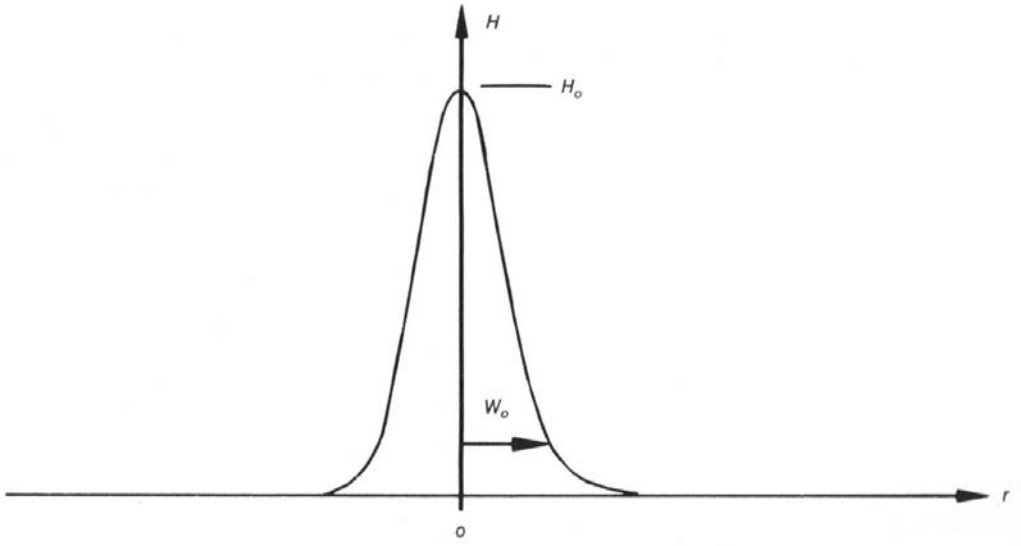

Figure 2.7 Gaussian half-width profile of beam intensity (Jacobs, 1992).

Lasers deliver high irradiance because they bring highly collimated light to a focus that intersects with the resin surface. The profile of a laser used in conventional SLA is typically gaussian. Figure 2.7 shows the shape for the laser profile in terms of intensity, H. A laser's spot size is defined the gaussian half width, W_0 (or sometimes written as ω_o) which is the radius of the laser beam where the intensity drops to $1/e^2$ (≈13.5%) of the intensity at the beam axis. The beam diameter ($2W_0$) in a conventional SLA is about 0.25mm.

The peak surface irradiance, H_0, is found by formulating the integral of the profile and solving for H_0 at r = 0 (with z = 0) given the following result (Jacobs, 1992):

$$H_o = 2P_L / (\pi W_o^2)$$

(2.3)

The average irradiance density is found by dividing the laser power with the area of the laser spot on the resin surface. The laser power, P_L, is specified at the wavelength used by the laser. Thus, average irradiance density is:

$$H_{av} = P_L / (\pi W_o^2)$$

(2.4)

The time of exposure, t_e, that the laser spot occupies a certain area for a given scanning velocity, V_s, is derived by:

$$t_e = 2W_o / V_s$$

(2.5)

The average irradiation, E_{av}, received by any area in the lasers path is thus:

$$E_{av} = H_{av} \times t_e$$

(2.6)

According to quantum theory, a ray of a certain wavelength consists of a stream of photons allowing calculation of the photon flux (photons per area) from Plank's equation for the photon energy (Joules per photon):

$$E_{ph} = \frac{\mathrm{hc}}{\lambda}$$

(2.7)

$$N_{ph} = \frac{E_{av}}{E_{ph}}$$

(2.8)

where h is Planck's constant (6.62 x 10^{-34} Joule.sec), c is the speed of light (3.00 x 10^{8} m/sec and λ is the wavelength of the laser. From (2.7, the shorter wavelengths have more energy than longer ones. (2.8 shows that the greater the intensity of a ray, the greater the number of photons.

2.4 Summary

In this chapter the various forms of Rapid Prototyping have been described. The quality of SLA as a prototyping standard has been reported. A brief history of the SLA form of prototyping has been provided. A brief explanation of how the conventional SLA work was given including the basic fundamentals of resin chemistry and laser technology. This information shows how far liquid based prototyping has been researched to the present day.

Now that the basic concept and fundamentals of SLA prototyping have been discussed, the next chapter reviews selected literature available on SLA and details how SLA technology has been researched and developed over the last decade.

3 Review of Integral Stereolithography and Related Research

This chapter is a literature review on the types of SLA that have been developed over the years. An understanding of what enabling technologies there are for fabricating layers by integral stereolithography is explained. Then the remainder of the chapter presents summaries of various research projects that fit into the following categories: SLA implementing DMD, SLA implementing LCD, and novel variations of SLA.

3.1 Types of Dynamic Pattern Generators

Dynamic pattern or masking generators have helped to enable the integral curing technique. The principle of integral stereolithography did not become feasible until the advent of dynamic pattern generators with adequate resolution in 1995. A dynamic pattern generator is able to display a bitmap that represents the two-dimensional profile of a layer to be cured. Software is used to slice a CAD file into these two-dimensional profiles that are oriented, scaled and converted to bitmap files (Bertsch et al, 2001). Liquid crystal displays (LCD) and new technology in the form of micro-electromechanical systems (MEMS), are now being used as pattern generators. MEMS are fabricated on a chip and include such devices as the digital micromirror device and the grating light valve (GLV).

Most of this new technology is only now becoming compatible with UV light. The resolution of current dynamic masks is more than adequate for small and micro scale part fabrication with the use of suitable optical systems. The size of the mask (i.e. super video graphics array (SVGA), extend graphics array (XGA), super extended graphics array (SXGA), etc.) in relation to the part size makes the integral curing approach more feasible and the fabrication of parts even more rapid.

3.1.1 Micro-electromechanical systems (MEMS)

Image projection technology has been able to advance in the form of micro-electromechanical systems (MEMS). MEMS is a technology that combines computer technology with micro-mechanical devices such as sensors, valves, gears, mirrors, and actuators embedded in semiconductor chips. Basically, a MEMS device contains micro-circuitry on a tiny silicon chip into which some mechanical device such as a

mirror or a sensor has been manufactured. Such chips can be built in large quantities at low cost, making them cost-effective for many applications.

MEMS finds applications in image projection technology as optical switching devices that can switch light signals over different paths at switching speeds up to 20-nanoseconds. Most advancement has been centred on projection TV systems.

Modern projectors used in current TV systems may use either one of two approaches to image projection. One method is known as transmittive and the other method is known as reflective. The transmittive method shines light through the pattern generator (i.e. a CRT tube or LCD panel) and then through the imaging optics. The reflective method uses the pattern generator to reflect light through the imaging optics.

3.1.2 Liquid Crystal Display

Liquid crystals exist as molecules in a liquid-like phase. Liquid crystal is neither a liquid nor a solid. The molecules are free to move around to different positions like a liquid but they maintain their orientation like the molecules of a solid. Most liquid crystals are rod-shaped and are categorised broadly as lyotropic or thermotropic. Lyotropic liquid crystals depend on the type of solvent they are mixed with and are used in the soaps and detergents. Thermotropic liquid crystals react to temperature and pressure change. Thermotropic liquid crystals are further classed into phases as isotropic phase or nematic phase. The difference between isotropic and nematic liquid crystals is the arrangement of molecules. Isotropic liquid crystals have random arrangements while nematic liquid crystals have a definite order (Tyson, 1998).

There are other several distinct phases with the more commonly known phase being the nematic phase (Tyson, 1998). The other phases are smectic and cholesteric. The differences in phases are usually in the orientation of the molecules as shown in Figure 3.1.

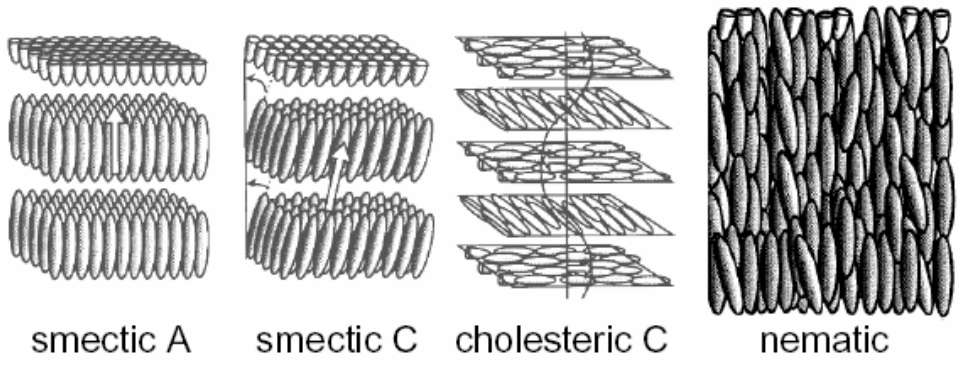

Figure 3.1 Phases of liquid crystal molecules (Mcartney, 2004).

Nematic liquid crystals are affected by electric current. There is a type of nematic liquid crystal, called twisted nematics, which is naturally twisted. When an electric current is applied to twisted nematics, they untwist to varying degrees depending on the magnitude of the current. In this way, the liquid crystals are used as a shutter that can control passage of light.

A liquid crystal display (LCD) works on the principle of using polarisers to control the amount of light passing through the display. A simple example of an LCD is shown in Figure 3.2. First there is a glass plate with a polarising sheet on the side closest to the incoming light. A special polymer is coated on the other side of this glass plate that creates microscopic grooves. The grooves lie in the same orientation as the molecules of the polarising sheet. The liquid crystal layer is composed of several layers of twisted nematics. A thin coating of nematic crystals is applied to the glass plate so that the grooves orient the first layer of crystals correctly. The same process is done to a second glass plate but it is rotated at 90 degrees to the first polarising sheet.

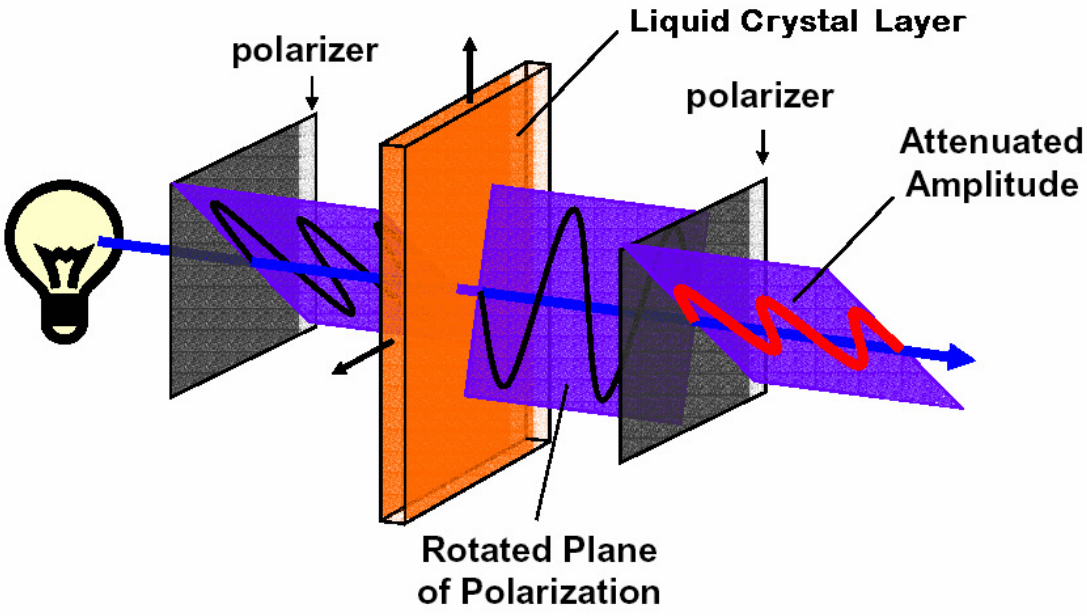

Figure 3.2 LCD structure (Mcartney, 2004).

Incoming light is polarized by the first glass plate and then the first coating of nematic crystals guide the light through the liquid crystal layer. The liquid crystals transmit and change the polarised light into the plane of vibration that matches their own orientation. When the light reaches the coating of nematic crystals on the second glass plate, it vibrates at the same angle as the grooves. Thus the final coating of nematic crystals is matched up with the second polarised glass filter and light passes

through. If a current is applied, the crystals untwist causing the angle of the light passing through them to no longer match the angle of the first polarizing sheet, thus blocking the light.

The practical fabrication of LCDs is quiet complex. An LCD is composed of thousands of pixels that are set up in a matrix. There are two approaches used to control the liquid crystal matrix. One is called a passive-matrix and the other is an active-matrix. In a passive-matrix, two glass substrates are used. One glass has columns and the other glass has rows made from a transparent conductive material (usually indium-tin oxide). These rows and columns are connected to integrated circuits that control the charge sent down a particular row or column. The liquid crystals are sandwiched between the two glass plates. To address an individual pixel in a passive-matrix, a charge is sent down the corresponding row and column. The charge causes the liquid crystals at that pixel to untwist.

The passive-matrix has simplicity but also a few major disadvantages. The response time is slow and charges are difficult to control. The slow response time causes “ghosting” of things in motion within the image. The imprecise control of charge means that the charge sent to a pixel has an influence on the adjacent pixels. Liquid crystals in adjacent pixels also partially untwist creating a blurred image and lack of contrast.

The active-matrix is a solution to passive-matrix problems. The addressing of individual pixels is achieved by having a layer of thin film transistors (TFT) arranged in a matrix on a glass substrate. When a pixel is addressed, the row is turned on and a charge is sent down the column. Because the only capacitor enabled to store a charge is at the intersection of the row and column, only that pixel receives charge enough to untwist the liquid crystals in that pixel.

There are a couple of major disadvantages with LCDs with regard to incorporating them in SLA. First, because an LCD is a transmittive device, light is absorbed by the liquid crystals leading to increased temperatures. As liquid crystals are extremely sensitive to temperature, the absorbed light can turn the liquid crystals in to a true liquid causing the LCD to operate incorrectly or not at all. In general, most LCDs that have been implemented on SLA only use the visible light spectrum as will be reviewed in Section 3.3.

Another disadvantage of LCDs is the fill factor. Fill factor is the ratio of area used by a pixel to the grid of wasted space that separates pixels from each other. The less

wasted space the higher the fill-factor becomes. This grid is visible to the observer in larger projected images. The grid is referred to as the “Screen Door Effect” due to its appearance. LCDs generally have a 50-60% fill factor.

3.1.3 Digital Micromirror Device (DMD)

The DMD comes from the field of entertainment media technology known as digital light processing (DLP). The DMD was invented by Dr. Larry Hornbeck in 1987 and developed by Texas Instruments (Texas Instruments Inc., 2005). The DMD is a chip that has anywhere from 800 to more than 1 million hinge-mount microscopic mirrors on it, depending upon the size of the array. Each mirror rests on support hinges and electrodes. Figure 3.3 shows some microscope images of a DMD array.

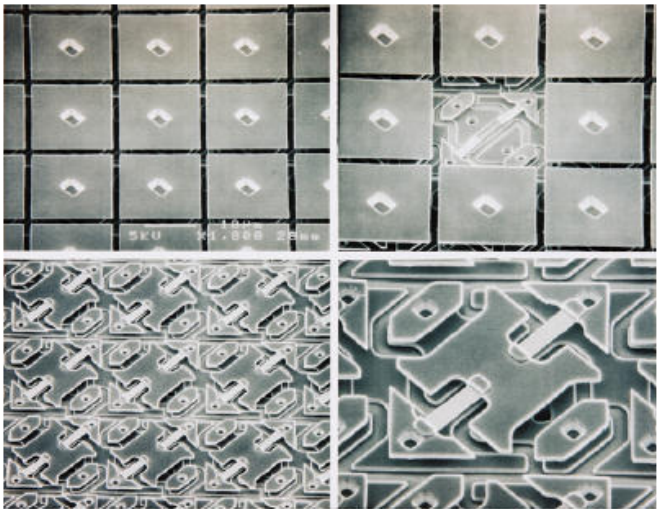

Figure 3.3 Enlarged view of DMD structure (Texas Instruments Inc., 2005).

The individual mirror size on a DMD is now as tiny as 13.7µm x 13.7µm and consists of three physical layers and two "air gap" layers as shown in Figure 3.4. The air gap layers separate the three physical layers and allow the mirror to tilt +10° or –10° (some of the latest DMDs allow ±12° tilt). The middle layer consists of two address electrodes (connected to SRAM) that are diagonally opposite each other and the torsion hinge and yoke mechanism (Figure 3.3, bottom right). When a voltage is applied to either of the address electrodes, the mirrors can tilt ±10°, representing "on" or "off" in a digital signal.

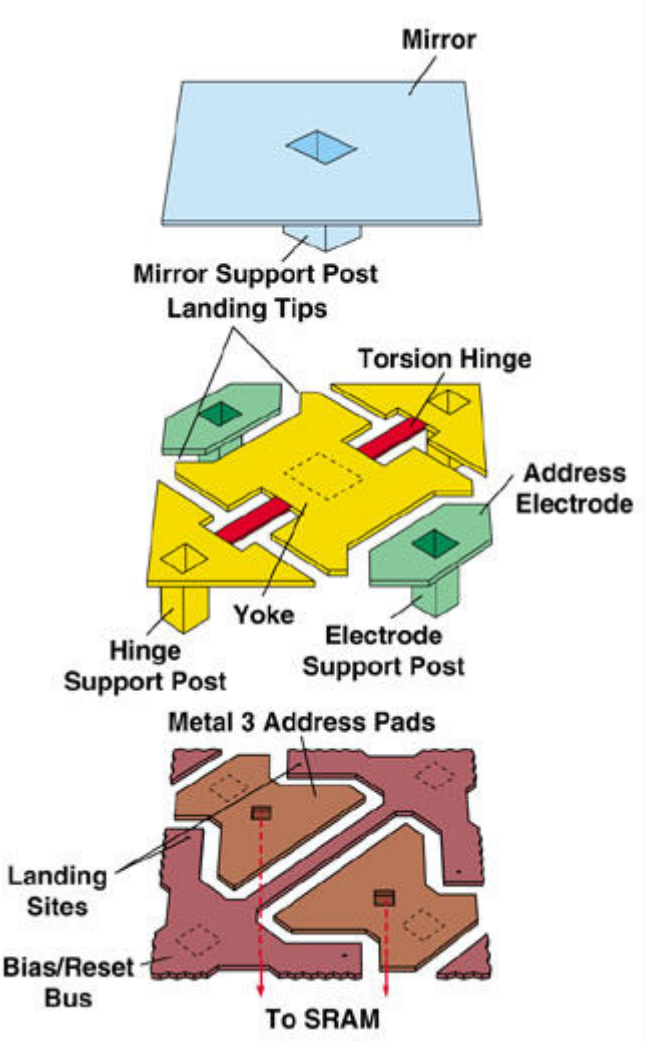

Figure 3.4 The three layers of the DMD (Texas Instruments Inc., 2005).

DMDs are found in many new multimedia projectors. The operation of the DMD is displayed in Figure 3.5. In a projector, the optical system conditions light before it reaches the DMD. Light hitting a micromirror that is in the "on" state reflects light through the projection lens to the screen. Light hitting a micromirror in the "off" state reflects light onto a light absorber. Each micromirror is individually controlled by SDRAM and is totally independent of all the other micromirrors. When all the micromirrors on a DMD chip are correctly coordinated and controlled, the resulting bitmap is reflected by the micromirrors through the imaging lens and on to a screen or surface. The system that comprises a projector's sophisticated electronic components is called Digital Light Processing (DLP) technology. This includes the digital video or graphic signal, the light source, the projection lens, and of course the DMD chip.

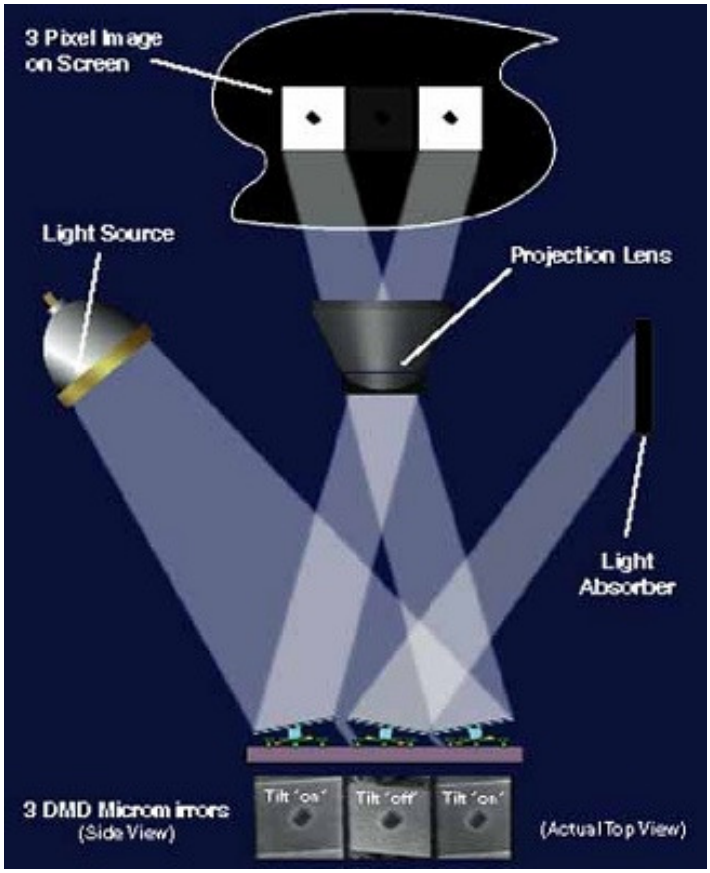

Figure 3.5 Operation of a DMD (Texas Instruments Inc., 2005).

The DMD was designed specifically as a visible light switching device. Early failure modes were explored in the 1990s. These included the hinge mechanism breaking, stuck mirrors, damaged mirrors due to handling, lifetime limitations due to high operating temperatures, and limited lifetime due to intense light (Douglass, 1998). Much effort has gone into the prevention of hinge breakage and stuck mirrors by the addition of spring tips (Douglass, 1998; Sontheimer, 2002)

Light exposure on the DMD is of interest when they are used in SLA as the UV light may damage or melt the mirrors. Douglass (1998) tested 300 DMDs by exposing them to intense, broad-spectrum light. The intensity is not stated. Some operated for more than 1000 hours and some operated for over 5000 hours. These tests showed no evidence that intense light exposure degraded DMD performance. However, Douglass noticed that more defects were occurring in DMDs exposed to UV light in the form of stuck pixels. A further test was done to discover if stuck pixels were a result of the UV light. Tests were conducted on actual projectors with different UV cutoff filters. Results showed that UV light below 400nm wavelengths caused the mirrors to stick. Now a UV filter is added to DLP optical paths to reduce the flux density to no more

than 0.7 mW/cm^2 below 400 nm (Douglass, 1998). Recent developments with DMD technology include DMD designed to work reliably with UV light.

DMD kit sets are available from several suppliers. However, the cost is expensive and the starter kit must be purchased first before any other accessories are bought. The costs of DMD are shown in Table 3.1. These costs prevent the option to buy a purpose-built DMD development kit for this research as the cost of the SLA is to be less that $10,000NZD.

DMD kitset	Starter Kit	Chip Set	Controller Board
VIS	$10,000US	$2,700US	$6,000US
UV	$13,000US	$6,000US	$8,700US

Table 3.1 Cost DMD (TyRex Services Group Ltd, 2007).

3.1.4 Grating Light Valves (GLV)

Another MEMS device is the grating light valve (GLV). GLV technology, licensed to Sony, was developed by Professor David Bloom at Stanford University, and is now produced by Silicon Light Machines in Sunnyvale, California (Kubota, 2002).

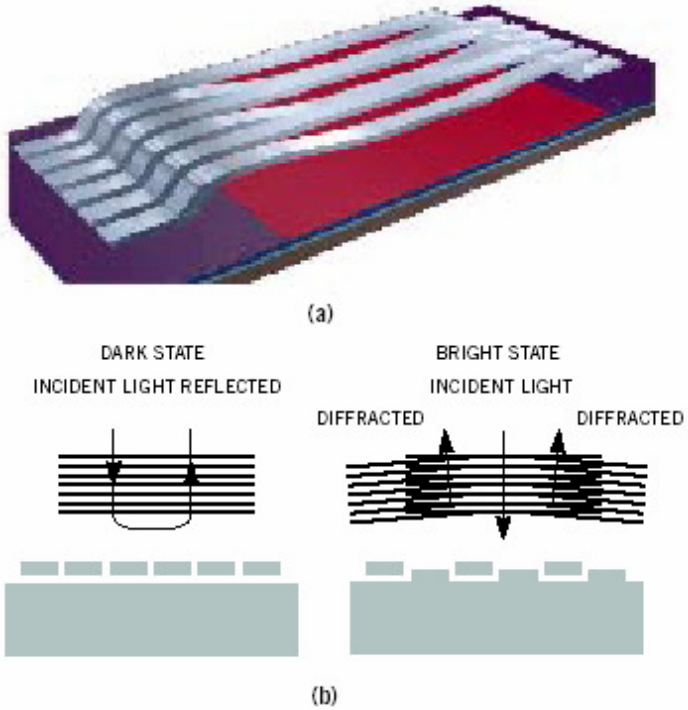

Figure 3.6 (a) Micro-reflective ribbons of the Grating light value. (b) Addressed ribbons flex and reflect pixels of an image toward the image plane (Lipman, 2000).

The GLV chip consists of micro-reflective ribbons mounted (Figure 3.6(a)) over a silicon chip. The ribbons are suspended over the chip with a small air gap between them. When a voltage is applied to the chip below a ribbon the ribbon moves toward the chip. The ribbon moves by a fraction of the wavelength of the illuminating light.

The deformed ribbons form a diffraction grating, and the various orders of light can be combined to form the pixel of an image as shown in Figure 3.6(b). The shape of the ribbons, and therefore the image information, can be changed in as little as 20 billionths of a second.

As the GLV is a recent development, the implementations of the GLV are limited to experiments with projectors. To construct a projector, the GLV pixels are arranged in a vertical line that is 1,080 pixels long. Light produced from three lasers, one red, one green and one blue, shines on the GLV and is rapidly scanned across the display screen at 60 frames per second to form the image.

A major advantage of GLV technology is that GLV chips can make high-resolution images at a relatively low cost. For example, because a 1,920 x 1,080 pixel image can be achieved by scanning a 1,080-pixel linear array, a GLV chip can be manufactured to achieve this resolution with only 1,080 pixels, instead of the 2 million needed for other technologies, such as LCD and DMD. Also, because the ribbons are aligned vertically, there are no horizontal gaps in the image, providing a much better quality image.

The GLV still needs to be tested to confirm whether it is suitable for the SL process. The thin ribbons of the GLV may not be suitable for UV light. Currently, there is no reported SLA using the GLV as a dynamic pattern generator.

3.2 SLA Implementing DMD Technology

The following section reviews implementations of the recent integral SLA research. Particular attention is given to SLA design specifics and theory. Most research experiments and apparatus have been conducted for microstereolithography. Nevertheless, the results from the research of each system describe challenges and requirements relevant to larger scale integral SLA. A summary of findings is given at the end of the chapter.

3.2.1 Ball Semiconductor, Inc.

Research conducted at Ball Semiconductor Inc. developed a unique application of the DMD for use on photoresist. The system, shown in Figure 3.7, used a low powered mercury lamp filtered for 435.8nm as a light source. The light was feed into the system through a fibre bundle. The DMD was UV enhanced and had 848 x 600 pixels. The first optical element was a 1:3 magnifying projection lens. The next

component was a micro-lens and spatial filter array (MLSFA) that focused corresponding DMD pixels onto what was considered as the first image plane. All the focal points are considered as a point array, which is put through a 5:1 reduction lens.

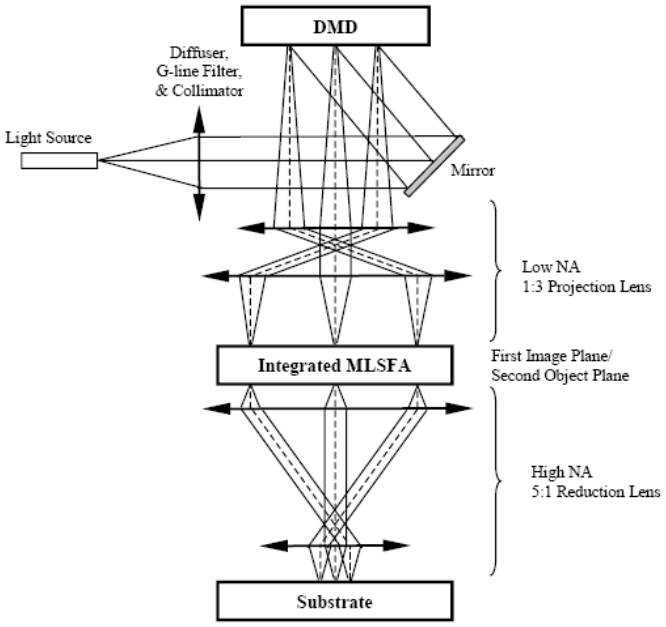

Figure 3.7 Block diagram of high-resolution lithography device (Chan et al, 2003).

The Ball Semiconductor system performed repeatable line-space patterns at 1.8µm making it a high-resolution device. The build stage was moved at 0.04mm/sec to effectively join the exposures of the point array. The stage had a step size of 0.1µm in the x- and y-axes and 0.01µm in the z-axis. The stage also had a rotational resolution of 0.01degrees. The build envelope was 8.47mm x 10.8mm (Chan et al, 2003).

3.2.2 University of California Los Angeles µSLA

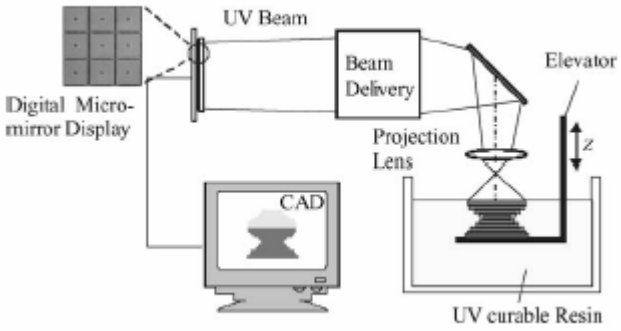

Figure 3.8 Schematic Layout of Projection µSLA (Sun et al, 2005).

Figure 3.8 shows a high resolution µSLA developed by Sun in 2005. Sun et al call the system a projection microstereolithography apparatus (PµSLA). The uniformity of the light being emitted from the mercury lamp was considered critical to maintaining process reliability. A fly-eye type optical homogeniser component was placed at the

output of the lamp. This homogeniser maintained illumination intensity to within a ±5% variation. A 5:1 projection lens filtered the light so that only a wavelength of 364nm was transmitted. Their system had a high contrast at 350:1. The elevator mechanism was motorised and coordinated by computer control. The layer translation had an effective precision of 0.1µm (Sun et al, 2005).

The high resolution of the PµSLA allowed feature sizes of 0.6µm to be made. The focus of their research was to address the process characterization issues of spatial resolution of the optical imaging and the resin's physical-chemical characteristics. Spatial resolution is important to projection µSLA as it is the ability to sharply and clearly define the extent or shape features within an image. Spatial resolution describes how close two features can be within an image for the features to still be resolved as unique (Richland County GIS, 2006).

Sun et al reviews the development of microstereolithography (µSL) from its foundation in MEMS technology. Advancements are discussed and the weaknesses are pointed out. MEMS began advancing with the use of lasers to induce chemical deposition of layers. Sun et al note that the first µSLA that used a focused laser spot to cure photopolymer resin. The tight focused laser allowed micron scale spatial resolution and then sub-micron scale through enhanced chemical processes. Further advancement moved away from the serial nature of the laser scanning process to the use of pattern masks. Now the laser was replaced with a collimated beam from a high-pressure lamp. The beam from the lamp was used along with multiple masks to cure the resin and create three-dimensional model. However, due to the amount of masks used dynamic mask generators were developed called Spatial Light Modulators (SLMs). LCD masks were implemented but soon the limitations of the LCD device restricted system performance. Another dynamic mask was sought because of the LCD's low pixel filling ratios, low switching speeds (20msec) and low contrast ratios. The DMD device does not have these limitations.

Sun et al observed what they refer to as the "cross-talk effect". Figure 3.9 shows part of a micro matrix made with the PµSLA that consists of three freestanding mesh layers suspended on an array of vertical posts. The non-uniform line width shows the cross-talk effect induced by light diffraction.

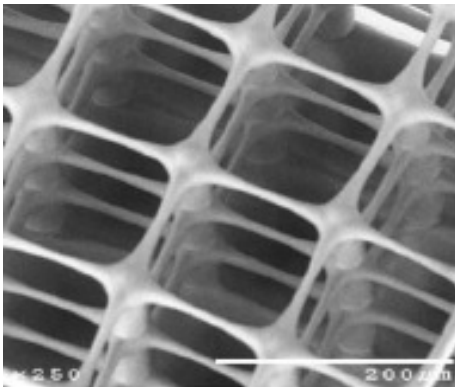

Figure 3.9 Cross-talk effect in a micro matrix (Sun et al, 2005).

Sun et al characterize the cross-talk effect with a numerical model. The model incorporates a point-spread function (PSF) to describe the radiation flux of a light spot originating from the image plane (i.e. the DMD). As shown in Figure 3.10, a gaussian distribution is used as a first order approximation of the PSF. The flux density contribution E(x) at given at position x is defined by the equation:

$$\mathrm{E}(x) = \mathrm{E}_0 \exp(-x^2 / w_0^2) \qquad \textbf{(3.1)}$$

(3.1 is the same used by Jacobs to describe the line-spread function of a scanned laser beam in resin (Jacobs, 1992). The gaussian radius quantitatively describes the spreading width of the light spot and thus the range of the cross-talk effect. The smaller dashed peak in Figure 3.10 represents a single light spot where the peak is E_0. E_{max} is the peak value of the whole intensity distribution.

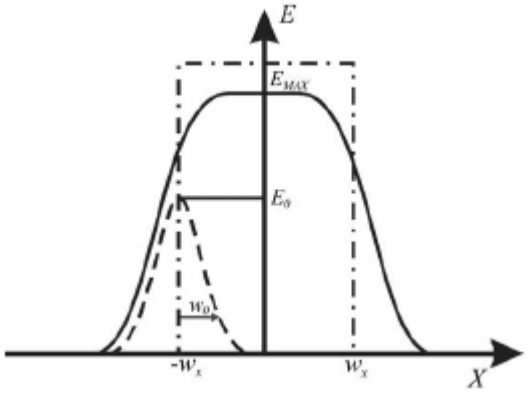

Figure 3.10 Intensity distribution along optical axis for a light spot intersecting at the image plane (Sun et al, 2005).

The intensity distribution is a summation of all gaussian distributions for each light spot. Sun et al show the intensity profiles of one pixel through to five pixels (the solid line in Figure 3.10). The importance of this graph is that E_{max} can be obtained by increasing the line width. The “flatten top” of the intensity profile occurs as the line

width becomes much larger than the gaussian radius. The intensity saturates when the line width approaches infinity and is defined as E_{inf}. The ratio of E_{max}/E_{inf} is dependant on the ratio of the pattern width w_L and the gaussian radius w_0 and is expressed as:

$$E_{max} / E_{inf} = \mathrm{erf}\left(\sqrt{2} \frac{w_L}{w_0} \right) \tag{3.2}$$

where erf(x) is the error function defined as:

$$\mathrm{erf}(x) = \int_0^x \exp(-t^2) dt \tag{3.3}$$

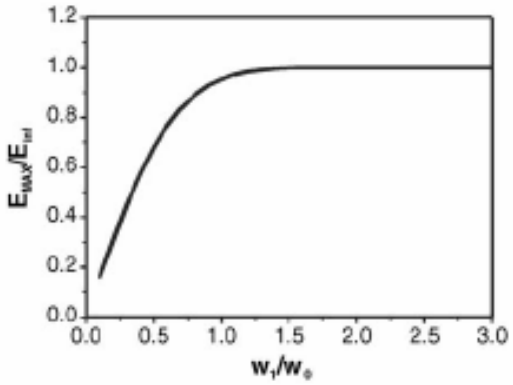

Figure 3.11 Relationship between E_{max}/E_{inf} and w_L/w_0 (Sun et al, 2005).

The importance of the relationship between these two ratios is that E_{max} converges to E_{inf} when w_L/w_0 is greater than two as seen in Figure 3.11. Sun et al assume that E_{max} can be substituted with the experimentally measured value for overall intensity, E_m. This assumption is considered viable because E_m is measured over a big projected square that is much greater than the gaussian radius. Note here that Sun et al may be assuming this in the context of μSL where the "big" projected square is able to fit on the measuring sensor and therefore only giving one reading for over all intensity.

(3.2 is further defined as the intensity correction term k that is introduced into the working curve equation.

$$C_d = D_p \ln(\frac{E_{max}}{E_c}) = D_p \ln(\frac{kE_m}{E_c}) = D_p \ln(\frac{E_{max}}{E_c^*}) \tag{3.4}$$

where $E_c^* = Ec/k$ is the effective critical energy that is directly calculated from the experimental measurements. D_p is also adjusted because penetration depth depends on where the exposure drops to $1/e$ of the E_m. However, E_m is E_{max} so the measured D_p^*

is where the intensity attenuates to $E = E_0/e = E_{max}/ke$. Therefore the penetration depth is expressed as:

$$D_p = \frac{D_p^*}{1 + \ln k} \tag{3.5}$$

Sun et al set up an experiment to test their model with regard to the line depth but not the line width. The experiment projected several line widths each 150 pixels long and zero to four pixels in width as shown in Figure 3.12. Two resins were used, one doped with 0.3% by weight UV absorber and one without UV doping. Results showed that the curing depth was greatly reduced in the UV doped resin thus proving that curing depth is controllable by tuning the concentration of UV doping. Also, E_c^* gave repeatable values for different doping levels within measurement tolerance by plotting experimental data using the cure depth equation. D_p^* was significantly reduced by increasing UV doping. As can be observed from Figure 3.12, the numerical model line width does not agree with increasing line width. It was believed that oxygen inhibition affected the photo-polymerisation reaction. Further research is aimed at incorporating line width in the model and conducting experiments in an oxygen free environment.

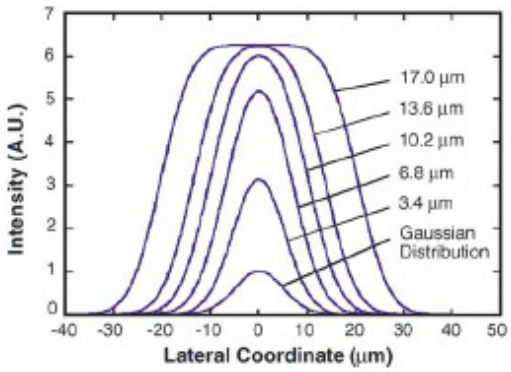

Figure 3.12 Intensity distribution of a line with different widths at image plane (Sun et al, 2005).

3.2.3 Saitama University Integral SLA

Several researchers at Saitama University, Japan used a DMD as an ultraviolet exposure system. They conducted tests for its applications in projection exposure systems for photoresists and rapid prototyping. The system consisted of several blocks: an optical system (UV source/ DMD/ lens), the mechanical system (xyθ-stage/ z-stage/ tank), and the control system (computer/ DMD controller/ pulse-stage controller) (Figure 3.13). The DMD used had an SVGA resolution of 600 x 800

pixels. A high-pressure mercury lamp was used as the optical source (Takahashi and Setoyama, 2000).

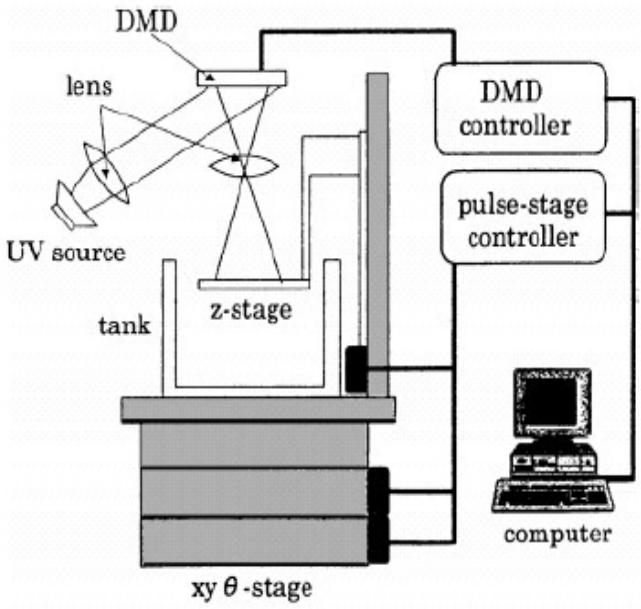

Figure 3.13 System construction (Takahashi and Setoyama, 2000).

Takahashi and Setoyama studied the accuracy of the projected bitmap and certain prototyping characteristics. For the photoresist that had a film thickness of 1.2µm, test results showed the exposure region extended to the exterior of the pattern as the exposure dose was increased and thus degraded the projected bitmap image. The extended exposure region was due to the limited lens resolution.

Takahashi and Setoyama's SLA, used with liquid resin (SCR-400 (JSR)), built a seven-layer prototype that had a layer thickness of 200µm and a pixel size of 50µm x 50µm (see Figure 3.14). Vertical grooves are observed on the sides of the prototype. The grooves are formed due to the gap between the micromirrors. Takahashi and Setoyama found that resin hardens in the gap and was not a problem for their research.

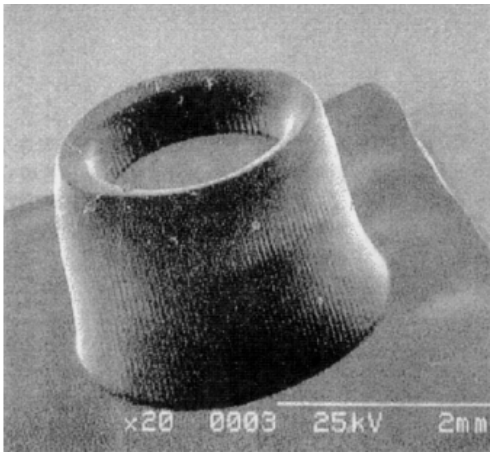

Figure 3.14 Rapid prototyped seven-layer stack (Takahashi & Setoyama, 2000).

In 2001 Takahashi built a miniature model of a skull composed of 103 layers at 150µm thick and a pixel size of 37µm x 37µm (Takahashi, 2001). Takahashi also showed the relationship between the exposure area and exposure time to obtain a certain layer thickness (Figure 3.15(a)). Experiments showed that, for an irradiance of 37mW at the resin surface, an exposure time of 14sec was required to cure a 48cm^2 area at 100µm layer thickness. In order to expose a larger area while keeping the exposure time constant, the irradiance needed to be increased. Figure 3.15(b) shows the relationship between exposure time and area for three irradiation levels that Takahashi experimented with.

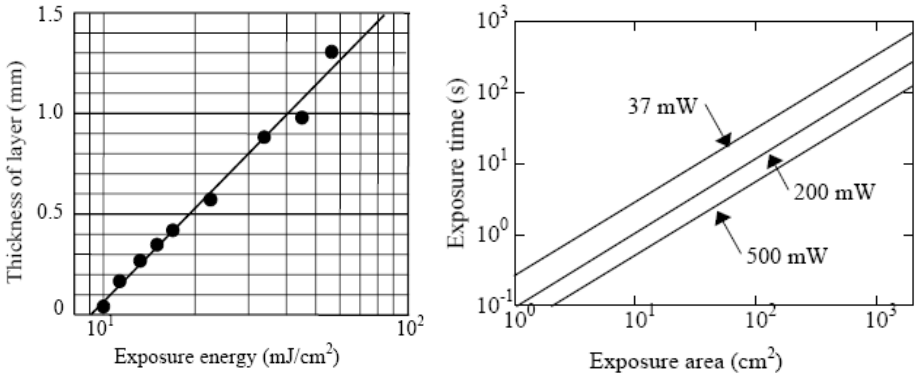

Figure 3.15(a) Layer Thickness vs Exposure Energy (b) Exposure Time vs Area (Takahashi, 2001).

Takahashi (2001) conducted an interesting experiment with gray-scale imaging. Takahashi used the modulation of the micromirrors of the DMD to proportionally develop photoresist. The photoresist was developed to different thicknesses depending on the percentage of gray-scale employed. Positive photoresist was used with a thickness of 60µm. Figure 3.16 shows the thickness trend as the photoresist was exposed from 30% to 75% gray-scale. Takahashi does not report a similar experiment for photopolymer resin.

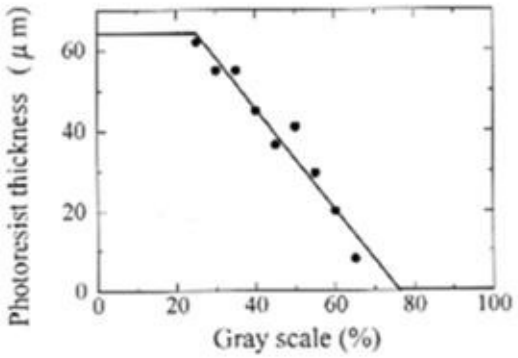

Figure 3.16 Thickness of photoresist trend when exposed to percentages of gray-scale (Takahashi, 2001).

Takahashi also analyzed the levelling operation for the resin between irradiation of layers. As the build process is additive, each new layer needs to wait a certain time, after the elevator has dropped down one layer depth, for the resin to flow on top of the previous layer. Levelling waiting times can be as long as 70sec or more depending on the viscosity of the resin. Takahashi was able to shorten the levelling time by vibrating the build platform between 15-50Hz using an electromagnetic coil. Results not only showed that levelling waiting times were reduced by more than 50% but also that it was possible to optimise levelling times by changing the vibration frequency corresponding to the size of the profile. The vibration of the build platform did not affect the quality of the part produced.

In recent research at Saitama University (Iwasawa et al, 2003; Tomita et al, 2005) the original system started in 2000 has been improved to have an irradiance of 500mW and maximum size of 200mm x 267mm. Table 3.2 shows the specifications of the improved system designed at Saitama University.

DMD			
Number of Pixels	600 x 800		
Contrast Ratio	200:1		
Reflection Area	90%		
Pixel's Gap Area	5%		
Pixel Size	17μm x 17μm		
Developed System	(Takahashi, 2001)	(Iwasawa et al, 2003)	(Yuki et al, 2005)
Levelling Method	Free	Free	Free
UV Source	250W Hg	200W Hg	200W Hg
Resolution	600x800	600x800	600x800
Pixel Size	21~100μm square	21~130μm square	21~330μm square
Illumination on resin surface	37mW	500mW	500mW
Minimum layer thickness	100μm	50μm	50μm
Maximum Model Size	60mm x 80mm	80mm x 100mm	200mm x 267mm

Table 3.2 μSLA specifications of Saitama University, Japan.

Iwasawa et al also demonstrated the effect of excess growth (Iwasawa et al, 2003). Other researchers have observed this phenomenon and refer to it as "print-through error" (Bertsch et al, 2000; Limaye and Rosen, 2005). Print-through error occurs due to light that penetrates into already cured layers. In Iwasawa et al, the mercury lamp used was a broadband light source. As a result the entire exposure area was irradiated with a wide spectrum of wavelengths. This meant that the longer wavelengths of light penetrated deeper into the resin than the shorter wavelengths causing excess curing in the previously cured layers. It was shown that, through the use of an optical filter, the effect that suppression of the excess growth had on making a part could be improved. Correct filtering of unnecessary wavelengths resulted in higher quality parts. Figure 3.17 shows the diminishing effect of print-through error as the filtering becomes better from (a) to (d).

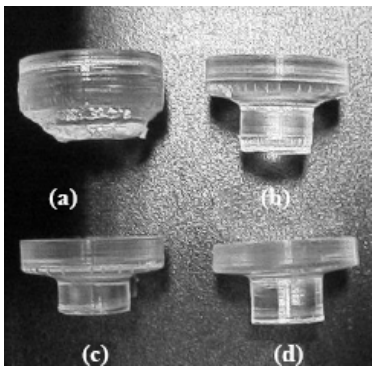

Figure 3.17 Suppression of excess growth (Iwasawa et al, 2003).

3.2.4 University of Wisconsin-Madison µSLA

Hadiposespito & Li designed a micro-SLA using a DMD to build meso/micro structures (meso scale is defined as sizes in the range of 100µm to 10mm) (Hadipoespito and Li, 2005). Their research was aimed at improving the layer thickness and process efficiency of existing µSLA. Figure 3.18 shows the layout of their system. A 100W mercury lamp was used as the UV light source. The resin was exposed to a broadband UV light ranging from 300nm to 470nm. The resin was optimised to cure at 355nm, without filtering the light. The light was put through a fibre optic light guide and collimated. A total internal reflection (TIR) prism was used to direct the light onto the DMD. The resolution of the DMD was 1024x768 (XGA) and the pixel size of each micro-mirror was 13.7µm x 13.7µm. The µSLA used a silica window, known as a "dip-in" window, coated with a Teflon film to prevent cured resin from sticking to the window.

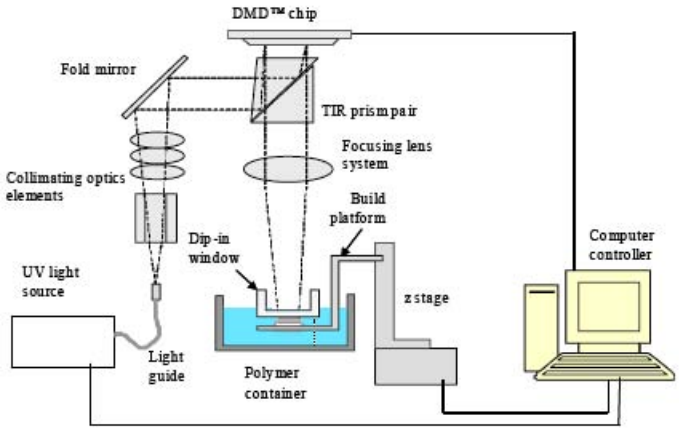

Figure 3.18 Diagram of µSLA (Hadipoespito and Li, 2005).

Experiments were conducted on the resin to determine the relationship between curing depth and exposure time. To find this relationship, Hadiposespito & Li rapid prototyped a thick support with a circular portion left uncured. The final layer closed the circle and was cured for a predetermined exposure time. Thus the curing depth was obtained from the measured thickness of the circle. The experimental procedure is depicted in Figure 3.19. Hadipoespito & Li found that the curing depth was directly proportional to the exposure time for the exposure time range that they tested. The exposure time range was from 0 to 20 seconds.

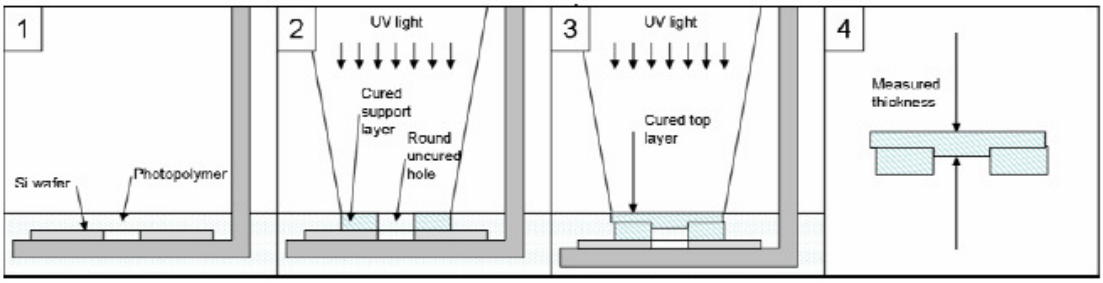

Figure 3.19 Experimental procedure to find curing depth (Hadipoespito and Li, 2005).

Hadipoespito & Li defined resolution of an SLA in the vertical and lateral directions. The vertical resolution was the minimum layer thickness that could be realized in the Z-axis and was limited by the mechanism of the Z-stage. Lateral resolution was the resolution in the X-Y plane and indicated the smallest feature possible in this plane. Their μSLA had a minimum vertical resolution (layer thickness) of 5μm and lateral resolution was 20μm. However, for lateral resolution, 20μm is said to dictate the smallest feature possible but is actually the gap between cured areas.

3.2.5 The Perfactory® by Envisiontec

Recent research has been conducted a Northumbria University on the Perfactory® made by Envisiontec. The Perfactory is unique in that it builds parts upside down and slowly draws parts out of the vat of resin. It uses visible light to cure an acrylate resin by projection through a window. The side of the window in contact with the resin is coated with a silicon membrane. The membrane prevents layers from sticking to the window once cured. This silicone membrane degrades when in contact with the resin and must be replaced. The lamp is reliable for roughly 500 hours and the focus and light intensity have to be recalibrated every few builds (Maalderink, 2003).

(Hackney et al, 2005) investigated the effect of pixel size, and also the effect of surface roughness depending on the build angle and build direction. The pixel size is the actual size of the pixel that is projected by the Perfactory's DMD onto the resin surface. The Perfactory allowed for variable build envelopes so pixel size ranged from 0.094mm to 0.148mm.

Hackney et al noted that the surface finish of a prototyped part is important so as to maintain dimensional accuracy and avoid manual post processing. A test part was made using the Perfactory that tested the effects of build angle and build direction on surface roughness. The part is shown in Figure 3.20. Figure 3.20 shows how the build

angle was assigned with up facing angles measured from the last layer built and down facing angles measured from the layer closest to the build platform. Build direction was designated as up and down facing according to the build angle. The test part included angles of 30°, 45°, 60°, and 70°. The layer thickness was set to 0.05mm.

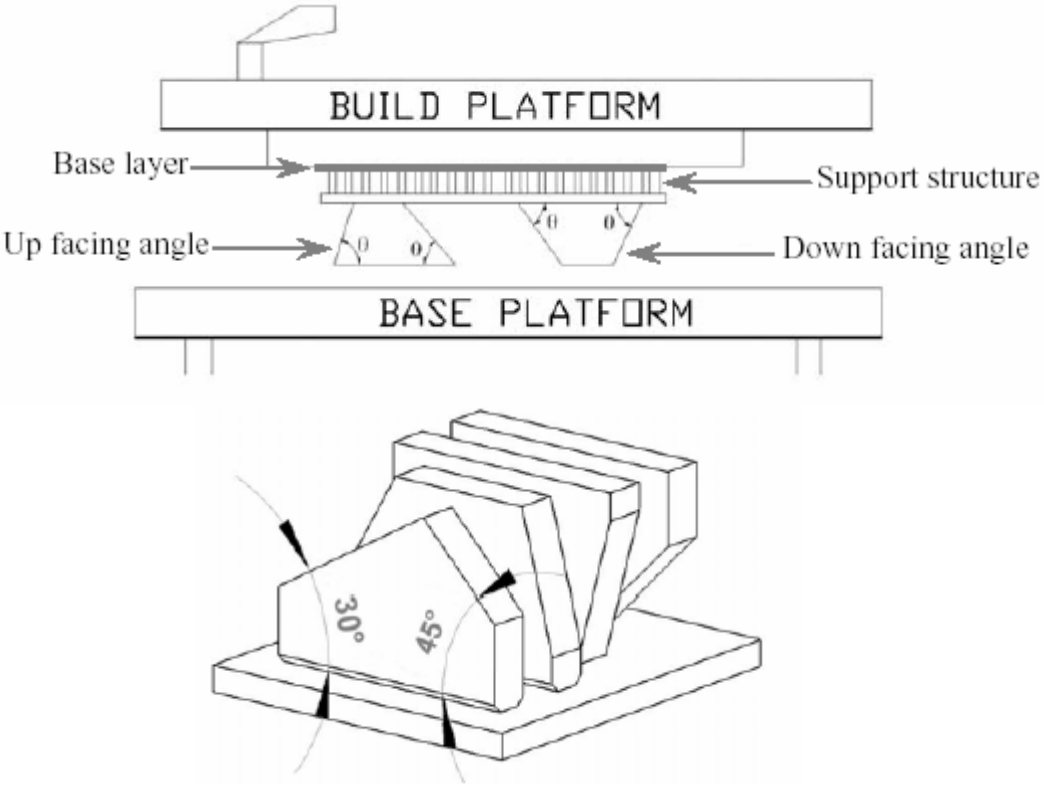

Figure 3.20 Test part explaining up and down facing angles (Hackney et al, 2005).

The surface roughness was measured using a Taylor Hobson Talysurf. The results showed that the surface roughness increases as the build angle increases. The results were compared with the surface roughness of parts made using three other RP technologies: conventional SLA, SLS, and FDM. The trend for these technologies was opposite to the trend for the Perfactory. The unique trend of the Perfactory showed that the surface finish was not only influenced by the layer thickness and build angle, but by pixel size.

The test part was inspected under a microscope to observe the surface roughness more closely. It was seen that the layer thickness at the edges had a staircase appearance. The edge was measured for the thickness along the build direction (Y) and the thickness perpendicular to the build direction (X). It was found that X closely matched the pixel size and hence that pixel size also affected the surface finish. The Y dimension was observed to increase as the build angle increased.

Surface roughness was better for up facing build angles. The build direction influenced the surface roughness. Angular faces built up facing had lower roughness values than the same angular faces build down facing. The smoother quality of up facing angles can be explained by Beer-Lambert's Law occurring at the edge of the cured layer.

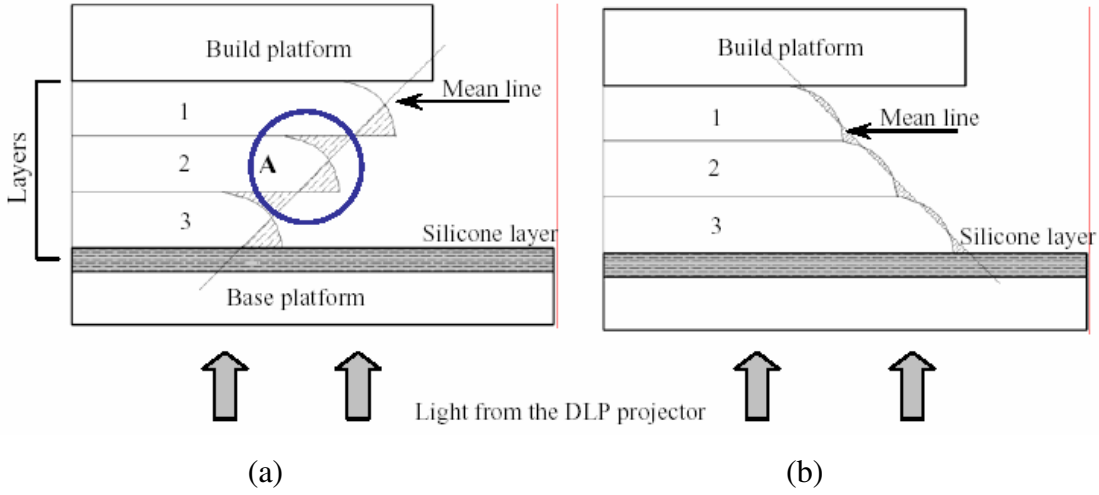

Figure 3.21 Surface finish. (a) Down facing build (b) Up facing build (Hackney et al, 2005).

As can be seen Figure 3.21, when the mean line is drawn for the edge, the magnitude of the area on either side of the mean line determines the surface roughness value, Ra:

$$\mathrm{Ra} = \frac{1}{L}\int_0^L |y(x)|dx \tag{3.6}$$

It is seen clearly that the area for the down facing angle is greater than the area for the up facing angle. This explains the lower Ra values for angular faces build in the 'up' direction.

In other research by (Hackney et al, 2005) on the Envisiontec Perfactory®, relationships between desired outputs and process parameters were established. Taguchi techniques and statistical tools were used to find the percentage contribution that the process parameters used in the study had on part strength, hardness, and accuracy. The process parameters used in the study were pixel size, peel velocity, waiting time, exposure time, orientation, and layer thickness. Results of the analysis showed that layer thickness and part orientation affected accuracy the most. The parameters that contributed least to part accuracy was pixel size and peel velocity. Obviously, pixel size was only tested within the range available on the Perfactory

system which was 0.094mm to 0.148mm. Waiting time and exposure time are critical for part strength. Layer thickness and exposure time contribute most to part hardness.

The study performed by Hackney used Taguchi techniques. A good knowledge of these techniques is required to interpret the Taguchi analysis as most of the graphs in the paper are not yet published.

3.2.6 The Georgia Institute of Technology μSLA

Limaye designed a μSLA that used a DMD with a pixel size of 13.7μm x 13.7μm (Limaye, 2004). The maximum part size made covered the area of 2mm x 2mm (450x450 pixels). A 50W mercury lamp was used as a light source and the light was emitted through a fibre optic light guide before the optical conditioning. An optical filter allowed a wavelength of around 365nm to pass.

Limaye characterised the curing properties of DSM Somos 10120 resin using his μSLA. A U-shaped part was used to support a cured thread because it offered easy handling (see Figure 3.22). The U-shaped part was built with the last layer having a thread cured across the top of the U-shape. The top layer was irradiated for different exposure times for each U-shaped sample. The vertical thickness, hence cured depth, of the thread was measured and plotted against exposure time in order to obtain the working curve of the resin.

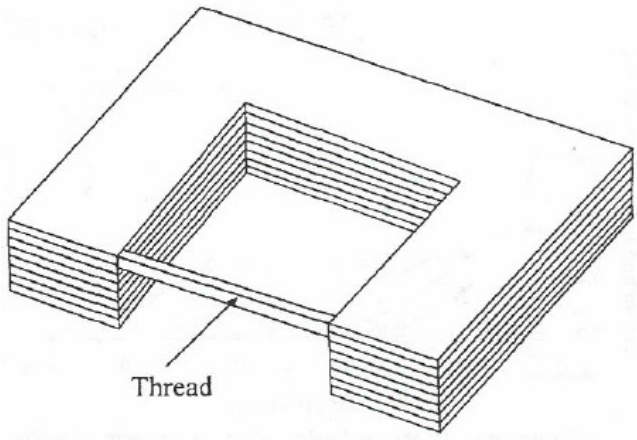

Figure 3.22 U-shaped part with thread for cure depth measurements (Limaye, 2004).

The smallest parts made from this machine had a layer thickness of 20μm and 6μm features in the lateral direction were obtained. Limaye describes a mathematical model for process planning. This model is discussed in more detail in Chapter 6.

3.3 SLA Implementing LCD Technology

3.3.1 UV laser LCD µSLA (Bertsch et al, 1998)

Bertsch et al (1998) applied an approach to the fabrication of micro three-dimensional structures. The limitation of available technologies in 1998, such as MEMS, was that only simple two-dimensional geometries were used to make a part by superimposing a few layers. True three-dimensional parts arrived with the advancements occurring in rapid prototyping. When the resolution of rapid prototyping became adequate, Bertsch et al investigated what would be the first research into what they termed "integral" microstereolithography.

Bertsch et al discovered that the mechanical control of the elevator of their µSLA could not accurately control the thickness of a resin layer, thus affecting the vertical resolution of the fabrication process. Bertsch et al also found that the most important parameter affecting the vertical resolution was the penetration depth of the resin. Penetration depth had to be controlled by the use of a high, light absorbing resin. If light penetrated deep into the resin and through already polymerised layers, the result was a loss of resolution in the already polymerised part. (Iwasawa et al, 2003) and (Limaye & Rosen, 2005) have also observed this phenomenon.

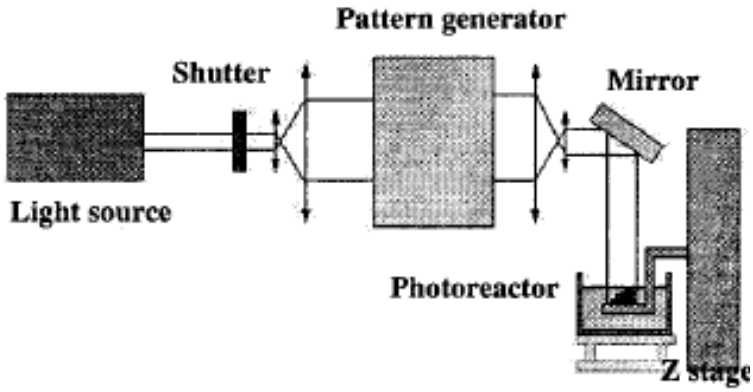

Figure 3.23 Layout of integral µSLA (Bertsch et al, 1998).

An acrylate resin was used where the peak absorption for photopolymerisation was in the visible range. The lateral resolution of the µSLA was 5µm. The type of pattern generator is not specified but from layout of the system (Figure 3.23), it is likely that an LCD was used. The pixel size was 5µm x 5µm after passing through reduction optics. The area of irradiance projected on the resin surface was 2.5mm x 2.5mm. Layers were cured with an exposure time of 1sec per layer. The recoating of the liquid resin limited the build speed of the µSLA to 1mm per hour with the layer thickness set to 5µm.

Bertsch et al discovered that with μSL, it is not possible to use supports when fabricating a part because the supports damage the part during removal.

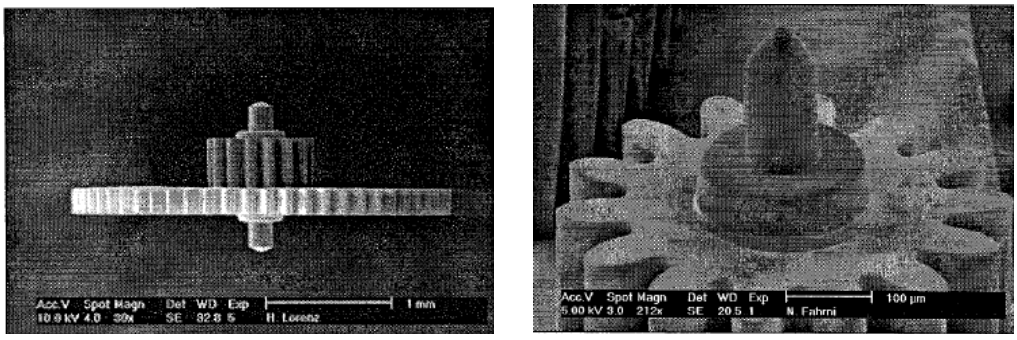

(a) (b)

Figure 3.24 (a) Watch gear fabricated completely by LIGA. (b) Axle fabricated using μSLA (Bertsch et al, 1998).

Bertsch et al were able to demonstrate the application of the μSLA by combining its use with the UV-LIGA fabrication process. An example of a watch gear is given in Figure 3.24. The structure of the gear is simple and can be completely fabricated by the LIGA process. However, the conical ends of the axle are obtained by a post-machining operation. Bertsch et al where able to create this axle using their μSLA (Figure 3.24(b)), thus not requiring post-machining. The axle was fabricated on top of the LIGA made gear by lining up the gear in the SLA with a trace pattern projected by the LCD. The wavelength of the trace was not cable of initiating polymerisation. This example only showed how their μSLA could be applied to existing technologies at that stage in 1998. It would be just as time-consuming to machine the axle, as it would have been to process it in the μSLA.

3.3.2 UV laser SLM μSLA (Farsari et al, 2000)

Farsari et al (2000) developed a μSLA with complex optical conditioning of a laser beam. Commercial SLA systems at that time were limited to a resolution of 0.1mm due to the use of a focused laser beam. The research aimed to increase the build speed and resolution of SLA prototyping by using a spatial light modulator (SLM) to cure an entire layer at a time. The resolution had to be fine enough to achieve the fabrication of features of 5μm. Farsari et al were one of the first research groups to use a UV laser (λ=351.1nm) in the design of an integral SLA so as to make use of the already commercially available UV-curable resins.

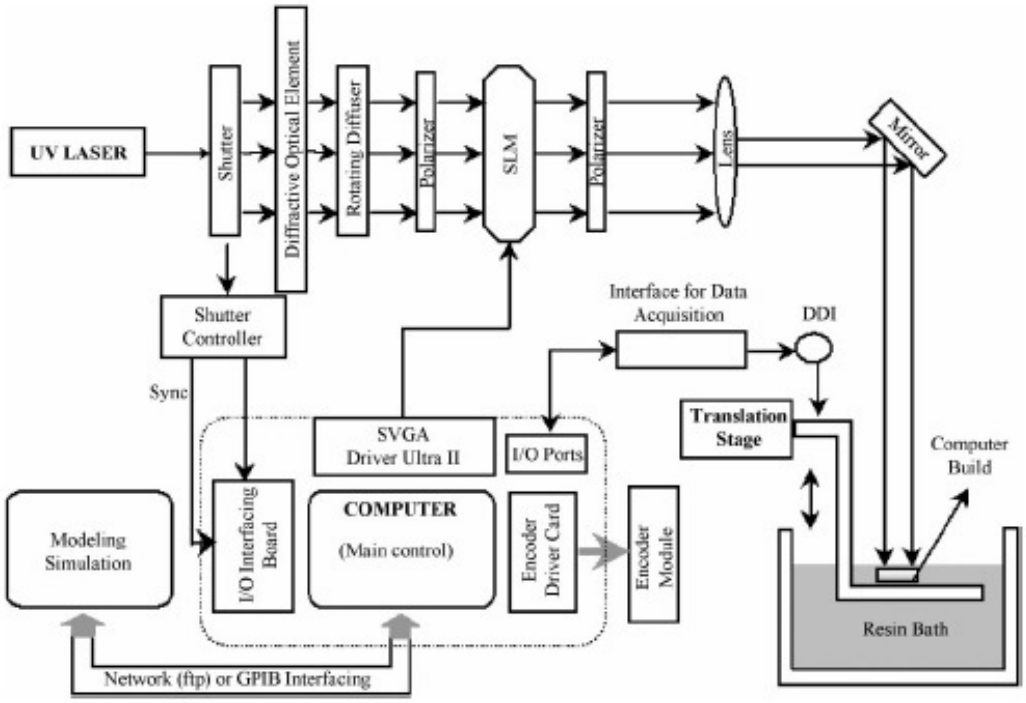

Figure 3.25 Layout of the Farsari SLA (Farsari et al, 2000).

The layout of the principle parts of Farsari's SLA are displayed in Figure 3.25. To achieve a resolution of 5µm, a multi-element reduction lens was implemented. The lens was able to reduce images for the SLM up to 10 or 20 times. The SLM had a resolution of 600 x 800 pixels with each pixel measuring 26µm x 24µm. The total active area of the SLM was 26.4mm x 19.8mm with a pixel fill factor of 50% and a contrast ratio of 200:1.

Perhaps the most interesting part of Farsari's work was how the gaussian laser beam was optically conditioned before the beam made its way to the focusing lens. To spread out the gaussian beam of the laser enough to fill the area of the SLM, a diffractive optical element was implemented. Called a gaussian to square beam convert (customized to requirements by Digital Optics Corporation), this optical element converts the laser beam input into a flat irradiance pattern. However, Farsari et al note that the argon-ion laser used gives a poor approximation of a gaussian distribution, which does not give the required flat irradiance pattern. To obtain an improved beam output, a rotating holographic diffuser was placed after the gaussian to square beam converter. The holographic diffuser removes spatial coherence of the laser beam and reduces speckle in the image plane. However, the holographic diffuser made the beam less collimated and depolarised. Farsari et al repolarised the beam before and after the SLM with the use of a linear polariser sheet.

To calibrate the μSLA, Farsari et al calculated the laser irradiance for a layer thickness of 50μm using Beer-Lambert's Law:

$$E(z) = E_0 e^{\left(-\frac{z}{D_p}\right)} \quad \textbf{(3.7)}$$

where z is the layer thickness, E_0 is the laser irradiance at the surface of the resin and D_p is the penetration depth of the material given by the resin manufacturer. E(z) was experimentally measured by building several layers. For each layer the laser irradiance was incrementally lowered until the top cured layer did not bond to the previous layer. Farsari et al does not specify the final laser irradiance at this point.

Farsari et al were able to build highly accurate microstructures with layers down to 5μm. The resin chosen was Ciba-Geigy Cibatool™ SL 5180. It was chosen out of several resins after holographic measurements that compared reactivity, rate of polymerisation and shrinkage. It had a low viscosity, which was found to suit Farsari's fabrication process the best. The resin data sheet is provided in Appendix E: Resin Data Sheets.

3.3.3 LCD μSLA (Monneret et al, 2001)

Monneret et al (2001) conducted research that implemented an LCD in a μSLA. The research was one of the first projects to implement an LCD and interest was aimed at seeing the potential of the efficiency of the dynamic masking technique over the conventional vector-by-vector process.

The setup of the SLA is shown in Figure 3.26. A high-pressure mercury lamp was used as a broadband light source. However, the power of the lamp is not specified nor is the wavelength given that the system was designed to transmit. An LCD with XGA resolution (1024 x 768 pixels) was employed but as some of the pixels were reserved, the masking zone was only 640 x 480 pixels. The LCD interface allowed it to be driven by the video adapter on a PC. The pixel size was 26μm x 26μm. and the contrast ratio was 100:1. Although the contrast ratio was low, black pixels were sufficiently dark enough to stop the transmission of light to the resin surface. After light passes through the LCD, the optics allowed variable magnification in order to control the size of the object.

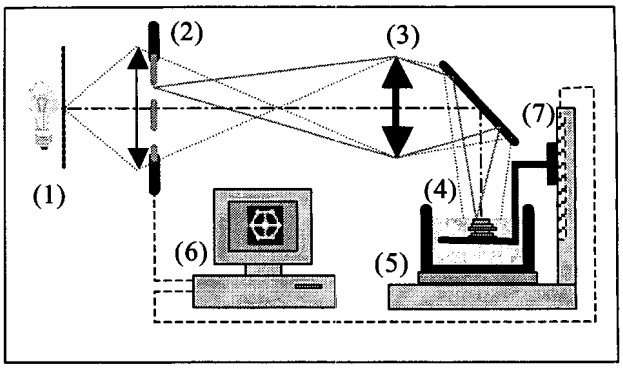

Experimental set-up of the current process
(1) high pressure Hg light source ; (2) LCD ; (3) imaging system;
(4) photoreactor ; (5) temperature regulation; (6) computer;
(7) vertical moving stage.

Figure 3.26 Experimental setup of LCD μSLA (Monneret et al, 2001).

Monneret et al state that the use of a recoating scraper could not be utilized in the manufacture of micro-objects as it could damage the previous layer of the micro-object. So, the "deep dip" method was used to apply fresh layers of resin. The disadvantage of the deep dip method is the settling time. This is the time it takes the fresh layer to form a homogeneous thickness. Monneret et al state that a low viscosity resin must be used to decrease the settling time and the layer thickness.

Monneret et al make some points about horizontal and vertical resolution. Several factors influence the resolution of objects such as the quality of the imaging optical system and the chemical and physical properties of the resin used. Horizontal resolution is determined only by the imaging system quality. In research by Monneret et al (1999), 2μm x 2μm pixel size was obtained reliably showing that horizontal resolution is defined by the masked pixel size on the resin surface. However, vertical resolution was very difficult to quantify with a single value. The main difficulties in characterizing vertical resolution were that it depended on the shape of the object being made and the penetration depth of the resin.

3.4 Novel Variations of SLA

3.4.1 μSLA Using the Super IH Process

Ikuta et al (1998) developed an advanced μSLA that overcame several problems of the layer-by-layer technique used by conventional laser-based SLA. Problems included: the depth resolution being limited by the thickness of the layer, viscosity of the photopolymer deforms solidified micro parts and the surface tension of the resin decreases the precision of fabrication. Ikuta et al called this advancement to μSL the Super IH (Integrated Harden) process.

The IH process developed a new solidification method where the problems listed above were solved. The new solidification method cures resin at a pinpoint position in 3D space by focusing a laser beam inside the vat of resin. Because the laser beam is focused inside the resin, there is no need for a recoating system hence reducing fabrication time. The viscosity of the resin used is such that parts were fabricated inside the resin medium without structural support material. Photopolymerisation of the resin did not occur in the column of the beam above the focused spot because the exposure intensity in the unfocused column was below the critical exposure (E_c) of the resin. Therefore, solidification of the resin was limited to the small area near the focused spot. Using this technique allowed the resolution of the μSLA to become less than 1mm.

The Ikuta μSLA consisted of a He-Cd laser emitting light at 442nm, a shutter, galvo-scanner set, an XYZ stage, and one objective lens, and the UV polymer was urethane-acrylate. Parts are fabricated upside down to conventional methods. The layout of the μSLA is shown in Figure 3.27.

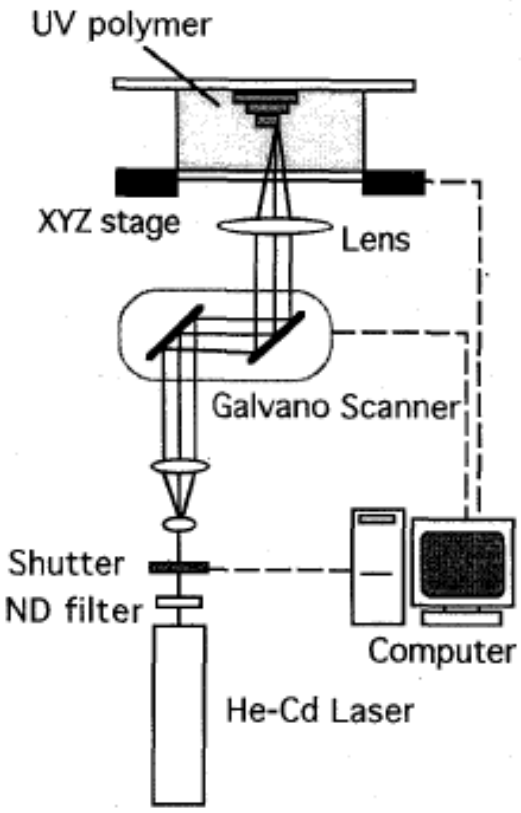

Figure 3.27 Layout of the Ikuta μSLA Super IH Process (Ikuta et al, 1998).

Ikuta et al were successful in fabricating complex parts without supports having a lateral resolution of 0.5μm. However, an indication of the accuracy of the new

process is not given. Although the parts built by the Ikuta μSLA show proof of the concept, most the experimental parts fabricated leave room for improvement.

3.4.2 A Novel SLA with Conventional UV Light

Wu at Xi'an Jiaotong University investigated a new novel SLA in 2001. Called the Compact Prototyping System (CPS), this novel SLA incorporated an optical fibre to cure resin. The expense of precision laser technology is eliminated with the use of a conventional UV light. Wu et al (2001) note that after the first SLA appeared, a number of other SLA were introduced that all operate based on the same principle. Differences between these SLA included aspects such as materials and resins used, light sources and curing processes. SLA that implement UV lasers to initiate photopolymerisation of a resin are recognised as the conventional method for SLA. Conventional methods are used as a comparison for Wu's new method (Wu et al, 2001). The basic layout of the CPS is shown in Figure 3.28.

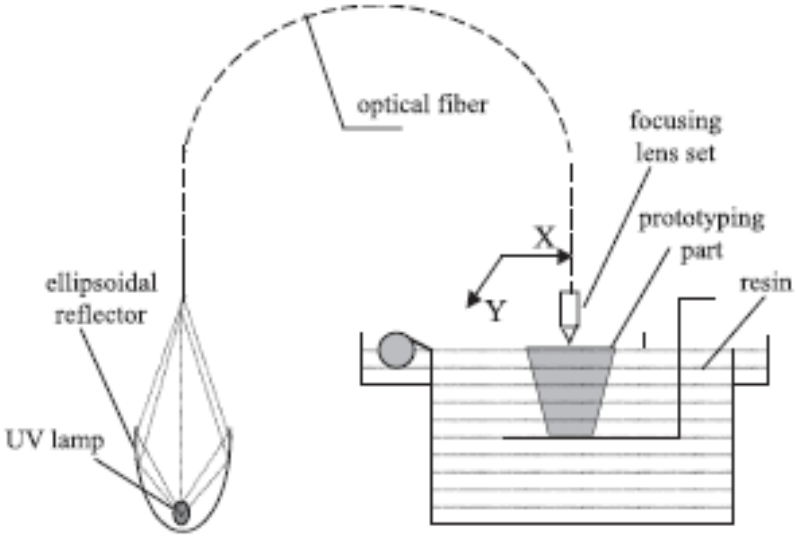

Figure 3.28 CPS Basic Layout (Wu et al, 2001).

Light from a UV lamp has several different characteristics when compared to light produced by a laser. A UV lamp emits a broad spectrum of light as opposed to the monochromatic light from a laser. The spectrum of the lamp needs to be examined for the range of wavelengths that will cause polymerisation of the resin used. Optical filters are used to obtain the required wavelengths. Also, the optical fibre transmits a beam of light that has a larger diameter than the beam diameter of a laser. The light intensity within the optical fibre's beam has a lower energy distribution than that of a laser beam. Therefore, a cured line from the CPS results in wider cured line width than a laser beam and reduced layer thickness due to the lower energy.

Wu et al conducted an experiment to characterise the beam of light coming from the optical fibre. The energy distribution of the fibre's beam was measured using a laser power meter. The meter had a very small sensor area that was 0.5mm in diameter ($0.2mm^2$). The meter was fixed to a moveable X-axis bench and measurements were taken every 0.04mm as the meter was moved across the radial line of the beam. The graph of these measurements showed that the intensity distribution is a gaussian distribution and that the intensity attenuates rapidly from the centre of the beam (Wu et al, 2001).

Wu et al report that exposure is a function of the scanning parameters and this affects the depth of cure. It was found that theory for curing a line and curing a layer contradicts each other. From theory, a scanning speed of 100mm/s the layer thickness is less than 0.1mm. This thickness is less than the resolution of the CPS, meaning consecutive layers will not bond to the previous layer. But from experiments at speeds of 100mm/s or more parts were made successfully. The reason for this behaviour is the contribution of energy from neighbouring lines. This overlapping results in an overall layer energy that is many times greater than the energy intensity of a single line. The amount of overlapping of these neighbouring lines is called the hatch gap. The hatch gap also changes the appearance of cured layer's bottom. The smaller the hatch gap, the more even the energy is distributed across the bottom of the layer. As the hatch gap widens, the energy fluctuates and the bottom is cured unevenly (see Figure 3.29 below).

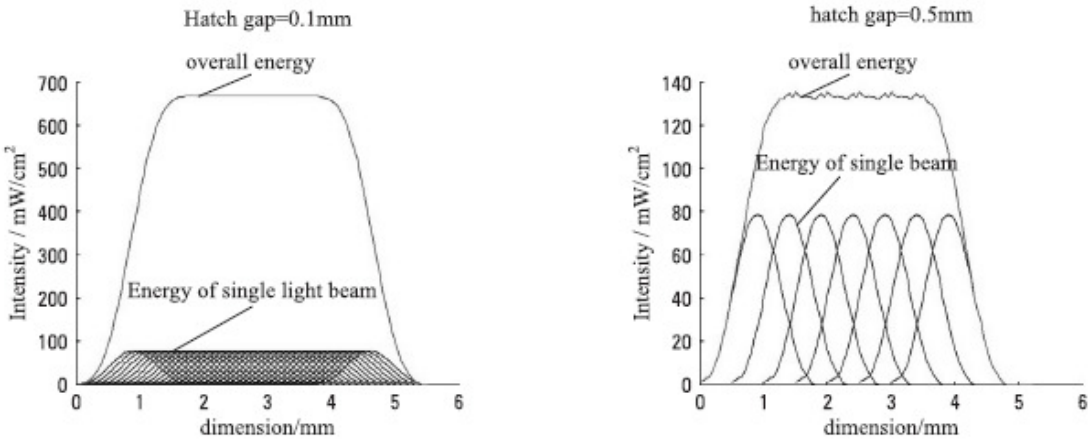

Figure 3.29 Overlapping of neighboring lines and hatch gap (Wu et al, 2001).

3.4.3 Stereo-Thermal-Lithography (STLG)

Stereo-thermal-lithography (STLG) is a recently new principle for rapid prototyping. STLG utilises both heat and UV radiation to cooperatively cure a polymer that has attractive advantages over conventional rapid prototyping. (Bartolo

& Mitchell, 2003) give an in-depth comparison of conventional SL and STLG. Conventional SL has a limitation in that parts require post curing in a UV oven. Inadequate cure can lead to warping due to relaxation, diffusion, evaporation of low-molecular weight components and post-cure shrinkages. STLG does not require post-cure operations due to the combination of UV radiation and heat. Also, the increased temperature leads to an increase in the reaction rate and degree of conversion.

The STLG resin consists of low concentrations of both photo- and thermal-initiators. This combination requires that both initiators be stimulated simultaneously to have sufficiently high radicals to initiate the polymerisation process. The low concentration of initiators allows for greater penetration depth of radiation. The greater penetration depth and simultaneously initiated polymerisation enables the build process to take place just beneath the surface of the resin as shown in Figure 3.30. Building inside the medium does away with the recoating system or deep dip method used in most conventional SLA when preparing a new layer. The timesaving with the new STLG principle makes it more efficient than conventional laser based SLA.

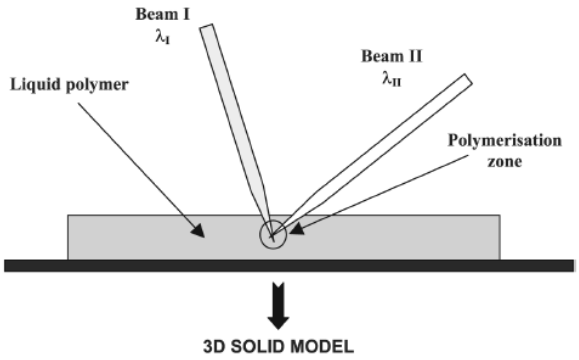

Figure 3.30 The STLG principle using dual lasers (Bartolo & Mitchell, 2003).

(Bartolo & Mitchell, 2003) set up a simple test SLA to compare parts made by an SLA using UV irradiation and the STLG using UV irradiation and heat. Separate resins were prepared for each technique. A mercury lamp is used as the UV light source and temperature was controlled by heating and cooling elements. A simple black cardboard mask was used that profiled a square shape and a triangle shape with known dimensions. The accuracy of lateral dimensions was measured and compared. Layer thickness was not tested. Experimental results showed that conventional UV radiation had around a dimensional 5% error and STLG only had about a 2% error validating the accuracy of the technique.

Although the STLG principle has some attractive benefits for rapid prototyping, it still needs further research. There is has been no more published information about STLG. Also, the resins for STLG are not commercially available.

3.4.4 UV Resin Spray Rapid Prototyping (UVRS-RP) Machine

(Chang, 2004) looks at novel way of producing prototypes with a UV resin spray rapid prototype apparatus (UVRS-RP). The UVRS-RP uses two spray nozzles to supply build and support material for each layer. The build material is a UV initiated resin that is hard and rigid. The support material is soft once cured and easily separated from the build material due to the differences in chemical properties of each. Spray nozzles are interchangeable and range in size from 0.06mm to 4.5mm in diameter. Nozzles are changed automatically from the automatic tool changer (ATC) that is part of the UVRS-RP.

(Chang, 2004) points out that the limitations of producing parts with current SLA are non-linear shrinkages as a result of the scanning laser technique to cure the resin, the expense of conventional SLA equipment, the cost of maintenance and material contaminations. The UVRS-RP reduces the distortion of non-linear shrinkages by irradiating an entire layer at once using a high power UV lamp. The UV lamp replaces the cost of an expensive laser reducing equipment costs.

Parts are created on the UVRS-RP by first tracing the perimeter of a layer's profile and then the interior is spayed with resin. Motion of the nozzles is accomplished using a gantry system. Movement has a resolution of 1µm in the X and Y-axes with the build platform being 460mm x 460mm.

The light source incorporates a 3.6kW UV lamp that has three power settings 100%(3.6kW), 75%(2.7kW) and 50%(1.8kW). The whole build platform area is irradiated in one exposure. A sample part is built in (Chang, 2004) (human torso model) and a curing time of 5msec is used at the 50% power setting.

(Chang, 2004) found that to obtain better accuracy in height and width, a twenty percent hatch gap overlap and a half-phase shift were applied to successive layers. However, (Chang, 2004) provides no information of dimensional measurements of test parts created using the UVRS-RP. The research lacks a comparison of the test part made using the UVRS-RP and the same test part made using conventional SLA part.

The advantages of the UVRS-RP do indeed make the build process more efficient than conventional SLA. As there are different nozzle diameters, the area to be sprayed can be done very quickly. Irradiation of the entire layer all at once reduces the build time also. The use of different support and build material shortens post-processing operations. However, the layer build time of the UVRS-RP is dependent on the layer profile.

3.5 Summary

In this chapter, the types of dynamic pattern generators were discussed. LCD, DMD and GLV have all benefited from advancements in MEMS technologies. These technologies have enabled the integral curing approach to stereolithography. LCD operation and construction was reported. LCDs with active-matrices use nematic crystals to act as an optical shutter. However, LCD technology has the disadvantage of UV absorption and inefficient fill factor limiting the use of LCDs in SLA. The origin and principles of operation of the DMD was explained. The DMD is most suitable for UV integral SLA. The only failure mode to be aware of is micromirrors that stick to the substrate underneath the mirror due to intense UV light reported by (Douglass, 1998).

The SLA research reviewed was primarily focused on design of working integral SLA systems. Most of these SLA have high resolutions below 0.05mm. However some important theory and experimental observations should be pointed out. Firstly, the research by Iwasawa et al (2003), Bertsch et al (2000) and Limaye and Rosen (2005) all notice layer curing errors due to print-through error. Iwasawa showed that effective wavelength filtering could minimise the effects of print-through error.

Takahashi (2001) showed photoresist could be proportionally developed by using modulation of the micromirrors of the DMD. Using gray-scale images, Takahashi was able to create three dimensional etching on the photoresist. This experiment was not reported to have been done on photopolymer resin. Using this technique of gray-scale imaging may be able to account for or minimise print-through error.

Secondly, there are several ways that layer thickness has been measured. Researchers have experimented with layer thickness in order to determine the relationship between curing depth and exposure time for a photopolymer resin. (Hadipoespito & Li, 2005) used the method that was depicted in Figure 3.19. Layers were built up in a donut pattern and then the last layer was circled and was used to

find layer thickness (cured depth) for the exposure time. (Limaye, 2004) used a U-shaped part to support a cured thread that was used to measure the cured thickness. The U-shaped part offered easy handling for cleaning and measurements under the microscope. Farsari et al (2000) calibrated cure depth for a desired layer thickness by reducing the irradiance power, keeping TOE the same, until the top layer no longer bonded with the previous layer.

The third interesting observation was reported by Hackney et al (2005). Hackney observed the surface roughness, which referred to the phenomenon occurring at the edges of part consecutive layers. Hackney quantified the area by drawing the mean line. However, the area on either side of the mean line is a relationship between layers and not edges so this classification of surface roughness may not be applicable for the research of this thesis.

And finally, there have been interesting ways that researchers have made the integral process more efficient. (Takahashi, 2001) managed to reduce the layer settling time by vibration of the elevator platform without affecting the dimensions of layers. Monneret et al (2001) notes that a low viscosity resin needed to be used to reduce the settling time. Monneret et al (2001) and Bartolo and Mitchell (2003) managed to cure layers just inside the resin surface to do away with the recoating process and resin settling time.

Some of the observations above can be implemented when designing and experimenting with the SLA designed in chapters 9 and 10 of this thesis. This chapter has reported several instances where SLA are used to characterise photopolymer resins. The next chapter reviews literature on the chemistry of photopolymer resins used for liquid-based stereolithography to gain more understanding behind resin properties and characteristics.

4 The Chemistry of Photopolymers

This chapter reviews literature on the chemistry of photopolymer resins. The review focuses on photopolymers used for liquid-based stereolithography to gain more understanding behind resin properties and characteristics and how these resin parameters are found when the composition is unknown. This chapter also analyses how resins cure and what parameters affect the cure. Section 4.1 and section 4.2 introduce photopolymers and the photopolymerisation process. Cross-linking and green strength are two concepts of photopolymer resins that are explained in section 4.3. Section 4.4 reports on analytical methods researchers have applied to photopolymers where the exact chemistry is not known.

4.1 Photopolymers

Liquid-based RP systems require build material that contains certain chemical properties. The build material is made from photopolymers. Liquid photopolymers contain a chemical cocktail of molecules that solidify when exposed to electromagnetic radiation. The forms of radiation include gamma rays, X-rays, UV and visible range, or electron-beam (EB). Most RP systems use photopolymers that cure in the UV range and other curing technology use mainly UV or EB radiation (Jacobs, 1996).

For a better understanding of photopolymers and for simplicity, they are a mixture of monomers and oligomers. There are a small variety of these UV-curable resins available, each contains fillers and other chemicals to achieve different chemical and physical properties (Chua et al, 2003). These resins can be classified into acrylate, epoxy, or vinyl-ether systems.

4.2 Photopolymerisation

Some UV-curable resins accomplish photopolymerisation by using a free-radical mechanism as depicted in Figure 4.1. These resins are acrylate-based polymers. These resins are a makeup of photo-initiators and reactive liquid monomers. When the resin is exposed to a UV light source, the photoinitiators absorb some of the radiant energy and are raised to an excited state. A fraction of these excited photoinitiators become reactive after going through various complex chemical transformations. These excited photoinitiators then react with the monomer molecules to form a polymerisation

initiating molecule. This is called chain initiation. Additional monomers react with polymerisation initiating molecules to form a chain. This is called chain propagation. The chain terminates due to an inhibition process determined by the polymerisation reaction. The longer the UV exposure time, the longer the chains become resulting in a polymer with a higher molecular weight (Chua et al, 2003). The total reaction time ranges from milliseconds to days. The reaction time is nearly always in the order of milliseconds for resins used in SL.

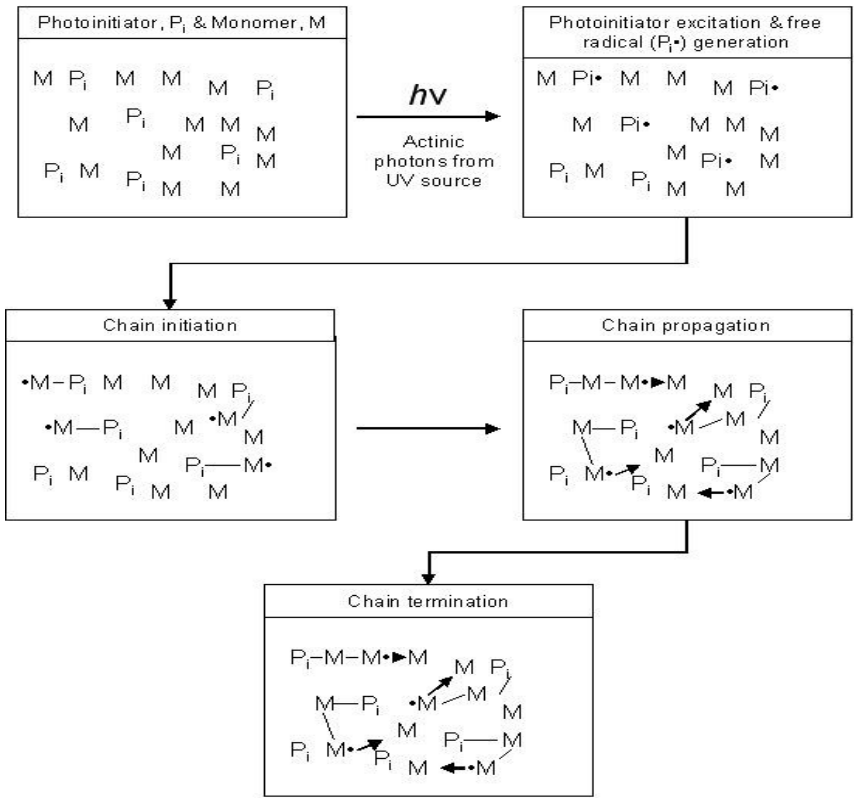

Figure 4.1 Free-Radical Photopolymerisation (Jacobs, 1996).

An advantage of acrylate-based polymers is that they have quite a high photospeed or photosensitivity, that is, they provide faster curing (Kunjappu, 2000). However, acrylates have disadvantages. One disadvantage is that oxygen must be kept from the acrylates environment as it retards the polymerisation reaction by removing free-radicals. This results in parts that are not cured enough and still in a "tacky" state. Another disadvantage of oxygen in the acrylate environment is the possibility of producing intolerable ozone caused by the reaction with the UV source.

To overcome the disadvantages of acrylate-based polymers, cationic photopolymerisation is more commonly used. In cationic photopolymerisation,

cationic initiators start the polymerisation. Cationic polymerisation is similar to the chain propagation that occurs with free-radical polymerisation, but in this case the growing polymer chain has an active end that is a positive ion. The two types of cationic monomers are epoxy resins and vinyl ether resins. These cationic resins have advantages in that they are not affected by ambient oxygen and they have a continued thermal curing after exposure to the UV source. However, they have some disadvantages. The polymerisation of cationic resin is affected by bases and water requiring a low humidity environment. Also, the photospeed is relatively slower when compared to acrylate-based resins (Jacobs, 1996). This can be overcome by using a higher power light source and also varies depending on the types of chemical components used (Chua et al, 2003; Kunjappu, 2000).

4.3 Cross-linking and Green Strength

An important part of the photopolymerisation process is cross-linking. Cross-linking that occurs in a resin generates an insoluble continuous network of molecules, especially a resin containing monomers with three or more reactive chemical groups. The parts that are made in these resins have strong structural strength due to the resulting chemical covalent bonds. Considerable heat is necessary to break these bonds and that is why parts do not melt upon applying heat. They soften at high temperature before thermally decomposing. Greater heat thresholds can be accomplished depending on the types of monomers used in the resin (Jacobs, 1996).

Immediately after SL prototypes are finished in the SLA, the resin that forms the prototype is in what is known as the “green” state. The green state is defined as the state at which cured layers can physically withstand the viscous forces generated during the SL fabrication process. The green state is when the photopolymer has been cured to have enough mechanical strength to support itself. The mechanical strength of the cured part is measureable in terms of elastic (Young’s) modulus and tensile or flexural strength (Jacobs, 1996) and also strain and hardness.

The state just before the green state is the gel point. The amount of energy required to reach the gel point is E_c (critical energy). As more energy is applied, the polymer starts to gain strength. This energy, E_x, is in excess over E_c. (Jacobs, 1992) defined an equation for E_x for the laser beam curing a polymer string, which is:

$$E_{\mathrm{x}} = \left(\frac{1}{C_d}\right)\int_0^{C_d}\left(E(z) - E_c\right)dz$$

$$E_x = \left\{\left(\frac{D_p}{C_d}\right)\left(\exp(\frac{C_d}{D_p}) - 1\right) - 1\right\}$$

(4.1)

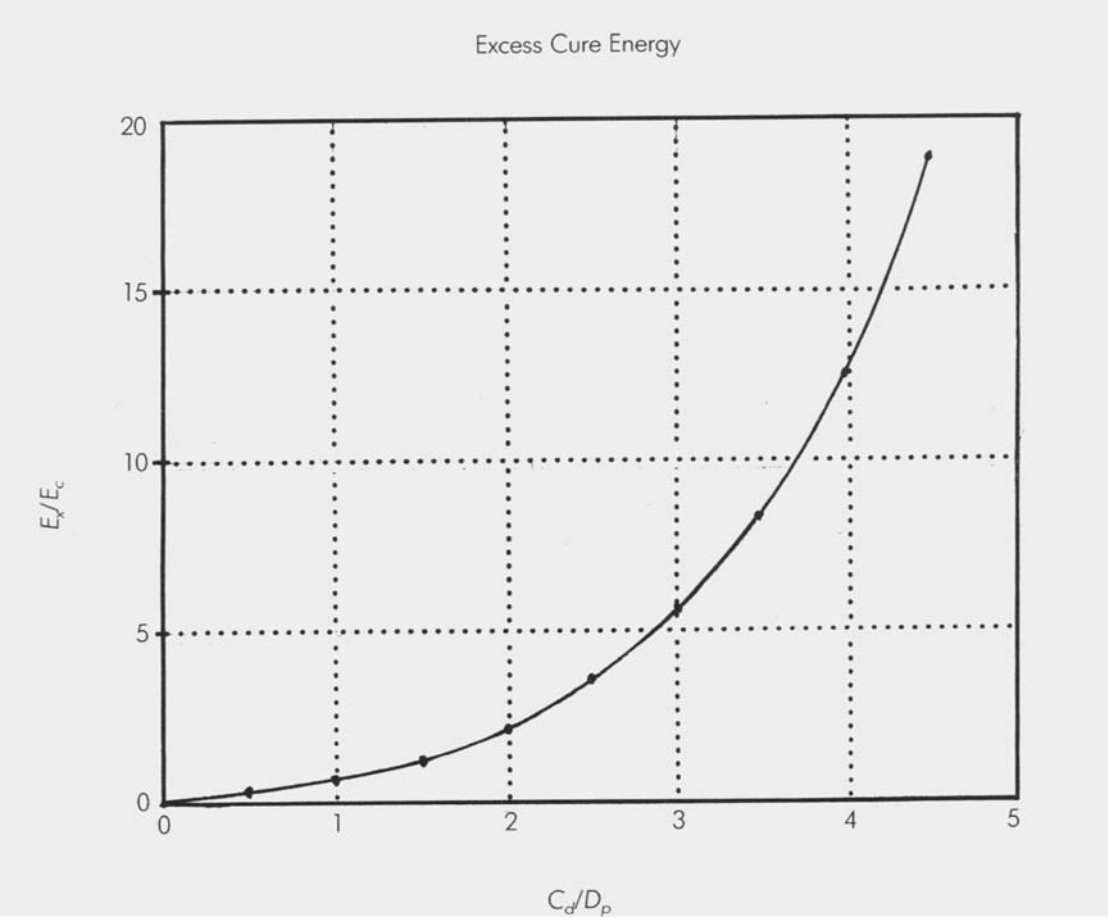

Figure 4.2 Graph of the exposure ration vs cure depth to penetration depth ratio (Jacobs, 1992).

Several important observations can be taken (4.1 and Figure 4.2. First, if E_c is lowered, while D_p is kept constant, green strength will decrease which may lead to insufficient mechanical strength. Secondly, decreasing initiator concentration and hence increasing the D_p, leads to decreased green strength. And lastly, at lower ratios of E_x/E_c and C_d/D_p it is very difficult to determine mechanical characteristics of resin in the green state.

The actual measurement of green strength was done in two ways according to (Jacobs, 1992) which depended on the intended purpose. For a comparison between resin properties, a single laser-cured string of polymer was used, as this cured string is

reproducible for a given C_d and laser beam profile. However, in 1992, beam profiles of He-Cd lasers were used and their profiles were not constant. To bypass this effect, about 15 overlapping laser scan lines were used to supply a sample for green strength testing. Typical specimen thickness for these single layers ranged from 0.3mm – 0.5mm. The other way testing for green strength was done was by using multiple layers which have higher green strengths than single layers. Higher green strengths are capable with multilayer laser-cured specimens due to overlapping, not only horizontally but also vertically, with the previous layer. Flexural modulus was used to define the structural strength of these multilayer parts. A 2.5mm x 150mm strip was cured 10mm thick (40 layers at 0.25mm thickness) for flexural testing.

In (Jacobs, 1996), the green strength was more standardised as green flexural modulus (GFM) but only for acrylate resins. The green strength tests of a 50mm x 10mm x 2.5mm specimens were measured on a Lloyds tensile test system. An equation for GFM was established for laser-cured parts in terms of laser beam diameter, hatch spacing, layer thickness and cure depth. No such system of green strength measurement exists for integrally cured, multilayered SL parts.

4.4 Resin Experiments & Research

In order for a photopolymer to be suitable for SL, it must provide certain characteristics. They must provide good rheological properties, low viscosity and low shrinkage (less than 1%). Because the composition of a resin is almost always proprietary information, reactivity and reaction rates of the photopolymer cannot be calculated. Ideally, if the concentrations of all the ingredients in the resin were known, the reaction rate at which the breaking of the carbon double bonds occurred could be calculated. This rate would correspond to each photon of light input into the resin. Because this calculation is not possible researchers have used analytical methods. The following subsections review several analytical methods used by researchers on photopolymers.

4.4.1 Fasari et al (1998) University of Sussex, UK

Farsari et al (1998) used holographic methods to characterise two commercial resins. These resins were the DuPont Somos 6100 and Ciba-Geigy Cibatool SL5180 resins which are no longer produced. However, Fasari et al describe how holographic gratings were used to compare the reactivity, rate of polymerisation and volume shrinkage of the two resins. Resin samples were prepared by placing a drop of resin

between two glass plates. The glass plates were separated by 0.1mm thick Mylar spacers. The sample was cured using an Ar-ion laser with a 1.57mm beam diameter at 351.1nm at 19°C. To create the holographic diffractive grating, the laser beam was split into two equal-power beams with a quartz cube beam splitter (Figure 4.3). The split laser beams are redirected to overlap on the sample generating a light pattern i.e. grating. To read the grating, a 5mW He-Ne laser with a wavelength of 632.8nm was shot through the sample. The wavelength of this laser did not cause polymerisation of the resin sample because the photoinitiators in the resins are not simulated at that wavelength. The He-Ne laser beam is diffracted as it passes through the sample and is detected by a silicon diode connected to an oscilloscope. This diode gives a way of measuring the refractive index change in the sample as the photopolymer is curing or in this case shrinking.

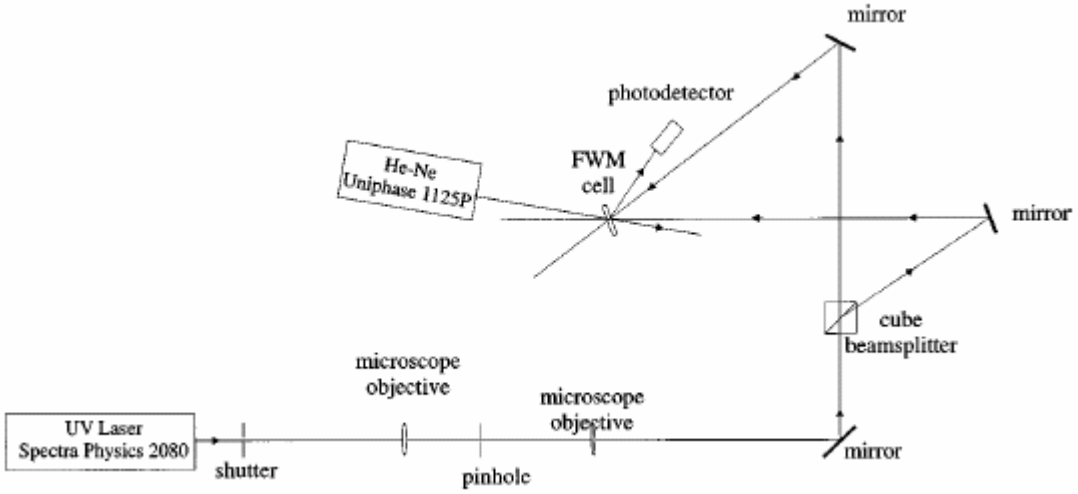

Figure 4.3 Experimental setup of holographic grating (Farsari et al, 1998).

Shrinkage in the resin causes curl. Fasari et al uses the diffraction efficiency of the photopolymer to indicate the amount of curl. Jacobs (1992) states that it has not been proven whether or not there is a direct relationship between volume shrinkage and the amount of curl. This is due to the unknown formulations of resins. Curl varies according to exact conditions such as the amount of exposure, the polymerisation rate, the exposure rate, total shrinkage and possible thermal effects.

The diffraction efficiency of the grating is the ratio of the intensity of the diffracted beam over the intensity of the incident beam. From the experimental data, Fasari et al showed that the induced refractive index change was non-linear with respect to the incident beam intensity which agrees with the classical resin working curve. The holographic grating spaces are calculated using refractive index of each resin. As the

refractive index was not specified by the manufacturer for each resin, an Abbe refractometer was used to measure the refractive index of each.

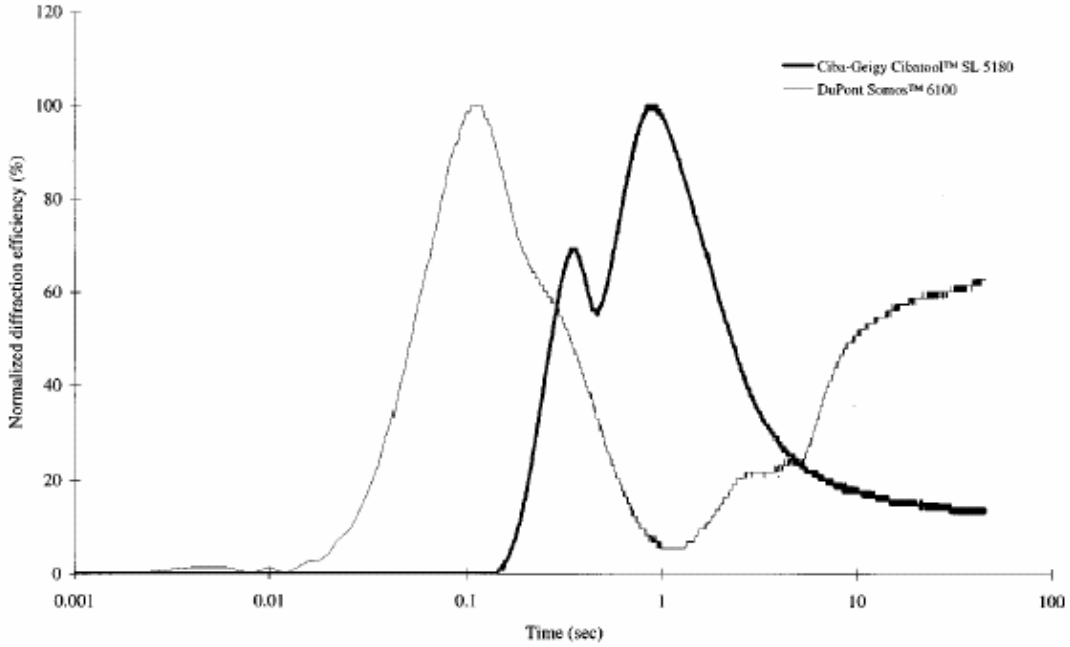

Figure 4.4 Plot of diffraction efficiency against irradiation time for both resins (Farsari et al, 1998).

In Figure 4.4, the diffraction efficiency is plotted against the logarithm of irradiation time for a beam power of 10mW (0.52W/cm^2) over 45sec. The resins showed different response characteristics. The initial peak in the DuPont Somos 6100 is an indication of the creation of cations and the second rise in diffraction efficiency is due to polymerisation. The Ciba-Geigy Cibatool SL5180 resin shows a different characteristic where polymerisation rapidly occurs after the creation of cations.

Fasari et al suggests that because polymerisation occurs in the resin regardless of the continuation of UV exposure, curing time is the time to the initial peak in the diffraction efficiency (maximum number of cations). The plot of diffraction efficiency versus irradiation time gives three pieces of information about the resin: delay time until diffraction begins, the final diffraction efficiency and the rate of diffraction. Delay time indicates the resin photosensitivity. The Somos resin had a ten times faster response than the Ciba-Geigy resin.

Fasari et al tested the diffraction efficiency for varying irradiance powers from 0.5-3.0W/cm^2. Irradiance was applied until the diffraction value was constant. Results showed that irradiance has no affect on diffraction efficiency. Diffraction increase was used as an indication of the reactivity of the resin. However, the diffraction increase rate can only be compared between the resins because the exact composition

of each resin is confidential (not allowing calculation of reactions per photon). The Somos 6100 resin proved to have a much higher diffraction increase with increasing irradiances and thus was prone to curl.

4.4.2 Scherzer & Decker (1999)

Scherzer and Decker (1999) used time-resolved FTIR (Fourier Transform Infrared) spectroscopy to study the kinetics of photopolymerisation. In FTIR spectroscopy, the concentration of specific functional groups in a chemical mixture can be monitored quantitatively. Conditions that were monitored included the photoinitiator concentration ([P]), light intensity (I), the thickness of the irradiated layer, how temperature affected the polymerisation rate (R_p), and the carbon double bond conversion or the degree of conversion.

The resin studied was a diacrylate called tripropylene glycol diacrylate (TPGDA) combined with a morpholino ketone as a photoinitiator known as Irgacure 369. A 100W mercury lamp with a monochromatic wavelength of 313nm was used as a UV light source to make use of the ketones high efficiency of absorption at that wavelength.

Several instruments were used to measure important elements of the experiments. UV light intensity was measured by a radiometer with a SiC detector calibrated for 313nm. An electronic shutter was used to control the exposure time of 1sec in coordination with the spectrometer computer. The thickness of the sample was controlled by a 4μm depression on a quartz plate, which covered the sample. Because the sample was covered, only the oxygen dissolved in the sample is relevant for inhibition.

Scherzer and Decker's first experiment looked at the effect of [P] in the resin. They varied [P] by weight from 0.1% to 3.0%. The increase in concentration led to an increase in polymerisation of the monomer and the maximum polymerisation rate was achieved earlier (Figure 4.5).

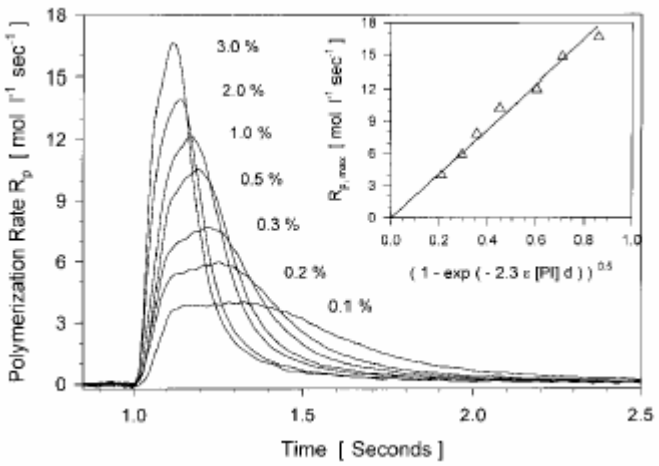

Figure 4.5 The effect of photoinitiator concentration on the reaction rate with an irradiance of 48mW/cm^2. The inset shows the dependence of R_{pmax} on the faction of absorbed light for various photoinitiator concentrations (Scherzer & Decker, 1999).

The relationship between R_p and [P] depended on the monomer conversion as the [P] was the parameter that was varied in the experiment. A plot of R_p versus [P] that was made at equal monomer conversion revealed that the maximum R_p occurred at the same degree of conversion as shown in Figure 4.6. This was at about 35% for the experiment.

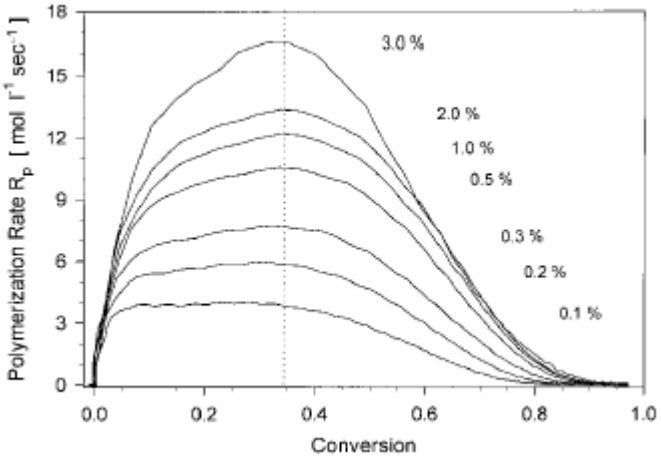

Figure 4.6 The dependence of polymerisation rate, Rp, with monomer conversion at various photoinitiator concentrations (Scherzer & Decker, 1999).

The second experiment tested the effect if incident light intensity. [P] was kept low at 0.3% for the experiment to stop the effects of over absorbance. The resin was exposed to three different intensities: 48mW/cm^2, 18mW/cm^2, and 9mW/cm^2. The increase in intensity resulted in higher maximum polymerisation rates that were reached sooner from the start time of the reaction (see Figure 4.7).

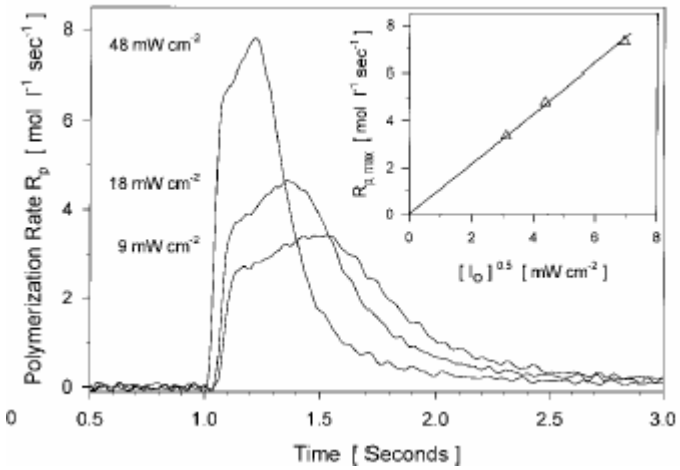

Figure 4.7 The effect UV light intensity on the polymerisation rate, R_p. The inset shows the dependence of R_{pmax} on the square root of incident light intensity (Scherzer & Decker, 1999).

The final experiment explored the effect of temperature. The TPGDA monomer with 0.1% photoinitator was irradiated at 48mW/cm^2 at different temperatures (25, 40, 55, 70, 85, 100°C). In contrast to other research by Broer et al (1991) and Lecamp et al (1997) who reported Arrhenius-like behaviour at lower temperatures, the results showed the maximum R_p was independent of temperature. A similar work by (Tryson & Shultz, 1979), where there was no effect from temperature for conversion rates less than 40%, agrees with Scherzer and Decker's findings. Figure 4.8 shows the results from Scherzer and Decker's temperature experiments.

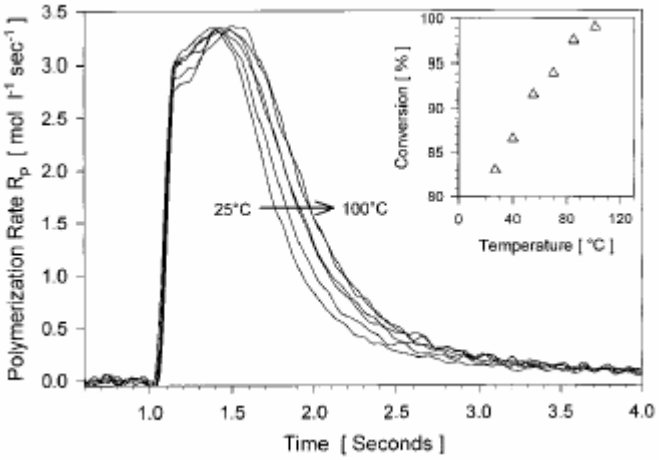

Figure 4.8 The effect of temperature on the polymerisation rate, R_p. of the acrylic double bonds of TPGDA. The inset shows the final conversion rate verses temperature (Scherzer & Decker, 1999).

Scherzer and Decker also found that there is an increase in the conversion of carbon double bonds at higher temperatures. This agrees with a study that used Darocure 1173 as a photoinitiator in TPGDA (Scherzer & Decker, 1999) and a study

on pigmented systems (Scherzer & Decker, 1999). The temperature rise makes more of the carbon-carbon bonds accessible for conversion due to the increased mobility of the network of molecules. In general, most observations found that R_p is not significantly dependent on temperature during exposure to UV, however, the final degree of conversion and thus the degree of cure increases with temperature. As the reaction is exothermic, Scherzer & Decker also considered the polymerisation heat for any influence on temperature. They found that the temperature increase was less than 10°C and therefore not significant enough to affect the reaction rate or degree of conversion.

Scherzer et al (1998) looked at other affects on acrylates from temperature. These included evaporation of the reactant, thermal degradation of the photoinitiator, and thermal polyerization. Results showed that these phenomena do not significantly affect the photopolymerisation of TPGDA with IC 369 under the test conditions.

4.4.3 Corcione et al (2004): Kinetic behaviour, Reaction Rate, Temperature effects

Kinetic behaviour provides a way of determining the cure time of a photopolymer resin. Analysis of the kinetic behaviour allows modelling of the heat transfer caused in the small zone around the laser beam incident on the resin surface. Epoxy-based resins commonly use the cationic mechanism for polymerisation and show continued curing after the irradiation is removed. This continued reaction is referred to as the dark reaction. The dark reaction of epoxy resins increases the green strength of parts substantially, whereas the dark reaction is negligible in acrylate-based resins.

Several researchers have studied resin kinetics (Apicella et al, 2005; Corcione et al, 2004).

Corcione et al studied the photopolymerisation kinetics of an epoxy-based resin in order to mathematically model the reaction. Their work was based on commercial SLA machines that use a laser beam to cure the epoxy resin. The resin used was SL5170 by Ciba (see data sheet in Appendix E: Resin Data Sheets). Corcione et al used a differential scanning calorimeter (DSC) and Fourier Transform Infrared Spectroscopy (FTIR) to obtain experimental results for the resin. These results were compared with a previous mathematical model presented by Nelson et al (1995).

The DSC was modified to allow a band of collimated UV light (325±nm) to cure a resin sample while it was in the DSC. 0.9-1.1mg resin samples 0.1mm thick were used where isothermal conditions and universal cure were achieved. In the first lot of

experiments, samples were cured at 30°C. Each sample was cured at a different intensity ranging from 1.44-4.33μW/mm^2. The second lot of experiments cured each sample at 2.48μW/mm^2 while beginning with each sample at a different temperature (30°C, 40 °C, 50°C, 60°C, 70°C). 70°C was chosen as the maximum as this is the glass transition of the resin (see data sheet). The cure was monitored with the DSC until the exothermal signal was minimal and considered complete.

The FTIR spectrometer was used to determine the composition and the reaction mechanism. A sample of resin was irradiated at 10sec intervals at 3.44μW/mm^2 until completely polymerised. After each exposure, the sample was examined by the FTIR spectrometer.

Corcione et al used the DSC measurements to formulate a relation between the heat evolved from polymerisation and the overall extent of reaction. The degree of reaction was defined as:

$$\alpha = \frac{H(\mathrm{t})}{H_{\max}} \tag{4.2}$$

Where H(t) is the partial heat of reaction developed during the DSC experiment and $H_{\max}$ is the maximum heat of reaction measured combining irradiation and heating.

The heat flow to determine the reaction rate was given by:

$$\frac{d\alpha}{d\mathrm{t}} = \frac{1}{H_{\max}} \cdot \frac{dH}{d\mathrm{t}} \tag{4.3}$$

The final degree of reaction, α_m, was given by the ratio of total heat developed and $H_{\max}$.

$$\alpha_{\mathrm{m}} = \frac{H_{\mathrm{total}}}{H_{\max}} \tag{4.4}$$

$H_{\max}$ was the sum of heat of photopolymerisation and the residual reactivity in the heated dark condition. The heat of photopolymerisation was found by high irradiation (4.33μW/mm^2) of a sample at the glass transition temperature (70°C). The heat of photopolymerisation was worked out to be 367J/g. Residual reactivity was found by heating the same sample to 250°C at 10°C/min in dark conditions. Residual reactivity was 43J/g. Results showed that α_m increases with increasing irradiation intensity. Corcione et al also note work by Maffezzoli and Terzi (1998) that states because irradiation intensity ultimately increases the reaction rate, $d\alpha/d$t, the rate of volume

shrinkage cannot keep up with the reaction rate. This leads to excess free volume which delays the resin's transition to the glassy state.

The effects of temperature on α_m, showed that α_m increased with temperature. There was an 8% increase in α_m with a 40°C temperature change.

Corcione et al report that the overall reaction rate is affected by two factors with regard to temperature and irradiance. The effect of diffusion as vitrification of the resin occurs and bulk viscoelasic effects (Kloosterboer et al, 1984; Maffezzoli & Terzi, 1998). This excludes kinetic effects.

The results from the FTIR analysis were used to find the composition of the resin. The various peaks from the FTIR spectrum confirmed the existence of various chemical groups such as vinyl ether at 1,637cm^{-1}, epoxy-cyclohexane at 810cm^{-1}, and glycidyl ether at 910cm^{-1}. Separate FTIR spectrums are taken for an uncured sample, a 10sec cure, and a fully cured sample (Figure 4.9).

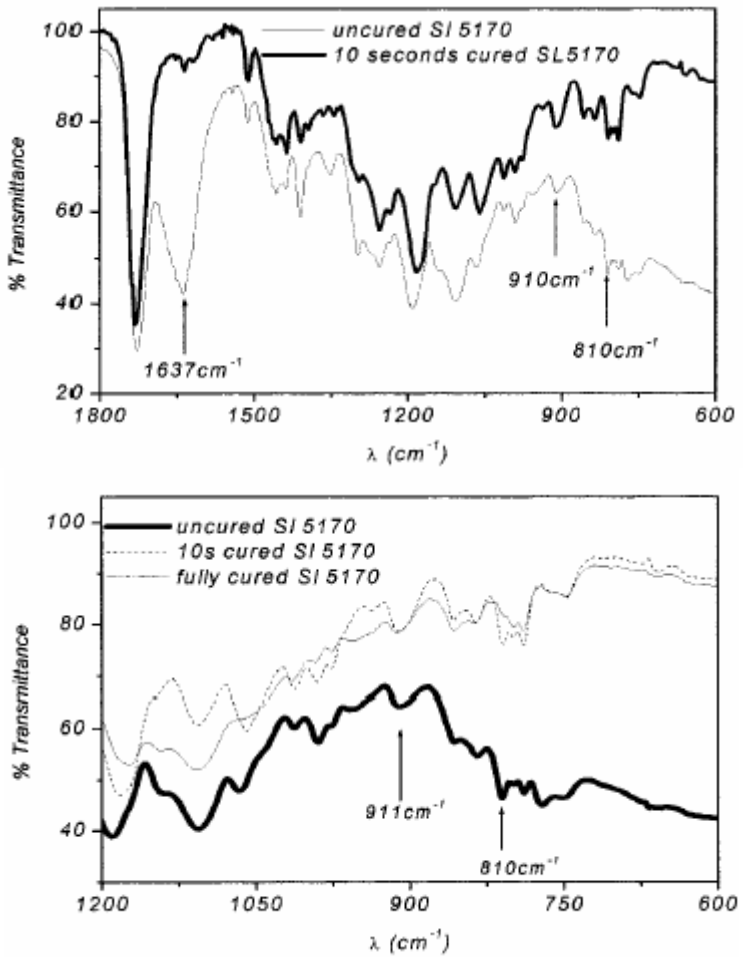

Figure 4.9 FTIR spectra and characteristic peaks of SL5170 sample (Corcione et al, 2004).

Comparison of the spectrums was able to show which groups reacted and which were consumed at different stages of polymerisation. Using these results made it possible to confirm that a double reaction mechanism was occurring. The vinyl ether group reacted rapidly upon a few seconds of exposure to irradiation. The epoxy-cyclohexane group was more sluggish and was independent of the vinyl ether reaction. The glycidyl ether group showed little reaction and therefore had a negligible contribution to the total heat flux.

The kinetic model of the reaction rate for cationic photopolymerisation was derived from the equations by Nelson et al (1995). Corcione et al showed that the equation for rate of monomer consumption could be given in terms of the reaction rate:

$$\mathrm{R_p} = \frac{d[\mathrm{M}]}{d\mathrm{t}} = -k_\mathrm{p}[\mathrm{M}][\mathrm{M}^+] \tag{4.5}$$

where [M] is the unreacted monomer, $[M^+]$ is the active centre concentration, and k_p is the propagation constant.

The concentrations are not known, as the exact resin composition is the intellectual property of Ciba. Corcione was able to find an expression for $[M^+]$ in terms of constants and photosensitizer concentration.

$$\frac{d[\mathrm{M}^+]}{d\mathrm{t}} = -k_\mathrm{i}^*[\mathrm{P}]_0 \exp(-k_\mathrm{i}^*\mathrm{t}) - k_\mathrm{t}[\mathrm{M}^+] \tag{4.6}$$

where t is time, k_i^* is the initiation constant, $[P]_0$ is the initial photosensitizer concentration, and k_t is the termination constant.

[M] was expressed as a function of the degree of reaction, α:

$$[\mathrm{M}] = [\mathrm{M}]_0(1-\alpha) \tag{4.7}$$

where $[M]_0$ was the initial monomer concentration. Substituting these expressions back into the (4.5 gave the expression for the reaction rate:

$$\frac{d\alpha}{d\mathrm{t}} = [\mathrm{P}]_0 \frac{k_\mathrm{p}k_\mathrm{i}^*}{k_\mathrm{t} - k_\mathrm{i}^*}(e^{-k_\mathrm{i}^*\mathrm{t}} - e^{-k_\mathrm{t}\mathrm{t}})(1-\alpha) \tag{4.8}$$

The *k* values were found by non-linear regression of a curve fitted to the experimental data for the reaction rate ((4.8). Each *k* value was calculated for each reaction mechanism at different values of temperature and irradiance. The product of $[P]_0$ and k_p was treated as one result as the photosensitizer concentration is not known.

The kinetic model was able to produce a good approximation of the experimental cure. Provided access to a UV modified DSC and FTIR spectroscopy technology, Corcione's kinetic model would provide a good estimate of the reaction rate of a resin that used the cationic mechanism for isothermal cure.

In a later work by Corcione et al (2006), Corcione was able to improve on his model to determine the evolution of temperature and degree of reaction in the resin. The work showed that increasing the energy at the resin surface increased the temperature. Temperature increase on the resin surface was found to be dependent on the energy dose. It was also shown that when a moving laser irradiates adjacent scans, the temperature evolved on the surface is much higher for faster scanning speeds than slower scanning speeds. This had a subsequent effect on overcure and reaction rate which can lead to higher shrinkage and curl distortion.

4.4.4 Apicella et al (2005): Shielding effect, degree of conversion/reaction.

Corcione et al (2006) found that the Lambert-Beer equation was only accurate for thin layers in agreement with Jacobs (1992). Similar research by Apicella et al (2005) in a dental study found that the shielding effect from already polymerised resin above an area undergoing photopolymerisation reduces the reaction rate. However, the degree of reaction was not influenced for sample sizes less than 1mm in thickness. The degree of reaction was shown to depend on the exposure time to light in the blue spectrum from a halogen lamp at 500mW/cm^2.

The experiment was conducted using a DSC modified to let the halogen lamp shine on a resin sample. The resin used was dental composite Z250 (3M ESPE) which is a blended dimethacrylate (USAF Dental Evaluation & Consultation Service, 2006). The experiment was done in four stages. First a 0.3mm thick resin sample was placed on an aluminium pan and positioned in the DSC. While maintained at 37°C, the sample was exposed to light four times at 100sec between exposures. One lot of samples were exposed to 20sec irradiance intervals and the other 60sec irradiance intervals. The next step used the already cured samples from the previous step and laid each over the top of a new thickness of resin. The experiment was then repeated to form a new resin composite with two layer thickness. The third step repeated step two so that a three layer resin composite was formed at about 1mm thick. This composite wafer was used

to act as the shield in the fourth step in which dentin adhesive (binds to tooth enamel) was exposed to irradiance.

4.5 Summary

In this chapter the chemistry of photopolymers has been covered to a brief extent. The photopolymerisation process was explained to show the chain of events occurring in a photopolymer upon exposure to the correct wavelength of light. It was discovered that epoxy-based resins have more desirable advantages over acrylate resins. Epoxy-based resins are not susceptible to reacting with oxygen in the air and have greater cured strength over acrylates.

Green strength of a resin is an important property. Green strength is measured in terms of the flexural modulus or GFM. However, no set test is established for epoxy-based resins. Although (Jacobs, 1992) reported in the context of laser-based SL, some of the observations and conclusions of green strength will be of interest to the green strength of integrally cured resin.

Several investigations by researches were reviewed where the compositions of the photopolymer are unknown due to intellectual property of the manufacturer. (Scherzer & Decker, 1999) were able to show that initiator concentrations led to faster maximum degrees of cure and quicker times till the maximum reaction rate. Also, increased light intensity showed faster reaction time and higher reaction rates.

Apicella et al (2005), Corcione et al (2004), Scherzer and Decker (1999) all use a DSC to maintain experiments at a constant temperature and to control exposure time. Each DSC had to be modified to allow UV light to pass through the sample. The common analysis technique where DSC are used is the ration of heat of polymerisation to overall heat of reaction to gauge the rate and degree of curing for a given irradiance, time and temperature. The trend from research data showed that in general, temperature does not significantly affect the degree of reaction.

Corcione et al (2004), Scherzer and Decker (1999) also use FTIR to determine composition of resins from which the reaction mechanism, polymerisation rates and degree of reaction are found. In fact, quite comprehensive analysis of a photopolymer can be conducted utilising DSC and FTIR technology.

Apicella et al (2005) analysed the shielding effect caused by cured resin closer to the surface. It is noted that for thin layer less than 1mm, the degree of reaction is not affected. Corcione et al (2004) found the degree of reaction through the ratio of heats

evolved by using the DSC. It should be noted that the degree of reaction or degree of conversion is an important quality of a cured layer. However, it is very time consuming to conduct degree of reaction experiments. This type of analysis of resin properties is more involved and more suitable to be conducted by qualified chemists.

Farsari et al (1998) also used a complex method of measuring polymerisation rate, exposure rate, shrinkage and thermal effects. Diffraction efficiency of a photopolymer was used to indicate curl. However, the experimental procedure used by Farsari et al is not easily reproducible. It is more common place to used DSC and FTIR analysis techniques.

Now that an understanding of photopolymers has been studied, the focus of the next chapter reviews the properties of light. Specific attention needs to be paid to the mathematically modelling of light and how models can be applied to physical situations. Then, using what has been learnt about photopolymers from this chapter, the modelling of the curing reaction can be assessed, particularly thin layers less than 1mm thick.

5 Properties of Light and Optics

The mathematical model devised for this thesis work requires knowledge of the properties of light and optics. Image formation is of particular interest to the mathematical model. The properties of light are presented in section 5.1. A review of geometric optics and raytracing is given in section 5.2. Section 5.2 introduces the fundamentals of raytracing and mathematical calculations for a raytracing algorithm. Section 5.3 discusses the cause of optical aberrations and how aberrations are minimised or corrected. Some common optics terms are defined for clarification in section 5.4. Finally, in section 5.5, several popular lens configurations are shown and discussed.

5.1 Properties of Light

Light can be thought of as particles, waves or rays. Light was thought of as having particle nature up until 1665, when wave-like properties were discovered. It was Heinrich Hertz who proved light travelled as an electromagnetic wave in 1887. It has been since 1930 with the development of quantum electrodynamics that both particle and wave properties have been comprehensively studied. The link between the wave and particle nature of light is that the emission and absorption of light has a particle aspect in the form of energy called photons or quanta. In general, the propagation of light is best described by waves while emission and absorption are best described by the particle nature of light (Young & Freeman, 1996).

The study of light is known as Radiometry and Photometry. The terminology is often highly confusing for both fields. The difference between the two is that Radiometry deals with radiant energy (i.e. electromagnetic radiation) of any wavelength whereas Photometry deals exclusively with radiation from the visible spectrum. The basic unit of power for Radiometry is the watt and the unit for photometry is the lumen. Thus, the field of light covered in this thesis is Radiometry as UV light is of primary concern to curing the photopolymer.

5.1.1 The Inverse Square Law

The inverse square law states that the illumination or irradiance on a surface is inversely proportional to the square of the distance from the source. Ideally, a light source is considered as a point source. However, as there is no ‘true’ point source, a

point source can be treated as fairly small relative to its distance from where intensity is measured.

Consider a point source that emits radiant energy equally in all directions at a rate of S watts (see Figure 5.1). Since the point source radiates energy into a sphere, the radiant intensity is *J* of S/4π watts per steradian. Now consider a surface r cm from the point source. One square centimetre of the surface subtends $1/r^2$ steradians from the source if the normal from the source to the surface intersects the surface. The radiant incident power per unit area is the irradiance *H*. *H* is found by multiplying the intensity of the source in watts per steradian by the solid angle subtended by the unit area (Smith, 2000).

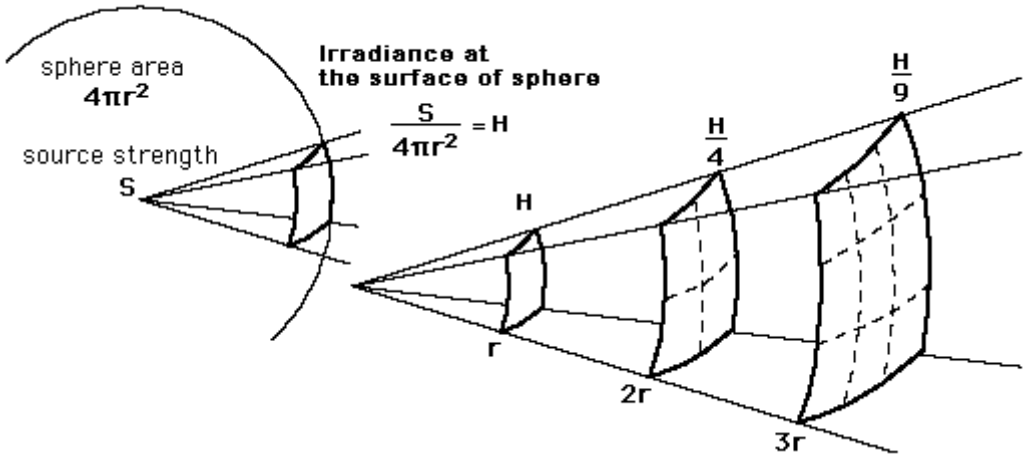

Figure 5.1 The inverse square law of light irradiance.

$$H = J\frac{1}{r^2} \qquad \textbf{(5.1)}$$

(5.1 is the inverse square law. The units of irradiance are W/cm^2. For example a 100W lamp (assuming it as a point source) will emit radiant energy with an intensity of $J = 100/4\pi = 8mW/ster$. The intensity *H* at 100cm from the source will be $8mW/cm^2$. If the surface is flat, the irradiance is only $8mW/cm^2$ where the surface is normal to the point source. As the distance along the surface from the normal increases, the source to surface distance increases by r/cos θ (see Figure 5.2). The effective projected area on the surface is reduced by a factor of approximately cos θ. This is a fair approximation if the source to surface distance is large compared with the size (diameter) of the source. Effectively both the solid angle subtended and the irradiance is reduced by $\cos^3 \theta$.

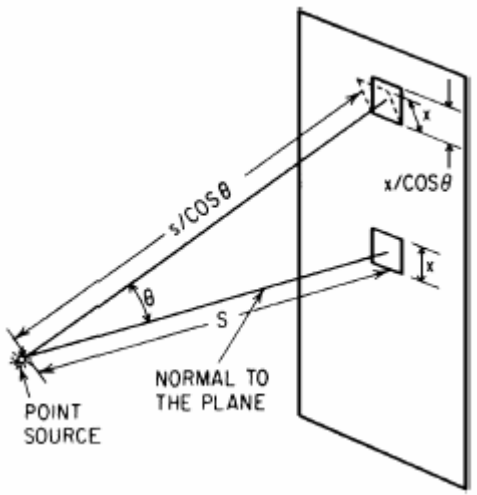

Figure 5.2 Geometry of a point source irradiating a plane showing how the solid angle and irradiance are reduced by $\cos^3\theta$ (Smith, 2000).

It is worth mentioning the term radiance as there is an important difference between radiance and irradiance. The unit of radiance takes into account that the source emits radiation per unit area. The usual units for radiance are W/ster·cm^2. Radiance is a term used to describe the intensity of an extended source. An extended source is a light source with significant dimensions. Extended sources follow Lambert's law of intensity rather than the inverse square law.

$$J_\theta = J_0 \cos\theta \tag{5.2}$$

where J_θ is the intensity of a small incremental area of the source in a direction at angle θ from the normal to the surface. J_0 is the intensity of the incremental area in the direction of the normal. It is important to note that even though the radiance is in W/ster·cm^2, the radiation is not uniform over the steradian or centimetre squared.

5.2 Geometric Optics and Raytracing

In order to understand how light can be represented graphically and mathematically, some geometric optics needs to be discussed. Thin lenses are the simplest form of optical device widely used. It can be used to show how the position and lateral magnification of an image may be found as in Figure 5.3 (Young & Freeman, 1996). s and s' are the object and image distances respectively and h and h' are object and image heights respectively. In general primed symbols denote dimensions that refer to the image and unprimed symbols refer to the object.

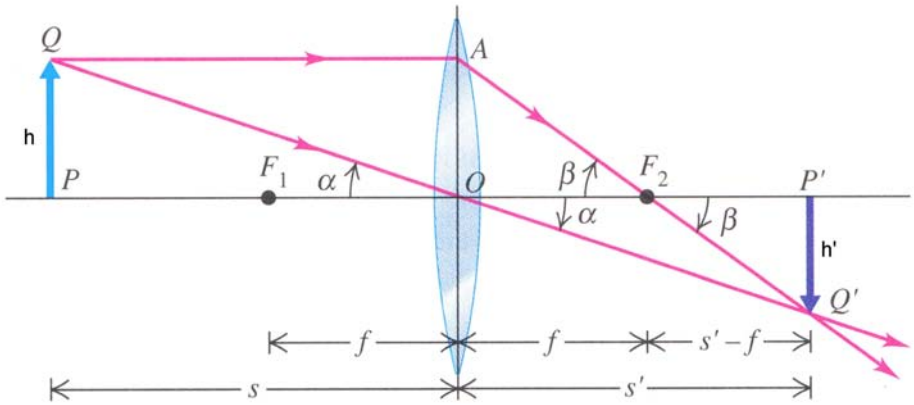

Figure 5.3 Thin lens showing the position and lateral magnification of traced rays (Young & Freeman, 1996).

A sign convention must be defined for consistency and so that there is no confusion between various optical diagrams. The following sign convention will be adopted throughout this thesis:

1. Light rays travel from left to right.
2. Heights above the optical axis are positive (e.g. PQ and AO).
3. Distances measured to the left of a reference point are positive. (e.g. OP is negative; OP' is positive).
4. The focal length of a converging lens is positive and the focal length of a diverging lens is negative.

The two angles, α, are equal making the right triangles PQO and P'Q'O similar triangles. The ratios of the corresponding sides are equal. This allows for the following relation:

$$\frac{h}{s} = -\frac{h'}{s'} \text{ or } \frac{h'}{h} = -\frac{s'}{s} \tag{5.3}$$

The negative sign indicates that the image is below the optical axis.

The two β angles are also equal and the two right angle triangles OAF_2 and $P'Q'F_2$ are similar, so as before, the ratios of corresponding sides are equal and given by:

$$\frac{h}{f} = -\frac{h'}{s'-f} \text{ or } \frac{h'}{h} = -\frac{s'-f}{f} \tag{5.4}$$

In (5.4, the optical system is in air (index of refraction equals one), therefore the focal lengths OF_1 and OF_2 are equal. Using this fact, equating (5.3 and (5.4, dividing the equation by s and rearranging allows the object-image relation to be obtained for a thin lens:

$$-\frac{s'}{s} = -\frac{s-f}{f}$$

Divide by s'

$$-\frac{s'}{s} = -\frac{s}{f} + 1$$

$$-\frac{1}{s} = -\frac{1}{f} + \frac{1}{s'}$$

$$\boxed{\frac{1}{f} = \frac{1}{s} + \frac{1}{s'}}$$

(5.5)

Also note that the ratio h'/h is the lateral magnification and therefore the magnification is the same as the ratio of –s'/s. The negative sign indicates that the image is inverted.

5.2.1 Refraction of a Light Ray at a Single Surface

A ray of light can be traced through an optical system with the use of Snell's Law which is written as:

$$n_1 \sin I_1 = n_2 \sin I_2$$

(5.6)

where *n* is the index of refraction of the medium through which the light ray travels. I is the angle of incidence that the light ray makes with the normal to the surface.

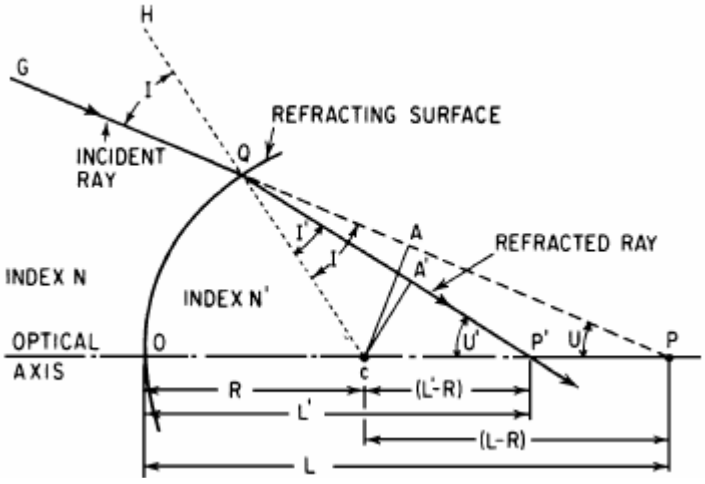

Figure 5.4 Refraction of a light ray passing through a single surface (Smith, 2000).

Figure 5.4 shows ray GQP as it passes through a single refracting surface. The surface has a radius R with the centre of curvature centred at point C. The surface divides two mediums of refractive index N on the left and N' on the right. All the unprimed symbols indicate qualities of the ray as if it did not undergo refraction. The primed rays indicate the path of the ray after refraction.

It is here that more rules for sign convention must be added:

5. A radius is positive if the centre of curvature lies to the right of the surface; negative if it is to the left.
6. The angles of incidence and refraction (I and I') are positive if the ray is rotated clockwise to reach the normal.
7. The slope angles (U and U') are positive if the ray is rotated clockwise to reach the axis.

The following set of equations trace the ray GQP so that the refracted ray's intersection with the optical axis, L', and its slope angle U' may be found. These equations are useful only if L and U are specified.

From right triangle PAC:

$$CA = (R - L)\sin U \tag{5.7}$$

From right triangle QAC:

$$\sin I = \frac{CA}{R} \tag{5.8}$$

Applying Snell's Law, the sine of the angle of refraction is:

$$\sin I' = \frac{n}{n'}\sin I \tag{5.9}$$

The exterior angle QCO of triangle PQC is equal to –U'+I and as the exterior angle of triangle P'QC is equal to –U'+I', –U+I = –U'+I'. Hence, the slope angle of the refracted ray is:

$$U' = U - I + I' \tag{5.10}$$

From right triangle QA'C:

$$\sin I' = \frac{CA'}{R} \tag{5.11}$$

Substituting Equation 5.8 and 5.11 into Equation 5.9 gives:

$$CA' = \frac{n}{n'}CA \tag{5.12}$$

The location of point P' is found by rearranging $CA' = (R - L')\sin U'$ from right triangle P'A'C into the equation below:

$$L' = -\frac{CA'}{\sin U'} \tag{5.13}$$

5.2.2 The Paraxial Region

The paraxial region is the name for the thread like region about the axis of an optical system. The paraxial region or rays are often referred to in optics and optical design because calculations, estimations and manipulation of equations are relatively quick and easy. The region is considered infinitesimally small so that the angles made by the rays traced in this region (the slope angles and the angles of incidence and refraction) may be set equal to their sines and tangents. Paraxial calculations are usually known as paraxial approximations and the calculations are used to estimate diameters of optical elements and approximation of image aberrations.

To indicate that calculations refer to the paraxial region, lower-case letters are used to indicate paraxial values. The paraxial equations can be easily derived from the equations for tracing a refracted ray as defined in the previous section. By substitution of the paraxial equations into (5.7 through to (5.13 and rearranging, the following equation is found that looks of similar form to (5.5 that relates the object and image distances:

$$\frac{n'}{l'} = -\frac{(n'-n)}{R} + \frac{n}{l} \qquad \textbf{(5.14)}$$

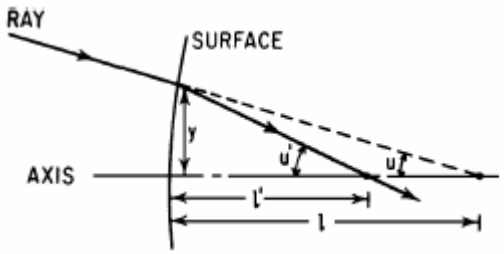

Figure 5.5 Enlarged view of the Paraxial region with finite height y (Smith, 2000).

Tracing a ray through more than one surface is essential. Figure 5.5 shows a ray passing through a surface with an added measurement for height y. The introduction of finite height y does not affect the accuracy of calculations even though all heights and angles cancel out in the above paraxial expressions. Ideally, the surface in the paraxial region is a flat plane and all angles approach their sines and tangents. Hence the slope angles can be expressed as:

$$\mathrm{u} = -\frac{\mathrm{y}}{l} \text{ and } \mathrm{u}' = -\frac{\mathrm{y}}{l'} \qquad \textbf{(5.15)}$$

By rearranging and substituting for l and l' in (5.14, the slope after refraction is found:

$$u' = \frac{nu}{n'} + \frac{-cy(n'-n)}{n'} \tag{5.16}$$

where c is the curvature of the surface.

When two or more surfaces are involved, a set of transfer equations are used to calculate y and u for the following surface. The distance that the ray travels between two consecutive surfaces is equal to *t* because in the paraxial region, the surfaces are considered as parallel planes. Also, as the slope of the refracted ray is the same all the way between two surfaces, the angle of the refracted ray is the same as the angle of incidence on next surface.

$$y_{i+1} = y_i + tu'_i \tag{5.17}$$

$$n_{i+1}u_{i+1} = n'_i\, u'_i \tag{5.18}$$

5.2.3 Skew Rays

Skew Rays are general rays that must be defined with three coordinates x, y, and z. The advancement of computer processing has aided in the application of skew rays in ray tracing software. The ray tracing equations originate from work done by D. Feder (Feder, 1951). Figure 5.6 shows the meanings of the coordinate system defining a skew ray. The ray vector is of unit length and originates from an x, y, and z coordinate on a surface where the origin is usually centred on the optical axis. The direction of the ray in space is defined by the direction cosines X, Y, and Z.

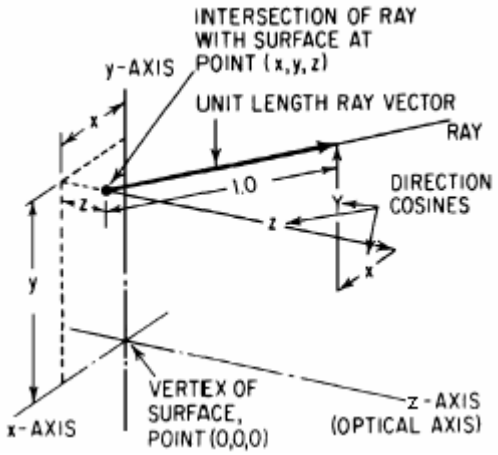

Figure 5.6 Skew Rays with direction cosines X, Y, Z (Smith, 2000).

The direction cosines are the cosines of the angles that a ray makes with each respective axis. Figure 5.7 shows ray OP that makes angles α, β, and γ with the x, y, and z axes respectively.

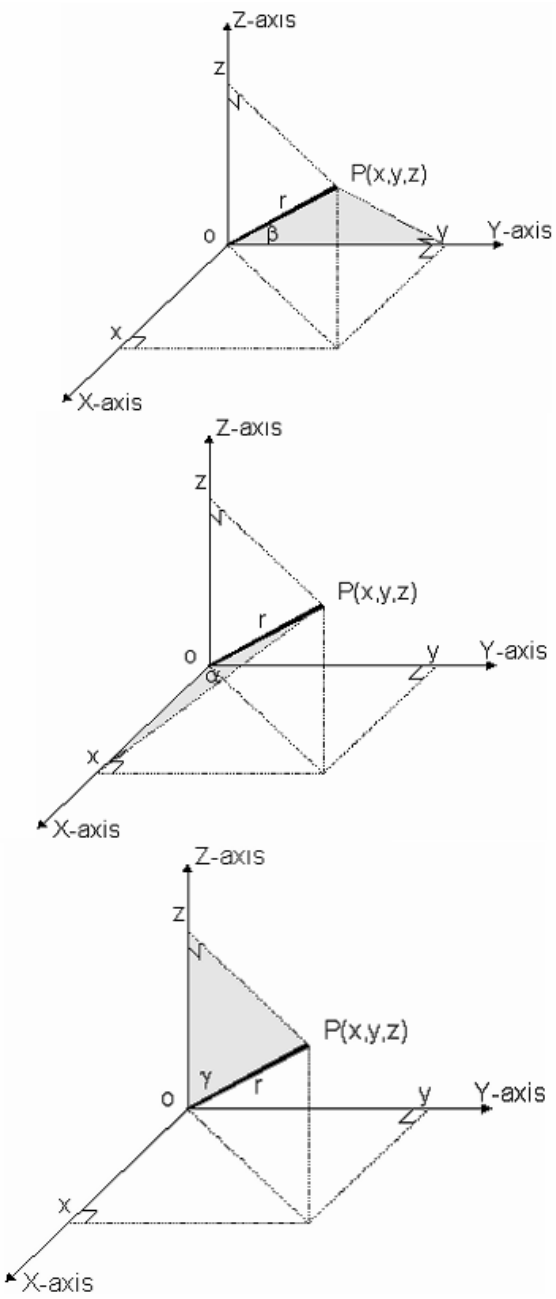

Figure 5.7 Coordinate definitions for direction cosines X, Y, Z.

Thus the direction cosines are calculated by:

$$X = \cos\alpha = \frac{x}{OP} \tag{5.19}$$

$$Y = \cos\beta = \frac{y}{OP} \tag{5.20}$$

$$Z = \cos\gamma = \frac{z}{OP} \tag{5.21}$$

A property of direction cosines is that the sum of their squares equals one (see (5.23 below). This property is used as a check to ensure that the ray calculations are correct.

The definition of a skew ray starts with selecting a reference surface. The reference surface can be a plane or a spherical surface and is positioned at or near the object. After the reference surface has been defined mathematically, the ray is traced through to the next surface with a set of refraction equations ((5.32 to (5.36). Iterations begin again at the start of the transfer equations ((5.24 to (5.31) and continue through each surface until the last surface (the image) is reached. Note that (5.22 is the equation for a sphere which becomes the equation for a plane when c = 1.

Opening (at the reference surface):

$$c(x^2 + y^2 + z^3) - 2z = 0 \tag{5.22}$$

$$X^2 + Y^2 + Z^2 = 1 \tag{5.23}$$

Transfer equations to the next surface:

$$e_i = t_{i-1}Z_{i-1} - (x_{i-1}X_{i-1} + y_{i-1}Y_{i-1} + z_{i-1}Z_{i-1}) \tag{5.24}$$

$$M_{iz} = z_{i-1} + e_i Z_{i-1} - t_{i-1} \tag{5.25}$$

$$M_i^2 = x_{i-1}^2 + y_{i-1}^2 + z_{i-1}^2 - e_i^2 + t_{i-1}^2 - 2t_{i-1}z_{i-1} \tag{5.26}$$

$$E_i = \sqrt{Z_{i-1}^2 - c_i(c_i M_i^2 - 2M_{iz}} \tag{5.27}$$

$$L_i = e_i + \frac{(c_i M_i^2 - 2M_{iz})}{Z_{i-1} + E_i} \tag{5.28}$$

$$z_i = z_{i-1} + L_i Z_{i-1} - t_{i-1} \tag{5.29}$$

$$y_i = y_{i-1} + L_i Y_{i-1} \tag{5.30}$$

$$x_i = x_{i-1} + L_i X_{i-1} \tag{5.31}$$

Refraction equations:

$$E'_i = \sqrt{1 - \left(\frac{n_{i-1}}{n_i}\right)^2 (1 - E_i^2)} \tag{5.32}$$

$$g_i = E'_i - \frac{n_{i-1}}{n_i} E_i \tag{5.33}$$

$$Z_i = \frac{n_{i-1}}{n_i} Z_{i-1} - g_i c_i z_i + g_i \tag{5.34}$$

$$Y_i = \frac{n_{i-1}}{n_i} Y_{i-1} - g_i c_i y_i \tag{5.35}$$

$$X_i = \frac{n_{i-1}}{n_i} X_{i-1} - g_i c_i x_i \tag{5.36}$$

5.3 Aberrations

Raytracing over the entire surface of a simple thin lens does not follow the paraxial equations. All the possible rays that pass through the lens do not have the same focal length for all the object points. This is due to various types of aberration. Classifying the types of image faults and having an understanding of their behavior, allows simplification and correction of the imaging problems into manageable calculations. The measure of aberration gives the amount by which rays miss the paraxial image point. The various types of aberration are classified as follows.

- Spherical aberration
- Astigmatism and Petzval Curvature
- Coma
- Distortion
- Chromatic Aberration

(Smith, 2000) provides a thorough description of the types of aberrations that occur in a symmetrically optical system which are discussed in this section.

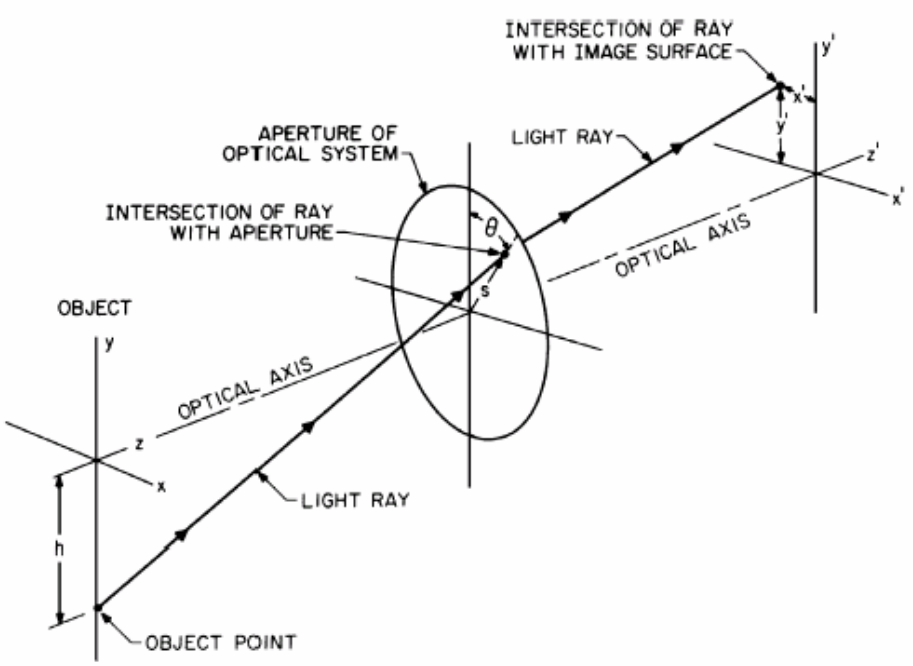

Figure 5.8 Symmetric optical system tracing a light ray from an object point to the intersection with the image plane (Smith, 2000).

In a symmetric optical system like the one in Figure 5.8, any point on the object plane can be ray traced to find its corresponding intersection on the image plane. If a ray is traced from the object plane at a point lying on the y-axis at a distance of *h* from the optical axis and passing through the system aperture at a point described by its polar coordinates (*s*, θ), the ray will intersect the image plane at the point *x'*, *y'*. The intersection with the image plane can be described as a function of *h*, *s* and θ.

$$\begin{aligned} y' &= A_1 s\cos\theta + A_2 h \\ &+ B_1 s^3\cos\theta + B_2 s^2 h(2+\cos 2\theta) + (3B_3 + B_4)sh^2\cos\theta + B_5 h^3 \\ &+ C_1 s^5\cos\theta + (C_2 + C_3\cos 2\theta)s^4 h + (C_4 + C_6\cos^2\theta)s^3 h^2\cos\theta \\ &+ (C_7 + C_8\cos 2\theta)s^2 h^3 + C_{10} s h^4\cos\theta + C_{12} h^5 + D_1 s^7\cos\theta + \cdots \end{aligned} \quad \textbf{(5.37)}$$

$$\begin{aligned} x' &= A_1 s\sin\theta \\ &+ B_1 s^3\sin\theta + B_2 s^2 h\sin 2\theta + (B_3 + B_4)sh^2\sin\theta \\ &+ C_1 s^5\sin\theta + C_3 s^4 h\sin 2\theta + (C_5 + C_6\cos^2\theta)s^3 h^2\sin\theta \\ &+ C_9 s^2 h^3\sin 2\theta + C_{11} s h^4\sin\theta + D_1 s^7\sin\theta + \cdots \end{aligned} \quad \textbf{(5.38)}$$

(5.37 and (5.38 are power series from which the general form can be determined. It can be seen that the *A* terms have s & h with exponents of unity. The *B* terms are third order as in s^3, s^2h, sh^2 and h^3. The *C* and *D* terms are fifth and seventh order respectively. Also notice that there are two first order terms, five third order, and nine seventh order and (n+3)(n+5)/8 – 1 nth order terms. There are only odd-order terms in

an axially symmetrical system. All the terms in both (5.37 and (5.38 are called "transverse aberrations". They represent the distance by which a ray misses the ideal image point (x', y') as described by the paraxial imaging equations given in section 5.2.2.

The A terms relate to the paraxial region. A_1 is the distance from the paraxial focus to the system image plane. A_2 is the magnification (h'/h). The B terms are commonly known as the Seidel or primary aberrations. B_1 is spherical aberration, B_2 is coma, B_3 is astigmatism, B_4 is Petzval, and B_5 is distortion. The C terms are known as secondary aberrations where C_1 is fifth-order spherical aberration, C_2 and C_3 are linear coma, C_4, C_5 and C_6 are oblique spherical aberration, C_7, C_8 and C_9 are elliptical coma, C_{10} and C_{11} are Petzval and astigmatism, and C_{12} is distortion. The terms in D follow on in a similar fashion and are called the tertiary aberrations. For most applications of (5.37 and (5.38, only calculations up to the secondary aberrations are required. In general, good results can be obtained by only accounting for the Seidel aberrations (Seidel aberrations are not reviewed in this thesis).

It is necessary to describe the different types of aberrations in order to gain an understanding of what characterises each type, their representation and their effects on the appearance of the image. Note that each aberration is discussed as if it were the only one present. However, in practice they are encountered in combination.

5.3.1 Spherical Aberration

When spherical aberration is present, it looks like a bright dot surrounded by a halo of light. It softens the image and blurs its details. Spherical aberration can be defined as the variation of focus with aperture. Figure 5.9 shows an exaggerated sketch of a lens forming an image of an axial object positioned some distance away from the lens. Rays close to the optical axis come to a focus near the paraxial focus. Rays further away from the optical axis come to a focus at a distance LA_R' from the paraxial focus. This distance is the longitudinal spherical aberration. Transverse spherical aberration is the vertical distance, TA_R', that a ray differs from the paraxial focus.

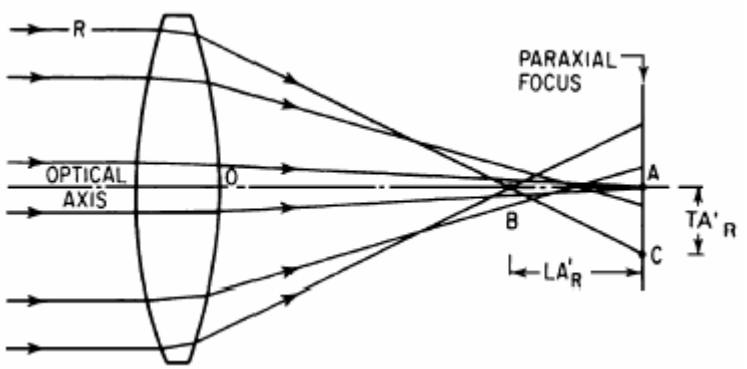

Figure 5.9 Longitudinal and transverse spherical aberration of a simple lens (Smith, 2000).

Spherical aberration is usually represented graphically as presented in Figure 5.10. Longitudinal spherical aberration is plotted with ray height and is used to understand the field curvature and axial chromatic. Transverse spherical aberration is plotted using the final slope of a ray and is called a ray intercept curve. The curve is usually an 'S' shape and when optimising transverse spherical aberration, it is important to have the slope at zero across the central portion of the graph. Graphing the ray intercept curve allows quick identification of what aberration is occurring in the optical system.

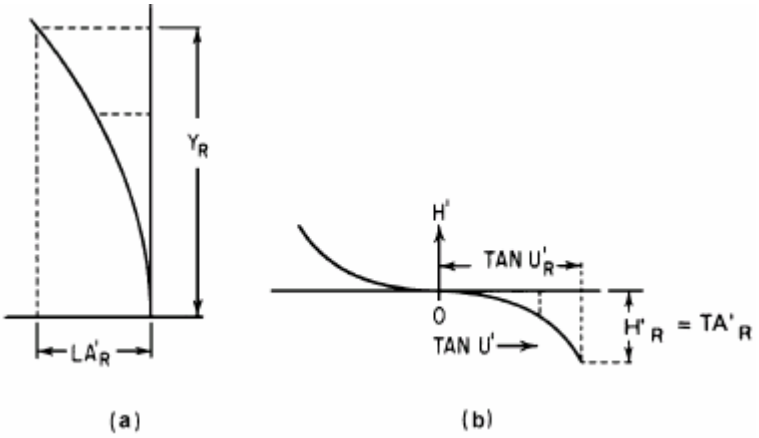

Figure 5.10 Graphical representation of spherical aberration. (a) Longitudinal aberration verses ray height. (b) Transverse aberration which is ray intercept height verses final ray slope. (Smith, 2000).

Spherical aberration is determined by tracing a paraxial ray and a ray of some height, h, from the same axial object point and finding their final intercept distances l' and L'. In Figure 5.9, l' is distance OA and L' (ray R) is distance OB. The longitudinal spherical aberration is given by:

$$LA' = L' - l' \tag{5.39}$$

Transverse aberration is given by:

$$TA' = -LA' \tan U_R' = -(L' - l') \tan U_R' \quad \textbf{(5.40)}$$

where U_R' is the angle that ray R makes with the optical axis.

Examples of ray intercept curves are given in Figure 5.11. Undercorrected spherical aberration is spherical aberration with a negative sign according (5.40. Overcorrected spherical aberrations are those with positive signs.

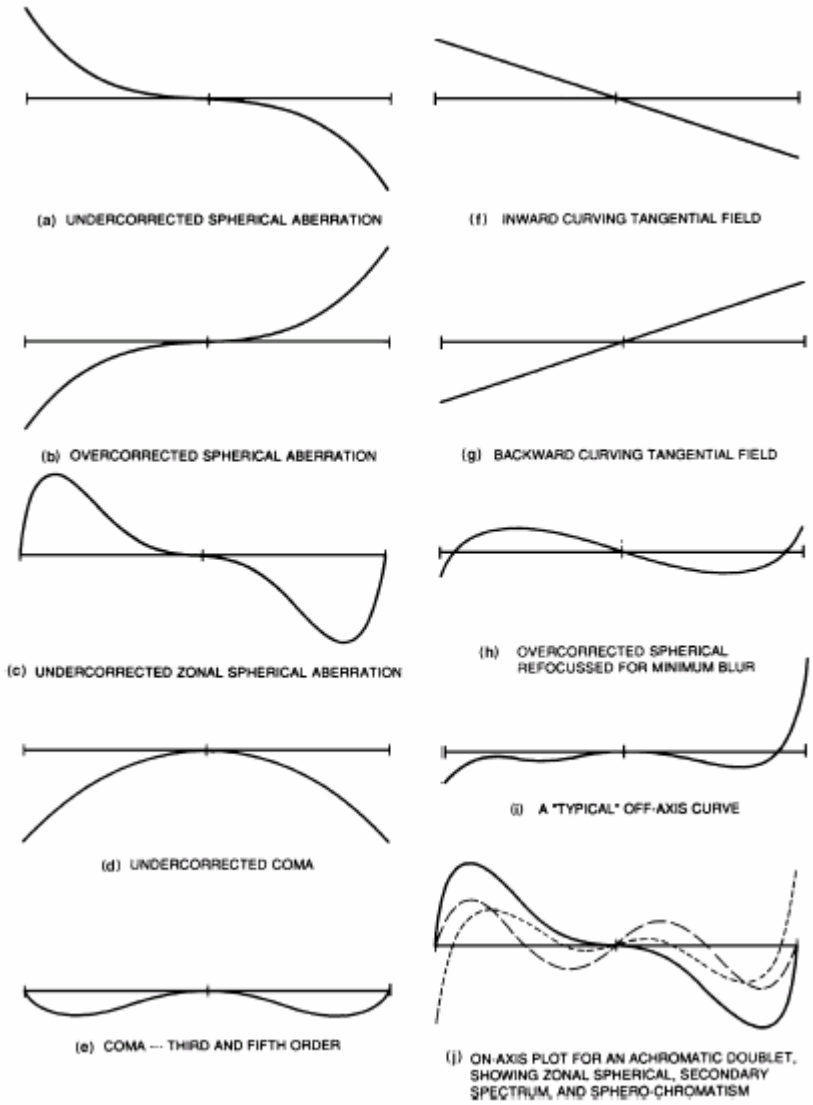

Figure 5.11 Ray intercept curves for various aberrations (Smith, 2000).

5.3.2 Coma

Coma is defined as the variation of magnification with aperture. It occurs when oblique rays pass through the edges of a lens and intersect at a different height than rays that pass through the centre of the lens. Figure 5.12 depicts how coma occurs.

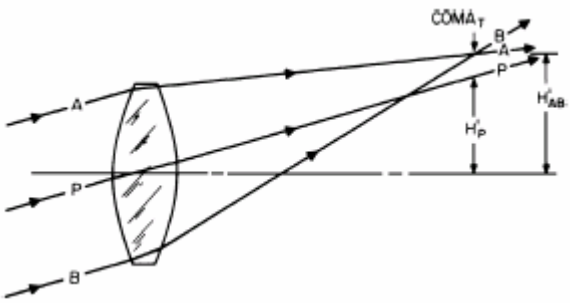

Figure 5.12 Ray diagram of coma (Smith, 2000).

The vertical distance from ray P to the intersection of rays A and B is called the tangential coma of the lens. The aberration appears comet shaped as shown by the point image or coma patch in Figure 5.13. This coma patch is used to show the relationship between rays that pass through the lens aperture and their position on the coma patch.

Figure 5.13 The comet shaped coma patch (Smith, 2000).

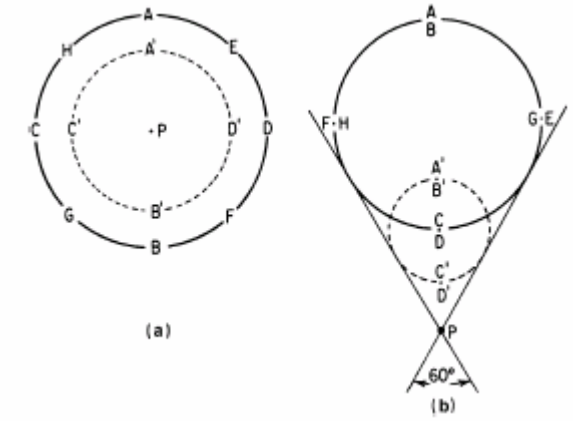

Figure 5.14 The relationship between lens aperture and the coma patch (Smith, 2000).

Figure 5.14 explains the relationship between lens aperture and the coma patch even further. Figure 5.14a views the lens aperture with rays indicated by letters A-H and A'-D'. Figure 5.14b shows the resulting coma. The rays that lie on the inner circle of the aperture form a smaller circle on the coma patch. However, as the rays go around the aperture circle once, they go around the corresponding coma circle twice in agreement with the B_2 terms of (5.37 and (5.38. The size of the circle of rays made

on the comatic image is proportional to the square of the diameter of the lens aperture circle. The combination of many different-sized circles form an image with all the ray circles lying tangent to a 60° angle with ray P at the point. As can be seen in Figure 5.13, there is a very high density of rays closer to the centre of the lens. In fact, about half of all the energy in the coma patch lies in the triangular area between P and CD. The distance from P to AB, in Figure 5.14b, is the tangential coma. The distance from P to CD is called the sagittal coma. Sagittal coma is roughly one third the size of tangential coma and because it lies in the high density region, it is used to measure the effective size of the image aberration rather than tangential coma.

5.3.3 Astigmatism and Petzval Curvature

In order to understand astigmatism, the terms "tangential" and "sagittal" require further discussion. Figure 5.14a has shown a diagram of rays from the view point of looking along the optical axis. The ray that lies along the plane of the vertical axis running through rays A, A', P, B' and B are called meridional or tangential rays. All other rays lying outside of the meridional plane are referred to as skew rays, with the exception of ray P which is known as the principle or chief ray. Rays that lie along the horizontal plane running from C to D are also called sagittal rays.

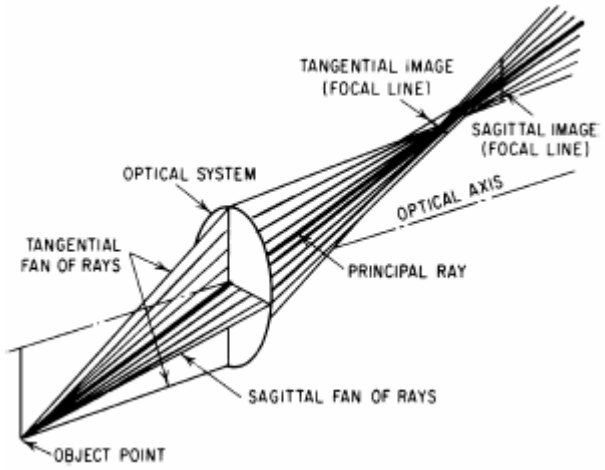

Figure 5.15 Astigmatism caused by a point object (Smith, 2000).

Figure 5.15 uses the example of a point object to show how astigmatism occurs. The figure shows that an oblique fan of rays in the tangential plane of the point object becomes a line in the sagittal plane of the image. Similarly, a fan of rays in the sagittal plane of the point object becomes a line in the tangential plane of the image. Astigmatism occurs when these two lines in the image do not coincide. The presence of astigmatism looks like an elliptical or circular blur caused by the two separate lines seen to the right of the lens in Figure 5.15.

The extent of astigmatism increases as a ray moves further away from the optical axis of the image. The image rarely lies on a perfect plane but rather a parabolic surface. When primary astigmatism is present in a simple lens, the image surface looks like the diagram given in Figure 5.16.

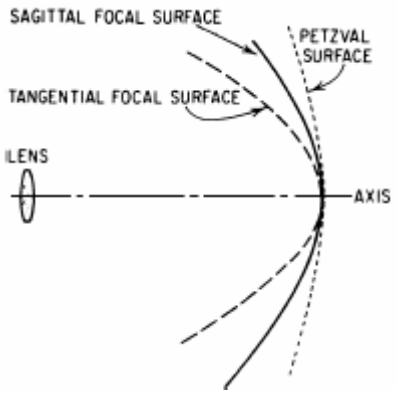

Figure 5.16 The primary astigmatism of a simple lens showing the tangential, sagittal and Petzval surfaces (Smith, 2000).

The amount of astigmatism in a lens is a function of the power and shape of the lens and its distance to the aperture of the optical system. In the case of a simple lens whose diameter is also the aperture; the astigmatism is equal to the square of the image height divided by the focal length of the element $-h^2/f$.

Every optical system has a basic field curvature, called the Petzval curvature. The Petzval curvature is a function of the index of refraction of the lens elements and their surface curvatures. Ideally, if no astigmatism were present, the sagittal and tangential images would lie on the Petzval surface. When the tangential image is left of the sagittal image as in Figure 5.16, the astigmatism is negative or undercorrected. If the tangential image is to the right of the sagittal image, the astigmatism is positive or overcorrected. Note that it is possible to have an overcorrected Petzval surface and undercorrected astigmatism, or vice versa. Also, positive lens elements introduce undercorrection to the Petzval surface and negative lens elements bring overcorrection.

5.3.4 Distortion

Distortion is an off-axis aberration caused by the image rays forming farther away from or closer to the axis than the image height would suggest as given by the paraxial equations in section 5.2.2. The distortion increases with the cube of image height.

There are two types of distortion observed, namely, pincushion and barrel distortion. Take for example the image of a rectangular shape as in Figure 5.17.

Pincushion or positive distortion, Figure 5.17a, is where the image is displaced outward resulting in flared corners. Barrel or negative distortion, Figure 5.17b, is where the image is pulled inward especially in the corners of the rectangle.

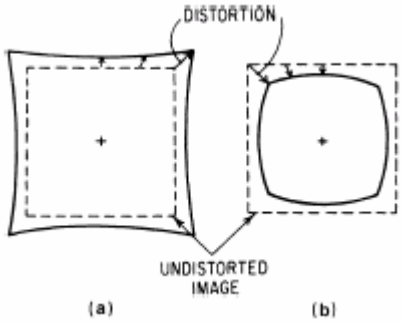

Figure 5.17 (a) Pincushion Distortion (b) Barrel Distortion (Smith, 2000).

Distortion can be cancelled out by reversing the object and the image. For example, if a camera lens, suffering from barrel distortion, is used to take a photograph, it can then be used in reverse to project the image, the projected slide will be distortion free.

5.3.5 Chromatic Aberration

Chromatic aberration occurs because shorter wavelengths are bent more than the longer ones. Put another way, the index of refraction is higher for blue light than it is for red light. For the purposes of this research, only a thin band of UV light is used to cure the photopolymer resin. Of this thin band of wavelengths, only one wavelength acts as the catalyst to initiate the photopolymerisation. Thus it is important to note that optical filtering must be used to reduce or eliminate the effects of chromatic aberration.

5.4 Optical Terms, Practical Considerations and Implementation

5.4.1 Field of View

Field of view (also known as angle of view) is a confusing term. The confusion is in the many definitions and interpretations used to describe it. Field of view is usually given in terms of a degree angle that defines the “view” of a lens. This angle can be defined by stating two angles, one between the optical axis and horizontal axis and the other between the optical axis and vertical axis, or by stating the angle between optical axis and the diagonal axis (the axis between the two diagonally-opposite corners of the pyramid base as depicted in Figure 5.18). The method with which the angle is measured should be clearly stated. The most common angle measurement is

the diagonal field of view and if the field of view type is not specified, the diagonal field of view is the assumed default (Kerr, 2006).

Considering the case for a camera layout, the lens used must be rectilinear, that is non-spatially-distorted. The field of view is the three dimensional space taken in by the camera's "view". This three dimensional space is shaped like a four-sided pyramid as shown in Figure 5.18.

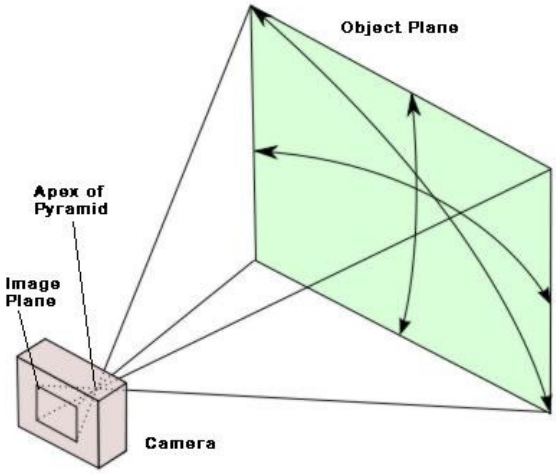

Figure 5.18 The pyramid shape encompassing the field of view for a camera (Lyon, 2006).

The apex of the pyramid should coincide with the centre on the optical axis and centre of the aperture spot. In some lens setups, an aperture stop is before the first node or principle point of the lens. It is important that the apex of pyramid is located wherever the aperture stop is positioned.

The method of calculation is to satisfy the angle of view (α) equation by choosing a dimensional length (horizontal, vertical, or diagonal) from the object plane of the pyramid as depicted in Figure 5.19 (McCollough, 1893).

$$\alpha = 2\tan^{-1}\left(\frac{d}{2f}\right) \tag{5.41}$$

where α is the angle of view, d is the chosen dimension and f effective focal length. The trigonometric diagram of (5.41 is shown in Figure 5.19.

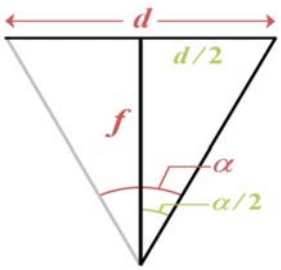

Figure 5.19 Derivation of the angle of view formula (McCollough, 1893).

Defining the field of view is preferred for practical implementation of optical imaging systems. Often magnification is used but it has no units or meaning in terms of field of view or resolution. Magnification is relative to the specification of object sensor size and the projected image size. Figure 5.20 shows the various parameters of a camera inspection system. Important parameters are the sensor size, working distance, field of view, resolution and depth of field (Fales, 2003).

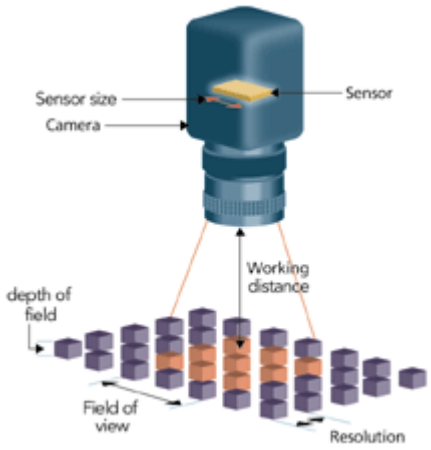

Figure 5.20 Parameters of camera imaging requirements (Fales, 2003).

Field of view is often defined by three factors because it is difficult to know exactly what angle must be made with the diagonal axis. These factors are: the choice of focal length, the desired image size and the distance at which the lens is focused. Most examples for field of view are for camera lenses where the object is large and the image is captured on a small CCD (couple-charged device), CMOS (complimentary metal-oxide semiconductor) device, or film. Projection works the same way but the object and image are reversed. Take for example an old 35mm camera. A lens with a greater focal length gives a small field of view and for a given film format. A short focal length (28mm) gives a large field of view. A larger field of view can also be obtained by increasing the image format size implying a wide angle

lens. In general using a short focal length results in a larger field of view if the film format or image capture device size is constant (Young & Freeman, 1996).

Lenses can be classed into terms that express their angle of view as shown in Table 5.1. Note however, these values are only general observations and not for any specific lens configuration.

Lens Class	**Angle of View Range**
Ultra wide-angle (fisheye) lenses	Up to180° or wider
Wide-angle lenses	60° to 100°
Standard lenses	25° to 50°
Telephoto lenses	10° to15°
Super Telephoto lenses	Less than 1° to 8°

Table 5.1 Classification lens types and ranges.

5.4.2 F-number (f/#), Radian Flux (φ_c) and Numerical Aperture (N.A.)

The intensity of light reaching the image is proportional to the area viewed by the camera and the effective area of the lens. The size of the area that the lens "sees" (clear aperture) is proportional to the square of the focal length of the lens and so is roughly proportional to $1/f^2$. The effective area of the lens is the diameter of the clear aperture. Hence, the effective area is proportional to D^2. Therefore the intensity of light reaching the image is proportional to D^2/f^2. The light gathering capability of a lens is often expressed as the ratio of focal length to clear aperture and is called the f-number (f/#) (Smith, 2000).

F-numbers are used in photography to describe the "speed" of a camera's optics. A low f/# indicates a fast lens. For singlet spherical lenses, the high performance imaging limit is about f/4. F-numbers between f/2 and f/1.5 are acceptable for condenser lenses in arc lamps (Newport Corporation, 2004).

The f-number of a lens is an indication of radiant flux, φ_c. For small angles less than 15°, the f/# is the ratio of a lenses focal length to clear aperture. Increasing the diameter allows the capture of more light radiation. Hence, the smaller the f/#, the greater the radiant flux collected by the lens. φ_c increases with the inverse of the square of f/# shown in (5.42 (Newport Corporation, 2004).

$$\varphi_c \propto \frac{1}{(f/\#)^2}$$

(5.42)

It makes sense then that decreasing f/# is a way to maximize light collection. However, there is a difference between the total flux collected and useful radiant flux collected. Lens aberrations determine the quality of the collimated output. Aberrations increase when f/# decreases. To increase performance at lower f/#, the number of optical elements must increase. For example, camera lenses have five or six components for an f/# around f/1. Microscopes have ten or more components to achieve f/0.5 (Newport Corporation, 2004).

It should be noted that the f/# of a lens is not necessarily fixed. The f/# is sometimes given to describe a particular lens configuration. Figure 5.21 illustrates how light collected by the same lens differs significantly when the distance from the source is varied, thus changing the half cone angle with the source. F-numbers go some way into describing lens or lens system ability to collect and image light.

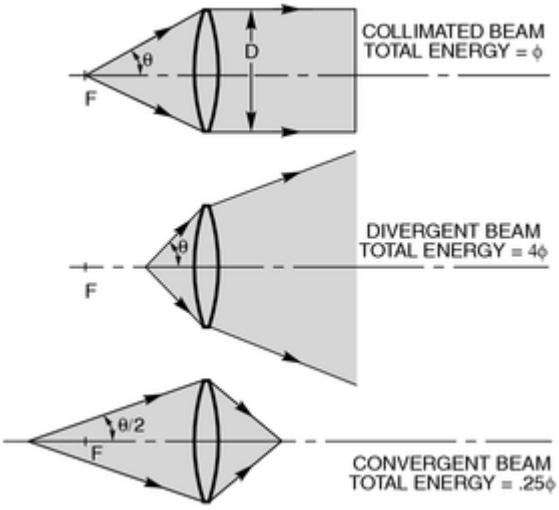

Figure 5.21 The light collection of a lens at different distances from the source (Newport Corporation, 2004).

Getting back to radiant flux, for angles greater than 15°, the half cone angle of radiation needs to be considered as depicted in Figure 5.22.

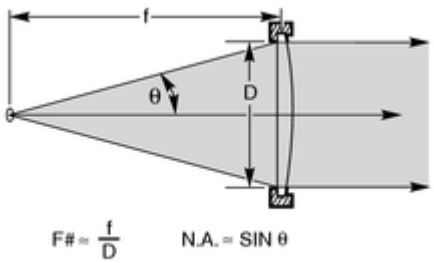

Figure 5.22 Graphical definition of f/# and numerical aperture (Newport Corporation, 2004).

The f/# is now defined by the following equation:

$$\text{f/\#} = \frac{1}{2n\sin\theta} \tag{5.43}$$

where n is the refractive index of the space in which the source is located and θ is the half cone angle of radiation.

For optical systems with high cone angles, numerical aperture, N.A., is the term used to describe light gathering ability. Numerical aperture is used more for systems that work at finite conjugates such as microscope objectives and fibre optics (Smith, 2000). N.A. is given by:

$$\text{N.A.} = n\sin\theta \tag{5.44}$$

where n is the refractive index of the medium. θ is the half cone angle measured from the optical axis to the marginal ray emanating from the centre of the object. Air is one of the most common mediums and has an N.A. of 1. A large N.A. implies a higher radiant flux (Newport Corporation, 2004).

Numerical aperture is related to f-number by the following equation:

$$\text{N.A.} = \frac{1}{(2\text{f/\#})} \tag{5.45}$$

5.4.3 Depth of Focus and Depth of Field

Depth of focus is often confused with depth of field. Depth of focus is the amount of image defocus which corresponds to being out of focus by one-quarter of a wavelength. This means that the optical path difference (OPD) between the real wavefront leaving the exit pupil at is outer periphery and a reference wavefront centred normal to the image plane is one-quarter of a wavelength of light.

Depth of field is a term more commonly used in photography to relate how acceptable an image looks to the eye. If a camera is focused at a given distance, how much further or closer from the camera than this distance will objects be in acceptable focus (Fischer & Tadic-Galeb, 2000).

Depth of field, to a great extent, is controlled by the f-number of a lens. In an ideal lens design, the f-number is the limiting factor in system resolution. Common machine-vision optics integrates an adjustable iris into the design, allowing the user to adjust for varying light levels and to control the depth of field. Increasing the size of the aperture decreases the depth of field, but will often increase the resolution of the lens (refer back to Figure 5.20). Decreasing the size of the aperture increases the depth of field, but decreases the effective diffraction limit of the lens (see section 5.4.5 for more about the diffraction limit). This degrades overall system performance (Fales, 2003).

5.4.4 Power of a Lens

Optical designers will sometimes refer to a lens by its power. The power of a lens or optical system is the reciprocal of its effective focal length. Usually, focal lengths are expressed in millimetres or centimetres. However, the unit of measure is dioptres where the focal length is given in meters (Smith, 2000). Dioptres are more commonly used in optometry to specify the power of lenses in eyewear.

5.4.5 Resolution of Optical Systems and Rayleigh Criterion

The resolution of an optical system is limited due to diffraction. Diffraction occurs when light passes through an aperture resulting in an Airy disk illumination pattern like that shown in Figure 5.23. The resolution is the spatial limit at which two features must be separated in order to be resolved as unique. To understand this concept, consider two adjacent micromirrors of the DMD that act like two point sources of light which shine the light thought the optical system. If each micromirror is imaged as an Airy disk, their individual diffraction patterns will overlap. When the separation distance is enough to indentify the two micromirror pixels instead of one, the micromirrors are said to be resolved.

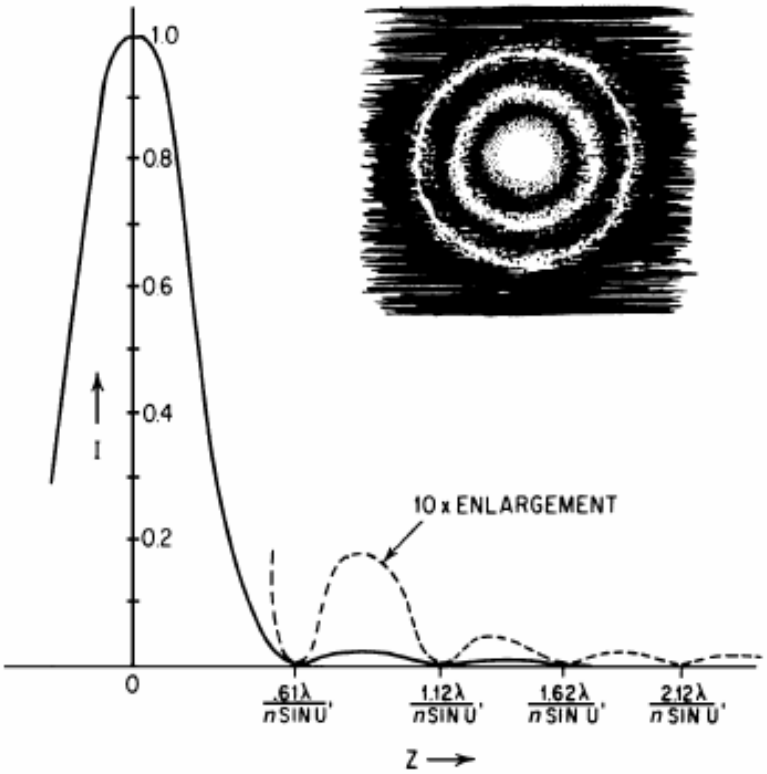

Figure 5.23 The Airy disk distribution of illumination. The Airy disk pattern is shown in the upper right (Smith, 2000).

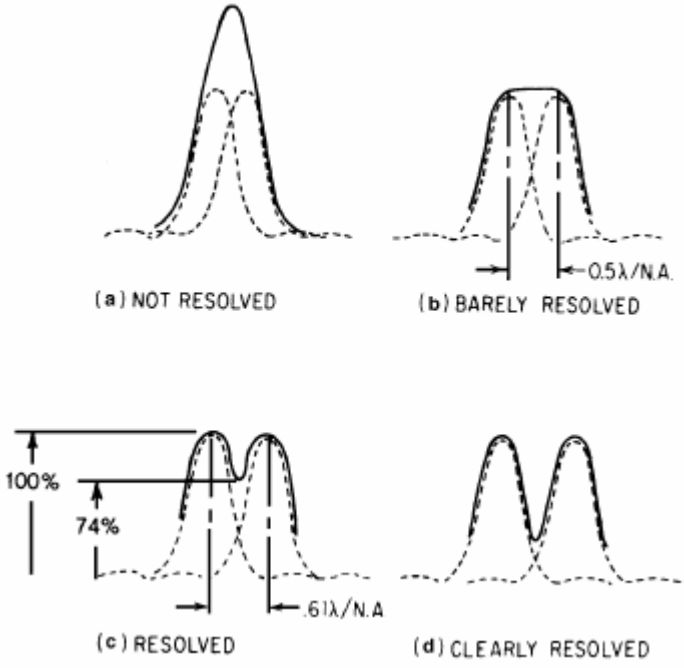

Figure 5.24 Diffraction patterns for two point sources of light (Smith, 2000).

The most widely used value for the limiting resolution of an optical system is called Rayleigh's criterion named after Lord Rayleigh (John William Strutt). Figure 5.24 shows several diffraction patterns of two adjacent points where the distance

between maxima are varied. The Rayleigh criterion (Figure 5.24c) is when the separation between maxima is:

$$Z = \frac{0.61\lambda}{NA} = 1.22\lambda(\text{f /\#}) \text{ for an ideal lens} \quad \textbf{(5.46)}$$

where NA is the numerical aperture. Z is the separation where the maximum of one micromirror coincides with the first dark ring of the other (Smith, 2000).

5.4.6 Reflectors for Arc Lamps

Newport Optics provides helpful information concerning selection of an optical system (Newport Corporation, 2004). This subsection gives practical information concerning the theories involved with the collection of light. Diffraction and coherent effects are not accounted for.

Ellipsoidal reflectors make use of the two conjugate foci of an ellipse as opposed to parabolic reflectors that reflect light as a collimated beam as shown in Figure 5.25. The light from one focus passes through the other focus after bouncing off the reflector. Ellipsoidal reflectors that surround the light source are much more efficient at collecting light than spherical mirrors or lens systems.

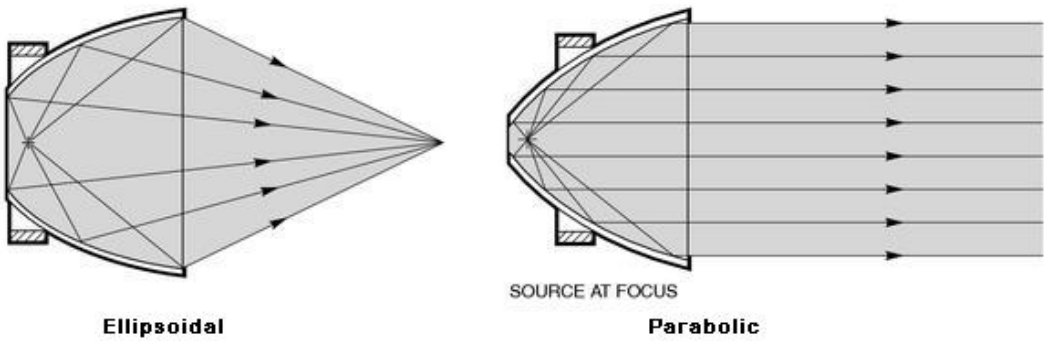

Figure 5.25 Ellipsoidal and Parabolic Reflectors (Newport Corporation, 2004).

Ellipsoidal reflectors have a significant effect on the image created by extended sources. As mentioned in section 5.1.1, there is no such thing as a true point source and arc lamps have some finite dimensions. All light rays do not exactly converge at the focus of the ellipse as they would with an ideal point source. The image becomes magnified and defocused. Figure 5.26 traces rays from point S, off the focus F_1, do not reimage at F_2. The defocusing makes ellipsoidal reflectors work best with small sources and light systems that are not concerned with image quality.

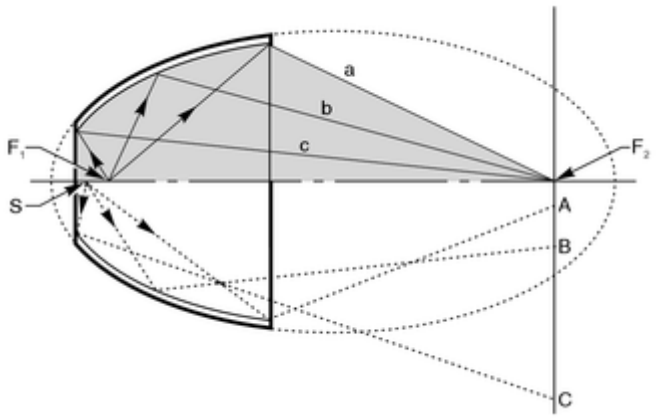

Figure 5.26 The two conjugate foci of an ellipsoidal reflector with ideal rays above the optical axis and defocused rays below the optical axis (Newport Corporation, 2004).

5.5 Optical Lens Configurations

Design forms and system configurations are discussed by (Fischer & Tadic-Galeb, 2000). A configuration includes the number of elements, relative optical power and the distribution of the elements within the system. The differences between several lens configurations are compared with regard to system specifications. The major factors influencing these specifications include field of view, performance requirements, f-number, packaging requirements and spectral range. Figure 5.27 shows diagrams of the lens types and configurations that are discussed in this section.

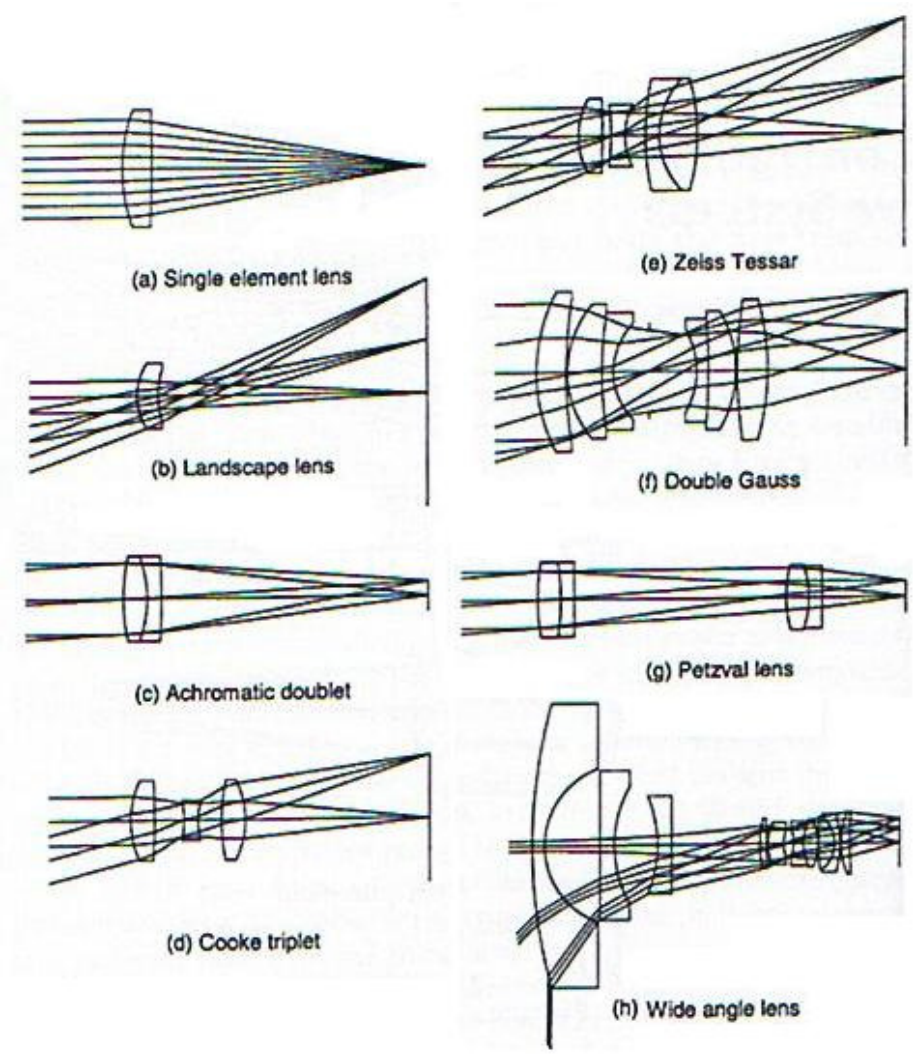

Figure 5.27 Lens Configurations (Fischer & Tadic-Galeb, 2000).

5.5.1 Single-Element Lens

With regard to imaging applications, a single-element lens provides poor image quality and a very small field of view. It will have bad chromatic aberrations and can only be used at high f-numbers.

5.5.2 Landscape Lens

Landscape lenses were used in early box cameras. A landscape lens is a single-element lens where the lens is bent or curved around the optical axis. The lens is bent symmetrically in order to reduce the angles of incidence on the surfaces of the lens. The reduced angles of incidence reduce off axis aberrations. A landscape lens is used in conjunction with a remote aperture. The aperture can be placed after the lens but better performance is achieved with the aperture in front as this reduces aberrations. The lens still suffers from chromatic aberrations and residuals of third-order aberrations.

5.5.3 Achromatic Doublet

The achromatic doublet consists of two lenses, typically a double convex lens with a plano-concave lens bonded together with optical cement. This lens brings the red and blue wavelengths to a common focus with the green and yellow wavelengths defocused slightly toward the lens. The achromatic doublet has a blur diameter 25 times smaller than an equivalent single lens. The performance of this doublet is only good over small fields of view (large image to object distances). It is not suitable for low f-numbers due to higher orders of spherical aberration.

5.5.4 Petzval Lens

The petzval lens is intended for smaller fields of view and is not suitable for wide angle applications, hence longer object to image distances. For example one application is aerial reconnaissance. It is only capable of moderate f-numbers around f/3.5 or slower. The power task is shared between two achromatic lenses.

5.5.5 Cooke Triplet

The Cooke triplet was first designed by H.D. Taylor at the “Cooke & Sons” optical company. It uses symmetry of design that minimises the angles of incidence of rays as they pass through the lens. The Cooke triplet allows for the optimisation and balancing of third-order aberrations and focal length control. There are eight variables in the Cooke triplet, six radii and two air spaces (element centre thicknesses generally do not significantly control aberrations), that can be used to control or optimise the following:

- spherical aberration
- coma
- astigmatism
- axial colour
- lateral colour
- distortion
- field curvature
- focal length

For a given f-number and focal length using these variables means that aberrations can be reasonably balanced against one another. However, at low f-number and wide fields of view, the performance of the Cooke triplet becomes poor. Low f-numbers

around f/1.5 lead to significant spherical aberration residuals. Wide fields of view around 30° lead to coma, astigmatism and other off-axis aberrations.

5.5.6 Zeiss Tessar

Paul Rudolph of Zeiss Jena created an improvement on the Cooke triplet. The third lens of the Cooke triplet is replaced with an achromatic doublet. This results in higher resolution, excellent contrast, and very low levels of distortion. The Zeiss Tessar lens also provides superior correction of axial colour. It performs well for f-numbers down to f/4.5.

5.5.7 Double Gauss

The double gauss lens further improves on the Cooke triplet and Zeiss Tessar lens by providing better performance at lower f-number and wide fields of view. The double gauss configuration capitalises on the previous designs by splitting optical power to minimise aberrations, use of negative-powered elements with small beam diameters for field curvature correction and the use of symmetry before and after the aperture stop to minimise angles of incidence on the lens surfaces. Symmetry also cancels out several off-axis aberrations. The double gauss lens can achieve good performance down to f/1.0 and it has superior light gathering capability. However, at this slower level of performance, the lens is not diffraction limited and material with higher refractive index is used to reduce aberrations.

5.5.8 Wide Angle lens

Mostly used in cameras, a wide angle lens is designed to converge light from a wide field of view. A strong negatively powered lens is used at the front, or a group of strong elements, to bend the wider rays so that all rays converge toward the image. From the wide angle lens shown in Figure 5.27h, there are two lens groups: a negatively powered three element group and a multi-element prime lens group. The prime lens group is actually converging the smaller field of view set by the negatively powered group.

5.6 Summary

There have been quite a few topics covered in this chapter concerning the properties of light. The properties of light presented in section 5.1 have covered the history of light theory and revealed that this thesis work is part of Radiometry. The

inverse square law and Lambert's law of intensity were explained for point sources and extended sources respectively.

Section 5.2 reviewed geometric optics and raytracing. Basic theory for thin lenses was developed and the object to image relation was proved. Raytracing a ray through lens surfaces was describe and how paraxial theory is used to simplify calculations. Then finally, a more practical raytracing algorithm was explained that traces skew rays in all three axes of an imaging system.

Section 5.3 discussed optical aberrations. Aberrations were described as to the cause of each type of optical aberration and how aberrations are minimised or corrected. With this knowledge of aberrations, the optical system of the SLA will be more understood as to its limitations and areas for improvement.

Common optics terms were defined for clarification in section 5.4. Field of view is used to define the viewing angle commonly measured across the diagonal of the projected image. F-number and numerical aperture are two ways that define the light gathering capabilities of lenses and lens systems. Resolution is the spatial limit at which two features must be separated in order to be resolved as unique. Resolution is also given by the diffraction limit which is defined by Rayleigh's criterion.

Finally, in section 5.5, several popular lens configurations were shown and discussed. The types of lenses more suitable for projection based, integral SL are multi-element lens systems. In many of the lenses shown, correction for various forms of aberration is provided by the element types and arrangements. The more complex lens systems accommodate low f-numbers and wide fields of view.

The essential theory for mathematically modelling projection-based, integral SL has now been covered. The next chapter explains a mathematical model, the Limaye Layer Cure model, which uses raytracing of light rays through an optics system. What has been learnt about the properties of light will be used to adapt the model to the SLA being designed for this research thesis.

6 Mathematical Model for Integral Cured layers

This chapter builds on previously reviewed theory and gathers it all into one for the purpose of creating a mathematical model. The Limaye Layer Cure model is explained which uses raytracing of light rays through an optical system

Mathematical models for the conventional SLA process have been well documented for both stationary and moving laser (Corcione et al, 2004; Corcione et al, 2006; Jacobs, 1992; Scherzer & Decker, 1999; Scherzer et al, 1998). However, mathematical models for integral SLA processes have not been so thoroughly reported. Investigations of integral SLA are still in the design, implementation, and experimental stage. Most research for integral SLA is reported for microstereolithography (μSL). Much of the integral μSL theory can be applied to the conventional SLA theory.

One of the only mathematical models for integral SL was created by (Limaye, 2004). Limaye developed a process planning method for a masked-projection microstereolithography apparatus (MPμSLA) (Limaye, 2004). In Limaye's theory, the field of irradiance of the imaging lens of the MPμSLA is limited to the micro-scale. However, the theory models the essential parts of the SLA system. The model incorporates the beam intensity, the DMD, the lenses of the optical system and the intensity of light at the image plane. Section 6.1 is an overview of the mathematical model for curing single layers. The principles of the Limaye's model are readily adaptable for this thesis work.

6.1 Mathematical Model for Single-Exposure Layers

The Limaye Layer Cure Model essentially uses ray tracing in combination with the cure depth equation ((2.2) to find how deep a layer is cured for a given exposure. The model allows the time of exposure to be calculated for a required layer thickness. Some experimental measurements of the irradiating beam are used to model the cure of the photopolymer resin. The description of the Limaye Layer Cure Model is discussed in the following subsection. The model for single layers is composed of two parts: the irradiance model and the layer cure model (Limaye, 2004).

6.1.1 Irradiance Model

When a collimated beam of light is reflected from a pattern displayed on a dynamic mask generator, such as a DMD, the light can be considered as rays

reflecting off infinitesimally small points. These points on the DMD can be arranged into an array or grid of equally spaced points, composed of n number of points: p_1, p_2,…, p_n where $n \rightarrow \infty$. An infinite number of rays can be traced from every point in the array through the imaging optics to the resin surface. Each ray irradiates an infinitesimally small area centred at the point where it strikes the resins surface and can be represented by direction vectors v_1, v_2,…, v_m where $m \rightarrow \infty$. The resin surface can also be divided into grid containing x number of points: pr_1, pr_2,…, pr_x where $x \rightarrow \infty$ (refer Figure 6.1).

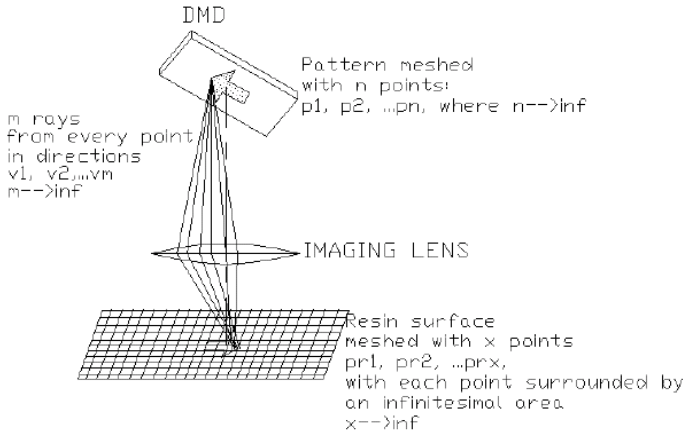

Figure 6.1 Nomenclature for Limaye's Model (Limaye, 2004).

With the use of a weighting equation that accounts for the irradiance distribution across the beam incident on the dynamic mask generator, the irradiance received at the surface of the resin can be obtained. The following equation is used to derive the irradiance (Limaye, 2004):

$$\mathrm{H}(pr_i) = (\mathrm{H_{av}}\,\mathrm{x}/\sum_{j=1}^{n} w_j m)\sum_{j=1}^{n}\sum_{k=1}^{m}\delta(p_j, v_k, pr_i) \qquad \textbf{(6.1)}$$

where $\mathrm{H}(pr_i)$ is the irradiance received by point pr_i on the resin surface; $\mathrm{H_{av}}$ is the average irradiance across the resin surface; w_j is the weight equation that accounts for the irradiance distribution across the beam incident on the dynamic mask generator; $\delta(p_j, v_k, pr_i)$ is a function which determines whether a ray from point p_j on the dynamic mask generator in the direction vector v_k will strike an infinitesimal area centred on point pr_i on the resin. The δ function is found from a ray tracing procedure described in (Smith, 1966) which was discussed in chapter 5.

Using (6.1 about the optical axis, the irradiance at every point on the surface of the resin can be found. The values from all the points on the resin surface are stored in an

array. Limaye verified the use of this equation on an arrow shaped bitmap (Limaye, 2004). A MATLAB program was created by Limaye to show the bitmap of the irradiance matrix.

In order to understand the data from the irradiance map, the data can be displayed as a colour map. Figure 6.2 shows the irradiance colour map resulting from (6.1 on a 15 x 25 pixel bitmap of the arrow shape. Figure 6.3 gives a 3D visual interpretation of how the irradiance is distributed.

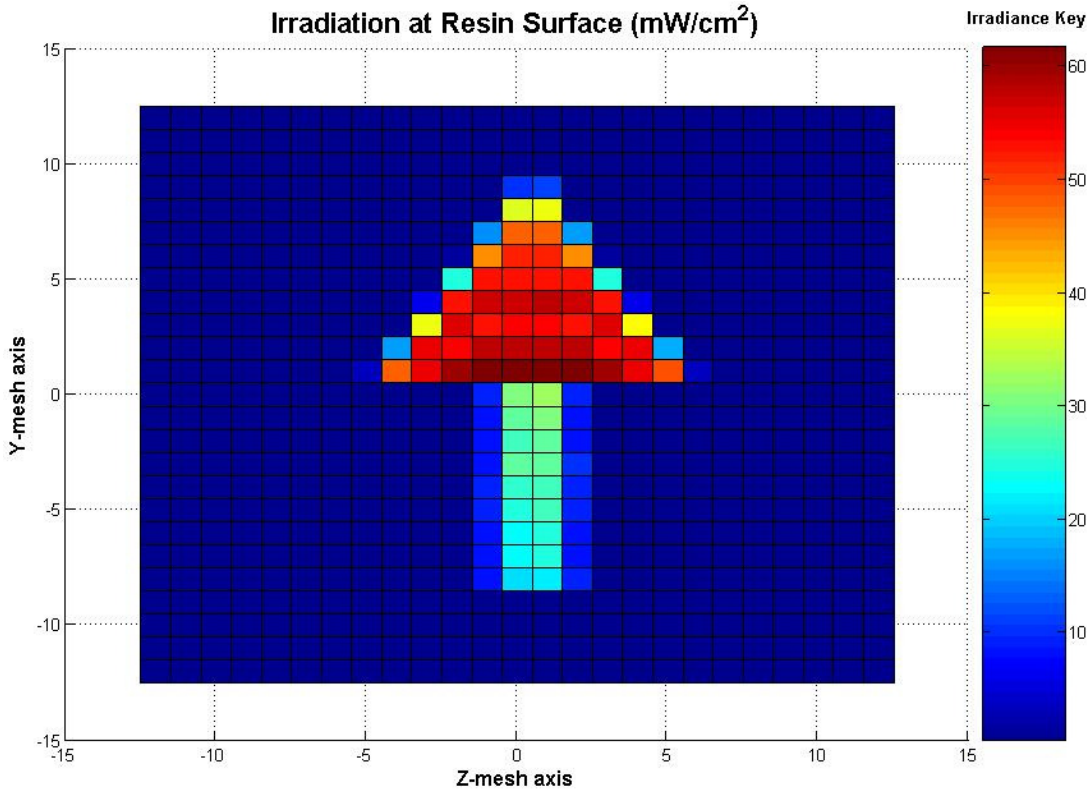

Figure 6.2 Irradiation map at the resin surface of arrow shaped bitmap.

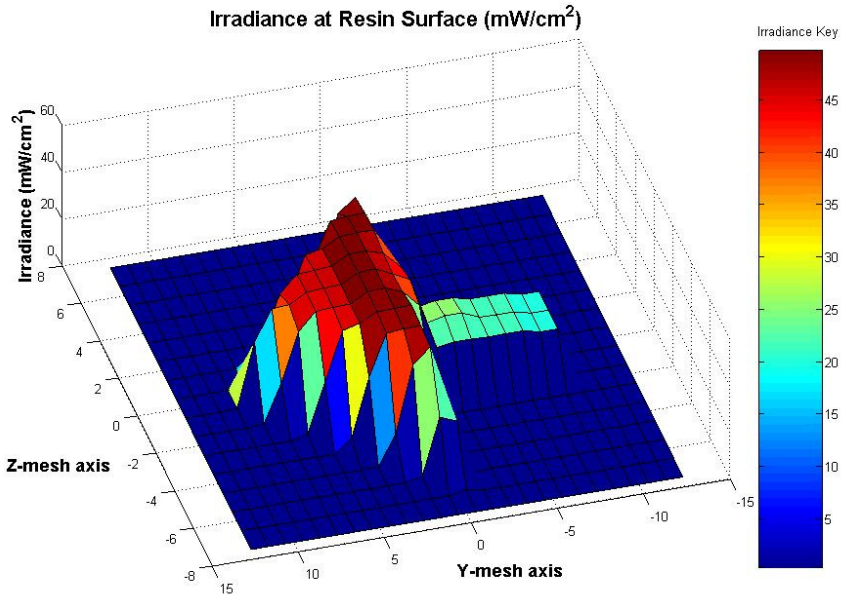

Figure 6.3 Irradiance distribution at resin surface using the Limaye Model.

6.1.2 The Layer Cure Model

Now that the irradiance at the surface of the resin is modelled, the curing of the photopolymer can be found. The Limaye Layer Cure Model uses the cure depth equation ((2.2) to calculate the cure in the layer. In the cure depth equation, E_{max} can be substituted for the $H(pr_i)$ value for every element in the irradiance map. (2.2, along with a given time of exposure (TOE), can be used to find the cure depth. By using the minimum irradiance value from the irradiance matrix and calculating C_d, the minimum layer thickness can be found to ensure that a layer is cured to a specified depth. A layer can be made with a certain layer thickness by rearranging (2.2 to find the TOE required and substituting C_d for the layer thickness (LT):

$$TOE = (E_c / H(pr_i))e^{(LT/D_p)} \tag{6.2}$$

6.2 Accuracy and Precision of the Limaye Model

With Limaye's model, accuracy errors were as high as 11% measured from test results. Calibration of the Layer Cure Model can reduce these errors. The other errors included incorrect alignment of the lenses in the optical system and defects in the optical material of the lenses (Limaye, 2004).

Precision errors give an indication of the machines repeatability. For micro-scale parts the lowest possible error is desired. Test results (Limaye, 2004) proved there was a 7% error the precision of the process. Precision can be increased by accounting

for the errors in variation of the resin height in the resin vat. This needs to be kept constant as it changes the image distance slightly. This results in enlargement or reduction of the projected image causing lateral scaling.

The resin curing characteristics also vary from experiment to experiment. As the vat of resin is exposed to radiation during the whole experiment, there may be a slight variation in the resins reaction properties. However, this error is difficult to account for, as the composition of the resins used is the intellectual property of the manufacturers.

Another factor that affects precision is the method that is used to clean the parts after curing. These post-cure operations involve washing the parts in isopropyl alcohol and then further curing them in a post-curing oven. Excess resin is a variant and depends on how long and rigorously the parts are cleaned.

6.3 Limaye Layer Cure Model Enhancements & Results

6.3.1 Problems with the Limaye Model

(Limaye, 2004) states that one of the limitations the model is that is only applicable to MPμSLA systems for which the diffraction effects are negligible. Ray tracing might be insufficient to model the image formation process of sophisticated imaging systems as aberrations become negligible and the diffraction effects dominate. This limitation may cause a problem in the application of the model to larger exposure areas.

A major deficiency of the Limaye Model is that it does not account for the half cone angle of rays. Although Limaye (2004) notes that half cone angles from 0° – 4° were tested, the MATLAB code does not incorporate half cone angles other than 0°. Incorporating for half cone angles adds more rays for the MATLAB code to process. This added amount of rays may prove limiting due to the increased processing time.

6.3.1.1 Problems with the Irradiance Model

According to Limaye's model, the points where rays on the DMD and resin surface (image plane or irradiance map) are in two separate arrays that Limaye calls meshes. Each mesh has different resolutions. The irradiance map consists of a mesh that is of a lower resolution than the actual DMD. That is, rather than each square of the mesh being of a 1:1 ratio with each micromirror of the DMD, the ratio is 1:4 micromirrors to mesh squares. This is a logical assumption considering that if the irradiance map had an equal or lower resolution than the DMD mesh, the values would only be the

same as irradiance value in the DMD mesh but attenuated according to the inverse square law. However, each square in the irradiance mesh represents an area on the resin surface not a point as in the DMD mesh. The total number of rays that land in the area of a square is multiplied by the weighting function for that particular area depending on the area's distance from the beam centre. The total sum of the ray intensity is then spread out across the area of the square. The DMD mesh is an array of points from which rays are traced. The more rays that are traced, and hence more points in the DMD mesh, the more accurate the irradiance map will simulate the irradiance from the DMD at the resin surface. This is an important difference between the DMD mesh and the irradiance map. Therefore, the resolution of the mesh on the irradiance map should be independent of the DMD mesh and should be increased to as high a resolution as possible in order to obtain a better understanding of the irradiance in a layer.

It is important to note that the value of H_{av} was found experimentally. A radiometer was used to measure the irradiance in mW/cm^2. The sensor on the radiometer had a diameter of 5mm and, given that the projected image covered a 2mm x 2mm area, the projected image, in its entirety, definitely lay on the sensor. The average irradiance was arrived at due to the projected image being micro in scale and completely fitting within the diameter of the sensor. Thus, the area of the sensor was used to find that average irradiance for the bitmap from the DMD.

Measurement of irradiance in areas larger than the area of the sensor is different. Previous researchers have failed to specify how the irradiance at the resin surface was measured practically. Thus, a simple measurement procedure was adopted for this research work as described in section 10.3.2.

6.3.1.2 Problems with the Layer Cure Model

The layer cure model relies on the minimum value in the irradiance matrix to cure a layer to a certain depth. The technique of the layer cure model does not provide a way of accounting for the overcure. A way of modelling the cure at the edges of a layer needs to be implemented in the model.

6.3.2 Proposed Improvements to the Limaye Model

The Limaye Model provides a theoretical foundation for the concept of modelling the irradiance at the resin surface. It differs from most other models in the field of SLA rapid prototyping. Most applications base their model around the light coming

from a laser or a highly collimated light source. Thus, the irradiance distribution of the beam incident on the dynamic pattern generator can be considered to have a gaussian profile. In integral stereolithography, rays incident on the dynamic pattern generator are ideally reflected vertically downward as a result of the highly collimated light.

Enhancements can be made to the existing Limaye Layer Cure Model. The way in which the irradiance map is calculated can be examined to find out how Limaye's MATLAB code processes the data that makes up the aerial image. Limaye's code is discussed further in section 6.4. In section 6.5, the weighting equation is experimented with to observe the results in the irradiance map from more evenly spread distributions. Section 6.6 proposes two techniques that use compensation of irradiance by application of the DMD to cure the resin surface more evenly.

6.4 Enhanced Irradiance Map & MATLAB Code

By analysing the irradiance map of the arrow shaped bitmap from Figure 6.2 and Figure 6.3, the irradiance does not seem to attenuate as expected. The irradiance would be expected to attenuate from the centre of the optical axis in a circular pattern. From the figures, it can be seen that the irradiance does not attenuate evenly from the centre of the bitmap. There seems to be a significant drop in irradiance in the rectangular portion of the arrow bitmap. However, the triangular portion of the arrow attenuates in a radial pattern as expected. The MATLAB code from Limaye's Layer Cure Model was analyzed to correct this discrepancy. It was found that the Limaye code divides the arrow shaped bitmap into two basic shapes: a triangle and a rectangle. The discrepancy in the irradiance maps of Figure 6.2 and Figure 6.3 results from separate meshes being used for each shape. Each mesh has different mesh spacing that leads to incorrect irradiance values.

MATLAB code was written to replace the way in which the mesh is applied to the arrow shaped bitmap (the code given in Appendix B: MATLAB Code). The new code treats the whole bitmap as one shape rather than dividing it up into two basic shapes. A single mesh is applied to the entire bitmap as a rectangular mesh. The mesh is just large enough to surround the extremities of the arrow shape. Algorithms are used to find the points in the new mesh that lie on the micromirrors of the DMD that are in the "on" state as opposed to the inactive space surrounding the arrow. These points

are stored in two arrays, one for row position and the other for the column position. The data from these two arrays are put through the ray-tracing algorithm.

The irradiance map is now calculated using constant mesh spacing over the entire bitmap. The new irradiance map shows how the rays and weightings are spread out more evenly across the entire shape of the arrow (see Figure 6.4).

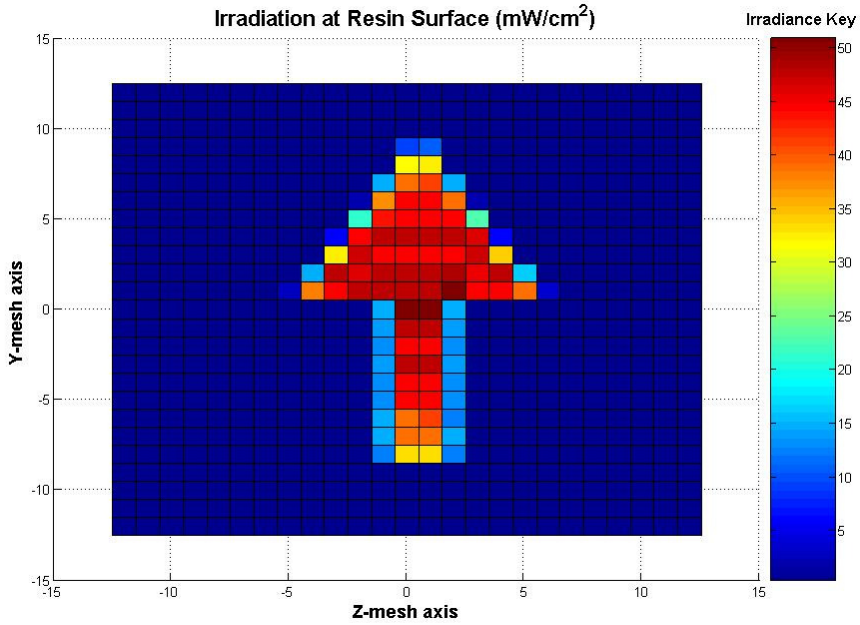

Figure 6.4 Irradiation map at the resin surface of arrow shaped bitmap with constant mesh spacing.

Another observation of Figure 6.4 is the low irradiance values at the edges of the arrow. These values occur at the edges due to ray density occupying only part of that mesh square's area. This density is spread across the mesh square's area resulting in lower values. In Figure 6.4, the irradiance map divides the resin surface up into a grid of 625 areas. This can be increased to about 5625 areas before the gridlines begin to dominate the figure. As the amount of areas is increased (the mesh density), the irradiance values at the edges remain in single squares around the parameter of the arrow as shown Figure 6.5. Note that the build envelope is 2mm x 2mm.

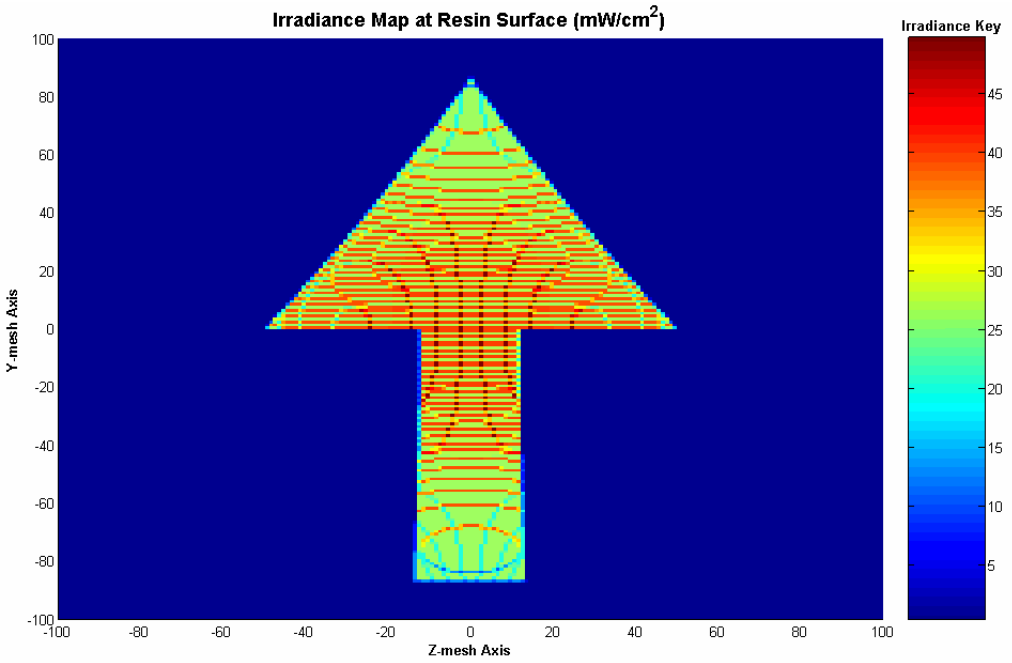

Figure 6.5 Irradiance map with the mesh density increased to 200x200.

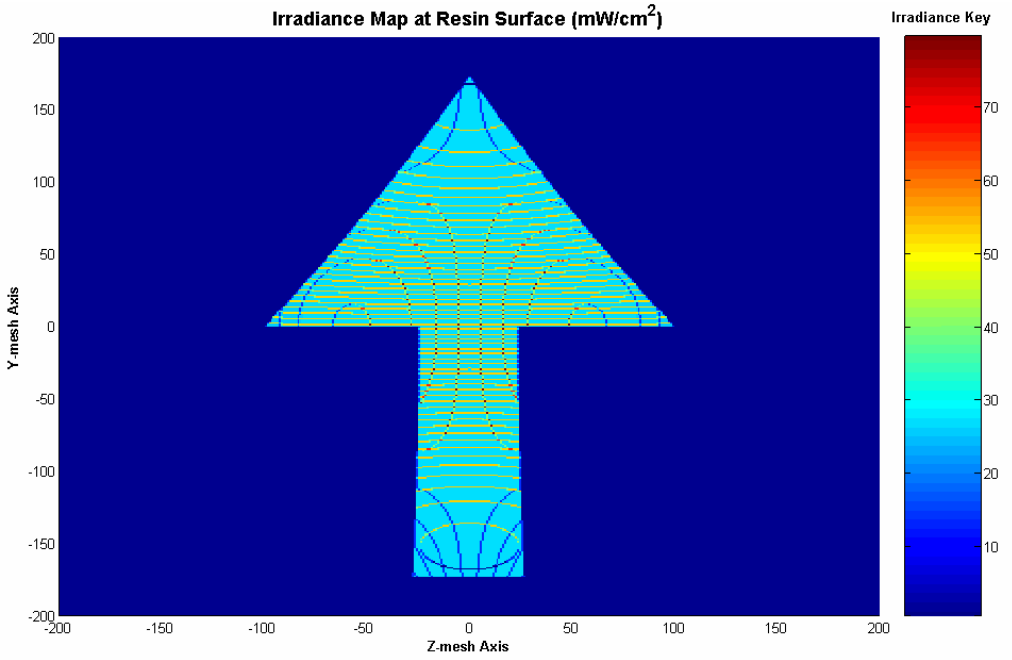

Figure 6.6 Irradiance map with the mesh density increased to 400x400.

Figure 6.6 shows the effect of increasing the mesh density to a 1:1 ratio with the mesh on the DMD. One immediate observation of both Figure 6.5 and Figure 6.6 is the circular patterns of irradiance. The circular patterns are caused by diffraction, noted by (Limaye, 2004) as a limitation of the raytracing technique on more sophisticated optical systems.

The irradiance in Figure 6.5 tends to concentrate around the central areas. Improvement of the irradiance can be improved by implementing a different type of lens system. For example, if a Cooke triplet was used instead of a single lens, the irradiance would be more evenly spread. MATLAB code was written and implemented using the new enhanced Limaye Model. The irradiance map is shown in Figure 6.7 where the single lens has been replaced with a Cooke triplet lens system. The build envelope has been modelled at 4mm x 4mm due to image magnification by the triplet.

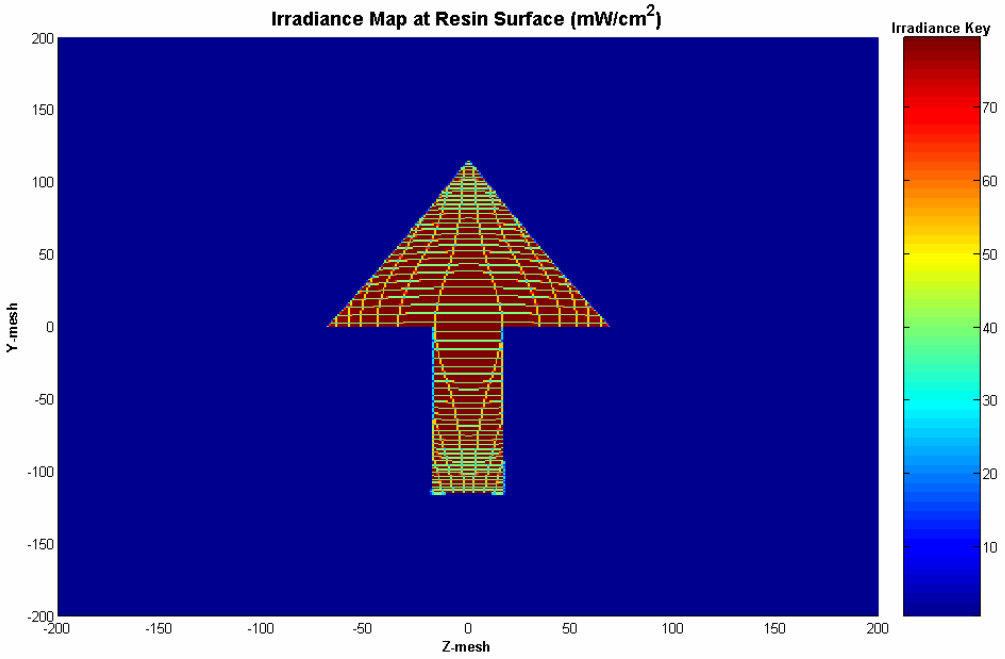

Figure 6.7 Irradiance map using Cooke triplet with Limaye's model.

The irradiance has become more evenly spread across the image and the diffraction effect has been reduced. However, the irradiance is not even over the top and bottom of the arrow shape. Although the lens system can be changed to obtain a better irradiance distribution, the lens system becomes very complex and expensive. Other techniques are worth exploring to achieve the same result. The next section will look at how the irradiance distribution of the light beam incident on the DMD affects the irradiance distribution.

6.5 Experiments with Weighting Functions

A key factor that affects the irradiance map is the weighting function. A weighting function accounts for the fact that all rays incident on the DMD do not carry the same amount of energy. The closer the weighting function is to a horizontal line, the more

evenly distributed the irradiance becomes and the more even the cure depth will be throughout the layer. Obviously it is expected that a unity distribution will result in an evenly spread irradiance. However, to obtain such an even distribution, very expensive optics must be used.

Limayes's Layer Cure Model uses a weighting function that was found experimentally. A radiometer was used to measure the intensity of light in the collimated beam. Measurements were taken across the radius of the collimated beam at a point just after the collimating lenses. However, the weighting function is not symmetric about the central axis. This equation can be experimented with to see how the irradiance map is affected. The following figure shows several different gaussian distributions that vary from Limaye's measured distribution to a near unity distribution.

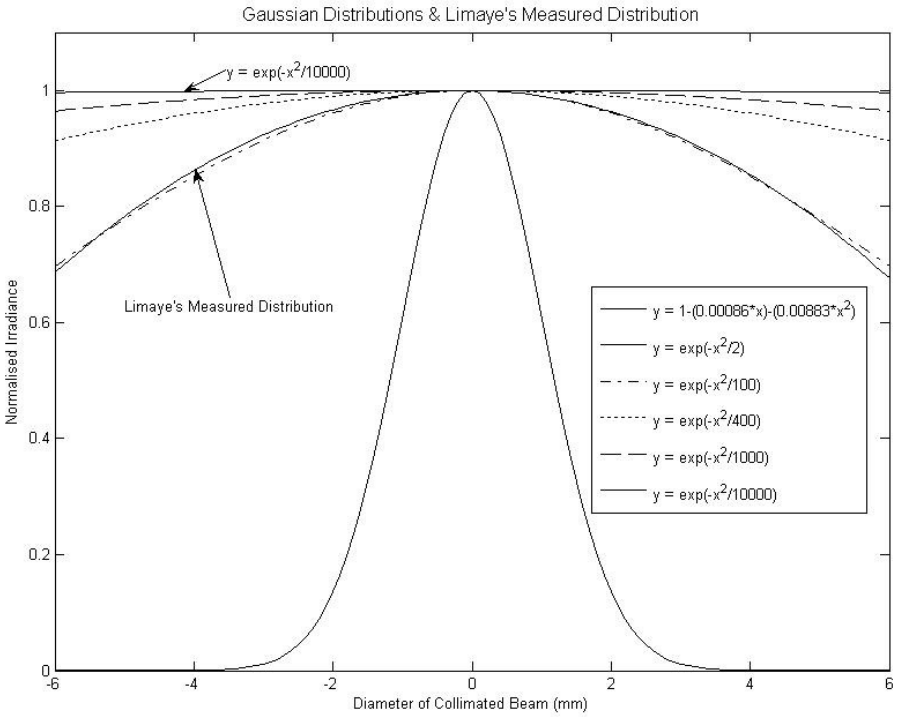

Figure 6.8 Gaussian distributions compared with Limaye's measured distribution.

It can be seen from Figure 6.8 that Limaye's measured distribution is not symmetric about the radius of the beam. The following equation best approximated Limaye's measured distribution.

$$y = e^{\left(-x^2/100\right)} \qquad \textbf{(6.3)}$$

The gaussian distributions experimented with here are, in fact, exponential equations. For the range of –6mm to +6mm, the exponential distribution approaches unity as the numerator of the exponential term approaches infinity as shown by (6.4. However, in practice, obtaining a suitable distribution usually requires very expensive optic hardware.

$$\lim_{u\to\infty} \; y = e^{\left(-x^2/u\right)} \tag{6.4}$$

The equations for each of the gaussian distributions were used with Limaye's Layer Cure Model to see how the irradiance distributions varied. Figure 6.9 shows the 200 x 200 grid irradiance map distribution when the weighting equation of the flattest gaussian distribution is used (where u = 10000 in (6.4).

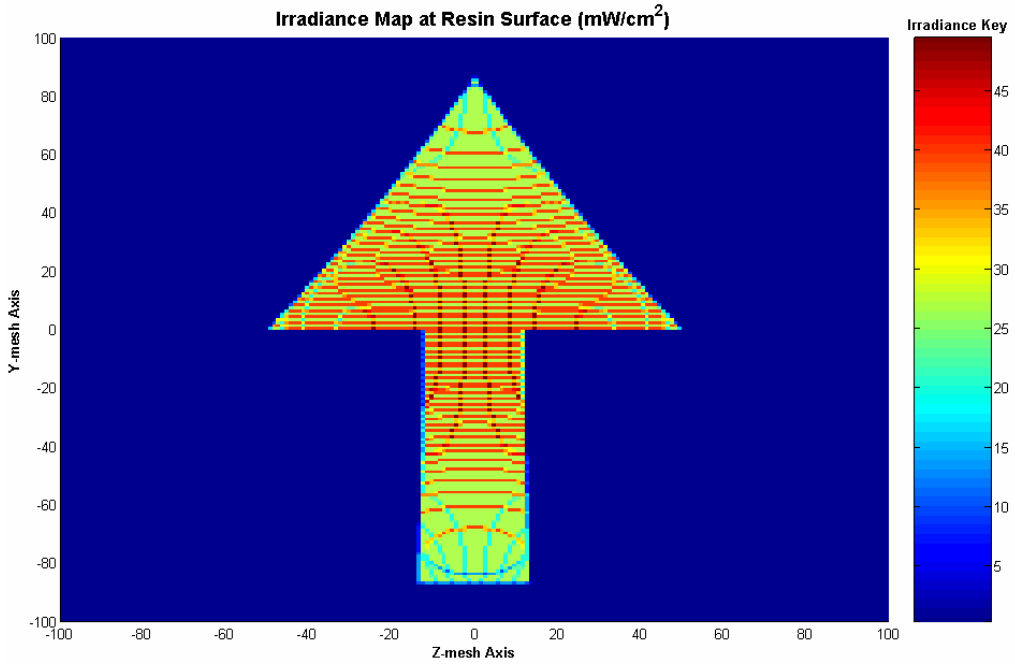

Figure 6.9 Irradiation map at the resin surface using a near unity weighting function for Limaye's model.

Examination of the irradiance distribution in Figure 6.9 does not show a more even spread of the irradiance in the arrow. The irradiance distribution is only slightly more even than the distribution of Figure 6.5. The weight equation was changed again to observe the effect of inverse of Limaye's weighting equation. However, there was no change in the irradiance map compared with Figure 6.9. Therefore, the application of a more complex lens system proves more effective at distributing the irradiance at the surface according to the model.

6.6 Compensation of Irradiance

A way of producing an even distribution can be achieved by using the micromirrors themselves. (Takahashi, 2001) briefly described a method in which the adjustment of the luminance modulation for each micromirror improved the nonuniformity of the projected illuminance. Each micromirror can be modulated at different frequencies using pulse width modulation (PWM) to vary the amount of irradiance projected through the lens. Takahashi's method used a CCD camera to take an unmodulated picture of the projected illuminance. The unmodulated picture is then processed to make the required compensated DMD bitmap. This section discusses how the irradiance map can replace the use of the camera like Takahashi implemented.

Two techniques can be used to cure the resin using irradiance compensation. The first technique, called bitmap irradiance compensation, evenly distributes the irradiance in the projected image by using the Limaye Layer Cure Model and the irradiance map. Dividing each element in the matrix by the lowest irradiance value from the irradiance map forms a normalized matrix. The minimum irradiance thus becomes the TOE for the layer.

As (Takahashi, 2001) discovered, gray scale tones can be achieved with each mirror of the DMD by modulation. The brightness of each mirror can be varied in 256 steps by PWM. This means that the darker the gray tone, the less irradiance is reflected towards the resin surface. All the micromirrors in the bitmap can be modulated at the right frequencies so that the result is an equal irradiance everywhere in the projected bitmap at the resin surface.

Each value in the normalized matrix represents the percentage of gray tone that needs to be modulated by the mirrors for that area on the resin surface. Multiplying the normalized matrix the number of gray tones available from the DMD, that is 256, and rounding to the nearest gray tone, a gray tone bitmap can be generated. The new gray tone bitmap can be sent to the DMD to project an evenly spread irradiance at the resin surface.

A problem occurs when normalizing the irradiance map to the lowest irradiance when the resolution of the irradiance map is to low. It is due to how the density of rays spread out equally across the respective mesh squares of the irradiance map. The percentage that results from such small irradiances in relatively large areas generates a

gray tone bitmap with spikes of irradiance at the edges and ineffective irradiances in the centre. However, when the resolution of the irradiance map is increased to a 1:1 ratio, the spikes do not appear. Figure 6.10 is the gray tone bitmap that shows the compensated irradiance map that is to be shown on the DMD in order to achieve an even cure at the surface. Experimental results for this technique of compensated bitmaps are shown in chapter 10.

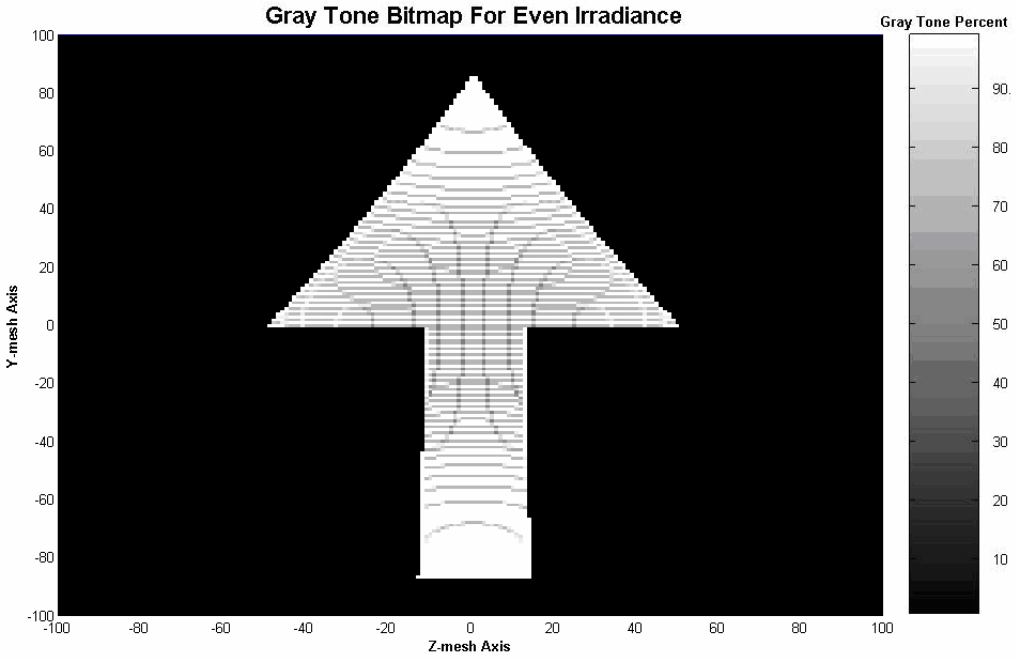

Figure 6.10 Proposed gray tone bitmap to obtain even irradiance.

The effect of compensated bitmaps on the irradiance map can not be observed with the mathematical model. The MATLAB code is not designed to accept gray-scale bitmaps and is the area of future research. Only through experiments, using the SLA design in this thesis, is the compensated bitmap tested.

With bitmap irradiance compensation, the TOE is the same for all micromirrors in the bitmap. The resin can be cured to the required cure depth based on this constant irradiance value. The advantage of this technique is that the layer is cured at an even rate over the entire layer.

The second technique is called “bit-wise TOE compensation”. Bit-wise TOE compensation ensures that each point on the resin surface is exposed to the same amount of irradiance. The same amount of irradiance is achieved by varying each area’s exposure time. By specifying the required cure depth, the amount of irradiance for each area can be applied by the respective micromirrors. The micromirrors stay in the “ON” position rather than modulating the micromirrors as in the previous

technique. Each micromirror is assigned a TOE value that is sufficient enough to irradiate the resin to the specified cure depth.

The TOE required by each micromirror can be represented as the percentage of time that each micromirror must remain in the "ON" position. The percentage in an area is relative to the percentage of the area on the resin surface that receives the highest irradiance shown on the irradiance map. First, the TOE equation ((6.2) is applied to the irradiance map matrix. A matrix showing the exposure times for each area of the mesh is obtained. The TOE values that each area receives can be normalized with respect to the shortest TOE value. The result gives the amount of exposure time (as a percentage) that each area requires in relation to the shortest TOE value given the required layer thickness. For example, suppose the maximum irradiance from the irradiance map matrix is 51.28mW/cm^2. By (6.2, for a layer thickness of 30µm, the TOE is 0.32sec using D_p = 0.056mm and E_c = 9.6mJ/cm^2 (Limaye & Rosen, 2005). The minimum irradiance near the edge requires 27,478% more exposure time. Hence the exposure time near the edge is 0.32sec x 27,478% = 87.90sec. The following matrix in Figure 6.11 (reduced to a 13 x 22 grid matrix for ease of viewing) shows the TOE percentages required for each area of the arrow shaped bitmap for a layer to be cured evenly to the required cure depth of 30µm.

0	0	0	0	0	0	0	0	0	0	0	0	0	0
0	0	0	0	0	0	0	0	0	0	0	0	0	0
0	0	0	0	0	4.1562	1.5577	1.5577	4.1562	0	0	0	0	0
0	0	0	0	0	3.5116	1.3161	1.3161	3.5116	0	0	0	0	0
0	0	0	0	0	3.5066	1.3142	1.2426	4.1444	0	0	0	0	0
0	0	0	0	0	3.7942	1.1568	1.1471	3.9024	0	0	0	0	0
0	0	0	0	0	3.898	1.1458	1.1458	3.898	0	0	0	0	0
0	0	0	0	0	3.6348	1.0684	1.0684	3.6348	0	0	0	0	0
0	0	0	0	0	3.8915	1.1438	1.1438	3.8915	0	0	0	0	0
0	0	0	0	0	3.6301	1.067	1.067	3.6301	0	0	0	0	0
0	0	0	0	0	3.4025	1.0000	1.0000	3.4022	0	0	0	0	0
0	21.25	1.3563	1.1516	1.0836	1.0681	1.0667	1.0666	1.0088	1.1522	1.1515	1.33	14.539	0
0	0	3.4813	1.0793	1.1148	1.0684	1.067	1.067	1.0601	1.124	1.075	3.0903	0	0
0	0	274.78	1.5844	1.0887	1.1453	1.1438	1.1438	1.1453	1.0887	1.4897	0	0	0
0	0	0	8.8377	1.1441	1.0697	1.0684	1.0684	1.0697	1.1206	8.0583	0	0	0
0	0	0	0	2.3781	1.182	1.1458	1.1458	1.1472	2.2792	0	0	0	0
0	0	0	0	24.866	1.3665	1.1568	1.1471	1.3267	24.868	0	0	0	0
0	0	0	0	0	3.3766	1.3142	1.2426	3.4622	0	0	0	0	0
0	0	0	0	0	136.85	1.6196	1.5641	68.426	0	0	0	0	0
0	0	0	0	0	0	5.3739	4.6452	0	0	0	0	0	0
0	0	0	0	0	0	0	0	0	0	0	0	0	0
0	0	0	0	0	0	0	0	0	0	0	0	0	0

Figure 6.11 TOE percentage matrix of arrow shape.

The bit-wise TOE compensation technique was not achievable for this thesis work. This compensation technique requires a specialised software program to accomplish the bit-wise control of pixels in the dynamic bitmap. This software program is another area for future research.

6.7 Summary

Most of these implementations are used to prototype micro parts. There has been little research done on the integral curing of medium to large sized parts for SLA that use UV light to cure epoxy based resins.

Several improvements have been proposed to the Limaye Layer Curing Model that will help attain more accurate predictions for the irradiance map. One improvement allows an irradiance map to be calculated for the entire arrow shaped bitmap so that one mesh is used rather than two. Improved MATLAB code was also developed to accept any bitmap image while still maintaining practical calculation times per layer.

The irradiance weighting equation was experimented with to see how different distributions improved the irradiance map. A symmetric exponential distribution equation was found that closely approximated Limaye's measured distribution. It was found that even when the weighting equation was a flat distribution or an inverted distribution, the irradiance map did not show an evenly spread distribution, in fact, little change was seen in the irradiance map. The most effective way of changing the irradiance was shown to be by improving the opical system to a Cooke triple.

The improved mathematical model analyses the irradiance map and accounts for errors in the optical system. Two techniques were proposed that used compensation of irradiance. Bitmap irradiance compensation used the modulation of the micromirrors to evenly distribute the irradiance in the projected image. The bit-wise TOE compensation technique used TOE of individual mirrors to evenly cure a layer to the required depth. The bitmap irradiance compensation technique proposed is put to the test by experiments reported in chapter 10. Bit-wise TOE compensation was not achievable for this thesis work as it requires specialised software.

This chapter has concluded the literature review. The next chapter will bring the topics and research covered into context in order to state several hypotheses to be tested in the remainder of the thesis.

7 Formulating the Research Question

Now that the background research has been discussed, it is time to bring the research of this thesis into context. Putting the research in context allows a summary of what has been reported thus far and to see where the research fits within the field of rapid prototyping. The focus of this chapter develops the research question, formulates the hypothesis and chooses the method used to test the hypothesis.

7.1 Putting the Research in Context

The previous chapters have given an overview of stereolithography and rapid prototyping. The literature review has presented the various types of rapid prototyping technologies and the placement of SLA technology at the top end of the prototyping market. Chapter 2 reported other ways that rapid prototyping is achieved by describing the technology commercially available.

The fundamentals of laser-based SLA showed that the laser raster on the resin surface has been modelled adequately and is well understood, having existed as a commercial technology for over 15 years. However, as discussed in chapter 3, integral SLA are still in an experimental phase although there are commercial SLA now available on the market, such as the Perfactory by Envisiontec and V-Flash by 3D-Systems. These systems provide relatively weak prototypes when compared with parts made on laser-based SLA. Most of the integral research available has been aimed at the new field of microstereolithography. Many of the μSLA have aimed to increase the lateral and layer resolution of such small-scale parts.

Chapter 4 briefly discussed the chemical process of photopolymerisation and the strength of epoxy chemical bonds over acrylate and vinyl based photopolymers. Several chemistry studies were reported with the hope that insight into the analytical and testing methods would prove helpful to the improvement of the mathematical model and analysis of the resin used for this research.

Chapter 5 revised the principles of light sources and geometric optics. Ray tracing provides an understanding of how light can be modelled as rays travelling through an optical system. This chapter provided a set of ray tracing equations that is highly useful for modelling the integral SLA process. Chapter 5 also reported the many factors that need consideration when dealing with optical systems. Many types of

aberrations hinder image quality. These aberrations need to be minimised and accounted for as much as possible. In addition, many other optics terms were discussed as well as practical aspects of optical systems.

7.2 Reassessment of the Research Objective

Now that the literature review has shed light on the research topic, it is time to reassess the research objective. A broad description of the research objective is:

> "to present a mathematical model for integral stereolithography that predicts the cure in a layer."

The purpose of rapid prototyping is to produce prototypes as quick as possible. Research into making rapid prototyping technology even more rapid, finding efficiencies in the fabrication process and reducing the lead-time are aspects of integral stereolithography that are of chief concern. Making the fabrication process faster for large parts is the aim of this research. Integral stereolithography offers faster fabrication because the cured layer is independent of area unlike laser-based SLA. However, the curing of layers requires more investigation into layer modelling and cross-sectional thickness.

During the search for existing mathematical models of the integral SL process, only one model was found, namely, the Limaye Layer Cure model. However, the model needs improvements and enhancements. Although the Limaye Layer Cure model was developed for microstereolithography, the model creates a foundation to create an improved mathematical model for an integral SLA with the purpose of building large parts.

There are many factors to consider when designing the optical system of the SLA. Aberrations, element misalignment, beam conditioning and beam divergence are all major factors that hinder uniform irradiance at the resin surface and hence dimensional accuracy of layers. The mathematical model must be able to show that it can account for these hindrances to some extent.

After a review of the research available on integral stereolithography, there are several gaps in the knowledge of the process. One gap is being able to know how to control the cure of the photopolymer in discrete areas known as voxels or pixels. The parameter to control is light intensity, which varies across the radial diameter of the beam. Ultimately, even cure throughout the layer is necessary. Particular attention to

controlling the uniformity of cure depth at the edges of a layer needs more investigation. Another way to word this part of the objective is that the light incident on the resin surface must be controlled to cure the resin to a predetermined cure depth.

Considering the concerns mentioned above, the primary objective is now redefined as:

> "To present an improved mathematical model for integral UV stereolithography that accounts for errors in the optical imaging system such that for a predicted irradiance at the resin surface (obtained from the model), an evenly distributed irradiance results."

7.3 Scope of the Research

The primary objective was broken down to sub-objectives as stated in the introduction of this thesis. The sub-objectives are summarized below:

1. The cost to the SLA must be restricted to a limited budget of $10,000NZD.
2. The SLA must accomplish the integral process for fabrication of parts.
3. The SLA must use UV light to cure an epoxy-based photopolymer resin.
4. The SLA is to cure a reasonably large area. A field of exposure of 270mm x 200mm or larger is expected.
5. A mathematical model must be created or found and adapted to model the SLA design proposed. The model should attempt to give an understanding of what to expect over an integrally cured layer.

Upon closer consideration of the sub-objectives, with the exception of sub-objective 5, these sub-objectives are not objectives but rather constraints on the primary objective. What the constraints are trying to do is limit the scope of the research. Thus the scope of this research is limited to a $10,000NZD budget. The research is only concerned with the integral cure of single layers of epoxy-based resin. The projected area is 270mm x 200mm or around this size.

The scope of the research is sometimes best described as to what it is not about. This research is not concerned with making parts but more about controlling dimensional repeatability to cure a single layer. It is not about making small parts for microstereolithography. It is not concerned with the chemical analysis of the photopolymer resin.

7.4 Research Questions and Hypotheses

The primary research objective is explored by asking the following research questions and stating hypotheses. The testing of each hypothesis is explained.

Question 1: How are SLA systems modeled mathematically to ascertain the dimensional cured thickness of a single layer?

Hypothesis 1: An SLA system can be modeled mathematically to find the cure depth throughout a single layer by modification of the Limaye Layer Cure model and application of the cure depth equation.

Testing of hypothesis 1: Hypothesis 1 is tested by measuring the cross-sectional thickness of a layer cured using the SLA constructed for this research. A modified version of the Limaye Layer Cure model is used to generate an irradiance map of a layer projected onto the resin surface. The layer profile used is an arrow shaped bitmap. Each arrow shaped layer is cut along the longest dimension before post curing. The cross-sectional thickness is measured empirically under a microscope. Several layers are made on the SLA with different exposure times. The cross-sectional thickness is compared with values from the mathematical model by applying the cure depth equation. The comparison is used to report the error in the mathematical model for layer thickness.

The Layer Cure model is also validated in a similar experiment conducted by Limaye. 15 layers are measured for lateral dimensional accuracy and repeatability. This experiment allows for some comparison with Limaye's test result for the Layer Cure model.

Question 2: How is the layer thickness of a photopolymer controlled accurately by a dynamic pattern generator to create an evenly cured layer?

Hypothesis 2: The layer thickness of a photopolymer is controlled accurately by modulation of individual pixels of the dynamic pattern generator to create an evenly cured layer.

Testing of hypothesis 2: One technique proposed uses compensation of the irradiance map generated by the Limaye Layer Cure model. The improved mathematical model from hypothesis 1 is used to generate a compensated grayscale bitmap of the arrow shape. The compensated bitmap is displayed on the dynamic pattern generator. The layer thickness is measured using the same test of the arrow

shaped bitmap used in hypothesis 1. The cross-sectional thickness is analysed and compared with the uncompensated thickness.

Question 3: How can the phenomenon at the edges of a layer, known as print-through error, be accounted for by control of the dynamic pattern generator?

Hypothesis 3: The dynamic pattern generator can control the print-through error by increasing the exposure time at the edges.

Testing of hypothesis 3: Hypothesis 3 is tested in a crude way by having a bitmap where there is a definite border around the arrow shaped bitmap. The border is much brighter than the rest of the bitmap. The bitmap is uncompensated apart from the border. The cross-section of several single layer exposures is examined and analysed in the same way as the tests conducted in hypothesis 1. The crudeness of this test is to see if there is a definite change at the edge of the cured layer.

7.5 Organisation of this Thesis

Chapter 8 describes the design methodology developed by (Dym & Little, 2004) for engineering design. Chapter 9 discusses the choices applied to the design of the SLA according to Dym and Little's design methodology. The specific numerical details of the SLA design are used as essential input data for the mathematical model.

Chapter 10 reports the experiments conducted throughout the SLA's development. This chapter also analyses the results from experiments to test the hypotheses.

Chapter 11 discusses the research experimental results and conclusions. The chapter concludes the research work with the contribution of the work to the rapid prototyping field and future work.

8 Research Methodology

8.1 Engineering Design

Engineering projects often involve the design of something. Research and development work frequently involves the design of something new or something that does not yet exist. The nature of this thesis work is to aid in the analysis of the research hypothesis and as such requires the design of a stereolithography apparatus. Therefore, an engineering design methodology is implemented.

Dym & Little (2004) give engineering design the following definition:

> "Engineering design is the systematic, intelligent generation and evaluation of specifications for artefacts whose form and function achieve stated objectives and satisfy specified constraints." (Dym & Little, 2004)

The artefact refers to the thing or things being designed. Form is the shape and geometry of the artefact. Function is what the artefact is supposed to achieve. The specifications are an exact description of properties and parameters for the artefact. These design specifications provide a way of evaluating the proposed designs.

Ertas and Jones (1996) offer a more thorough definition of engineering design:

> "Engineering design is the process of devising a system, component, or process to meet desired needs. It is a decision making process (often iterative), in which the basic sciences, mathematics, and engineering sciences are applied to convert resources optimally to meet a stated objective. Among the fundamental elements of the design process are the establishment of objectives and criteria, synthesis, analysis, construction, testing and evaluation." (Ertas & Jones, 1996)

There are many design methodologies (i.e. Delphi, Pahl and Beitz, De Bono techniques) and design processes (Dym & Little, 2004; Ertas & Jones, 1996). In general some models are descriptive while others are prescriptive. Descriptive models only attempt to describe elements of the design process. Prescriptive models are more specific in that they list what should be done during the design process (Dym & Little, 2004). Care needs to be taken not to use a design process that is too abstract, or

on the other hand, one which is overly restrictive or too detailed. General design processes can be found where variations or even elimination of stages in the process can be applied to suit the application.

8.2 Dym & Little Design Process

Dym & Little (2004) present a five-stage prescriptive model of the design process shown in Figure 8.1. Each stage begins with an input and has certain design tasks that must be performed in order to produce the required output. The starting point of the model is the "need" or client's statement and then proceeds through each stage of the process until the endpoint which is the final product. Figure 8.1 also includes internal and external feedback loops for verification and validation of the design.

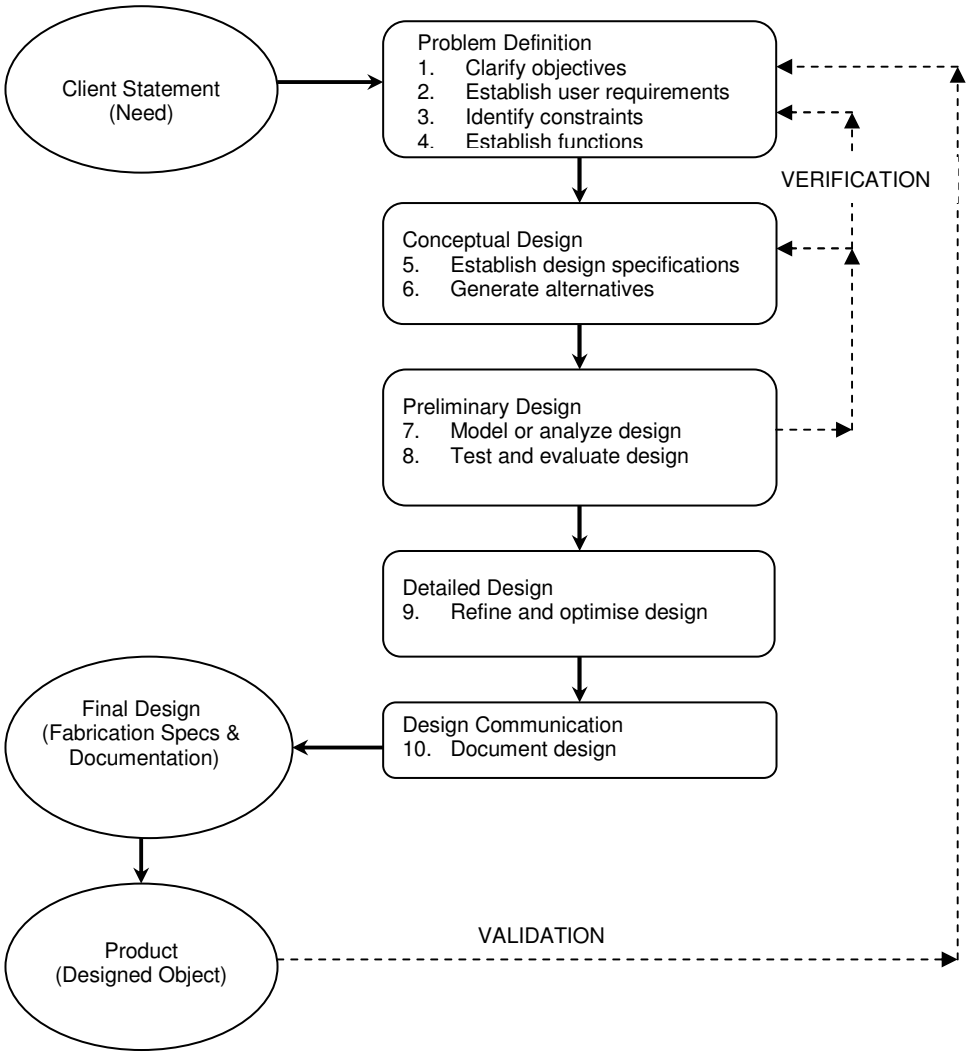

Figure 8.1 A five-stage prescriptive model of the design process with internal and external feedback (Dym & Little, 2004).

The client statement must be capable of being meet by engineering effort. Client statements must be fully understood. Often the client statement is a problem and the

problem has to be completely defined. Understanding the problem helps identify the correct solution or solutions. Client statements may come in a number of ways such as formal or informal requests, unsolicited proposals, assignments from supervisors, needs associated with products, etc.

8.2.1 Problem Definition

During the problem definition stage the client's objectives are clarified. Important information is gathered to develop an engineering statement of the client's need. The sources of information may be obtained through literature research, brainstorming, expert interviews, function-means trees, functional analysis, attribute lists and/or requirement matrices.

Part of the problem definition stage is to define the design objectives, constraints, functions and means. There is a subtle difference between objectives and constraints. Objectives are the desired attributes of a design and constraints are limits that a design must meet in order to be successful. Functions in the design sense are defined as the actions that the designed object must do in order to be successful. A helpful tool to use in the identification of functions is verb-noun pairs. Means are ways of implementing functions and are specific as to how a function is to be met.

Functions can be divided into basic and secondary functions. Basic functions are defined as the specific work that the object is designed to accomplish. Secondary functions are the other functions needed for or that result from performing the basic function. Secondary functions become the sub-functions of the system.

Secondary functions are further classified into required and unwanted secondary functions. Required secondary functions are those functions that are needed for the basic function. Unwanted secondary functions are the undesirable by-products of basic or secondary functions.

Performance specifications are necessary to give targets for the functions to achieve. Performance specifications identify performance levels for the achievement of desired functional behaviour. These specifications allow for measurement and verification of a function's performance. The performance specifications must describe the desired functional behaviour and how well it must perform. Performance is determined by the way functions are measured and the units of measure.

It can often be difficult to separate the functions from objectives and vice versa. It usually requires a lot of experience and a practical feel for design. A key to disguising

between functions and objectives is to remember that objectives describe what the design will be like and what qualities it will have. Objectives are usually characterised by the use of present participles such as “are” or “be”. Functions describe what the designed object will do. The focus is on what input is being transformed into an output. Functions are characterised by active verbs.

The main tasks that are achieved in the problem definition stage are to:

1. Clarify design objectives
2. Establish user requirements
3. Identify constraints
4. Establish Functions

8.2.2 Conceptual Design

The outputs from the problem definition stage acts as inputs to the conceptual design stage. The conceptual design stage is an abstract and open-ended stage where concepts or schemes are proposed with which to achieve a solution to the client’s need. Two or three concepts are created where each concept or scheme provides an outline to the solution. The means to achieve the major functions are specified as are spatial and structural relationships of principle components. Cost estimates, intended use, aesthetic values are also worked out in this stage.

Two tools that are used to generate alternative concepts are morphological charts and functions-means trees. Morphological charts are a matrix of functions and possible means. The morphological chart helps in the generation of concepts. The first column of the matrix lists the features or functions of the design. Each row of the matrix lists at least two or more possible means by which each function can be implemented. Thus, by selection of one means from each row, a possible concept is formed to solve the design problem. The structure of a morphological chart is shown in Table 8.1.

Means Feature/Function	Means 1	Means 2	Means…
Feature Function 1			
Feature Function 2			
Feature Function …			

Table 8.1 Structure of a morphological chart.

There are several guides when using morphological charts. It is important to choose features and functions at the same level of detail. This means choosing features and functions from the same level of the objectives tree or function-means tree. The number of possible combinations becomes quite large, so it is important to apply the design constraints, physical limitations and common sense to the feasibility of possible combinations.

Two tasks done in the conceptual design stage are to:

5. Establish design specifications
6. Generate design alternatives

8.2.3 Preliminary Design

The preliminary design stage, also known as the embodiment of schemes, is the third stage of the design process. In this stage, the higher-level objectives of the conceptual design are expanded on with lower-level attributes. These attributes include performance specifications and operating requirements. More specific detail and general calculations are used that reflect the designer's experience. The final decision of what concept to accept of the proposed concepts is made before continuing to the next stage in the process.

The tasks completed during the preliminary design stage are to:

7. Model and analyze conceptual designs
8. Test and evaluate conceptual designs

8.2.4 Detailed Design

The detailed design is where the chosen concept is refined even further. Much greater detail is specified on the preliminary design down to part types and dimensions. A proposed fabrication specification is prepared. Relevant knowledge to accomplish this is found in handbooks and catalogues and should be familiar to the design engineer. The task completed in the detailed design stage is to:

9. Refine and optimise the chosen design

8.2.5 Design Communication

Design communication is the final stage of the design process. This stage details what happens after the detailed design stage. It serves to document and present the final design of the concept that was chosen at the end of the preliminary design stage. This includes the fabrication specifications and their justification. The final task to complete in the design communication stage is:

10. Document the completed design

8.2.6 Feedback and Iteration

Verification is an internal feedback mechanism where tests and evaluation tasks are fed back to verify that the design performs as intended. Verification is an ongoing part of the first three stages: problem definition, conceptual design and preliminary design.

Validation is an external feedback mechanism. Feedback is given by the client or user that provides validation on whether or not the final design solution is a success.

After validation, the design process becomes iterative. Iterations are done by repeating the methods or steps in the design process. Repetitions may occur at a different scale that started the whole design process from the beginning. For example, the conceptual, preliminary, and detailed design may only be revisited in some detail while keeping the original objectives as a guide to ensure the principles of the final design are not lost.

8.3 Summary

In this chapter a design process methodology by (Dym & Little, 2004) has been presented. In this thesis, Dym and Little's design process serves as a guideline for the design of an SLA that will meet the objectives of this thesis. Figure 8.2 shows how the design of the SLA has been adapted to align itself with Dym and Little's five-stage prescriptive model of the design process.

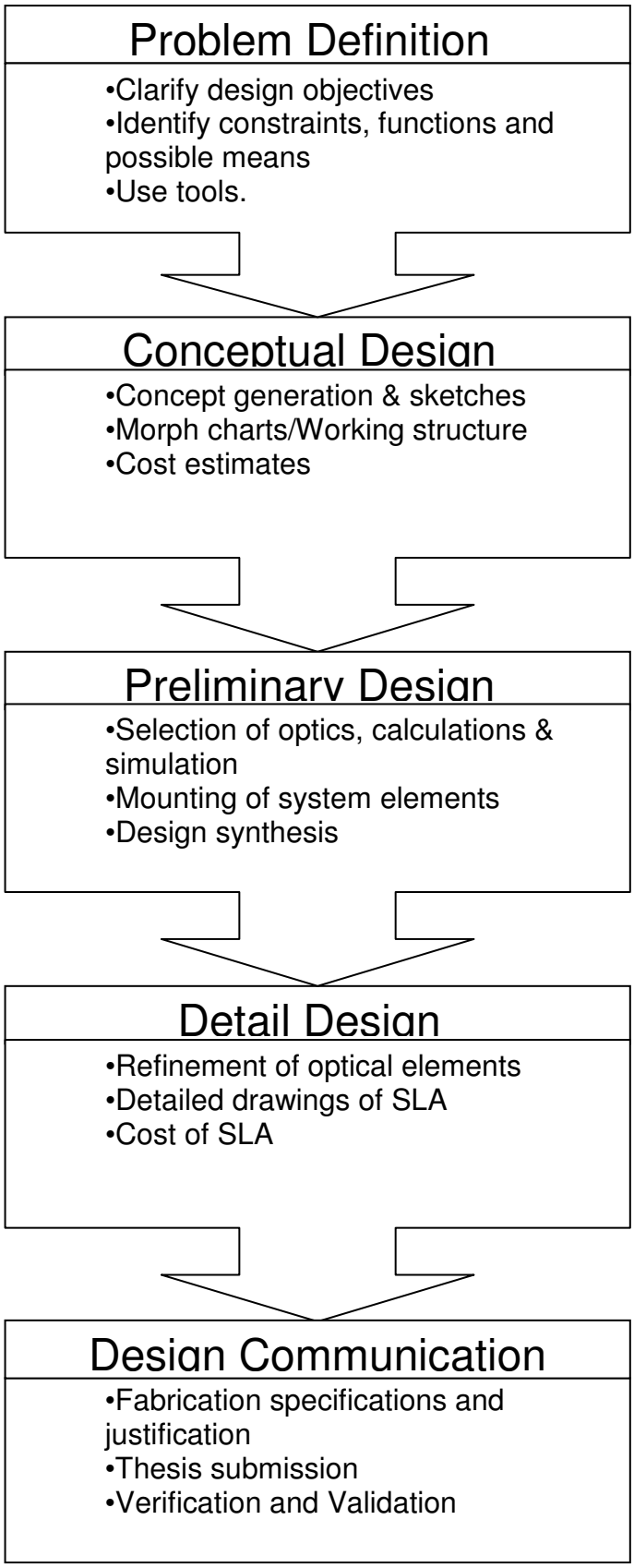

Figure 8.2 Design methodology used to design and develop the SLA.

9 Design of the Integral SLA System

In chapter 8, Dym and Little's design process was discussed as a design methodology. Section 8.3 showed how Dym & Little's five stage design process is adapted to the design of an integral SLA for the research of this thesis. In this chapter the adapted design process is implemented.

9.1 Defining the Problem

9.1.1 Identifying Objectives

The primary objective of this thesis is to provide an improved model for integral UV stereolithography. The essence of the integral SLA is to build rapid prototyped parts faster than conventional laser-based SLA. The specific aspect of the problem, as shown by the literature review, is predicting and controlling the irradiance distribution for a large projected area. There are also many other factors that affect the irradiance distribution. So in order to aid in meeting the design objectives of the SLA, an attributes list is used. In Table 9.1, attributes generated by brainstorming about the SLA are listed and each attribute is labelled as to whether it is a constraint (C), function (F), means (M) or objective (O).

Label	Attribute
O	SLA must cure profiles on the resin surface
O	SLA should increase build speed of plastic parts
O	SLA should provide the ability to analyse the light & resin reaction
F	SLA should cure a relatively large area
F	The light path should be tuneable
M	A projector or a DMD from a projector should be used to save costs
C	SLA must be used in an environmentally controlled room
M	Could be made out of rigid plastic or metal, but not wood or flimsy material
C	SLA should use a commercially available photopolymer
O	SLA should be safe to avoid direct exposure to UV light
O	SLA should be stable, sturdy, and durable
O	SLA must be able to hold the weight of a small vat of resin and the projector parts
F	SLA transmits UV light
O	SLA is used to control the optical distances
O	SLA is to be used indoors on a flat or level surface
O	Adjustments to movable parts should be manually controllable
C	Must be within a budget of $10,000
C	Movement should be achievable to 0.1mm

C	The resolution must be greater that 0.1mm or greater
O	SLA should be able to control the exposure time
Key	O = objective, F = function, M = means, C = constraint

Table 9.1 Attribute list for the integral SLA design

The attributes list is pruned to just the objectives and allows the formation of an objectives tree for the design of the integral SLA. The objectives tree shows the hierarchy of objectives as it expands and similar ideas are clustered together. A benefit of constructing an objectives tree is that it helps question why certain objectives are chosen. The questions generate simplified objectives at the higher levels of the tree and thus make it clear what the main design objectives become.

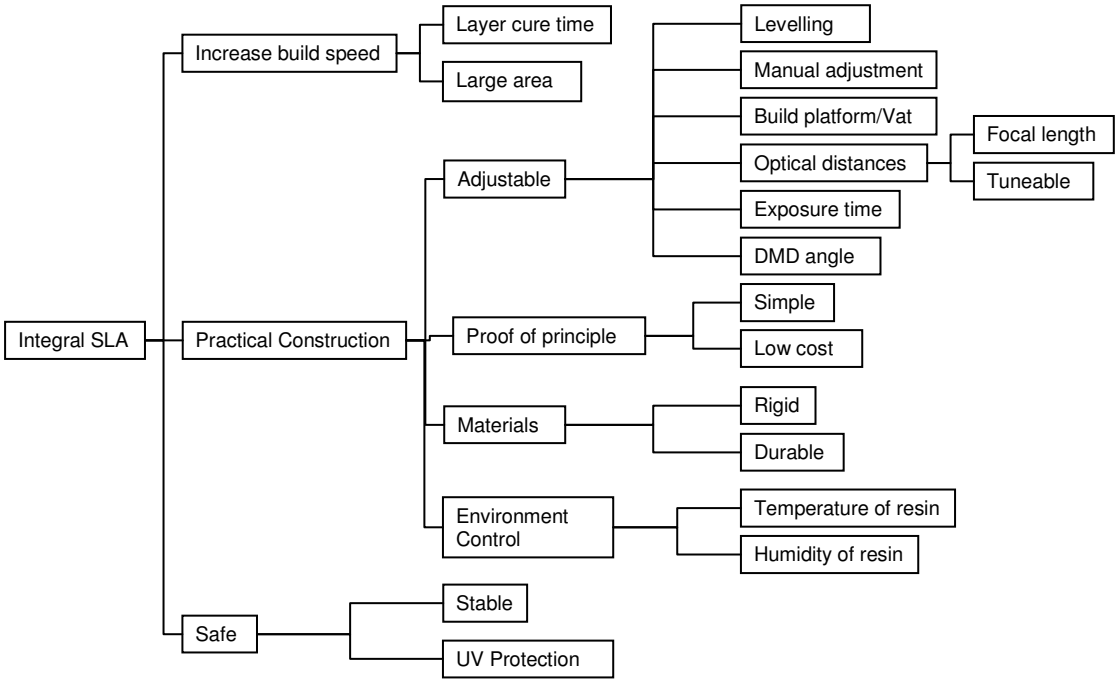

Figure 9.1 Objectives tree for the integral SLA.

As seen in Figure 9.1, the main design objectives are to increase the build speed of parts while keeping the design practical for construction and safe to use. Practical construction encompasses the parts of the design that need to be adjustable while realising that this SLA is a research tool so as to prove the theory being tested.

9.1.2 Identifying Functions

From the literature review, several SLA layouts were presented. The common features of these SLA designs are as follows:

- Light source
- Collimation and conditioning

- Filters
- Pattern generator
- Imaging or Focusing lens
- Z-stage
- Vat of resin

Several other elements are used. For the light source, the type of lamp selected depends on the required wavelength. A light guide can be used to collect and direct light into the collimation system. The collimation systems can be quite complex involving beam expanders, polarizing elements, diffractive elements, and directional elements such as mirrors and prisms. Pattern generators are controlled by dedicated controllers which linked to computers. Some SLA utilise single element focusing lenses. There are also different ways in which a part can be built using the Z-stage to ensure a level resin working surface. For example, working surfaces are levelled by using a dip-in-window, wiper blade, building the part upside down, vibration of the vat, and the deep-dip method.

There are a few techniques that are used to identify the various system elements and the necessary functions that need to be performed. The enumeration technique is used to determine the functions of the SLA design that were not readily identifiable from the attributes list. The key to enumeration of functions is finding verb-noun pairs. Enumeration has a major weakness, in that ideas rely solely on a brainstorming session to find the readily identifiable functions. The enumeration list is given in Table 9.2. The functions in the list are then classed into basic and secondary functions. Also, the unwanted secondary functions are considered and their resulting new required functions are added to the list.

Function	Description	Function	Description
BF	Builds plastic parts	RSF	Collimates light
BF	Supplies power	BF	Irradiates resin
RSF	Cures layer	SF	Focuses light
SF	Polymerises resin	RSF	Conditions the beam
RSF	Contains resin	BF	Supplies light
RSF	Controls exposure time	SF	Tunes light intensity
SF	Holds optics	RSF	Controls exposure time

RSF	Generates pattern	SF	Filters light
RSF	Reflects light	SF	Adjusts DMD
RSF	Controls DMD	RSF	Moves build platform
SF	Modulates light	SF	Adjusts vat height
RSF	Images pattern	SF	Levels resin
SF	Projects image	RSF	Supports weight
USF	Generates heat	NRSF	Cools hot elements
USF	Generates vibration	NRSF	Dampens vibrations

Key: BS = Basic Function SF = Secondary Function
RSF = Required Secondary Function USF = Unwanted Secondary Function
NRSF = New Required Secondary Function

Table 9.2 Enumeration list of functions for the integral SLA design.

To overcome the weakness of the enumeration technique, the black and transparent boxes technique is used to show an input-output model. This technique is good at identifying functions that were overlooked by enumeration. The black box tool aids in relating inputs to outputs and the transformations between them. The transparent box shows how all the secondary functions are related. The transparent box reveals how the inputs are transformed into outputs. It even identifies where the unwanted outputs occur. Figure 9.2 shows the black box of the system and Figure 9.3 is the transparent box of the SLA showing how the secondary functions are related. Even the unwanted secondary functions are linked into where they occur.

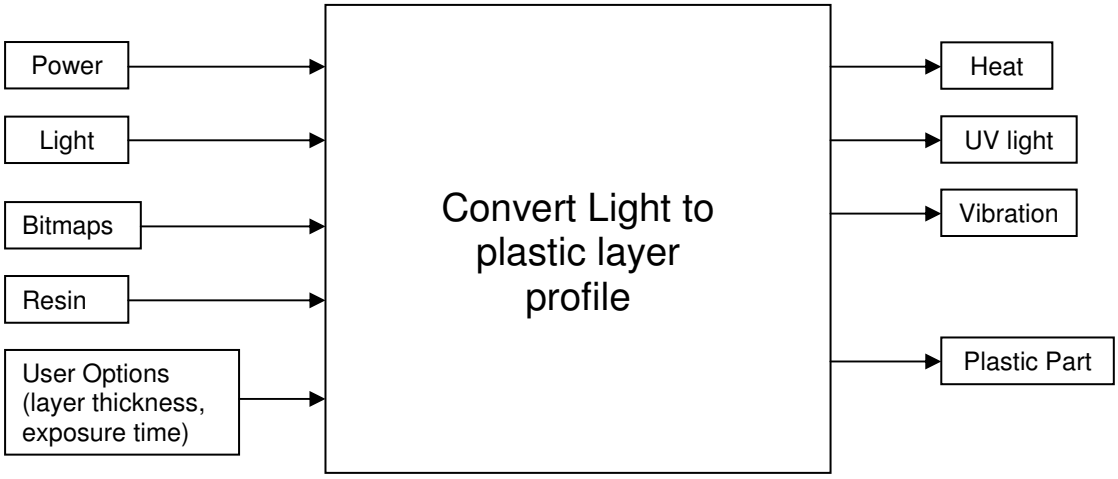

Figure 9.2 Black box for the integral SLA.

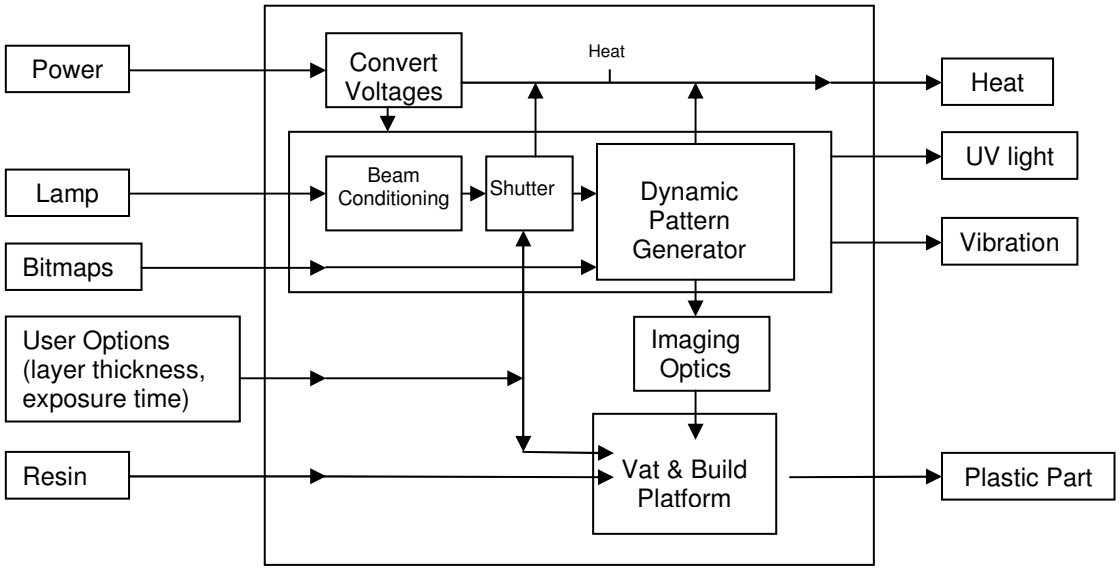

Figure 9.3 Transparent box for the integral SLA

Out of all the functions, there are four main functions. These are beam conditioning, dynamic pattern generation, imaging optics and the control of the vat and build platform. Further definition of these four main functions will become the goals that the SLA design should achieve.

The beam conditioning takes as much light from the lamp as possible and collimates it so that the light rays travel fairly parallel with each other. The beam condition includes the collection of light, the collimating lens or lenses and filtering to the necessary wavelength. The beam profile should emerge as a gaussian distribution.

The dynamic pattern generator used in this research implementation is the DMD. The DMD is part of the DLP technology of the projector donated for the research. The DMD has been a popular choice in previous research in recent years. It also has a good contrast ratio and fill factor when compared with LCD technology.

To obtain the bitmaps that will be displayed using the DMD, the CAD file is sliced into layer profiles of the required thickness. The DMD functions by reflecting the incoming, conditioned beam of light toward the resin surface. The DMD reflects only the profile wanted by tilting individual micromirrors to form the correct bitmap profile. The bitmaps are supplied one at a time from a dedicated computer.

Before the reflected light beam reaches the resin surface, it must pass through the imaging optics. The function of the imaging optics is to control the collection of light and other desired requirements such as field of view, depth of field, resolution, and working distance.

Movement of the vat and build platform is necessary for part building. Adjustment of the build platform enables selection of the desired layer thickness and recoating of the cured surface in between layers. Control of the vat allows for changes in the working distance as the level of the resin rises. The resin level changes as the build platform is lowered into the vat.

9.2 Conceptual Design

To begin the conceptual design stage, the functions are reassessed to determine the design specifications. The means to achieve the major functions are specified using a function-means matrix. Two or three concepts are created, where each concept or scheme provides an outline to the solution.

9.2.1 Performance Specifications

With the functions now determined, performance specifications are required. In this section, the performance specifications provide guidelines or targets for the final design of the SLA. They are not locked-in and may be revisited for adjustment.

It can become difficult to distinguish if a function is actually an objective, and vice versa. So in order to confirm the functions, a list (Table 9.3) was created using relevant items on the enumeration list. These items were given performance specifications and then assessed to establish whether the item was a function or an objective.

Objective or Function	**Enumeration**	**Performance Specification**
Objective	Builds parts	The parts built should be made from a photopolymer resin. The layer thickness should be between 0.10-0.25mm as is standard in commercial SLA. The resolution must be a minimum of 0.5mm in the X- and Y-axes.
Objective	Irradiates resin	The light intensity at the resin surface must be at least 9mJ/cm^2 to initiate polymerisation. The range of irradiance for practical curing speed is 30-100mW/ cm^2.
Function	Supplies power	The required power supply must convert 230V_{ac} into the necessary 5-6V logic voltage, 12V for the

		cooling fans and be able to start the arc lamp.
Function	Collimates light	The beam collimation lenses must accept a beam diameter of 15-20mm and collimate the incoming light to at least a 10 degree or less divergence angle.
Objective	Tunes light intensity	The beam to DMD distance needs to be tuneable, to so that the intensity of the light can be varied.
Function	Filters light	A wavelength of 354±5nm must be used to obtain the correct wavelength of light to initiate polymerisation of the photopolymer.
Function	Controls exposure time	Exposure time of the light to the resin must be controllable to 1sec or less.
Function	Generates pattern	The pattern generated to be displayed on the DMD must be sent via the AV video connection from the computer to the projector. The format of the bitmap must be greyscale or monochrome.
Function	Adjusts DMD angle	The DMD should be adjustable to 0.1mm in X- and Y-axes. This adjustment allows the micromirrors to be aligned to reflect the incoming light directly at the resin surface.
Function	Moves build platform	The build platform must move in the Z-axis to within 0.1mm which is the minimum layer thickness. The range of travel for the build platform must be a minimum of 30mm into the resin.
Objective	Contains resin	The SLA must hold a vat of resin with enough resin to cover the highest part to be built for experiments by 10mm (to allow for deep-dip recoating). So the required vat depth must be a minimum of 40mm. The width and length must be 200mm x 270mm respectively according to research sub-objective 4 (see Section 1.1).
Function	Adjusts vat	The SLA must be adjustable to within 0.1mm to

	height	maintain the working distance as the resin level changes. This will also allow for working distance changes that result from imaging requirements and light intensity variation.
Function	Supports weight	The SLA must be rigid. It must support the weight of the projector and the vat of resin. The projector weight is 3.08kg (About Projectors, 2006) and the weight of the volume of resin is approximately 3kg (weight of resin and vat given by the dimensions in 11. above).
Function	Monitors temperature	The SLA must monitor resin temperature variations and stop if the resin temperature is outside 25-28±0.5°C. These temperatures are required for constant resin viscosity.

Table 9.3 Performance Specification List and Function/Objective Classification.

Four of the items in Table 9.3 were re-classified as objectives. The reason for their reclassification is because they are more descriptive in character rather than actually detailing specifics that do an action or perform a function. Even though some of these items had numerical specifications, they were not seen as critical to the SLA's operation.

9.2.2 Concept Development

Morphological charts are used to generate various means to accomplish various functions. The main functions are the focus of the morphological chart in Table 9.4 with some extra important consideration noted from previous SLA. Concept combinations are devised and analysed for their feasibility. Constraints, objectives, practical issues and common sense are observed in the analysis. Each feature and function is discussed separately to highlight the favoured means with some cost estimations.

Means Feature/Function	Means 1	Means 2	Means 3	Means 4
Light source	Laser	Tube	Light guide	Arc lamp
Beam conditioning	Single element collimator	Multi-element collimator	TIR prisms	Beam expander
Pattern generation	DMD	LCD	GLV	Disposable mask
Imaging optics	Single lens	Wide angle lens	Zoom lens	Other multi-element lens
Working distance control	Vertical ball screw	Power screw	Volume displacement	
Elevator motion	Threaded rods	Rods & clamps	Pulley system	Automated control
Resin levelling	Deep-Dip	Vibration	Wiper	Dip-in window

Table 9.4 Morphological Chart of main SLA functions.

9.2.2.1 Light Source

Light sources can be expensive, so the light source chosen must bear in mind the cost constraint. This constraint rules out the use of a laser, as lasers are often priced over $NZ10,000. UV tubes are costly at the wattage required. Efficient light collection is necessary, as the light is emitted from a cylinder and not in one direction. A fibre optic light guide can be used for high wattage high pressure lamps. The problem, faced with implementing a light guide, is the limited size of the optical fibre. Sizes usually range from approximately 5.0-10.0mm in diameter, which would require a beam expander for this SLA design. Also, high pressure UV lamps are expensive. The lamps require special power supplies that range in the thousands of dollars, not to mention the hundreds of dollars that the lamps cost. The projector donated for the project has a 270W metal halide lamp, which does provide a small amount of UV light. However, the lamp requires collimation and filtering to the required wavelength.

9.2.2.2 Beam Conditioning

The beam conditioning systems vary in complexity and depend on the light input into the system. Arrangements of optical elements cost anywhere from several hundred dollars to thousands of dollars.

The main objective of beam conditioning is primarily collimation. Lasers provide a fairly collimated beam at a specific wavelength so a filter, single collimating lens and a focusing lens can be used to bring the beam to a focal point on the pattern generator (or galvo mirrors) as Ikuta et al (1998) used. Lamps and tubes supply broad spectrum light which requires collection, collimation and filtering. As seen in the literature review, a set of collimating lens are used followed by a filter to only let the necessary wavelengths through. Complex elements such as homogenisers and projection lens assemblies can be used to achieve high collimation and spatial resolution (Sun et al, 2005). Many of the μSLA utilise light guides to illuminate the pattern generator. A combination of a simple or multi element collimating lens and filter are used in most cases.

Preference for the beam conditioning for this research is limited by cost to less than $NZ1000. So to keep the design simple, a multi element collimating lens set with a narrow band filter is desired as this provides for ease of design and selection of off-the-self components.

9.2.2.3 Pattern Generation

The choice of dynamic pattern generator has already been decided for this research as the projector donated for the project is equipped with a DMD. The literature review showed that the DMD has been the most used dynamic pattern generator over recent years. The DMD also has several other performance benefits over LCD such as switching speed, contrast ratio, resolution and suitability for use with UV light.

One other important consideration is the DMD mounting. (Hadipoespito & Li, 2005) used a TIR prism to change the angle of the input light beam so that it was normal to the DMD and resin surface (Figure 9.4a). Some researchers, such as Chan et al (2003), Takahashi and Setoyama (2000), use a mirror to reflect the light beam onto the DMD so that the DMD is mounted upside down, facing normal to the resin surface (Figure 9.4b). These techniques make mounting the DMD straight forward and simple.

Figure 9.4c shows how Limaye (2004) mounted the DMD at a 45° angle to the incoming beam of light. This method does not require additional optical elements

such as a mirror or a refocusing lens. However, careful attention must be made to the mounting angle and the mounting must compensate for the 10° tilt of the micromirrors when they are switched on.

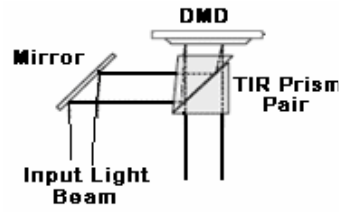

(a) Horizontal DMD mounting with light directed by prism pair.

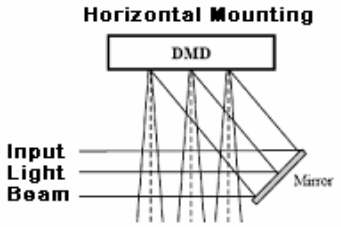

(b) Horizontal DMD mounting with light reflected by mirror.

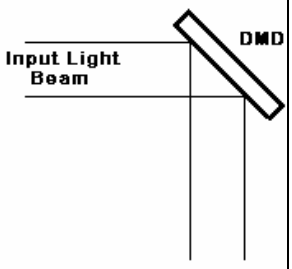

(c) DMD at 45° with light reflected toward resin surface.

Figure 9.4 Concepts for DMD Mounting.

9.2.2.4 Imaging Optics

The imaging optics has the task of focusing the object on the image plane, in this case the resin surface. All the SLA covered in the literature review had some form of imaging optics. The imaging optics ranged from a single focusing lens to multi element projection lens assemblies. Successful single and multi element focusing lenses were used by Limaye, Takahashi, and Hadipoespito and Li. A single element imaging lens is looked at for the SLA and a simple multi element focusing system.

9.2.2.5 Working Distance Control

The resin level must be controlled so that the image plane (resin surface) remains at a constant distance from the object (DMD). This object-to-image distance is called the working distance. The resin rises slightly each time the build platform and elevator mechanism are moved lower into the vat of resin as a part is built. For μSLA applications, the working distance change is negligible because of the small layer increments. It should be noted that the amount by which the resin level changes depends on the surface area of the vat and the amount of material that is lowered into the vat in one layer step. For most cases, the resin level change is indeed negligible. If the working distance does change, adjustment can be made to the vat's absolute height, but it must be achieved whist maintaining a 0.1mm gap between the previously cured layer and the next new layer.

The working distance adjustment can be accomplished by three different mechanical methods as devised in the morphological chart (Table 9.4). The first is a

vertical ball screw (Figure 9.5a). The vat would need to be supported by a right angle bracket or cantilever. The second method, shown in Figure 9.5b, is a power screw that supports the vat from underneath and allows for vertical motion by turns on a thread. And the last method is to use material displacement by having a movable volume that is capable of moving in and out of the vat. Figure 9.5c shows a rectangular mass that emerges out of the resin to lower the resin level and vice versa.

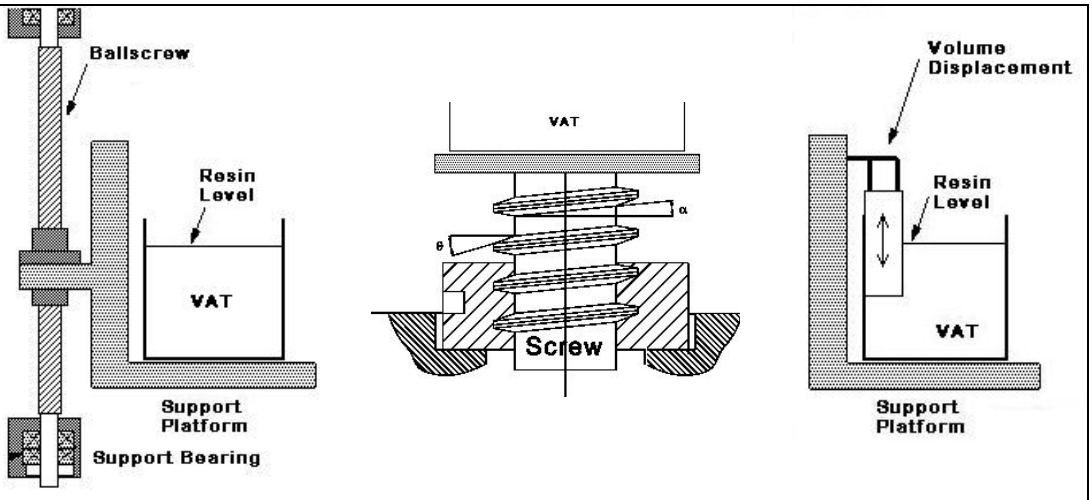

(a)Ball Screw (b)Power Screw (c) Volume displacement

Figure 9.5 Concepts of vat motion for resin level control.

9.2.2.6 Elevator Motion

The elevator controls the layer step size and the movement of the build platform in and out of the vat. The steps size needs to be measured in at least 0.1mm increments for each layer. Automated control and the ball screw are the best way to approach controlled motion of the elevator. However, the cost for motors and associated controllers can be expensive and time consuming to implement. Ball screws have the advantage of having no backlash in the connection between the ball screw and lead, however, they are expensive. A simple mechanical elevator attached to a threaded rod with an appropriate method of accounting for the backlash is affordable and easy to implement. A measurement gauge or micrometer would be attached to achieve accurate motion. The disadvantage of this manual movement of the elevator is that the building process will be extremely slow and tedious.

9.2.2.7 Resin Levelling

After each layer is complete, the elevator lowers the build platform into the vat of resin by one layer step. Before the next exposure can be performed, time must be

allowed for the resin to settle so that the layer is flat. The deep-dip method is where the elevator lowers the build platform approximately 5mm beneath the resin surface, then slowly brings the elevator to the correct position ready for the next layer. The 'deep' dipping allows for the resin to flow over the previous layer and deposits enough material for the next new layer.

Elevator vibration was experimented with by (Takahashi, 2001). By vibrating the build platform, resin levelling and settling time is shortened by up to 50%. In order to accomplish build platform vibration, a special adaptor between the elevator and the build platform is required. It would be interesting to try vibration of the vat instead of the build platform to see if this type of vibration had an effect on the resin settling time.

The commercial SLA systems developed by 3D Systems incorporate a patented wiper blade called the Zephyr™ recoating system. The wiper is positioned close to the resin surface enough to create a meniscus. The distance between the resin surface and the edge of the wiper blade is known as the blade gap witch is typically 0.1mm (≈0.004in). The inside of the wiper blade is hollow and this cavity is filled with resin by the application of a vacuum controlled by a remote vacuum pump. The wiper is moved over the resin surface after the elevator has lowered the build platform down one layer step. This type of recoating system effectively creates and evenly spread layer over the previous layer.

(Hadipoespito & Li, 2005) implemented a dip-in window on their μSLA. A quartz dip-in window can be used to create an even, flat surface. The window is positioned inside the surface of the resin and creates an even working thickness between the previous layer and the window. Care must be taken when lowering the build platform once a layer has been cured because the layer can stick to the window. Often the bottom of the dip-in window is coated with silicon to prevent sticking.

The most suitable method for the SLA design of this research is the deep-dip method. It is simple to implement, requires no additional components, and satisfies the design objectives. The settling time can benefit from implementing a motor to vibrate the vat or the elevator. The wiper method is a patented technique and requires a lot more time spent on set up and fine tuning. The dip-in window requires a large piece of quartz glass for the intended application. The quartz also acts as another transfer medium and the UV intensity will diminish a small amount before it reaches the resin. Thus, the deep-dip method is best method to implement on the SLA.

9.2.2.8 Combined Concept Layouts

Two concept layouts of the overall SLA system to be designed are shown in Figure 9.6 and Figure 9.7. There are in fact many combinations of functions and means conceivable but only the most favoured means are chosen. The modularity of the various means allows for a mechatronic approach to the implementation of different means as interchangeable modules for each function.

Figure 9.6 shows the layout of a high pressure arc lamp as a light source. The beam conditioning system involves several collimating lenses to collect and output fairly parallel light rays. The beam is filtered through a narrow bandpass filter before striking the DMD. The DMD is mounted at 45° so that the beam is reflected toward the resin surface. In this concept, a single imaging lens is used to magnify the image onto the resin surface. The elevator and vat both achieve motion by threaded rods. And finally, the deep-dip method is how resin levelling is achieved in between layer exposures. Note that the optical system is modular (indicated by the boxes) and by applying a mechatronic approach to the SLA design, these modules can be easily swapped with other means.

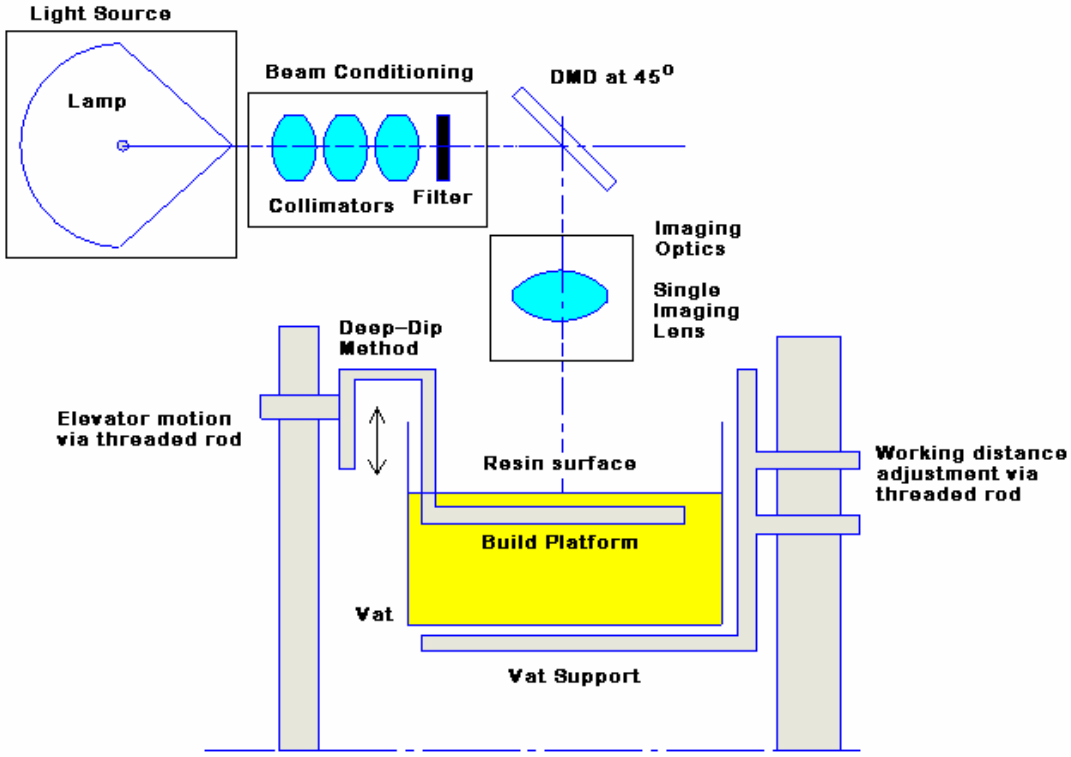

Figure 9.6 Concept Layout 1.

The second concept layout, as shown in Figure 9.7, makes use of a high pressure arc lamp that has a fibre optic light guide attached. The light guide outputs a fairly

collimated beam, so only one collimating lens is implemented before the beam is transmitted through a narrow bandpass filter. The DMD is still mounted at a 45° angle. The imaging optics is changed to a simple multi-element projection lens arrangement. The elevator mechanism still remains the same but the vat is raised and lowed by a power screw. Resin levelling is assisted by an electric motor that vibrates at a controlled frequency.

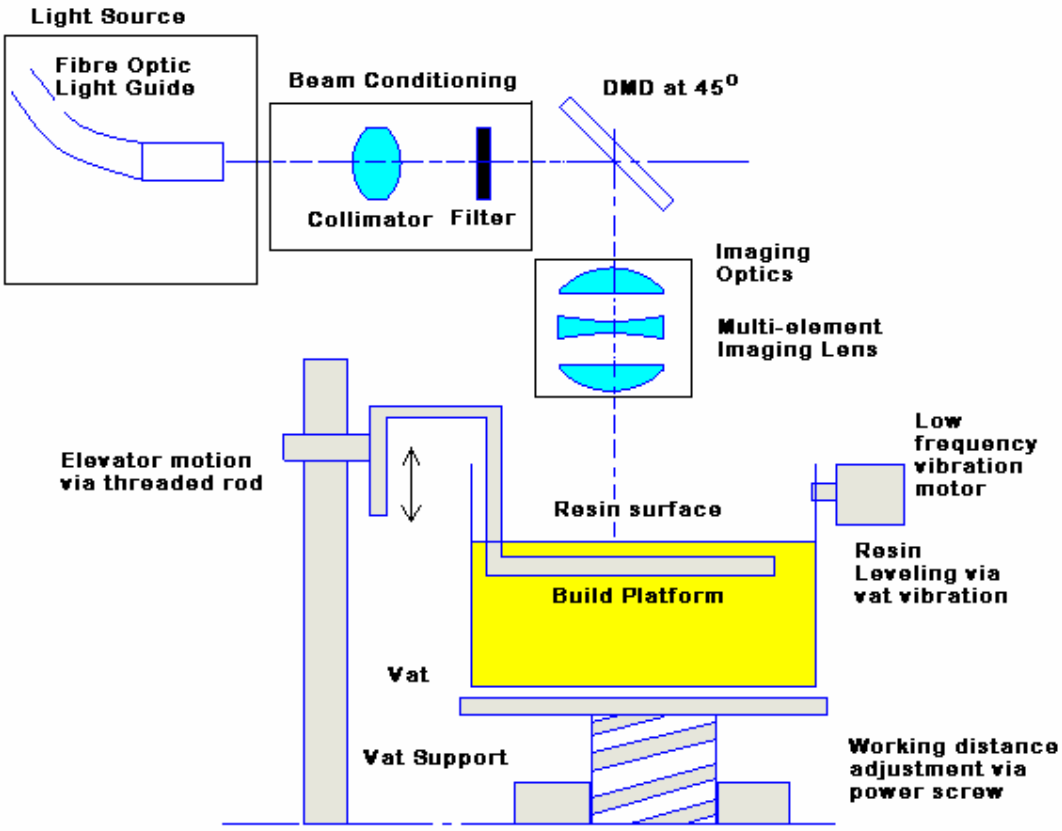

Figure 9.7 Concept Layout 2.

9.3 Preliminary Design

The next stage of the design process is preliminary design. The preliminary design stage involves testing and evaluation of each of the above concepts. From the knowledge and research into the mathematical model, areas such as optics, properties of light and the chemistry of photopolymers will be used to access the most suitable concept.

Numerical values need to be added to the SLA design to obtain specific dimensional and functional requirements. An appropriate place to start is the maximum size of a part to be fabricated. Part size involves several parameters such as layer resolution, XY resolution, and overall irradiated area. The irradiated area

depends on the imaging systems. The imaging system also limits the spatial resolution in the XY dimensions, that is, the smallest feature achievable in the XY-axes. The DMD mounting angle has some effect on the XY resolution also. All of these aspects are discussed in the following subsections.

9.3.1 Part Size Requirements

9.3.1.1 Layer Thickness and Lateral Resolution

Layer resolution in the Z-axis has been mentioned previously in chapter 1 as being between 0.01mm to 0.25mm for commercial SLA machines. 0.25mm creates a fairly coarse surface for medium sized parts, but for larger models, the layer steps are not too noticeable due to the relative size of larger parts. A resolution of 0.1mm provides a more favourable surface finish for medium and small parts. The design of the elevator mechanism is adjustable manually on a threaded rod, so this allows for experimental tests to find the best resolution for layer step size. As (Hadipoespito & Li, 2005) found, minimum layer thickness is limited by the mechanism of the Z-stage (elevator and build platform). An arc lamp takes longer to cure thicker layers, so it would be of interest to observe the difference in cure time.

The theoretical lateral resolution of the commercial SLA Viper system is roughly the width of the laser beam (0.250±0.025mm) if the effects of over absorption are ignored. The practical lateral resolution achievable however is 0.4mm in the X- and Y-axes. This size allows for the resin to polymerise enough to form adequate structural stability. Solidification of the resin at smaller resolutions than 0.4mm merely floats away in the vat. The Perfactory system by Envisiontec has a pixel size resolution of 0.148mm for a projected area of 190mm x 152mm. The official 2007 Perfactory release now has a pixel resolution of 0.125mm for a smaller projected area of 175mm x 131mm (EnvisionTec, 2007). Therefore a realistic lateral resolution to aim for is anywhere between 0.15-0.25mm for large projected areas.

As reported in the literature review, Sun et al (2005) studied spatial resolution. Spatial resolution is important to the optical imaging as it determines how close two features can be resolved as unique. The minimum resolution is given by using the Rayleigh criterion to find the diffraction limit which is discussed in section 5.4.5.

9.3.1.2 Image Size, Object Size, Field Angle and Focal Length

The image size relates to the desired field angle of the lens. Objective 4 (Section 1.1) of this thesis stated that a field of exposure of 270mm x 200mm is required for

large parts. Lenses with specified focal length are found in the Edmond Optics catalogue to work out some calculations. A good place to start would be the imaging lens that (Limaye, 2004) used. Limaye used a double convex lens with a focal length of 25.4mm. Limaye chose this lens based on the spatial constraints imposed by the system. Ultimately the decision was based on magnification required, the sum of the image and object distances by the object-image relation because of light intensity constraints. Therefore, this section explores the desired magnification and finds the object to image distances.

The size of the object, which is the DMD, to be projected can be calculated. The DMD from an InFocus LP400 projector is used for the project. The user manual for the projector claims a resolution of 800 x 600. However, DMD around the time of the projector were manufactured with a resolution of 848 x 600 micromirrors each having a pitch of 17µm (Douglass, 1998). Each micromirror is 16µm wide with a 1µm gap separating each mirror. This works out to the following dimensions:

X = 848 x 0.017mm = 14.4mm

Y = 600 x 0.017mm = 10.2mm

The required magnification can be calculated using the dimensions of the object and desired image size. Then by the object-image relation from Section 5.2, the required focal length is given. Once the focal length is found, the equation for field of view ((5.41) is complete.

Calculation of magnification (using largest dimension):

$$\frac{270\text{mm}}{14.4\text{mm}} = 18.75$$

Thus, the smaller dimension of in projected image is:

$$18.75 \times 10.2\text{mm} = 191.25\text{mm}$$

The projected image becomes 200mm x 191.25mm. The resulting pixel resolution is 16µm x 18.75 = 0.30mm. This resolution roughly agrees with the target resolution of 0.25mm stated in Section 9.3.1.1. Now, by the object-image relation, the total object-to-image distance can be found in terms of the focal length where s = object, s' = image and M = 18.75 $\Rightarrow$ s = s'/18.75:

$$\frac{1}{f} = \frac{1}{s} + \frac{1}{s'}$$

$$\frac{1}{f} = \frac{18.75}{s'} + \frac{1}{s'}$$

$$\frac{1}{f} = \frac{19.75}{s'}$$

$$s' = 19.75f$$

$$\therefore s = \frac{19.75f}{18.75} = 1.053f$$

$$s + s' = 1.053f + 19.75f$$

$$s + s' = 20.803f$$

The value of the object-to-image distance is dependant on several design requirements. For this research, the main requirement is image size, however, in order to make the layer curing times practical, the light intensity reaching the resin surface ultimately becomes the major design constraint. As it will be observed in the experimental chapter (Section 10.2), practical curing times of under a minute for the 270W projector lamp occur at distances less than 250mm above the resin surface. So for an example, the imaging lens that Limaye used had an effective focal length (EFL) of 25.4mm. This results in an object-to-image distance of 20.803 x 25.4mm = 528.4mm which is far too long for practical layer curing times.

Replacement of the light source with a higher wattage lamp is one option, but the cost for a lamp and power supply varies between $3,000 to $5000, which is outside the budget for this research. Another option would be to acquire a lens with a smaller focal length, but suitable lens specifications are not possible with the off-the-shelf lenses available. The best alternative is to reduce the magnification of the imaging system, and hence the image and pixel size, to a suitable object-to-image distance around 250mm. The change in image size will not effect to overall goal of the SLA which is to compare actual layer curing with the predicted cure from the mathematical model.

At a resolution of 0.15mm per pixel, the resulting magnification is 150µm/16µm = 9.375. Using the object-image relation as before where s = object, s' = image and M = 9.375 $\Rightarrow$ s = s'/9.375:

$$\frac{1}{f} = \frac{1}{s} + \frac{1}{s'}$$

$$\frac{1}{f} = \frac{10.375}{s'}$$

$$s' = 10.375f$$

$$\therefore s = \frac{10.375f}{9.375} = 1.107f$$

$$s + s' = 11.482f$$

If the same 25.4mm focal length lens is used, the object-to-image distance is 11.482 x 25.4mm = 291.63mm. So, for a resolution of 0.15mm per pixel the object-to-image distance is not acceptable. An even lower resolution is considered in the interest of quicker curing times. Below is the calculation for a 0.1mm resolution. The magnification is 100µm/16µm = 6.25 $\Rightarrow$ s = s'/6.25:

$$\frac{1}{f} = \frac{1}{s} + \frac{1}{s'}$$

$$\frac{1}{f} = \frac{7.25}{s'}$$

$$s' = 7.25f$$

$$\therefore s = \frac{7.25f}{6.25} = 1.16f$$

$$s + s' = 8.41f$$

Now, for the 25.4mm focal length lens, the object-to-image distance is 8.41 x 25.4mm = 213.61mm which would yield more practical layer curing times. At this resolution, the projected image size becomes:

X = 6.25 x 14.4mm = 90.00mm

Y = 6.25 x 10.2mm = 63.75mm

The field of view can now be calculated using (5.41. First, the diagonal of the projected image is found so that the diagonal field of view is obtained.

$$d = \sqrt{90.00^2 + 63.75^2}$$

$$d = 110.29\text{mm}$$

$$\alpha = 2\tan^{-1}\left(\frac{d}{2f}\right)$$

$$\alpha = 2\tan^{-1}\left(\frac{110.29}{2(25.4)}\right)$$

$$\alpha = 130.5^\circ$$

A diagonal field of view of 130.5° falls into the class of an ultra wide angle lens. This diagonal field of view implies that the focal length is quite short for the task and therefore, the image will suffer from severe aberration and distortion effects. The use of a single double convex lens in this case results in poor image quality. A high

f/number must be achieved which ultimately means a very small aperture and field of view. However, the f/number is very small because the focal length is nearly the same as the clear aperture of the lens. Limaye (2004) permitted using this particular lens because only a very small portion through the centre of the lens was utilised, limiting the effects of aberrations.

Due to the amount of aberrations inherent with implementing a single lens, a multi-element lens needs to be investigated to improve the image quality. The next logical step is a Cooke triplet because it involves only three lenses whose design specifications can be achieved from off-the-shelf lenses. The Cooke triplet allows for optimisation of third-order aberrations (coma, astigmatism, distortion, field curvature) and focal length. However, the design limits of the Cooke triplet are low f/numbers around f/1.5 and fields of view around 30° as discussed in Section 5.5.5. Putting a field of view of 30° into (5.41 to find the require focal length gives a focal length of 205.80mm. This focal length implies an f/number of f/10.7 (using 19.2mm as the clear aperture diameter) and an object-to-image distance of over 1.7m! Obviously, this is not suitable for the irradiation intensity at such a long object-to-image distance.

In order to test how well a Cooke triplet will work for the SLA imaging system, optical software is necessary. There are a few software packages, such as ZEMAX and OSLO, available that offer free download and access to a few modelling features. The optical software used for the optical analysis of the Cooke triplet is OSLO-EDU 6.4.3 by Lambda Research Corporation. The software is restricted to modelling ten surfaces or less which is adequate for modelling the lens assembly.

Three different Cooke triplet arrangements were analysed using off-the-shelf lens specifications by Edmund Optics. Each arrangement was modelled and adjusted to find the effective focal length, optimal and approximate image size and spacing distances. The analysis sheets of both lens setups are given in Appendix F: Cooke Triplet simulations. The analysis shows the lens data, optical layout, ray-intercept curves, distortion plot and radial energy distribution. The beam input is slightly diverging and the wavelength tested is 354nm.

The first arrangement has an effective focal length of 26.43mm and an approximate image diagonal of 100mm. The best ray-intercept curve occurs at an image distance of 210mm from the last lens surface. Substituting the focal length of 26.43mm into the calculation for 0.1mm resolution, the object-to-image distance becomes 191.62mm, which is good for the light intensity. However, the field of view

calculates to 124° which means the triplet will suffer from severe degrees of coma and astigmatism off the optical axis. The distortion is roughly 4% at 10mm from the optical axis (see Appendix F: Cooke Triplet simulations distortion plots). The f/number is f/1.38 which is lower that f/1.5 so the spherical aberration will have significant effect (note that the clear aperture is 19.2mm to account for the lens mounting rings).

The second Cooke triplet arrangement uses a negative element with a smaller diameter to reduce the clear aperture and thus creates a lower field of view and higher f/number. The effective focal length of the lens is 49.13mm which makes the f/number = f/4.86 (note that the clear aperture is 10.1mm due to the mounting ring of the 12.7mm diameter negative element lens). Distortion is about 0.5% at 10mm from the optical axis which is better than the previous Cooke triplet. However, the distortion is grows more to just over 6% out at 25mm from the optical axis. The performance is optimum at a distance of 200mm from the last lens surface and results in an image diagonal of about 46mm. Therefore, the field of view is calculated to be 50°. This field of view is still fairly wide so bad levels of coma and astigmatism will occur off the optical axis for this Cooke triplet. But the major disadvantage is that the object-to-image distance is 306.6mm which is too great a distance for practical curing times.

The final arrangement aims to create better performance with 25.4mm lens set by varying the spacing between the lenses. The best ray-intercept curve occurs at an image distance of 179mm from the last lens surface when the effective focal length is 29.53mm. The approximate image diagonal is 200mm. The object-to-image distance for 0.1mm resolution is 248.35mm which is just within the limit required for the light intensity. However, the field of view calculates to 147° which means the triplet will suffer from severe degrees of coma and astigmatism off the optical axis. The effects caused by wide field of view can be minimised by using only a portion of the image diagonal. The distortion peaks at roughly 3.5% for distances ≥5mm from the optical axis (see Appendix F: Cooke Triplet simulations distortion plots). An advantage of this arrangement is that the f/number is f/1.54 which reduces the impact of spherical aberration.

Cooke Triplet	Pros	Cons
First Arrangement	Short focal length Good object-to-image distance Good image size	Large field of view Small f/number Severe aberrations Bad distortion
Second Arrangement	Good f/number Better quality of image	Field of view too large Large focal length Small image size Object-to-image distance too great Bad aberrations Bad distortion
Third Arrangement	Highest f/number Acceptable object-to-image distance Good image size Smallest distortion	Field of view too large

Table 9.5 Comparison of the three Cooke triplet arrangements.

Table 9.5 shows the pros and cons of each Cooke triplet. From the comparison the first and third arrangements are the best choices. The third arrangement is the better of the two as it best satisfies the image size objective and object-to-image distance requirements. The third arrangement provides less distortion and spherical aberration than the first triplet. The seconded arrangement is good because of the improved image quality at the expense of image size. The major disadvantage is that the object-to-image distance does not provide practical curing times. Thus, the best choice of imaging system is the third arrangement. This imaging assembly is the one selected in Concept 2.

The Cooke triplet selected is composed of three fused silica lenses. Fused silica material transmits 350-360nm UV light at slightly more than 90% and has a refractive index of 1.45848 (Edmund Optics Inc, 2007). The two outside lenses are plano-convex lenses with the convex surfaces positioned facing opposite to each other. The middle lens is a double concave lens. The cost of these three lenses is roughly $NZ600.

9.3.2 Build Platform, Elevator Mechanism and Vat Size

The build platform has to be large enough to support the irradiated area. From the arrangement of the third Cooke triplet, the image diagonal is about 200mm. However, to minimise the effects of coma and astigmatism from the ultra large field of view, the useable image size is roughly 80mm x 60mm (roughly half the image diagonal). So the build platform dimensions of 100mm x 80mm will be sufficient.

Build platforms on the commercial SLA Viper 250 system have several hundred holes machined into the build platform. These holes allow for the resin to flow readily on to the build platform. The build platform for the SLA design is a piece of Perspex with an array of holes drilled in to it.

The elevator mechanism found for the project is an old camera bellows. The bellows is the Asahi Pentax K series auto bellows. It achieves motion by turning a plastic helical gear on a linear track. It has a linear travel of about 140mm. Stable motion of the build platform in the vertical direction is achieved by mounting an aluminium extrusion to the bellows. The mounting of the extrusion allows 45mm of travel for the build platform in to the resin from the very top of the vat. This is enough to build 30mm high parts as stated in the performance specification list (Table 9.4). A CAD drawing of the elevator mechanism and build platform is shown in Figure 9.8. The build platform will be held in place by pins or clamps so that it does not move during the build process.

The helical gear of the bellows has backlash associated with it. The backlash occurs because the teeth of the gear do not mesh together perfectly. The backlash is most noticeable whenever there is a direction change in gear rotation. To account for the backlash, tension must always be applied against the natural forces trying to push the elevator down. The deep-dip method serves this purpose well. The platform is “dipped” down into the resin and then raises it up to the new layer position without backlash as long as the new layer position is not passed. To ensure correct layer position, a 150mm micrometer is mounted to the elevator to increment and measure any Z-axis movement for the next new layer step.

Levelling is achieved by the deep-dip method. This is the most suitable method for the SLA design because it is simple to implement, requires no additional components, and satisfies the design objectives. The only disadvantage is the natural waiting time for the resin to settle itself.

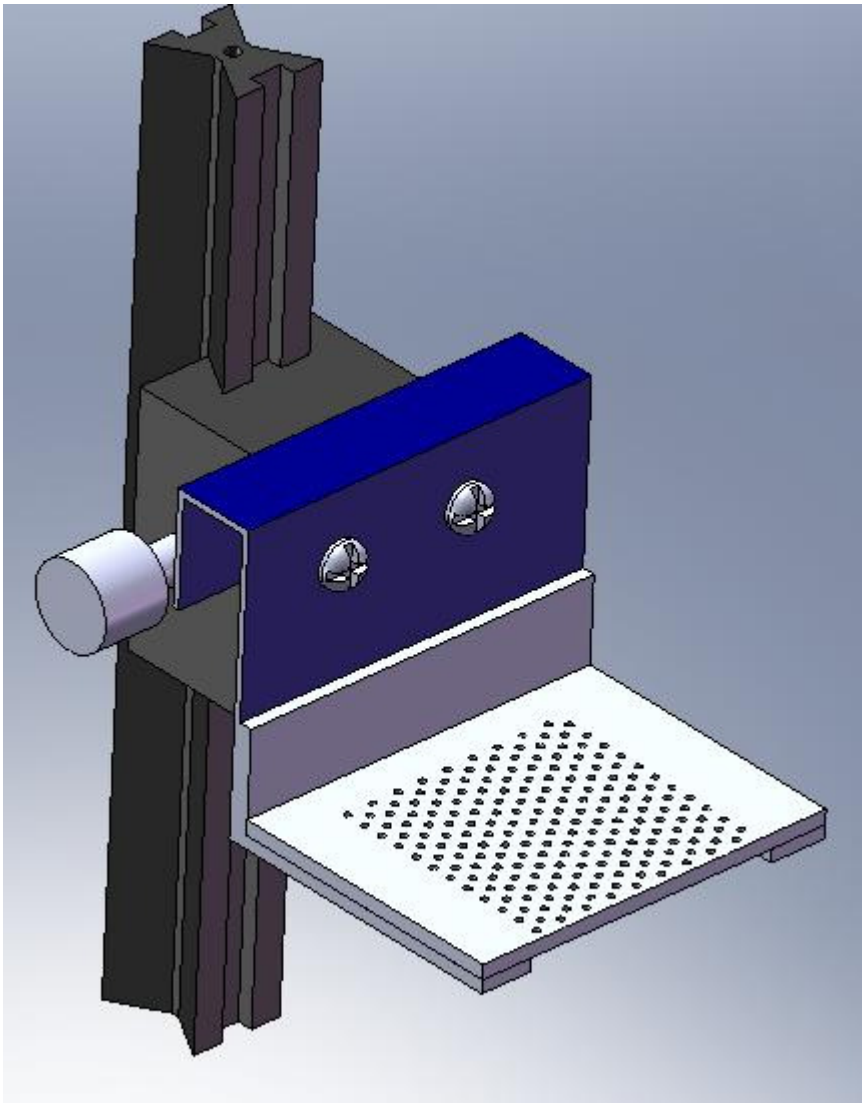

Figure 9.8 CAD drawing of elevator mechanism and build platform.

The working distance control and elevator mechanism is chosen from Concept 1 as the method to achieve the fabrication of layers. M10 threaded rods are easy to source and implement than ball screws or power screws. The vat and working distance will not have to be adjusted very often once set in position.

9.3.3 The DMD Mounting

The DMD mounting at 45° has two aspects to consider. Firstly, the mounting of the DMD has to account for the 10° tilt of the micromirrors. When the micromirrors are switched on, each individual micromirror must be at a 45° to the horizontal axis (Y-axis). So the mounting of the DMD at 45° is not an accurate description of the DMD mounting. Secondly, the two dimensional profile that is reflected toward the resin surface should be considered because this affects the pixel shape.

The first aspect was analysed by (Limaye, 2004). He found that because the micromirrors tilt on their diagonals, the DMD must be mounted at 45° to the horizontal axis (Y-axis) and then rotated 10° about its diagonal to account for the 10° switching of the micromirrors when are switched on to reflect the light on toward the resin. The angle made by the DMD is split up in to its X- and Y-axis component angles.

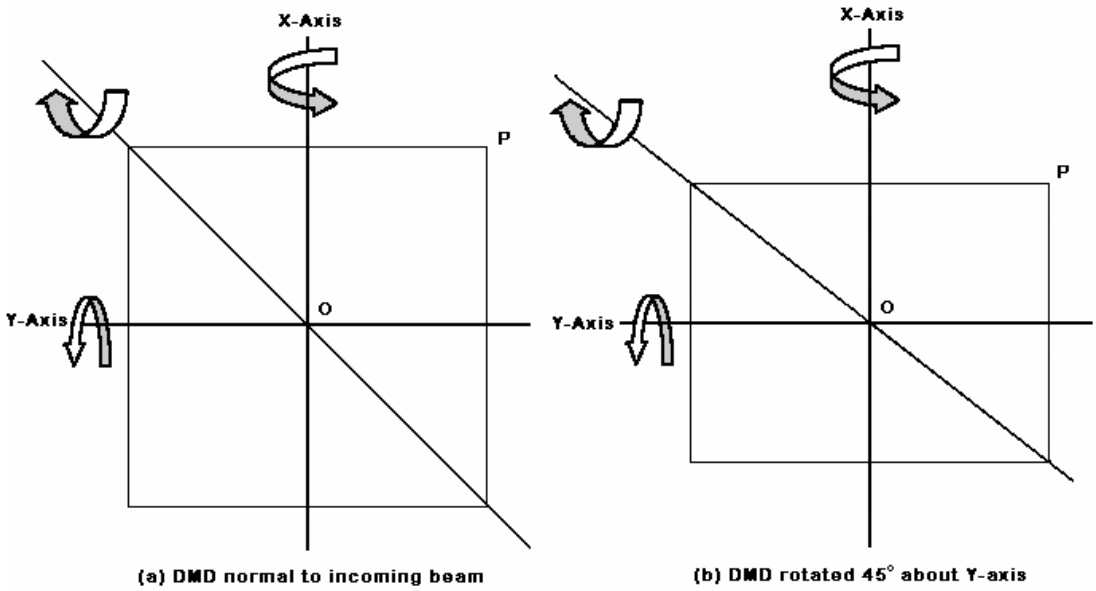

Figure 9.9 Calculating the angle of the DMD into X- and Y-axis components

The component angles are calculated by using some trigonometry. Figure 9.9a shows the DMD as if it were mounted with the mirrors normal to the incoming beam. An assumption is that the DMD is square rather that rectangular for example, using 800 x 800 pixels instead of 800 x 600 pixels. Consider point 'P' on the corner of the DMD in Figure 9.9b which has been rotated 45° about the Y-axis. Notice that the profile of the DMD has become rectangular if looking at DMD along the optical axis. Now the X- and Y-axis components of point P must be determined caused by the 10° rotation about the diagonal. In Figure 9.9a, let each side of the square be of length *d*. The diagonal from corner to corner, through the centre 'O', becomes $d\sqrt{2}$. The distance from the centre 'O' to point P is $d\sqrt{2}/2 = d/\sqrt{2}$. Thus a rotation of 10° about the diagonal axis results in point P being moved by $d/\sqrt{2}\sin 10°$. This value equals the combined X and Y component rotations. Because the DMD is a square, both the X and Y rotations are the same value except the Y-axis rotation is offset by 45°. Let α be the angle that each axis must be rotated. So the expression for the

amount point P moves in each X- and Y-axis is $(d/2)\sin\alpha$. The angle α is found by the following calculation:

$$2\left(\frac{d}{2}\right)\sin\alpha = \frac{d}{\sqrt{2}}\sin 10^\circ$$

$$\sin\alpha = \frac{1}{\sqrt{2}}\sin 10^\circ$$

$$\alpha = \sin^{-1}\left(\frac{1}{\sqrt{2}}\sin 10^\circ\right)$$

$$\alpha = 7.05^\circ$$

(9.1)

Thus, the angle made by the DMD about X-axis is 7.05°. The angle with the Y-axis is 45° + 7.05° = 52.05°.

When the DMD is rotated 45° about the Y-axis (Figure 9.9b), the DMD's projected area is reduced a factor that is the cosine of the angle made with the optical axis (as discussed in Section 5.1.1). The profile also changes slightly if the 10° diagonal rotation is included. The resulting profile of the DMD projected on the resin surface is shown in Figure 9.10. The figure is a SolidWorks drawing of the projected sketches (toward the resin surface) of the DMD rotated 45° about the Y-axis and the DMD at 10° rotation about the 45° diagonal. It can be seen that there is a 0.55° profile change in the X-axis and a greater change of 4.69° in the Y-axis. It should be noted that the dimensions of the projected profile are for parallel rays reflected off the DMD at 45° and is not an indication of dimensional size on the resin surface. Figure 9.10 shows the profile is before it passes through the imaging optics and indicates the image will be slightly twisted.

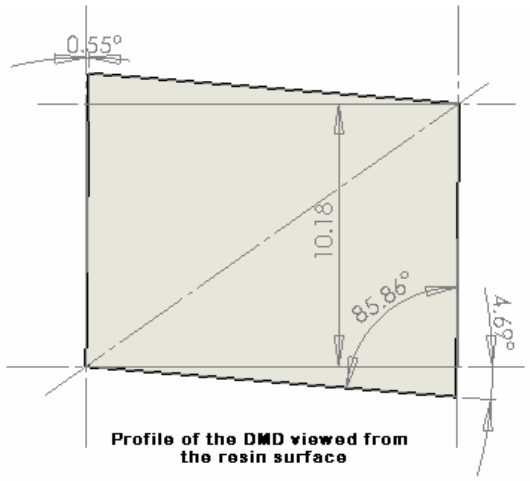

Figure 9.10 The projected DMD profile on the resin surface incorporating the 45° rotation about the Y-axis and 10° diagonal rotation.

9.3.4 Light Source

The preferred light source for the SLA is a high pressure mercury lamp. Costing enquires into adequate powered lamps from Newport Optics Ltd and New Zealand Lamp Specialists Ltd proved that purchasing a lamp system exceeded the project budget. Newport Optics quoted around $12,700NZ for lamp and power supply and Lamp Specialist $2,235NZ for the power supply and $687NZ for the lamp. UV tubes were not researched in depth as the use of a point source seemed easier to apply from a theory perceptive and more practical from a light conditioning point of view. Thus, Concept 1 (on page 142) depicts the light source that is to be used for the SLA.

The projector donated for the project has a 270W metal halide lamp. From simple experiments (see Section 10.2), the lamp provides enough broad spectrum light to cure the photopolymer resin.

The power supply for the lamp is provided with the electronics that came with the projector. The lamp housing incorporates an elliptical reflector, a temperature sensor to protect the life of the lamp and a cooling fan. Figure 9.11 and Figure 9.12 show the hardware layout of the projector with the covers removed.

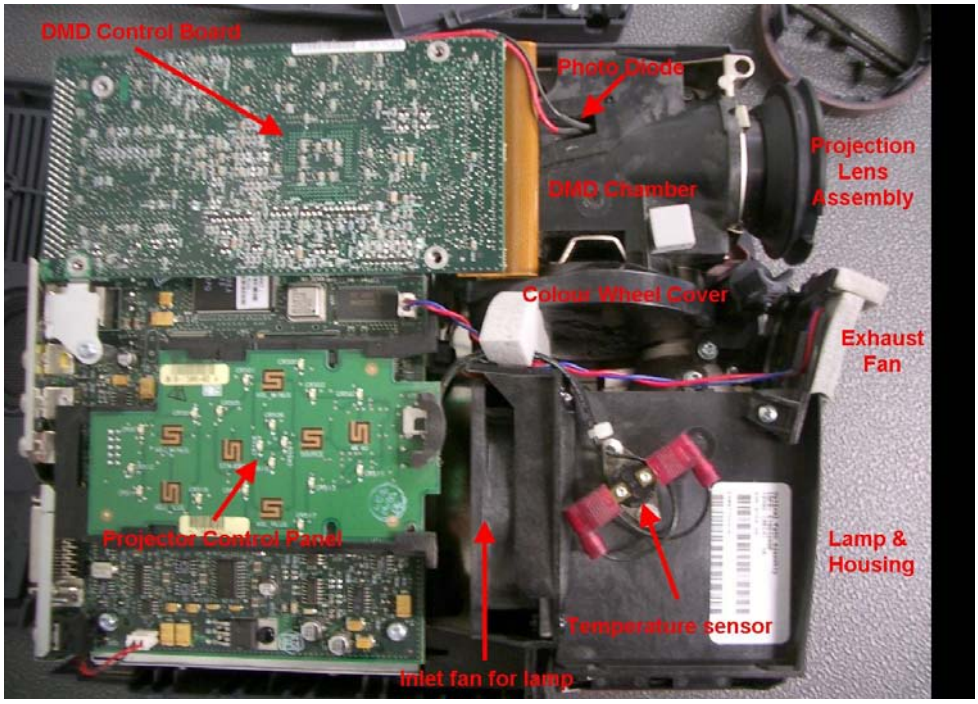

Figure 9.11 Top view of the projector hardware layout.

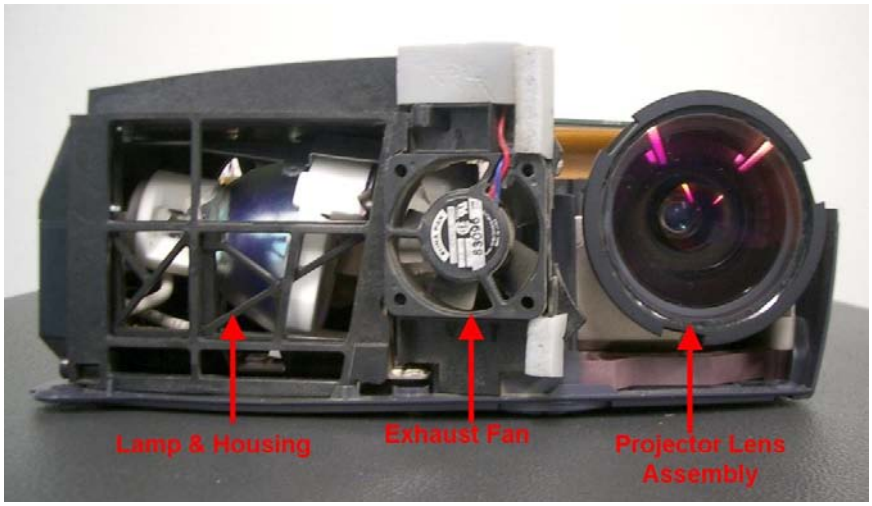

Figure 9.12 Front view of the projector shown the lamp housing, exhaust fan and projector lens assembly.

The lamp and its housing need to be separated from the projector to bring it inline with the DMD and to direct the air from the projector fans away from the resin and build chamber. The lamp also needs an enclosure because the cooling of the lamp when it was mounted in the InFocus projector relied on the inlet fan and exhaust fan moving a certain volume of air to keep the lamp at operating temperatures.

9.3.5 Beam Conditioning

Due to using the lamp option of Concept 1, the beam conditioning of Concept 1 is the more likely candidate for the SLA. The lamp housing incorporates several beam shaping and conditioning lenses. The lamp has an elliptical reflector that collects the

light emitted in the wrong direction and refocuses it in front of the source. The light is focused at a short focal length into an aspheric lens. The beam is then shaped further through a trapezoidal aperture. Two collimating lenses collimate the light into a beam with a 20° half cone angle. Figure 9.13 is a lens diagram of the lenses in the beam conditioning system for the projector simulated with OSLO optical design software. The diagram shows that rays are highly collimated onto the DMD for a 10° half cone angle. The middle two collimating lenses also redirect the beam slightly at an angle. The angle was manufactured into the original InFocus projector design because of space requirements. Finally the last lens focuses the beam onto the DMD.

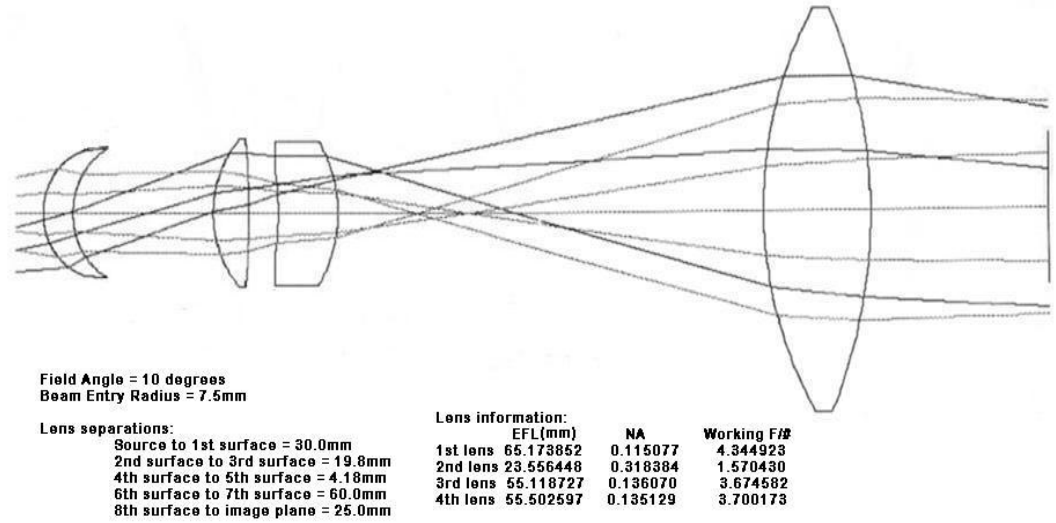

Figure 9.13 Lens Diagram for the original projector beam conditioning system.

Replacement beam conditioning systems were investigated due to several drawbacks of the projectors conditioning system. One of the purposes of the beam conditioning system for the SLA is to create a uniform distribution across the beam. The angle created by the last two collimating lenses distorts the beam profile and beam intensity preventing beam uniformity. Secondly, the lenses have an anti-reflection coating on them that does not readily transmit UV light. Removal of the anti-reflection coating can improve UV transmission. Also, the 20° half cone angle could be reduced to utilise more of the power output from the source. And finally, the conditioning system needs to filter the visible and infrared content of the beam before it reaches the DMD. Infrared light contains a lot of heat which could damage the micromirrors. And unnecessary wavelengths cause inaccurate dimensions in the cured part.

Investigations into the fused silica lenses proved that out of the off-the-shelf aspheric lenses, there was no suitable match for the necessary beam size. Simulated

lens combinations using the OSLO software could not better the collimation of the beam created by the existing projector collimation design. Also, the non-uniformity of the beam profile is not critical to the overall goal of the project as it is proposed that the DMD is capable of accounting for beam non-uniformity by using modulated bitmaps to vary the intensity reflected by a micromirror. Therefore, the existing collimation system is used to for beam conditioning with modifications to filtering and removal of the anti-reflection coating from the lenses.

9.3.6 Detailed Design

The final design of the SLA is shown in the CAD image below (Figure 9.14). The design incorporates working distance adjustment, lamp intensity adjustment, levelling of the imaging plane and UV protective shielding for the operator. Figure 9.15 is a photograph of the final SLA construction. The structure is predominately made from aluminium for rigidity. The following is a list of specific feature details:

Build platform size: 100mm x 80mm

Resolution:

DMD: 800 x 600 pixels (17µm pitch/micromirror)

Image: 400 x 400 pixels

Layer: 0.01mm

Lateral: 0.1mm (theoretical)

SLA overall dimensions: 600mm x 400mm x 710mm

Object-to-image distance: 248.35mm

Field of View: 147°

F-number: 1.54

Lamp: 270W metal halide

Beam Divergence: 20° ± 2°

Power at resin surface: 8mW/cm^2 - 25mW/cm^2

Filter: Edmond Optics NT46-085 360nm narrow band filter

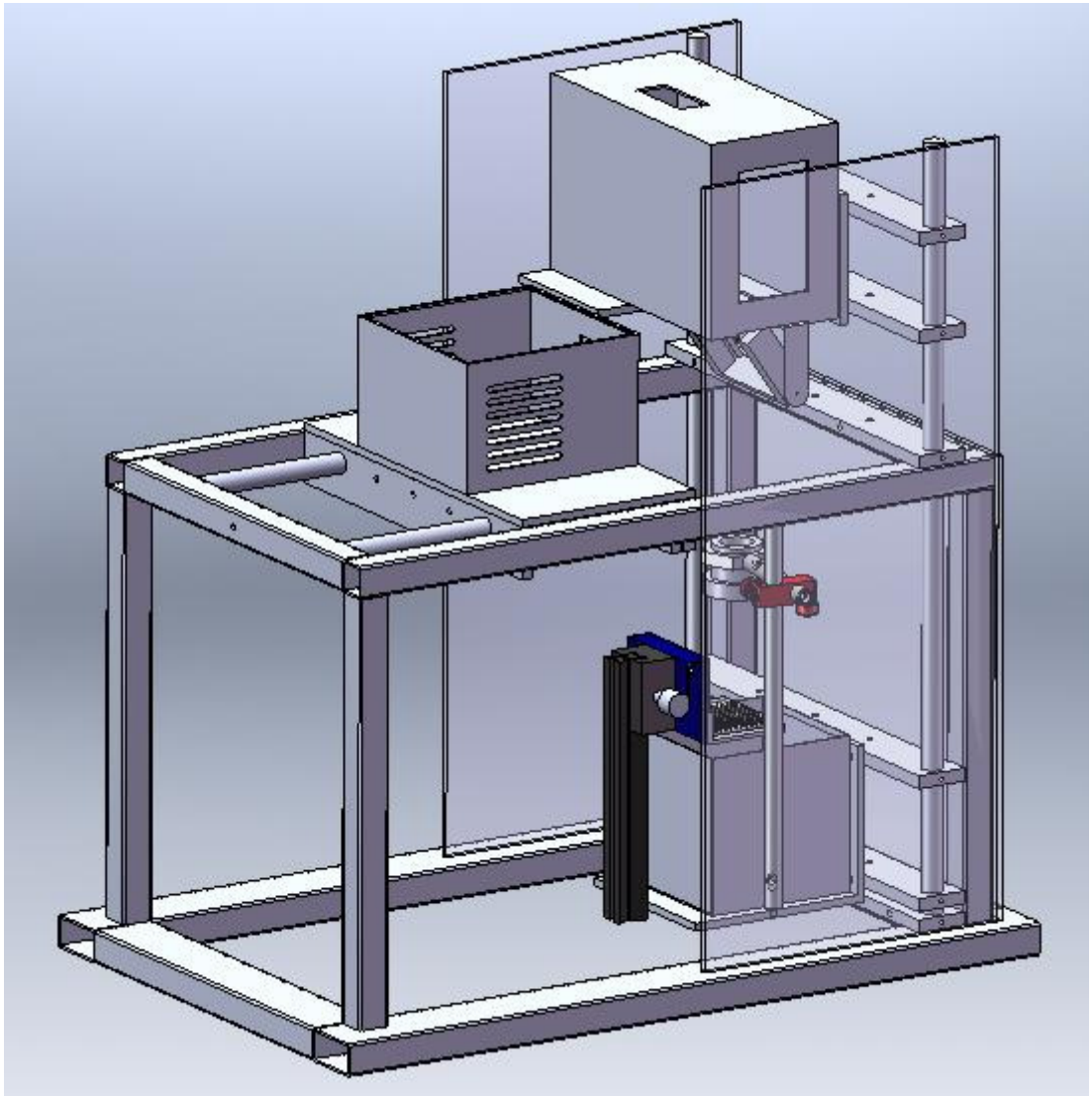

Figure 9.14 CAD rendering of the final SLA design.

Figure 9.15 Final SLA construction.

There are several small changes to the final construction that differ from the CAD design. The issues that were attended to were the aluminium boxes for housing the lamp and the projector, the mounting bracket for holding the DMD, adjustable legs for the main frame and additional spacers to prevent “chatting” for the elevator and projector levels. The design of the boxes was simplified to accommodate for the lamp and projector in order to make it easier to get the components in and out. The mounting bracket to hold the DMD was rapid prototyped to get the angle exact. The design changes were made to account for these unforeseen issues.

9.4 Summary

In this chapter the Dym & Little (2004) design process has been used to develop the SLA. The objectives and the constraints have been identified. The major functions were established and various means to achieve each function were devised. Two concepts of the SLA have been drafted that present solutions to the SLA design objectives. The modules of each design were expanded upon in the preliminary design stage. Modules were accessed and selected from the two concepts presented. The final detailed design was proposed with exact specification of feature details. The resulting SLA was also presented with a photograph.

The next chapter explains the experiments done on the SLA to prove the thesis hypotheses.

10 Experiments

In this Chapter, experiments are reported that were carried out to confirm or deny the ability of the SLA to cure layers. Preliminary experiments are reported to show the progression of the project understanding. Test layers are analysed in greater detail to observe the uniformity of the cure.

10.1 Adaption of the Projector Electronics

10.1.1 Replacement circuit for the photodiode

One of the first problems encountered with the function of the projector had to do with the colour wheel. When removing the colour wheel from its place in the optical system and unplugging it from the DMD controller board, the electronic protection circuitry prevents the projector from being switched on. If the colour wheel is left plugged in but removed from the path of the optical system, the projector powers up. However, light from the metal halide lamp would not be projected through the final projector lens assembly. The mirrors of the DMD would not switch to the "ON" position, i.e. no light was reflected through the projection lens assembly.

Upon closer inspection of the system, it was noted that there are only two electronic devices incorporated in the light chamber once the collimated light enters. These electronic devices are the DMD and a photodiode mounted between the last focusing lens and the DMD seen here in Figure 10.1.

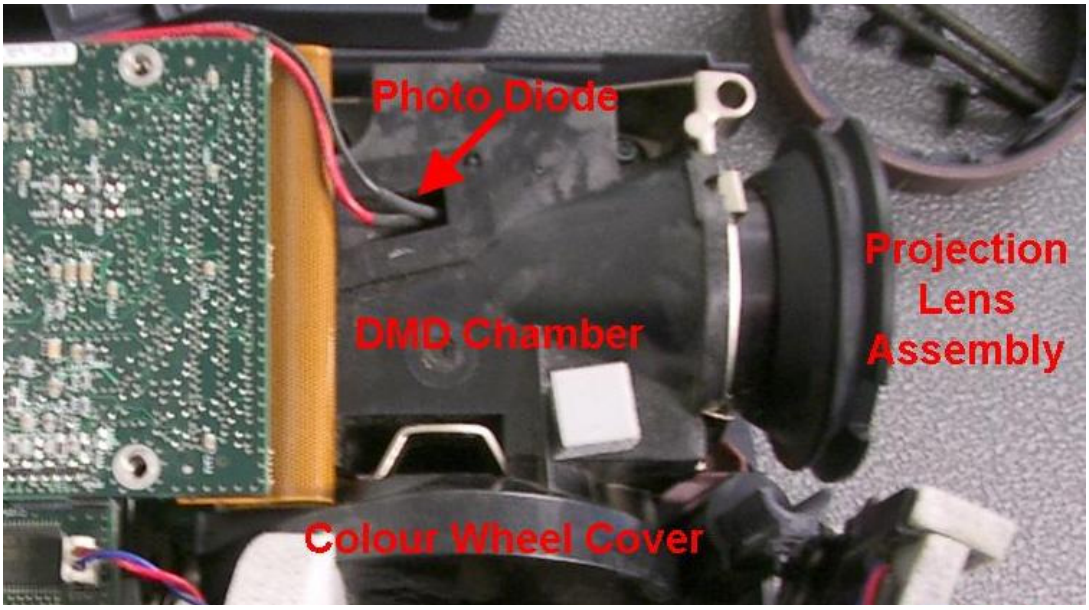

Figure 10.1 Location of the photodiode on the DMD chamber.

The colour wheel has four distinct sections of coloured glass glued onto a stepper motor. Three of the glass sections are used to create colours in the projected image. The last section is a clear piece that is used for the photodiode detection electronics on the DMD control board (see Figure 10.2). The photodiode and associated electronics counts the frequency of the clear glass part of the colour wheel. If the photodiode does not pick up the frequency of the clear glass, the lamp is not started. Using an oscilloscope, the frequency seen by the photodiode in order to allow the lamp to turn on is roughly 60Hz.

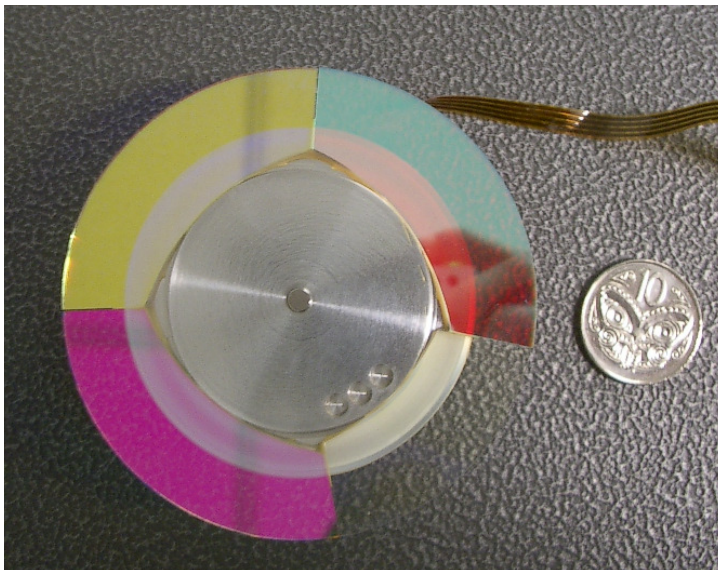

Figure 10.2 The InFocus LP400 colour wheel.

Like most elements of the InFocus projector, the glass on the colour wheel blocks the transmission of UV light. Removing the colour wheel from the optical path leads to the problem of the lamp not switching on because of the incorrect signal on the photodiode. Therefore, a simple replacement circuit for the photodiode signal was devised. The schematic diagram is shown in Figure 10.3.

The replacement circuit incorporates a 555 timer chip to generate the required frequency. The duty cycle is roughly set at 50%. A variable potentiometer is implemented in the design so that the signal output duty cycle can be fine tuned when connected to the control board electronics. The output of the 555 timer is input into an inverter so that the logic levels switch between 0V and 5V. The outputs of the circuit are connected to the cathode and anode inputs of the photodiode.

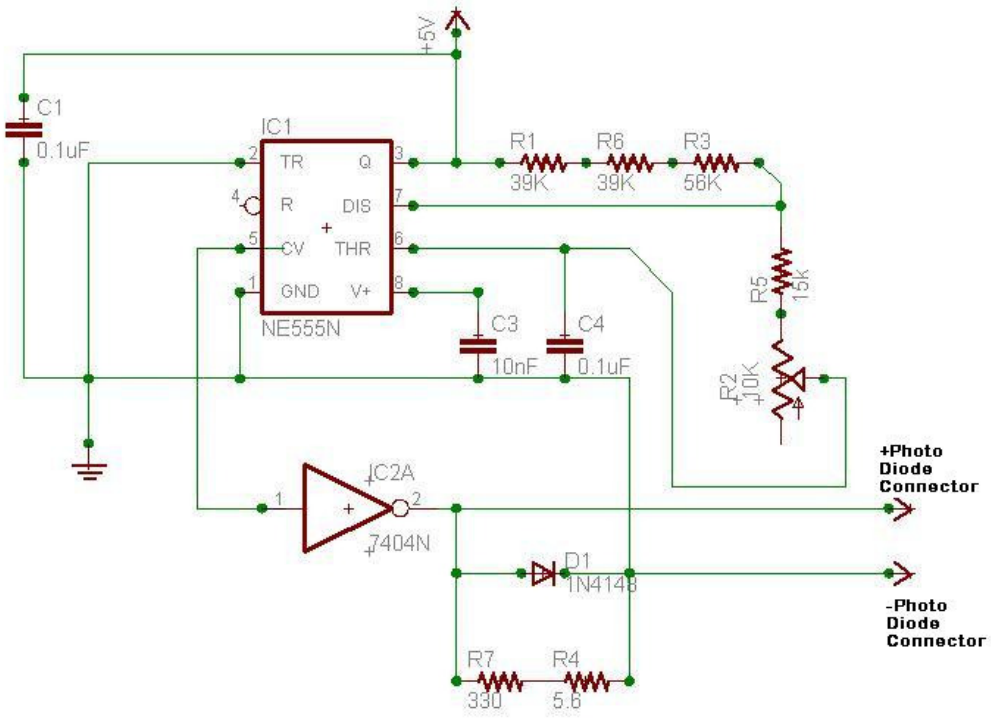

Figure 10.3 Replacement photodiode signal circuit.

10.2 Preliminary Curing Experiments

10.2.1 Testing the projector to cure the photopolymer

Now that the projector functioned with all the exterior housing and colour wheel removed, some preliminary experiments are observed. The distance at which the resin can be cured must be found so that practical curing times are achievable. Firstly, a simple experiment was done to prove whether or not the projector was capable of curing a thin film of photopolymer resin at a distance of approximately one foot or less. The resin was exposed to light from the projector for over two minutes without any reaction starting, i.e. there was no evident thickening of the resin. The experiment proved that the lenses in the projector completely filtered all the wavelengths of useful UV light required to set off the photoinitiators in the photopolymer resin.

The next step in experimentation involved just shining the arc lamp at a film of resin to initiate the cure. This experiment proved successful with the lamp curing the resin after about 60 seconds. A further test was done by observing the effect on curing time when the projector beam collimating lens system was added on. With the collimated output, the photopolymer resin cures readily with exposure times of 20-25 seconds.

10.2.2 Exposure time vs distance for the lamp and collimating lenses

To obtain more quantitative data, a set of experiments were conducted on a simple test rig made from wood. An MDF box was made to house the projector and keep it in place vertically. The box was positioned between a slot that could be setup at one of three set distances from a datum. The resin film was placed at the datum. The three distances from the datum were 100mm, 200mm, and 300mm. A photograph of the test rig is shown in Figure 10.4.

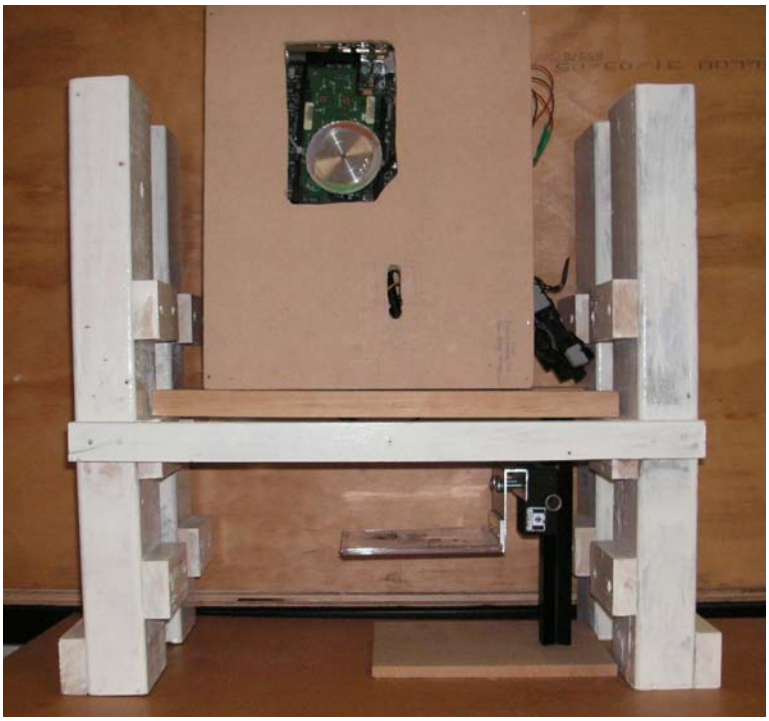

Figure 10.4 Test rig to measure the irradiance at three distances 100mm, 200mm and 300mm.

	Distance from light source (mm)			
	100	200	300	Thickness of sample
Just Metal Halide	7sec	20sec	60sec	0.3-0.8mm
Halide & reflector housing	15sec	30sec	50sec	0.3-0.7mm
Halide & 1st collimating lens	20sec	50sec	No Cure	0.3-0.6mm
1st collimating lens (polished)	15sec	30sec	No Cure	0.3-0.6mm
Halide & 3 collimating lenses	10sec	15sec	25sec	0.3-0.6mm

Table 10.1 Cure times (sec) vs distance (mm) for different arrangements of the collimating system.

Quantitative data was collected for the light irradiating the resin with different parts of the collimation lens system in place. Table 10.1 reports the experimental results. It is interesting to note that removing the anti-reflective coating from the first collimating lens improves the transmission of the required UV wavelengths resulting in faster cure times. It is also noticeable the effect that collimation of the beam has on the curing time of the resin. The exposure time is roughly halved when the light is collimated.

10.2.3 Irradiance measurements of the projector lens system

The next sets of experiments were aimed at finding what elements of the projector lens system limited the light output. Irradiance measurements were taken to find the irradiation output from the DMD and with each lens of the projection assembly added progressively (Figure 10.5). A separate experiment was also done with each element in the system individually (Figure 10.6). The projection assembly incorporates seven lens elements. An ELSEC 763 UV monitor was used for measurements where the irradiance scale was in mW/m^2.

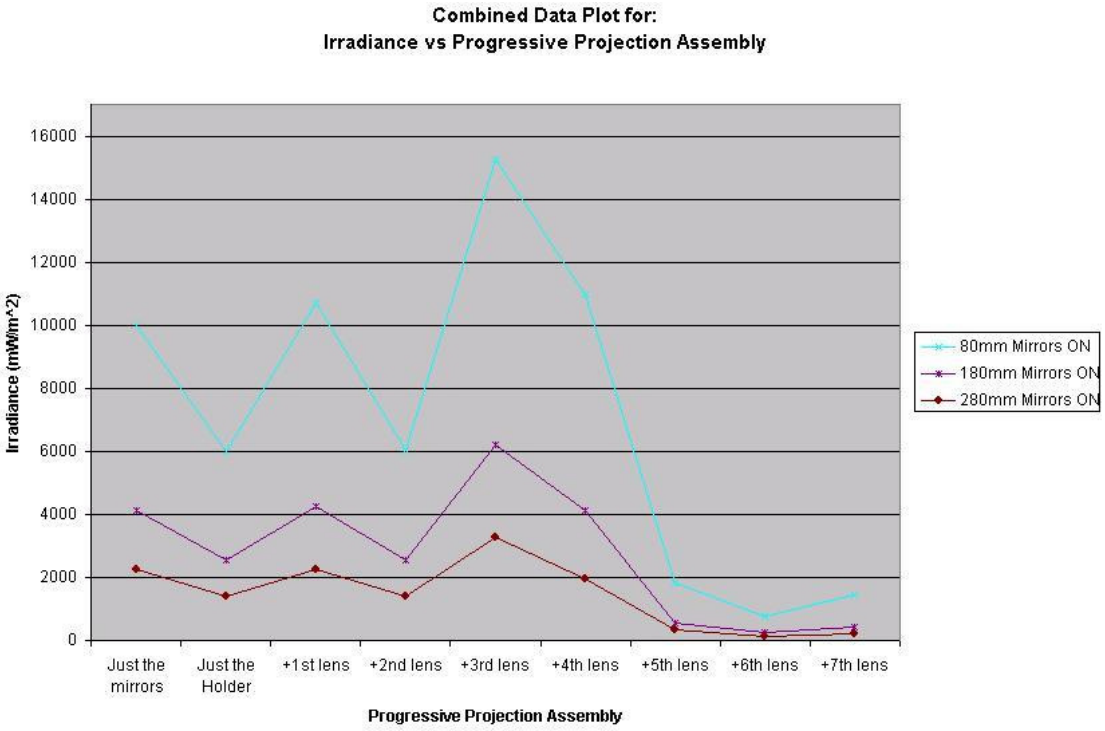

Figure 10.5 Plot of irradiance vs different arrangements of the projection lens assembly.

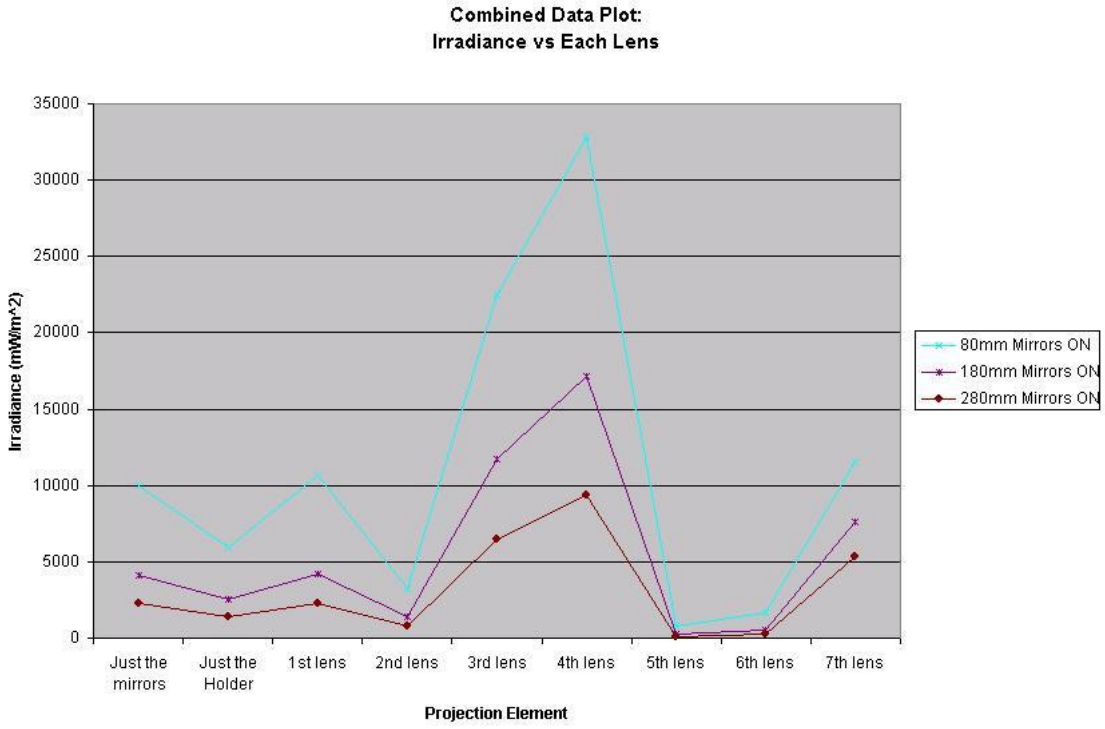

Figure 10.6 Plot of irradiance (mW/m^2) vs each lens individually.

The experiment data shows a large peak in irradiance with the third and fourth lens in place. Unfortunately the light intensity is only about $33W/m^2$ which is still not powerful enough to cure the photopolymer (the resin has an E_c of $9.6mW/cm^2$). The

image is out of focus too. Irradiance drops off with the addition of the fifth and sixth lenses. However, there is a rise in irradiance when the seventh lens is included.

Two conclusions can be deduced from these experiments. Firstly, the amount of lens focusing has an effect on the output irradiance. And secondly, due to the lens material, the lens elements need to be replaced with elements that transmit UV light in the wavelength required to initiate cure in the photopolymer. Fused silica lenses are suitable for this purpose.

10.3 Light Intensity Measurement

In order to obtain the weighting function for the beam intensity profile and the light intensity maximum at the centre of the image on the resin surface, the intensity of light needs to be measured. These two values are necessary for the mathematical model. The method of measurement is detailed in this section for completeness and for comparison in the event that the measurement procedure is improved in future research.

10.3.1 Beam Intensity Profile

The beam profile is measured in order to input the correct data of the light intensity in to the mathematical model. The beam intensity is measured using an Ophir Optronics radiometer where the sensor is moved across the beam diameter. The sensor was 12mm in diameter and was mounted on a slider perpendicular to the beam. The slider and sensor were positioned at the same distance away from the beam at which the DMD is positioned. Measurements are read as the slider is moved at 0.5mm increments. The centre of the beam is then found by setting the peak irradiance as the centre of the beam.

The beam profile data is presented in Table 10.2. The beam data was normalized before a polynomial equation was fit to the curve of the normalized beam profile data.

Reading of the radimeter (W/m^2)	Distance from beam centre (mm)	Normalized Irradiance Distribution
0.930	0.00	1.000
0.930	0.50	0.995
0.930	1.00	0.989
0.925	1.50	0.984
0.920	2.00	0.978
0.915	2.50	0.968
0.910	3.00	0.968
0.900	3.50	0.957
0.900	4.00	0.941
0.890	4.50	0.941
0.875	5.00	0.925
0.875	5.50	0.903
0.860	6.00	0.892
0.840	6.50	0.876
0.830	7.00	0.871
0.815	7.50	0.860
0.810	8.00	0.839
0.800	8.50	0.806
0.780	9.00	0.812
0.750	9.50	0.774
0.755	10.00	0.753
0.720	10.50	0.720

Table 10.2 Beam profile intensity measurements.

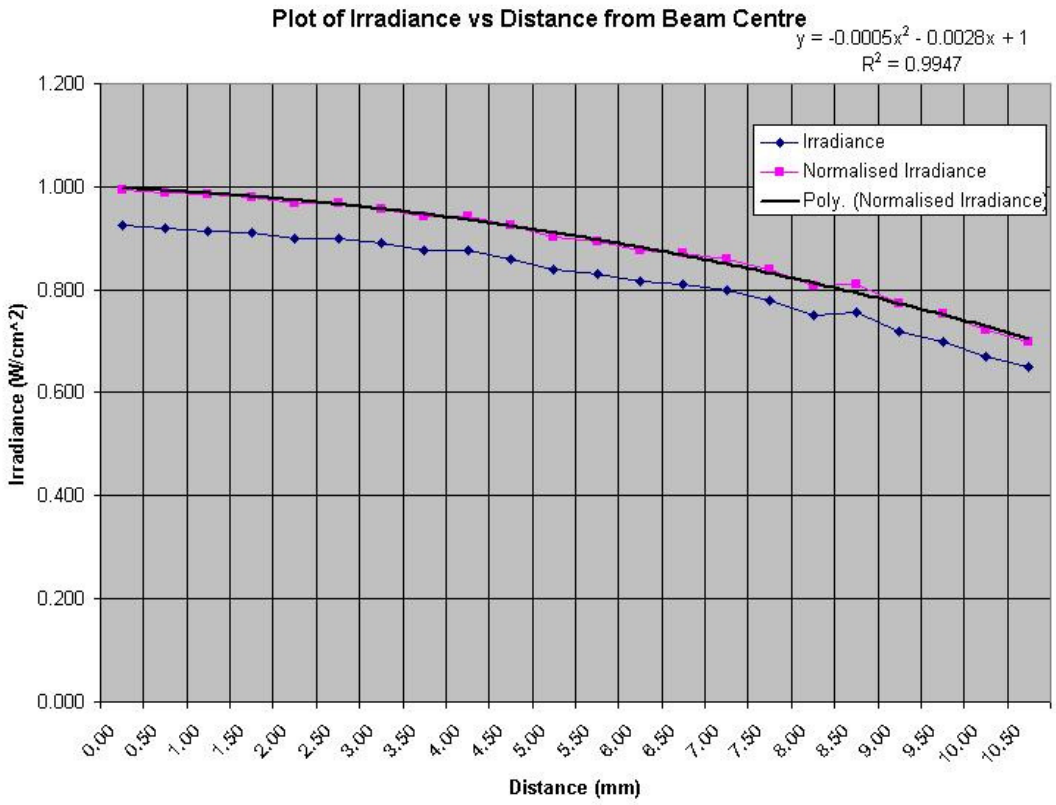

Figure 10.7 Beam Profile Measured Experimentally.

Figure 10.7 shows the plot of the beam profile data. The equation for the irradiance of the beam incident on the DMD is given by (10.1.

$$y = \mathrm{I}_{irr} = 1 - 0.0028x - 0.0005x^2 \tag{10.1}$$

where I_{irr} is the normalized irradiance and x is the radial distance from the centre of the beam incident on the DMD. (10.1 serves as the weighting function in the mathematical model.

10.3.2 Maximum Intensity Measurement

The maximum light intensity is used in the cure depth equation for the layer cure part of the mathematical model. The method of maximum intensity measurement of irradiance for areas larger than the area of the sensor is different than the technique used for microstereolithography. Previous researchers of large integral SLA have failed to specify how the irradiance at the resin surface was measured practically. A simple measurement procedure was adopted for this research work. The sensor plane of the Ophir Optronics radiometer was placed on the elevator of the SLA and set to the required image distance. The irradiance reading was taken as the maximum when the sensor was placed in the centre of the image.

10.4 Uniformity of Cure and Dimensional Accuracy

This section reports the experiments conducted on cured layers made using the SLA. The cross-section of a layer is examined to compare the cure depth of a layer with the cure depth predicted by the mathematical model. Layer compensation using the type of projected image is also examined to explore the effect on the uniformity of cure depth.

The phenomenon at the edge of the layer is analysed. The roundness at the edge of a layer due to Beer-Lambert's Law is measured for different exposure times. The projected image is experimented with to observe any change at the edge of a layer.

The last part of the experiment reproduces the experimental procedure that Limaye used to find the dimensional accuracy and precision of layers. The experiment was reproduced in this thesis work to allow comparison of the improved model with the old model.

10.4.1 Defining Accuracy and Precision

Before presenting the experimental results for the uniformity of cure, the terms accuracy and precision need clarification. Accuracy and precision are often confused terms. They both have two totally different meanings. Accuracy is difficult without good precision. Precision, however, does not ensure accuracy. Precision with calibration results in accuracy (Instron, 2006). Calibration is the ability to reach the desired target value. The interrelationship between accuracy and precision is seen in Figure 10.8.

Accuracy is defined as the "closeness of the agreement between the result of a measurement and a true value" (International Organization for Standardization, 2004). As there is no such thing as a true value, a true value is a value that is assigned as the closest value that is known. Accuracy is often a qualitative term. For example, a group of measurements can be in close agreement and thus can be described as having excellent, good or poor accuracy. However, for accuracy to have scientific meaning, it needs to be quantified.

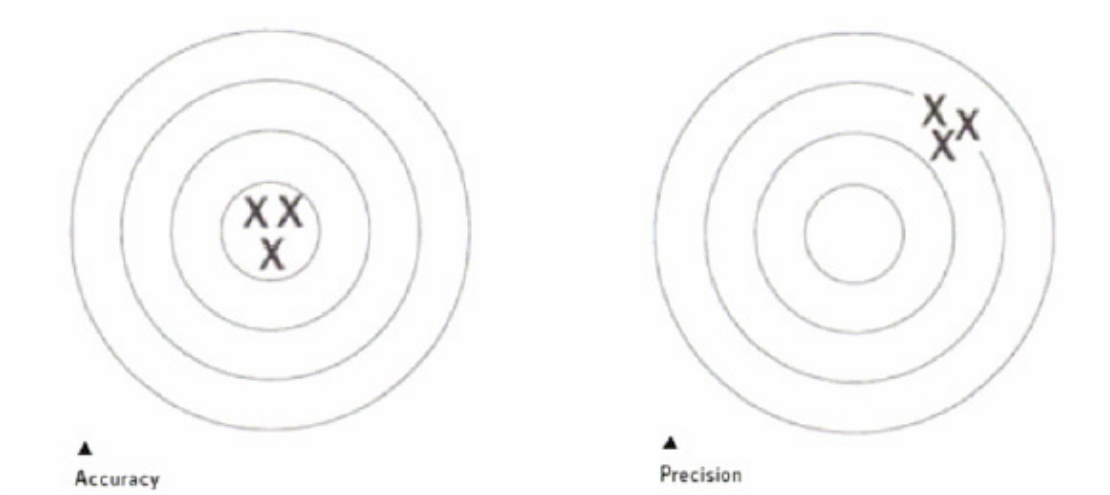

Figure 10.8 The interrelationship of accuracy and precision (Instron, 2006).

In order to quantify accuracy, the term "error" is introduced. The error is the difference between the measured result and the true value. In the case of the simulated arrow shaped bitmap, the error is the difference between the simulated values and the measurements of the cured layers made with the SLA.

Precision is described as how close in agreement a group of results are amongst themselves. It is an indication of the ability of the results to be repeatable within a certain margin of error. The precision characterizes the ability of the SLA to reproduce layers of the same dimension and thickness.

Repeatability and reproducibility have slightly different meanings. Repeatability expresses how close in agreement a group of results are between successive measurements using the same conditions of measurement, whereas reproducibility is repeatability under changing conditions. For example, the conditions of measurement might include the measurement procedure, the observer, the measuring equipment, location, and time. For repeatability, conditions of measurement would be the same. For reproducibility, the conditions of measurement may change (Gaines, 2006).

Quantitatively, precision is given by the deviation of results from the mean value of a set of results. Standard deviation and the arithmetic mean are used to find the precision. In general, most data values lay within a bell shaped curve. The standard deviation (σ) accounts for 63% of all results. Three times the standard deviation ensures that 99% of all results lie between the 3σ.

Error is categorised into random and systematic error. Random error is associated with measurements in that it affects the precision of measurements. A good assessment of random error is given by standard deviation. A way to reduce the effect

of random error is to use more data samples. Statistical analysis of a large number of observations provides a better average of random error.

Systematic error affects the accuracy of results. Systematic error is error that is fixed that can displace or offset measurements by a fixed amount. This form of error is usually introduced by instrumentation and human factors. For example, a measuring instrument that is incorrectly calibrated will be out by a fixed amount for every measurement, or the instrument may be incorrectly used by the experimenter. Many systematic errors can be repeated to a high degree of precision. Good precision does not indicate good accuracy because of systematic error. When setting up an experiment it is important to identify and eliminate or minimize the systematic error. Independent confirmations of experimental results are often required to prove that the same phenomenon is observed. For example, different apparatus at different places may be affected by different systematic effects.

10.4.2 Arrow shaped bitmap

In order to measure the uniformity of cure depth, a suitable bitmap is needed. The bitmap needs a dimension that traverses the maximum distance of both X and Y axes of the projected area, preferably through the centre. The bitmap must also provide a repeatable location to make a suitable cross-sectional cut. The arrow shaped bitmap, used by Limaye (see Figure 10.9), satisfies the above requirements. The data collected using the arrow shaped bitmap also serves well as a comparison with the Limaye's test data.

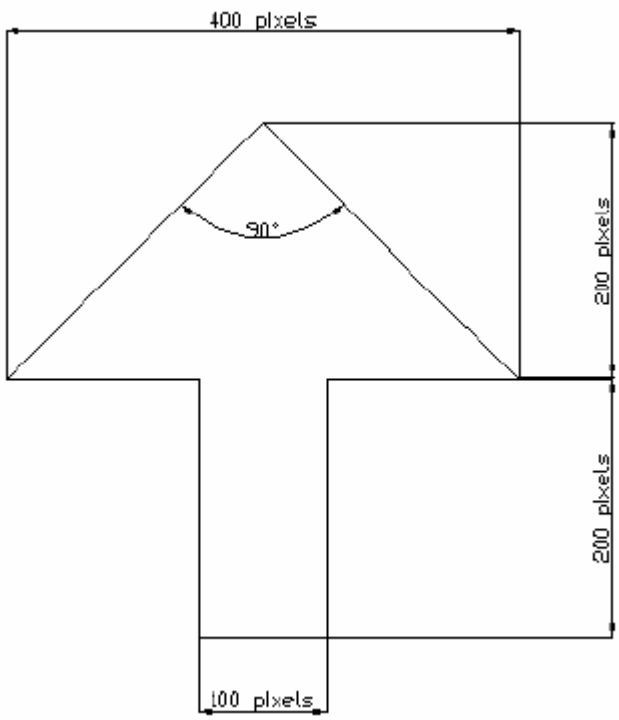

Figure 10.9 Bitmap displayed on the DMD (Limaye, 2004).

10.4.3 Experiments to Find Cure Thickness

In order to observe the uniformity of cure, a total of 12 arrow-shaped layers were cured with the SLA. Three exposure times were found that produced layers that could survive handling and washing in isopropyl alcohol (IPA), namely 45sec, 50sec and 55sec. The experimental procedure involved making a layer sequentially with regard to exposure times and stirring the vat between each exposure. The procedural sequence went in the following steps:

1. 45sec of exposure for the resin to UV light
2. Remove layer from the vat and place on cleaning tray
3. Stir the vat
4. Top up the vat
5. 50sec of exposure for the resin to UV light
6. Repeat steps 2 – 4
7. 55sec of exposure for the resin to UV light
8. Repeat steps 2 – 4
9. Repeat from step 1 for next set of 3 layers

The above procedure was performed using an uncompensated bitmap and a compensated bitmap. The first bitmap ensured that all the micromirrors were in the "on" state. The second bitmap was a compensated bitmap estimated by the model

code. Two layers were cured at each exposure time for each bitmap displayed on the DMD.

The samples were rinsed in isopropyl alcohol and air dried with gentle compressed air. One sample was destroyed during the cleaning process. Next the layers were dissected across the lower part of the triangle of the arrow. This was followed by 10 minutes post-curing in a UV oven. This position was chosen to get the widest possible length of cross-section due to its proximity to the centre of the bitmap, and thus the greatest irradiated part of the layer.

The triangle layers were set up under a microscope so that the thickness of the cross-section was viewed. The microscope was equipped with a 10 mega-pixel camera. A photo was taken of the centre of each sample. Each photo was taken with a ruler scale with an accuracy of 0.5mm at the top of the photo. Each picture was manually calibrated by finding how many pixels there were per 0.5mm. Five to eight measurements were made of each cross-section. The data is displayed in Table 10.3. It should be noted that the UV filter on the SLA was destroyed during the setup of the experiment. Therefore, the samples will be affected by stray broadband light.

	Pixels	**mm**	**Pixels**	**mm**	**Pixels**	**Mm**	**Pixels**	**mm**
Sample#	1a45CN		1b45CN		2a45CC		2b45CC	
Pixels/0.5mm	53	0.0094	100	0.0050	86	0.0058	47	0.0106
	87	0.8208	237	1.1850	191	1.1105	97	1.0319
	91	0.8208	232	1.1850	192	1.1105	97	1.0319
	92	0.8679	234	1.1700	198	1.1512	95	1.0106
	90	0.8491	236	1.1800	186	1.0814	93	0.9894
	94	0.8868	237	1.1850	179	1.0407	94	1.0000
	91	0.8585			178	1.0349	91	0.9681
	94	0.8868			176	1.0233	88	0.9362
							91	0.9681
Average	91.29	0.86	235.2	1.18	185.71	1.08	93.25	0.99
Analytical X-section ave		1.3071		1.3071		1.3071		1.3071
	Error	0.45		0.1271		0.2271		0.3171
	Error(%)	34.21		9.72		17.37		24.26
	Pixels	**mm**	**Pixels**	**mm**	**Pixels**	**Mm**	**Pixels**	**mm**
Sample#	1b50CN		1a50CN		2a50CC		2b50CC	
Pixels/0.5mm	46	0.0109	47	0.0106	45	0.0111	48	0.0104
	108	1.1739	113	1.2021	117	1.3000	145	1.5104
	110	1.1739	115	1.2021	109	1.3000	150	1.5104
	115	1.2500	117	1.2447	109	1.2111	146	1.5208
	119	1.2935	122	1.2979	112	1.2444	129	1.3438
	115	1.2500	123	1.3085	115	1.2778	105	1.0938
	113	1.2283	120	1.2766	114	1.2667	103	1.0729
	112	1.2174	120	1.2766	114	1.2667	109	1.1354
	110	1.1957	115	1.2234			102	1.0625
Average	112.75	1.22	118.13	1.25	112.86	1.27	123.63	1.28
Analytical X-section ave		1.3248		1.3248		1.3248		1.3248
	Error	0.10		0.0748		0.0548		0.0448

	Error(%)	7.91		5.65		4.14		3.38
	Pixels	**mm**	**Pixels**	**mm**	**Pixels**	**mm**	**Pixels**	**mm**
Sample#	1b55CN		2a55CC		2b55CC		3a55CT	
Pixels/0.5mm	132	0.0038	47	0.0106	45	0.0111	47	0.0106
	340	1.2879	103	1.0957	115	1.2778	115	1.2234
	345	1.2879	110	1.0957	119	1.2778	115	1.2234
	347	1.3144	108	1.1489	119	1.3222	113	1.2021
	360	1.3636	106	1.1277	120	1.3333	108	1.1489
	359	1.3598	108	1.1489	117	1.3000	101	1.0745
			108	1.1489	116	1.2889	101	1.0745
			107	1.1383			100	1.0638
Average	350.2	1.32	107.14	1.13	117.67	1.3	107.57	1.14
Analytical X-section ave		1.3408		1.3408		1.3408		1.3408
	Error	0.02		0.2108		0.0408		0.2008
	Error(%)	1.55		15.72		3.04		14.98
			Pixels	**mm**	**Pixels**	**mm**	**Pixels**	**mm**
Sample#			3a115CT		3a120CT		3b120CT	
Pixels/0.5mm			47	0.0106	47	0.0106	46	0.0109
			127	1.3511	173	1.8404	154	1.6739
			130	1.3511	172	1.8404	167	1.6739
			130	1.3830	172	1.8298	175	1.9022
			130	1.3830	181	1.9255	156	1.6957
			130	1.3830	187	1.9894	115	1.2500
			130	1.3830	188	2.0000	103	1.1196
			128	1.3617			102	1.1087
							102	1.1087
Average			129.29	1.37	178.83	1.9	134.25	1.44
Analytical X-section ave				1.3726		1.3798		1.3798
	Error			0.0026		-0.5202		-0.0602
	Error(%)			0.19		37.70		4.36

Sample Code Key
CN = centre photo of cross-section with all micromirrors "on"
CC = centre photo of cross-section using compensated bitmap
CT = centre photo of cross-section using 10 pixel wide brighter border

Table 10.3 Cross-sectional thickness for three exposure times and compensated and uncompensated arrow shaped bitmaps.

Referring to Table 10.3, the first set of samples show a thickness of around 1.0mm. The uncompensated samples seem to vary a lot more than the compensated samples at 45sec of exposure. Both the uncompensated samples account for the minimum and maximum error which fell between 9.7% and 34.2% respectively.

The second sets of samples have a thickness of around 1.25mm. The compensated samples have a similar average thickness as well as being thicker than the uncompensated samples. The compensated samples have the least amount of error at 3.4% whereas the uncompensated samples have a maximum error of 7.9%.

One of the samples in the third set was destroyed during cleaning. The remaining 3 samples of the third set seem to be around 1.3mm. Compensated sample 2a55CC seems to be thinner and has an error of 15.7%. The other two samples, 1b55CN and

2b55CC, have a similar thickness and share a low error of 1.6% and 3.0% respectively.

Table 10.3 also shows a set that was made using a bitmap with a brighter boarder that was 10 pixels wide. The exposure times were made longer to allow the centre of the layer to cure to a reasonable thickness. This was made to test if the edges can be made thicker to account for the drop in irradiance at further distances from the centre.

In general, the cross-sectional thickness data is inconsistent and would benefit from more experimentation. More samples are necessary to account for random errors. There seems to be inconsistent results between sets making it difficult to predict the behaviour of cured thickness. One explanation for the variation of thickness could be attributed to the inaccuracy of where each sample was cut. The experimental method may need to be reassessed to provide a more consistent cut position.

10.4.4 Analysis of Layer Edge Phenomenon

The following analysis investigates the curing phenomenon due to Beer-Lambert's Law at the edge of a cured layer. The same samples that were cured for the cure thickness experiment in the previous section (section 10.4.3) are examined near the edges. Each cross-section is measured from microscope photos. The length is found empirically over which the Beer-Lambert's Law occurs at the edge of each cured layer. Only the left edge of the each layer is examined as the right edge was not usable because the ruler covered the right edge in most of the microscope photos. The microscope photos of the left edges are displayed in Appendix D: Experimental Layers.

	Pixels	mm	Pixels	mm	Pixels	mm	Pixels	mm
Sample#	1.1_45LN		1.2_45LN*		2.1_45LC*		2.2_45LC	
Pixels/0.5mm	46	0.0109	66	0.0076	72	0.0069	47	0.0106
Length	94	**1.0217**	74	**0.5606**	196	**1.3611**	63	**0.6702**
Max Thickness	44	0.4783	53	0.4015	84	0.5833	51	0.5426
Min Thickness	6	0.0652	29	0.2197	24	0.1667	13	0.1383
	Pixels	mm	Pixels	mm	Pixels	mm	Pixels	mm
Sample#	1.1_50LN		1.2_50LN		2.1_50LC*		2.2_50LC	
Pixels/0.5mm	47	0.0106	46	0.0109	48	0.0104	46	0.0109
Length	104	**1.1064**	92	**1.0000**	73	**0.7604**	51	**0.5543**
Max Thickness	47	0.5000	74	0.8043	33	0.3438	43	0.4674
Min Thickness	6	0.0638	7	0.0761	12	0.1250	12	0.1304
	Pixels	mm	Pixels	mm	Pixels	mm	Pixels	mm
Sample#	1.1_55LN		1.2_55LN*		2.1_55LC*		2.2_55LC	
Pixels/0.5mm	Sample destroyed during cleaning		47	0.0106	47	0.0106	47	0.0106
Length			63	**0.6702**	203	**2.1596**	263	**2.7979**
Max Thickness			51	0.5426	79	0.8404	82	0.8723
Min Thickness			15	0.1596	19	0.2021	16	0.1702
	Pixels	mm	Pixels	mm	Pixels	mm		
Sample#	3.1_115LT*		3.1a_120LT*		3.1b_120LT*			
Pixels/0.5mm	47	0.0106	47	0.0106	46	0.0109		
Length	195	**2.0745**	126	**1.3404**	61	**0.6630**		
Max Thickness	62	0.6596	71	0.7553	69	0.7500		
Min Thickness	5	0.0532	12	0.1277	53	0.5761		

Sample Code Key

* Difficult to differentiate between irradiance drop off and edge drop off in these samples

LN = Left of photo cross-section with all micromirrors "on"

LC = Left of photo cross-section using compensated bitmap

LT = Left of photo cross-section using 10 pixel wide brighter border

Table 10.4 Measurement data for the left edge curing phenomenon.

Of the thirteen samples analysed in Table 10.4, only about 50% of the samples have discernible edge phenomenon. The edge phenomenon cannot be clearly determined as to whether it is caused by the drop in irradiance due to the beam profile, or Beer-Lambert's Law. Figure 10.10(a) shows the edge phenomenon that is thought to be caused by Beer-Lamberts's Law. Figure 10.10(b) is an indiscernible edge and shows a drop in cure depth over a relatively long distance. This may be caused by the lamps beam profile. However, indiscernible edges are evident in both compensated and uncompensated samples.

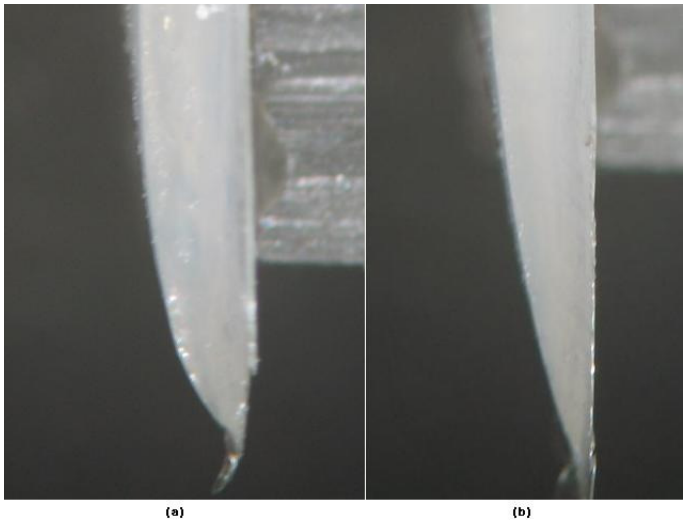

Figure 10.10 Edge phenomenon: (a) Discernable edge (b) Indiscernible edge

A possible explanation for the inconsistent results in the edge phenomenon could be the settling of the resin during post cure. When the samples are removed from the vat after exposure, the resin is not 100% cured. Even in conventional SLA, the resin is only about 70% cured when removed from the vat. It would be safe to assume that the samples are less than 70% cured due to the weak bonding strengths of the samples, as they can be destroyed easily by handling. The cleaning process in isopropyl alcohol also weakens the bonding strength. During the post-cure operation in the UV oven, the resin in the samples could be settling out to some extent thus causing the edge phenomenon seen in Figure 10.10(b). Again, more experimentation or improved experiment procedure would be necessary to find the cause of the inconsistency in results.

10.4.5 Dimensional Accuracy and Precision of Layers

Figure 10.11 displays the resulting plot of all the ray point intersections with the image plane simulated by the layer cure model (see Appendix B: MATLAB Code). Several dimensions of the arrow shape are labelled. These values are used as analytical target values for comparison with experimental results of dimensions recorded in Table 10.5.

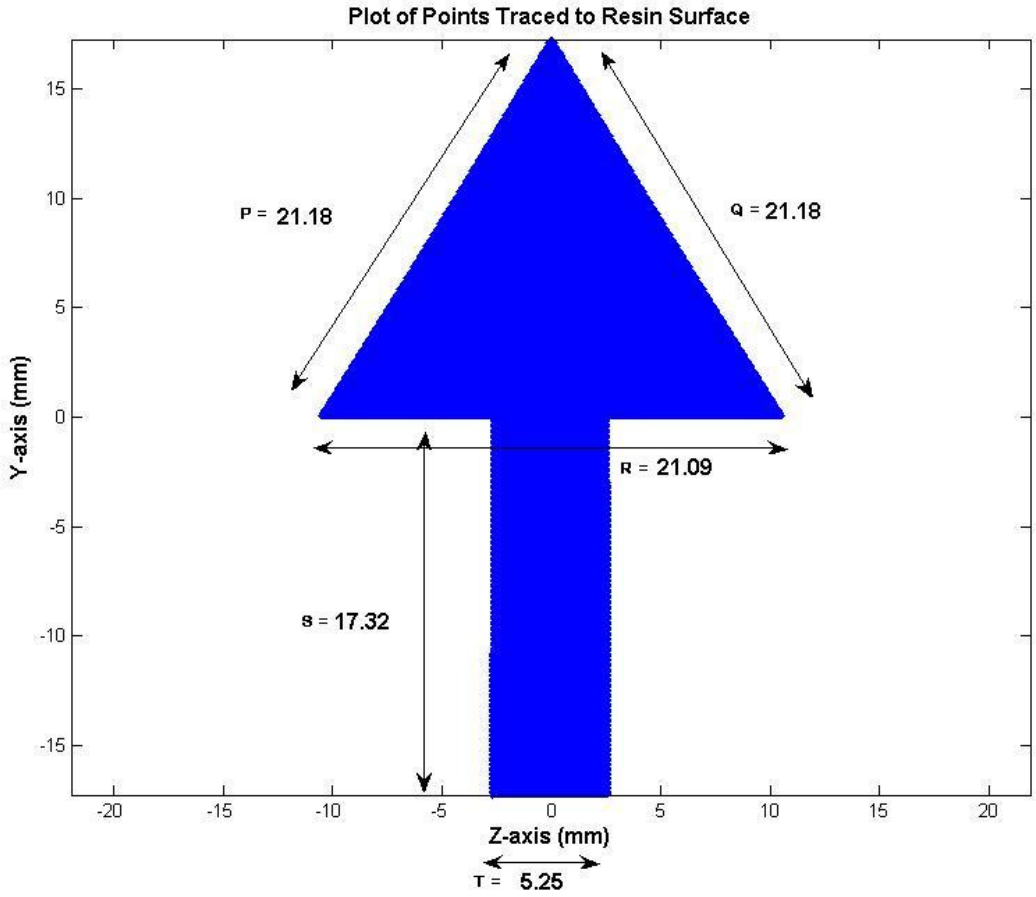

Figure 10.11 Arrow shape generated form layer cure model.

In this experiment, 15 layers were cured on the SLA at an exposure time of 45sec. Each layer was measured and compared with the dimensions given in Figure 10.11. The measurements were made with a digital vernier calliper accurate to ±0.01.

	Dimension in millimeters					β
Layer#	P	Q	R	S	T	Angle in Degrees
1	17.67	17.61	27.8	10.85	8.93	106
2	18.87	19.69	28.86	11.76	11.6	99
3	19.25	17.51	28.96	12.03	10.6	104
4	20	18.25	31.2	10.93	10.31	108
5	19.74	18.86	28.91	11.58	10.2	99
6	19.1	18.06	29.18	10.62	9.78	107
7	21.15	17.96	30.87	10.17	10.12	112
8	18.85	17.58	28.84	10.82	9.4	104
9	18.52	16.08	27.74	10.38	10.48	104
10	18.23	17.74	29	10.32	9.9	106
11	18.6	18.23	29.08	11.25	9.78	105
12	19.27	17.8	28.34	10.74	9.49	101
13	19.12	17.06	28	10.9	9.89	102
14	18.34	17.31	28.64	10.64	10.06	105
15	18.96	17.53	28.9	11.28	10.01	106
Average Dimension	19.0447	17.8180	28.9547	10.9513	10.0367	104.5333
Standard Deviation (σ)	0.8250	0.8090	0.9637	0.5363	0.6076	3.3989
3σ	2.4750	2.4270	2.8912	1.6090	1.8228	10.1966
Percent Precision	12.9958	13.6210	9.9851	14.6927	18.1611	9.7544
Analytical Dimension	21.1822	21.1822	21.0920	17.3190	5.2512	60.0000
Error	2.1375	3.3642	-7.8627	6.3677	-4.7855	-44.5333
Percent Error	10.0910	15.8820	37.2780	36.7669	91.1327	74.2222

Table 10.5 Dimensional precision and error of the arrow shaped layers.

The results of Table 10.5 show that there are precision errors as great as 18.2% which is quite high. The error is even greater when compared with the simulated analytical dimensions. The error is 92.1% in the axis of dimension T.

10.4.6 Improving accuracy and precision of the SLA

There are several factors that affect the accuracy and precision of the results. These factors are listed below:

- Misalignment of the optical system's elements.
- Errors in optical components.
- Errors in the image distance caused by differences resin level between exposures.
- Errors in the resin chemistry as the vat of resin is slowly exposed to UV light during the experiment.
- Errors caused by the cleaning process.
- Errors caused by the post-cure operation.

Misalignment of the optical elements was the greatest hindrance to the projected image. Once the alignment of the elements was set, they were not changed through out the experiments. One difficulty in setting up the optical components is measuring the alignments exactly, particularly the angle of the DMD. The mount for the DMD

was prototyped from a CAD model to get the exact angle. However, even this had to be modified slightly to obtain the projected image in the right location i.e. at a right angle to the incoming beam. These adjustments need to be corrected in the mathematical model.

The resin level was monitored by ensuring the level was up to a line marked on the vat. However, there is always a little bit of defocusing caused by differences in the resin level from experiment to experiment. Limaye managed to factor out the resin level changes by using the ratio of dimension. There was a noticed improvement in the precision and accuracy.

Through out the experiment, it has been assumed that the resin curing characteristics do not change as the resin is exposed to UV light. With commercial SLA, the resin in the vat last approximately two years. Considering the size of the vat and daily usage of a commercial SLA, there should be little effect on the resin.

Cleaning the layers in alcohol and post curing varies results. As handling the parts afterwards is quite difficult, the cleaning procedure varies for each part. During the post-cure operation in the UV oven, the resin in the samples could be settling out to some extent thus causing the edge phenomenon and dimension differences. Accounting for these variables is difficult to consider and is not factored into the mathematical model.

10.4.7 Result comparison with Limaye's SLA

The accuracy and precision experiment was conducted previously by Limaye using his μSLA. The following table is a comparison of the accuracy and precision averages and percentage for Limaye's experiment and the experiments of the SLA used in this research.

	P	Q	R	S	T	β
Percent Error (accuracy)	10.0910	15.8820	37.2780	36.7669	91.1327	74.2222
Percent Error (accuracy) Limaye	1.365175	0.44041	2.87704	0.961124	10.9015	5.512821
Difference	**8.7258**	**15.4416**	**34.4009**	**35.8058**	**80.2312**	**68.7094**
Percent Precision	12.9958	13.6210	9.9851	14.6927	18.1611	9.7544
Percent Precision (Limaye)	4.320562	5.491152	2.07149	3.073353	6.669961	12.88405
Difference	**8.6752**	**8.1298**	**7.9136**	**11.6193**	**11.4912**	**-3.1296**

Table 10.6 Comparison of the average accuracy and precision percentages with the Limaye results.

Table 10.6 shows that the new SLA only improves on the Limaye experiment in one aspect. The precision of angle β is roughly improved by 3%. However, all the

other dimensions are far out to a high degree. The accuracy is worse by as much as 80.2%. The precision is worse by about 8% - 12%.

10.5 Summary

In this chapter, several experiments have been accomplished in order to answer the research questions. The experiments have been reported in the order that they were done to show a logical thought process to the experiments. First, the projector was adapted to operate with the replacement diode circuit. The replacement circuit generated the required duty cycle to act as a dummy signal to allow the projector to operate normally.

Secondly, the preliminary experiments were conducted on a thin film of photopolymer resin. Various setups of the lamp and lenses were tested at distances of 100mm to 300mm to find the curing ability of the projected image. Various thicknesses of cure (0.3mm-0.8mm) were achieved within 7sec – 60sec of exposure. The conclusion of the preliminary experiments were that lens focusing affected the cure time and that fused silica lenses were needed to prevent the filtering of UV light by the existing projector lenses.

The beam intensity profile was measured empirically to obtain the weighting function for the mathematical model. (10.1 now serves as the weighting function in the mathematical model.

The uniformity of cure was analysed by measuring the cross-section of several layers cured at exposure times of 45sec, 50sec and 55sec. The accuracy in thickness when compared with that predicted by the mathematical model ranged from 1.6% to 34.2%. The cross-sectional thickness data was inconsistent and would benefit from more experimentation. There seemed to be inconsistent results between sets making it difficult to predict the behaviour of cured thickness.

Layers were examined near the edges. The edge phenomenon could not be clearly determined as to whether it was caused by the drop in irradiance due to the beam profile or Beer-Lambert's Law. More experimentation or improved experiment procedure would be necessary to obtain more consistency in the results.

The accuracy and precision data was compared to the data of Limaye's experiments. In general, all but one dimension were out to a high degree. The accuracy was worse by as much as 80.2%. The precision was worse by about 8% - 12%.

Overall the experiments have shown mixed results. The research would benefit from both more and improved experiments. The next chapter will discuss the meaning of the experimental results and answer the research questions.

11 Conclusions

This chapter discusses the conclusions and how this research affects the field of rapid prototyping especially in the area of integral stereolithography (SL). Section 11.1 answers the research questions. The research contribution is stated in section 11.2 and also what new knowledge has been added. Section 11.3 lists and explains the limitations and assumptions of the research. The implications of the research are noted in section 11.4. And finally, future work is suggested in section 11.5.

11.1 Answering the Research Questions

In chapter 7, the objective of this research was stated:

> "To present an improved mathematical model for integral UV stereolithography that accounts for errors in the optical imaging system such that for a predicted irradiance at the resin surface (obtained from the model), an evenly distributed irradiance results."

Research questions were asked based on the assessment of the literature review which explored work done by previous researchers. Thus to distinguish the value that this research has added to the field of rapid prototyping, the research questions are answered in this section.

Question 1: How are SLA systems modeled mathematically to ascertain the dimensional cured thickness of a single layer?

Hypothesis 1: An SLA system can be modeled mathematically to find the cure depth throughout a single layer by modification of the Limaye Layer Cure model and application of the cure depth equation.

Results of testing hypothesis 1: Hypothesis 1 was tested by measuring the cross-sectional thickness of a layer cured using the SLA constructed for this research. The Limaye Layer Cure model was modified and improved to provide a predicted irradiance map at the resin surface and the cured thickness. The cure depth equation was modified to incorporate time of exposure. The rearranged cure depth equation was applied to the irradiance map to obtain a three-dimensional representation of the cured layer. Any cross section of the layer modeled can be analyzed. The cross-sectional thickness of actual cured layers was compared with values from the mathematical model. The comparison was used to report the accuracy and precision of the cured layers with the layer thickness predicted by the mathematical model.

Question 2: How is the layer thickness of a photopolymer controlled accurately by a dynamic pattern generator to create an evenly cured layer?

Hypothesis 2: The layer thickness of a photopolymer is controlled accurately by modulation of individual pixels of the dynamic pattern generator to create an evenly cured layer.

Results of testing hypothesis 2: Hypothesis 2 was tested by taking an improved irradiance map and generating a compensated grey-scale bitmap of the projected image. The compensated bitmap was displayed on the dynamic pattern generator which modulates the individual pixels to create an image on the resin surface with an even irradiance throughout the layer. The resulting layer thickness of cured layers was measured and compared with the thickness predicted by the mathematical model.

Comparison of the compensated cross-sections with the uncompensated cross-sections showed that the uncompensated cross-sections were more uniform. Therefore, this hypothesis was proved incorrect. Further tests need to be conducted to completely disprove this hypothesis.

Question 3: How can the phenomenon at the edges of a layer, known as print-through error, be accounted for by control of the dynamic pattern generator?

Hypothesis 3: The dynamic pattern generator can control the print-through error by increasing the exposure time at the edges.

Testing of hypothesis 3: Hypothesis 3 was tested by using a bitmap which had a definitely brighter border. The border was much brighter than the rest of the bitmap. The bitmap was uncompensated apart from the border. The cross-section of several single layer exposures were examined and analysed in the same way as the tests conducted in hypothesis 1 and hypothesis 2.

The edges of the bitmap with the brighter boarder were examined under the microscope to observe any difference in curing behaviour and thickness at the edges. Comparison with the edges of the compensated and uncompensated layers revealed indiscernible change at the edge of the cured layers which had brighter borders. It should be noted that the UV filter was damaged setting up the experiments. Indeed more tests would be necessary to rule out suppression of growth at the edges, as Iwasawa et al (2003) described.

11.2 Research Contribution

Within the field of rapid prototyping, laser-based stereolithography has dominated for over a decade as an industry standard for quality functional prototyped parts. The technique of laser-based SLA has been sufficiently modelled for the vector-by-vector curing of layers. Much research has been aimed at developing SLA that use dynamic pattern generators and the integral layer curing technique. Integral SLA are able to fabricate prototypes faster due to layer curing being independent of surface area. Integral SLA are also much more cost effective because there is no expensive laser systems involved.

However, research on integral SLA has several limitations when it comes to improving on commercial laser-based SLA. Firstly, most research has only been aimed at describing and designing integral SLA. Little research has detailed the process parameters or modelled the process. Secondly, most integral SLA designs have been intended for fabrication of tiny, micro scale parts. In depth research has gone into finding the finest spatial resolutions. As a result, there is no research that observes the effects involved with irradiation of larger surface areas so that medium to large parts can be created.

The primary contributions of this thesis are in two areas of integral stereolithography. First, improvement of mathematical modelling of integral SL toward curing medium sized layers has been accomplished. The Limaye Layer Cure Model has been the basis for much of the theory for the mathematical model so it is necessary to point out what new aspects have been added to the model. And secondly, use of the dynamic pattern generator to allow layer thickness compensation to create evenly cured layers of a photopolymer resin has been assessed. Similar work on layer compensation using the dynamic pattern generator was briefly reported by (Takahashi, 2001), however, this was focused on photoresist and not photopolymer resin. The details of the work of this thesis' contributions to integral stereolithography are as follows:

1. The Limaye Layer Cure Model has been improved in several ways. The improved model now accounts for:
    - Cure depth.
    - The half cone angle of rays.
    - Any layer profile as a bitmap input into the model.

- Generates compensated layer bitmaps.

2. Results from experiments showed that the thickness of a layer could not be controlled accurately by modulation of individual pixels of the dynamic pattern generator to create an evenly cured layer. Note that this is only in this instance of the mathematical model.
3. Experimental results proved that the dynamic pattern generator could not control the print-through error by increasing the exposure time at the edges. The edge phenomenon was inconsistent for uncompensated, compensated and overly compensated layer experiments.

11.3 Scope and Limitations of the Research

The research conducted in this thesis was limited to a $10,000NZD budget. The research was only concerned with the integral cure of single layers of epoxy-based resin. Although the projected area was aimed to be around 270mm x 200mm in size, the physical and chemical limitations of the SLA have proved that a large projected area was not possible. It is hoped that future research will be able to expand the projected area.

It should be restated that this research was not concerned with making parts but more about controlling dimensional repeatability to cure single layers. It was not intended for microstereolithography. Lastly, it was not concerned with the chemical analysis of the photopolymer resin.

The SLA developed in this thesis is a simple implementation to allow easy computation of the SLA system. The SLA incorporates a slightly more complicated imaging system than Limaye's SLA and is intended for the purpose of fabricating medium to large layers as opposed to μSLA layers. Although the improved mathematical model is still limited, the model is intended for use with medium to large sized parts. This research is only a first step in developing the mathematical modelling of large irradiated layers for liquid-based stereolithography.

There are several limitations of this research that lead to some assumptions. The limitations are listed as follows with assumptions and explanations of each limitation:

1. One of the main limitations that Limaye warns about is that that Layer Cure Model's use of ray tracing may not account for diffraction effects occurring in sophisticated imaging systems. It is assumed in this thesis work that the

diffraction effects do not affect the cured layer. This may not be a correct assumption as diffraction effects are evident in the irradiance map.

2. The dimensional measurements may have been affected by systematic error having to do with the graphics card on the PC used to project the image. The estimation of the graphics card driver, to make pixel-for-pixel mapping of bitmaps, was measured before the projector was disassembled for implementation on the SLA. In these measurements the projected bitmaps had up to ±5 pixels when compared with the actual bitmap. The error would depend on the position of the bitmap features within the field of view and how fine the bitmap features were. It is the assumption of this thesis work that the error in estimation does not significantly affect the dimensional results of cured layers.
3. It is assumed that the optical alignments of elements in the SLA are in perfect agreement with the mathematical model. This surely cannot be true. The collimating lenses of the SLA are mounted in the mounting of the original projector, which bends the beam slightly at an unknown angle. Therefore, the shape of the beam is slightly distorted when it is focused on the DMD. The angle of the DMD was found to be rotated more than the calculated value in order to project vertically downward on the resin surface. This angle has not been accounted for in the model.
4. The mathematical model assumes that the light source used is a point source. In reality, the lamp has a specific volume and displays evidence that it acts as an extended source. However, it is assumed that the distance covered between the lamp and image is great enough to model the light source as a point source.
5. The mathematical model only accounts for a half cone angle of 5°. The measured half cone angle of the light source after collimation was roughly 18° - 20°. This problem is a result of the MATLAB program parameters and was not able to be fixed before the submission of this thesis work.
6. The compensated bitmap generated by the mathematical model is not presented in a form to display directly on the DMD at a pixel-for-pixel level. The bitmap used in these experiments was scaled to fit the required dimensions. As a result, the compensated image may not have been

accurate enough for the experiment. The MATLAB code to handle 256 shades of gray-scale pixels was not finished within the thesis time frame.

7. The beam profile that is used in the mathematical model is a symmetric profile from the centre of the beam. It is not a true representation of the three-dimensional beam profile which can cause errors between the predicted irradiance map and the actual cured layer. A way of incorporating the three-dimensional beam profile is an area of future research.
8. The errors due to vat variation have been assumed negligible because a large vat was used compared to the image size. However, there may still be errors in the resin level of the vat which changes the image to object distance. Variations in resin level result in small defocusing errors increasing or decreasing the image size. Limaye accounted for this error by using the ratio of dimensions, which resulted in a better accuracy and precision result of the mathematical model.
9. It is assumed that the chemical curing properties do not change during the experiments. A UV filter was not used during the experiments because the filter was damaged during the setup of experiments. The effects of broad band irradiation may have changed the resin curing characteristic.
10. The SL7545 resin used in the experiments is primarily formulated for laser-based SLA. This may explain the weak bonding strength of thin layers. However, it is of interest to use SL7545 resin for comparison with laser cured samples in future research.
11. The placement of the cross-sectional cut of the sample layers is assumed to be the same as the simulated cross-section. However, it is difficult for the practical and theoretical cross-sections to be cut in exactly the same place.

11.4 Implications

There are several implications of this research that support current integral SL theory. This research has proved that a simple integral SLA can be accomplished with most of the primary components contained in modern day DPL projectors. The research has shown resourcefulness and accomplished an inexpensive integral SLA for under $10,000.

This research supports the Limaye Layer Cure model as an appropriate mathematical model for integral SL. The theory of using ray tracing to effectively

predict the irradiance at the resin surface has been proved. The new improved model has verified that it can be used on larger scale integral SLA and not just applicable to the field of microstereolithography.

Experiments have observed the effects of print-through error due to broadband irradiance on the resin surface. This observation agrees with other research by Bertsch et al (2000), Iwasawa et al (2003), Limaye and Rosen (2005). However, experiments to compensate for the print-through error were not successful by modulating areas of the bitmap displayed on the DMD. Takahashi's theory and practice of irradiance compensation of the beam by modulation of a DMD's individual micromirrors has not been easily repeated. Further experiments are needed to provide a definitive result.

A new theory has been added to existing theory involving integral SL. The theory proposes that by mathematically modelling the irradiance at the resin surface, given certain process parameters, a compensated bitmap can be displayed on the dynamic pattern generator to account for uneven curing caused by the optical system. With calibration of the model, adaption of the model for almost any type of integral SLA may be possible.

The research conducted in this thesis fits in with current trends in rapid prototyping where manufacturers, such as Envisiontec and 3D Systems, are implementing integral machines with faster production times. Where this research differs with the latest integral SLA available is that a primarily epoxy-based photopolymer was used instead of an acrylate-based resin. Epoxy-based resins are known to produce much stronger prototypes. Whereas acrylate-based prototypes are pure form-and-fit parts made for aesthetics, epoxy-base prototypes are also functional.

11.5 Future Work

Immediate future work will focus on reducing some of the limitations and assumptions pointed out in section 11.3. It would be of great interest to perform the experiments on curing thickness and dimensional accuracy. Many more samples are necessary to get a more confident report of the results. These experiments also needed to be conducted with UV filtering.

The improved mathematical model needs to be updated with the actual DMD angle. The DMD was manually adjusted in the mounting system to bring the image into a more central point directly at a right angle to the incident beam. This correction to the model data will bring the simulated layer thickness and dimensions closer to the

actual layer. Two other aspects of the model that can be fixed in the near future are the allowance for larger half cone angles and generation of pixel-for-pixel compensated bitmaps in 256 shades of gray-scale.

Additional work on the mathematical model can be improved in two areas. The light source modelling can be improved to model the light source as an extended source rather than a point source. It would be of interest to see any changes in the predicted layer. The other improvement to the new model would be to accommodate three dimensional beam profiles rather than using the radial intensity distribution. The modelling of a three dimensional beam profile will provide a better estimate of the overall irradiance of the beam so that the compensated bitmap can account for irregularities in the irradiance, thus allowing more even cure.

It is also of interest to conduct a comparison of the bond strengths for prototypes made using the integral SLA and those made with laser cured parts. The layers made in this thesis had very weak bonds. It is of interest to quantify this property to be more confident of functional prototypes as opposed to aesthetic prototypes. Perhaps there is some manipulation of the chemical mixture that will increase the cure strength in integrally cured prototypes.

Even further future work will go into making parts. It is hoped that future work will lead to more efficient fabrication of large parts. The SLA is not automated, however, with the addition of stepper motors and control software, the SLA could be readily automated.

12 References

3D Systems. (2007). *Products: SLA Systems.* Retrieved 17th June, 2007, from http://www.3dsystems.com/products/sla/index.asp.

About Projectors. (2006). *InFocus LP400 DLP Projector.* Retrieved 25th Feb, 2008, from http://www.aboutprojectors.com/InFocus-LP400-projector.html.

Apicella, A., Simeone, M., Aversa, R., Lanza, A. and Apicella, D. (2005). Light shielding effect of overlaying resin composite on the photopolymerization cure kinetics of a resin composite and a dentin adhesive. *Dental Materials, 21*, 954–961.

Atkins, P. & de Paula, J. (2005). *Elements of Physical Chemistry.* (4th Ed). Virginia, W. H. Freeman & Company.

Bartolo, P. & Mitchell, G. (2003). Stereo-Thermal-lithography: a new principle for rapid prototyping. *Rapid Prototyping Journal, 9*(3), 150-156.

Bertsch, A., Bernhard, P. and Renaud, P. (2001). Microstereolithography: Concepts and applications. *8th International Conference on Emerging Technologies and Factory Automation (ETFA 2001)*, Antibes-Juan les pins, France, October, 2001, pp.289-298.

Bertsch, A., Bernhard, P., Vogt, C. and Renaud, P. (2000). Rapid prototyping of small size objects. *Rapid Prototyping Journal, 6*(4), 259-266.

Bertsch, A., Jezequel, J. and Andre, J. (1997). Study of the spatial resolution of a new 3D microfabrication process: the microstereophotolithography using a dynamic mask-generator technique. *Journal of Photochemistry and Photobiology A: Chemistry 107*, 275-281.

Bertsch, A., Lorenz, H. and Renaud, P. (1998). Combining Microstereolithography and Thick Resist UV Lithography for 3D Microfabrication. *Proceedings of the 11th IEEE Workshop on Micro Electro Mechanical Systems (MEMS '98)*, Heidelberg, Germany, pp.18-23, IEEE.

Broer, D., Mol, G. and Challa, G. (1991). Temperature effects on the kinetics of photoinitiated polymerization of dimethacrylates. *Polymer, 32*(4), 690-695.

Castle Island Co. (2007). *Selective Laser Sintering.* Retrieved 8th May, 2008, from http://home.att.net/~castleisland/sls_int.htm.

Chan, K., Feng, Z., Yang, R. and Mei, W. (2003). High Resolution Maskless Lithography by the Integration of Microoptics and Point Array Technique.

MOEMS Display and Imaging Systems, San Jose, California, pp.37-43, SPIE Society of Photo-Optical Instrumentation Engineering.

Chang, C.C. (2004). Rapid prototyping fabricated by UV resin spray nozzles. *Rapid Prototyping Journal, 10*(2), 136-145.

Chua, C., Leong, K. and Lim, C. (2003). *Rapid Prototyping: Principles and Applications* (2nd Ed). Singapore, World Scientific Publishing Co. Pte. Ltd.

Corcione, C., Greco, A. and Maffezzoli, A. (2004). Photopolymerization Kinetics of an Epoxy-based Resin for Stereolithography. *Journal of Applied Polymer Science, 92*, 3484-3491.

Corcione, C., Greco, A. and Maffezzoli, A. (2006). Temperature Evolution During Stereolithography Building With a Commercial Epoxy Resin. *Polymer Engineering and Science*, 493-502.

De Laurentis, K., Mavroidis, C. and Kong, F. (2004). Rapid Robot Reproduction. *IEEE Robotics & Automation Magazine*, 86-92.

Douglass, M. (1998). Lifetime Estimates and Unique Failure Mechanisms of the Digital Micromirror Device (DMD). *36th Annual International Reliability Physics Symposium*, Reno, Nevada, pp.9-16, IEEE.

Dym, C. & Little, P. (2004). *Engineering Design: A Project-Based Introduction* (2nd Ed), John Wiley & Sons, Inc.

Edmund Optics Inc. (2007). *Glass Material Specifications.* Retrieved 23rd Nov, 2007, from http://www.edmundoptics.com/techsupport/displayarticle.cfm?articleid=259&search=1.

EnvisionTec. (2005). *Perfactory - Description.* Retrieved 28th March, 2006, from http://www.envisiontec.com/21hdesca.htm.

EnvisionTec. (2007). *PERFACTORY® Technical Data.* Retrieved 23rd Nov, 2007, from www.envisiontec.com.

Ertas, A. & Jones, J. (1996). *The Engineering Design Process* (2nd Ed). New York, Wiley.

ESG Associates Corporation. (2003). *3D Printing Services.* Retrieved 8th May, 2008, from http://www.esgn.com/services/3d_printing_process.htm.

Fales, G. (2003). *Ten lens specifications you must know for machine-vision optics.* Retrieved 20th Mar, 2008, from http://www.tmworld.com/article/CA331843.html.

Farsari, M., Claret-Tournier, F., Huang, S., Chatwin, C., Budgett, D., Birch, P., Young, R. and Richardson, J. (2000). A novel high-accuracy microstereolithography method employing an adaptive electro-optic mask. *Journal of Materials Processing Technology, 107*(1-3), 167-172.

Farsari, M., Huang, S., Young, R., Heywood, M., Morrell, P. and Chatwin, C. (1998). Holographic characterization of epoxy resins at 351.1 nm. *Optical Engineering, 37*(10), 2754–2759.

Feder, D. (1951). Optical calculations with automatic computing machinery. *Journal of the Optical Society of America, 41*(9), 630-635.

Fischer, R. & Tadic-Galeb, B. (2000). *Optical System Design.* McGraw-Hill.

Gaines, P. (2006). *ICP Operations: 14. Accuracy, Precision, Mean and Standard Deviation*. Retrieved 19th Mar, 2008, from http://www.ivstandards.com/tech/icp-ops/part14.asp.

Hackney, P., Arulraj, A., Chinnaswamy, G. and Nair, B. (2005). Investigation into the Perfactory Process for Production of Accurate and Strong Functional Parts. *6th National Conference on Rapid Prototyping, Rapid Tooling and Rapid Manufacturing*, Buckinghamshire Chilterns University College, High Wycombe, UK.

Hackney, P., Chinnaswamy, G., Arulraj, A. and Nair, B. (2005). Investigation into Surface Finish of Parts Built by the EnvisionTec PerFactory® Rapid Prototyping Process. *6th National Conference on Rapid Prototyping, Rapid Tooling and Rapid Manufacturing*, Buckinghamshire Chilterns University College, High Wycombe, UK.

Hadipoespito, G. & Li, X. (2005). Microstereolithography Based on Digital Micromirror Device for Complex Meso/Micro Structures. *Transactions of NAMRI/SME*, Columbia University, New York, pp.105-111, Society of Manufacturing Engineers.

Ikuta, K., Maruo, S. and Kojima, S. (1998). New Micro Stereolithography for freely movable 3D Micro Structure - Super IH Process with Submicron Resolution. *Proceedings of the 11th International Workshop on Microelectromechanical Systems*, pp.290-295, IEEE.

Instron. (2006). *Definition: Accuracy, Precision, Calibration.* Retrieved 19th Mar, 2008, from www.instron.com.au/wa/library/streamfile.aspx?doc=449.

International Organization for Standardization. (2004). *International vocabulary of basic and general terms in metrology (VIM).* Retrieved 19th Mar, 2008, from http://www.ntmdt.ru/download/vim.pdf.

Iwasawa, A., Kanoya, D. and Takahashi, K. (2003). Wide Range and High Speed Rapid Prototyping System Using a Digital Micromirror Device. *Proceedings of the Sensor Symposium on Sensors Micromachines and Applied Systems, 20*, 437-440.

Jacobs, P. (1992). *Rapid Prototyping & Manufacturing: Fundamentals of StereoLithography.* Michigan, Society of Manufacturing Engineers.

Jacobs, P. (1996). *Stereolithography and other RP&M Technologies - from Rapid Prototyping to Rapid Tooling.* Dearborn, Society of Manufacturing Engineers.

Kerr, D. (2006). *Field of View in Photography.* Retrieved 7th Feb, 2008, from http://doug.kerr.home.att.net/pumpkin/Field_of_View.pdf.

Kloosterboer, J., van de Hei, G., Gossink, R. and Dortant, G. (1984). The effects of volume relaxation and thermal mobilization of trapped radicals on the final conversion of photopolymerized diacrylates. *Polymer Communication, 25*, 322-325.

Kochan, A. (1997). Features Rapid prototyping wins widespread acceptance. *Assembly Automation, 17*(3), 218 - 221.

Krar, S. & Gill, A. (2003). *Exploring Advance Manufacturing Technology.* New York, Industrial Press Inc.

Kubota, S. (2002). The Grating Light Valve Projector. *Optics & Photonics News,* 50-53.

Kunjappu, J. (2000). *Radiation Chemistry in EB-and UV- Light-Cured Inks.* Retrieved 21st March, 2005, from http://www.pcimag.com/CDA/ ArticleInformation/features/BNP__Features__Item/0,1846,11435,00.

Lecamp, L., Youssef, B., Bunel, C. and Lebaudy, P. (1997). Photoinitiated polymerization of a dimethacrylate oligomer. *Polymer, 38*(25), 6089-6096.

Lexico Publishing Group LLC. (2000). *The American Heritage® Dictionary of the English Language,* (4th Ed). Retrieved 3rd April, 2006, from http://dictionary.reference.com/search?q=prototype.

Limaye, A. (2004). *Design and Analysis of a Mask Projection Micro-Stereolithography System.* (Master's thesis, Georgia Institute of Technology

Atlanta, GA, 2006). Retrieved from http://www.srl.gatech.edu/Members/alimaye/MSthesis_Ameya.pdf

Limaye, A. & Rosen, D. (2005). Process planning method for curing accurate microparts using Mask Projection Micro Stereolithography. *VRAP 2005, 2nd International Conference on Advanced Research in Virtual and Rapid Prototyping*, Leiria, Portugal, September 2005, pp.441-447.

Lyon, R. (2006). *Angle of View.* Retrieved 7th Feb, 2008, from http://en.wikipedia.org/wiki/Angle_of_view#cite_ref-1.

Maalderink, H. (2003). The EnvisionTec Perfactory, a class of it's own? Experiences from TNO. *Newsletter of the Thematic Network*, The Sare consortium, 2-4.

Maffezzoli, A. & Terzi, R. (1998). Effect of irradiation intensity on the isothermal photopolymerization kinetics of acrylic resins for stereolithography. *Thermochim Acta, 321*(1-2), 111-121.

Mcartney, D. (2004). *Fundamentals of LCDs - How Liquid Crystal Displays work.* Retrieved 7th May, 2007, from http://www.national.com/onlineseminar/2004/lcds/lcds.html.

McCollough, E. (1893). *Photographic Topography.* San Francisco, Industrial Publishing Company.

Monneret, S., Loubere, V. and Corbel, S. (1999). Microstereolithography Using a Dynamic Pattern Generator and Non-coherent Visible Light Source. *Proceedings of the SPIE*, 553-561.

Monneret, S., Provin, C. and Le Gall, H. (2001). Micro-scale rapid prototyping by stereolithography. *Proceedings of 8th IEEE International Conference on Emerging Technologies and Factory Automation*, 299-304, IEEE.

Nelson, E., Jacobs, J., Scranton, A., Anseth, K. and Bowman, C. (1995). Photo-differential scanning calorimetry studies of cationic polymerizations of divinyl ethers. *Polymer, 36*(24), 4651-4656.

Newport Corporation (2004). Optics: Technical Reference. *The Newport Resource: Experience - Solutions*, Newport Corporation, 547-580.

Richland County GIS. (2006). *GIS Glossary.* Retrieved 4th March, 2008, from http://www.richlandmaps.com/training/glossary/q_s.html.

Sachs, E. (1997). Rapid Prototyping in Europe and Japan: Rapid Prototyping Machine Design. *J. W. P. Report.* Loyola College, Maryland.

Scherzer, T. & Decker, U. (1999). Kinetic investigations on the UV-induced photopolymerization of a diacrylate by time-resolved FTIR spectroscopy: the influence of photoinitiator concentration, light intensity and temperature. *Radiation Physics and Chemistry, 55,* 615-619.

Scherzer, T., Decker, U. and Mehnert, R. (1998). The effect of temperature on the curing behavior of printing inks. *Proceedings of the RadTech '98 North America Conference*, Chicago, p.746.

Smith, W. (2000). *Modern optical engineering: the design of optical systems.* (3rd Ed). New York, McGraw Hill.

Sontheimer, A. (2002). Digital Micromirror Device (DMD) Hinge Memory Lifetime Reliability Modeling. *4Oth Annual lnternational Reliability Physics Symposium*, Dallas, Texas, April, pp.118-121, IEEE.

Stratasys, I. (2005). *Accurate, Rapid Manufacturing and Prototyping Systems.* Retrieved 4th April, 2008, from http://intl.stratasys.com/sys_fdm.html.

Sun, C., Fang, N., Wu, D. and Zhang, X. (2005). Projection micro-stereolithograhpy using digital micro-mirror dynamic mask. *Sensors and Actuators A: Physical, 121*(1), 113-120.

Takahashi, K. (2001). A New Application of DMD to Photolithography and Rapid Prototyping System. *8th International Display Workshops*, 1339-1342.

Takahashi, K. & Setoyama, J. (2000). A UV-Exposure System Using DMD. *Electronics and Communications in Japan, Part 2, 83*(7), 92-94.

Texas Instruments Inc. (2005). *How DLP™ Technology Works*. Retrieved 21st March, 2005, from http://www.dlp.com/dlp_technology/ dlp_technology_overview.asp.

Tomita, Y., Iwasawa, A. and Takahashi, K. (2005). High Speed and Wide Range Rapid Prototyping System Using a Digital Micromirror Device. *IEEJ Transactions on Sensors and Micromachines, 125-E*(2), 89-94.

Tryson, G. & Shultz, A. (1979). A calorimetric study of acrylate photopolymerization. *Journal of Polymer Science: Polymer Physics Vol.17*, 2059-2075.

TyRex Services Group Ltd. (2007). *DMD Discovery™ 1100.* Retrieved 7th April, 2007, from http://www.tyrexsales.com/dlp/.

Tyson, J. (1998). *How LCDs Work.* Retrieved 7th July, 2007, from http://electronics.howstuffworks.com/lcd.htm.

Upcraft, S. & Fletcher, R. (2003). The Rapid Prototyping Technologies. *Assembly Automation, 23*(4), 318-330.

USAF Dental Evaluation & Consultation Service. (2006). *Filtek Z250 Universal Resin Composite.* Retrieved 11th June, 2007, from www.dentalcompare.com/ review.asp?rid=99.

Wohlers, T. (1999). *Rapid Prototyping and Tooling State of the Industry: 1999 Worldwide Progress Report*, Wohlers Associates.

Wu, M., Zhao, W., Tang, Y., Li, D. and Lu, B. (2001). A novel stereolithography technology with conventional UV light. *Rapid Prototyping Journal*, pp.268-274.

Yang, Y., Fuh, J. and Loh, Y. (2001). An Efficient Scanning Pattern for Layered Manufacturing Processes. *IEEE International Con-ference on Robotics & Automation Proceedings*, Seoul: Korea, May 21-26, pp.1340-1345, IEEE.

Young, H. & Freeman, R. (1996). *University Physics.* (9th Ed), Addison Wesley.

Z Corporation. (2008). *Spectrum Z510.* Retrieved 8th May, 2008, from http://www.zcorp.com/Products/3D-Printers/Spectrum-Z510/spage.aspx.

13 Appendix A: Research Costing

Project costings					
Item#	**Qty**	**Description**	**Manufacturer**	**Actual Cost**	**Estimated Cost**
1	1	LP400 projector	InFocus	free	$1,200.00
2	1	VIS DMD & Controller	Digital Light Innovations		$12,600.00
3	1	100W Mercury Lamp	Lamp Specialists		$686.72
4	1	Lamp Power Supply	Lamp Specialists		$2,235.00
5	1	Laptop (with video out)	Toshiba	$1,600.00	$1,600.00
6	1	W46-335 DCV	Edmund Optics	$206.55	$206.55
7	2	W46-226 PCX	Edmund Optics	$401.04	$401.04
8	2	W46-084 filter	Edmund Optics	$194.44	$194.44
9	1	W46-085 filter	Edmund Optics	$76.16	$76.16
10	3	LH-1 Lens Holder	Newport Corp	$92.65	$92.65
11	4	CA-1 Right Angle Clamp	Newport Corp	$73.13	$73.13
12	3	M-SP-6 post	Newport Corp	$37.81	$37.81
13	1	M-SP-12 posts	Newport Corp	$19.67	$19.67
14		Aluminium for SLA and Fabrication Cost	Ulrich Aluminium Fabricators	$1,000.00	$1,000.00
15		Machining costs		free	$500
16		Miscellaneous parts:			
17		nuts, bolts, threaded rod		$100.00	$100.00
18		SEM microscope use (Auckland University)		$210.00	$210.00
19		Renshape SL7545 Resin		free	$300.00
			Total	$4,011.45	$21,533.17

Note: Prices do not include tax or shipping charges to New Zealand

14 Appendix B: MATLAB Code

The following program is the MATLAB7 code for the enhanced Layer Cure Model. The code was adapted to and modified during the course of the reseach (see code notes). The code is highly commented to make clear the intent of each part of the code.

```
%MATLAB script written to model the aerial image and the irradiance
%distribution across the image for arrow shaped bitmap

%8th July 2004---Script written by Ameya on

%June 2006---Script was highly modified to take in a solid-shaped bitmap
%without hollows or overhangs. The initial setup of lens curvature and
%element thickness and distances is required at the start of the program.
%By Zyzalo

%August 2006---Script was simplified to have one ray in the center of each
%mirror reflectparallel to the optical axis rather than have a mesh spacing
%of 1.6:1 by Zyzalo

%November 2006---Script was modified to model a Cooke Triplet. Changes done
%by Zyzalo

%November 2006---Added code to plot a 3D representation of the cure depth
%by substituting the irradiance matrix value for Emax in the cure depth
%equation Cd = Dp*ln(Emax*TOE/Ec) By Zyzalo

%February 2008---Changed to code to model the new SLA lenses and distances
%Added code to create and output the compensated bitmap (800x800) to be
%displayed on the DMD to achieve even/uniform layer curing. Also, added the
%ability to brighten the profile while keeping the background black.
%By Zyzalo

%May 2008---Changed code to handle different thicknesses (distances)
%between the object and the image. This allows interchangeable lens
%configurations. Also added the code to accomodate upto 2degree half cone
%angle with 9 rays traced from a point on the DMD. By Zyzalo
```

```
clear all;
%Inputing the Imaging system parameters:

c(1) = 0;              % c is the curvature of surface
c(2) = 0.046664;
c(3) = -0.046664;
c(4) = 0;
t(2) = 10.9;           %t is the distance
t(3) = 32.95-5.45;
number_of_thicknesses = 3;
sum_of_thicknesses = 0;
for (i = 2:1:number_of_thicknesses) %sum of all the distances from the
   sum_of_thicknesses = sum_of_thicknesses + t(i);%object except t(1)
end                                  %which changes for every ray.
image_plane_tnumber = number_of_thicknesses + 1;
objectdistance = 113;
N(1) = 1;              %N is the refractive index
N(2) = 1.45848;
N(3) = 1;
Irradiance_map_resoltion = 200; %Note: The irradiance map is a square.
build_envelope = 2; %square dimension of the resin surface in mm
number_of_vectors = 1; %Should be 1, 5, or 9 to be symmetric.
% Code accommodates for up to 9 vectors. 1 parallel, 4 at 1degree half cone
% angle and 4 at 2degre half cone angle.
%{
c(1) = 0;              % c is the curvature of surface
objectdistance = 113;%18.78; %distance from object to first lens surface
%object_image_dist = t(1)+t(2)+t(3)+t(4)+t(5)+t(6)+t(7)
% object to image distance is declared later after t(1) is defined.
c(2) = 0.057405;
c(3) = 0;
t(2) = 7.25; %t is the thickness/distance of medium.
          %t(2) is the thickness of the lens
t(3) = 0.88; % t(3) includes spacer gap and the curvature gap of the lens
c(4) = -0.0108601;
c(5) = 0.0108601;
t(4) = 2.5;
t(5) = 8.58;
c(6) = 0;
```

```
c(7) = -0.057405;
t(6) = 7.25;
t(7) = 32.95-5.45;%179; %179 is the best simulated distance using
                    %OSLO software.
%Limaye made t(7) (his t(3))the distance to the image,
% which I don't need to do, plane from the lens center
c(8) = 0; %resin surface
number_of_thicknesses = 7;
sum_of_thicknesses = 0;
for (i = 2:1:number_of_thicknesses) %sum of all the distances from the
   sum_of_thicknesses = sum_of_thicknesses + t(i);%object except t(1)
end                                    %which changes for every ray.
image_plane_tnumber = number_of_thicknesses + 1;

N(1) = 1;              %N is the refractive index
N(2) = 1.45848;
N(3) = 1;
N(4) = 1.45848;
N(5) = 1;
N(6) = 1.45848;
N(7) = 1;
Irradiance_map_resoltion = 400;  %800%Note: The irradiance map is a square.
build_envelope = 4; %100       %square dimension of the resin surface in mm
number_of_vectors = 1; %Should be 1, 5, or 9 to be symmetric.
% Code accommodates for up to 9 vectors. 1 parallel, 4 at 1degree half cone
% angle and 4 at 2degre half cone angle.
%}
DMDangley = 7.052*3.142/180;
DMDanglez = 52.05*3.142/180; %This is the angle at which the DMD is
                        %mounted to the horizontal
layer_bitmap = zeros(800,800);
total_pixels = 800*800;      % =640,000 pixels for a 800x800 bitmap
layer_bitmap = imread('arrow400x400.bmp', 'bmp');%bitmap with 0's & 1's
% square3x3.bmp test400x400.bmp square400x400.bmp
% arrow400x400project800x800EdgeTest192blank.bmp
% CompensatedGreyscale800x800.bmp
% Plus100x100X221x450Y100x315.bmp Plus200x399Y150x349.bmp
% arrow400x400project800x800.bmp
                                    %1's for the layer
                                    %1 = white, 0 = black
```

```
%*************************************************************************
raycount = 1;
%Getting the extents of the bitmap and store rows in 'bitmap_ysize' &
% columns in 'bitmap_zsize'
[bitmap_ysize,bitmap_zsize] = size(layer_bitmap);

%Specifying the offsets
y_offset = 0;
z_offset = 0;
bitmap_ymin = (y_offset - bitmap_ysize/2)*16/1000*cos(DMDangley);
bitmap_ymax = (y_offset + bitmap_ysize/2)*16/1000*cos(DMDangley);
bitmap_zmin = (z_offset - bitmap_zsize/2)*16/1000*cos(DMDanglez);
bitmap_zmax = (z_offset + bitmap_zsize/2)*16/1000*cos(DMDanglez);

%*************************************************************************
% This section finds the bounds of the bitmap image (stored in layer_bitmap
% ()) only. ie. without surrounding whitespace. It stores the "ON" points
% in the y-rows and z-columns in the following vectors:
% bitmap_y_tempON %these arrays are temp because not all the array is used
% bitmap_z_tempON % They are reduced later after the loop to bitmap_yON
% Note: old mirror size = 13.7
step_Ay = 16*cos(DMDangley)/1000; %actual mirror size in y
step_Az = 16*cos(DMDanglez)/1000; %actual mirror size in z

column_flag = 1;
row_notempty_flag = 0;
z_sum_total = 0;
tempcounty = 1;
mintempcountz = bitmap_ysize; %need to keep track of the min & max index of
maxtempcountz = 0;            %any row in the bitmap for mesh spacing
                              %algorithm. This can be confussing, but
tempcountz = 1;               %the min or max column index indicates how
                              %far along the row an "ON" point is.
i = 1;
bitmap_y_tempON = zeros(1,bitmap_ysize); % need to change this for the
                                         % case where yON < ysize
bitmap_z_tempON = zeros(1,total_pixels);
row_len = zeros(1,bitmap_ysize);
for tempy = (bitmap_ymin+(step_Ay/2):step_Ay:bitmap_ymax-(step_Ay/2));
                              %This loop searches each row and
```

```
   j = 1;                    %searches each column for 'ON' pixels
   for tempz = (bitmap_zmin+(step_Az/2):step_Az:bitmap_zmax-(step_Az/2));
      if ((i<=bitmap_ysize)&(j <= bitmap_zsize)&(layer_bitmap(i,j)==1));
                                % else it must equal one(white).
         if (column_flag == 1);
            bitmap_y_tempON(tempcounty) = tempy; %if the pixel is on,
                                %then store the point information.
            tempcounty = tempcounty + 1; %Note: for this if statement,
                                %bitmap_y_tempON {the row} only gets
            column_flag = 0;  %stored once for every column in the row.
         end
         bitmap_z_tempON(tempcountz) = tempz; %column z is incremented
               %in this for loop until it reaches the end of the row.
         if (j > maxtempcountz);%These two if statements track the width
               maxtempcountz = j; %of the bitmap in order to find the
                                %spread for all rows.
         end      %The min & max are used in the mesh spacing algorithm.
         if (j < mintempcountz);
               mintempcountz = j;
         end
         tempcountz = tempcountz + 1;
         row_notempty_flag = 1;
      end
      j = j + 1;
   end
   column_flag = 1;
   if (row_notempty_flag == 1); %this if statement keeps track of the
                           %number of 'ON' mirrors in a row.
      row_len(tempcounty-1) = (tempcountz-1) - z_sum_total; %keep track
      z_sum_total = tempcountz-1; %of the number of "on" points in bitmap
      row_notempty_flag = 0;  %reset flag
   end
   i = i + 1;
end
clear tempy tempz i j column_flag row_notempty_flag tempcounty tempcountz;
bitmapsizeyON = nnz(bitmap_y_tempON);%nnz(A)=matrix operation that returns
for i = (1:1:bitmapsizeyON);        %the number of non-zero elements in (A)
   bitmap_yON(i) = bitmap_y_tempON(i);
end
bitmapsizezON = nnz(bitmap_z_tempON);
```

```
bitmap_zON = zeros(1,bitmapsizezON);
for i = (1:1:bitmapsizezON);
   bitmap_zON(i) = bitmap_z_tempON(i);
end
total_num_pixelsON = bitmapsizezON;
clear bitmap_y_tempON bitmap_z_tempON;
%*************************************************************************
%Selecting the point on the bitmap grid and calculating the object distance
%for it
%Now the bitmap has been processed into a mesh bitmap of lower resolution.
%This mesh bitmap is represented by
xpos = zeros(1,total_num_pixelsON);
ypos = zeros(1,total_num_pixelsON);
zpos = zeros(1,total_num_pixelsON);
w = zeros(1,total_num_pixelsON);
count_zbitmap = 1;
pupilpoint_y = 0;
pupilpoint_z = 0;
for count_ybitmap = (1:1:bitmapsizeyON);%meshy+1
   startpoint_y = bitmap_yON(count_ybitmap);
   for bitmap_row_len = (1:1:row_len(count_ybitmap));%meshz+1
      startpoint_z = bitmap_zON(count_zbitmap);
      %Now, the distance of the pattern-point from the center of the beam
      %is calculated. This distance is stored as p and then the weight of
      %the rays emitting from this point are calcuated as the column
      %matrix w
    p=sqrt(startpoint_y^2*sin(DMDangley)+(startpoint_z*sin(DMDanglez))^2);
    t(1) = objectdistance - startpoint_z*tan(DMDanglez)
                                - startpoint_y*tan(DMDangley);

      %object_image_dist = t(1)+t(2)+t(3)+t(4)+t(5)+t(6)+t(7);
      object_image_dist = t(1)+sum_of_thicknesses;
%*************************************************************************

      %pupilpoint_y = startpoint_y;
      %pupilpoint_z = startpoint_z;
      %length = sqrt((pupilpoint_y-startpoint_y)^2 +
      %          (pupilpoint_z-startpoint_z)^2 + object_image_dist^2);
      %X(1) = object_image_dist/length;
      %Y(1) = (startpoint_y-pupilpoint_y)/length;
```

```
%Z(1) = (startpoint_z-pupilpoint_z)/length;
for (vector_num = 1:1:number_of_vectors)
   if (vector_num == 1)
      X(1) = cos(0*pi/180);
      Y(1) = cos(90*pi/180);
      Z(1) = cos(90*pi/180);
   elseif (vector_num == 2)
      X(1) = cos(1*pi/180);
      Y(1) = cos(89*pi/180);
      Z(1) = cos(90*pi/180);
   elseif (vector_num == 3)
      X(1) = cos(1*pi/180);
      Y(1) = cos(91*pi/180);
      Z(1) = cos(90*pi/180);
   elseif (vector_num == 4)
      X(1) = cos(1*pi/180);
      Y(1) = cos(90*pi/180);
      Z(1) = cos(89*pi/180);
   elseif (vector_num == 5)
      X(1) = cos(1*pi/180);
      Y(1) = cos(90*pi/180);
      Z(1) = cos(91*pi/180);
   elseif (vector_num == 6)
      X(1) = cos(2*pi/180);
      Y(1) = cos(88*pi/180);
      Z(1) = cos(90*pi/180);
   elseif (vector_num == 7)
      X(1) = cos(2*pi/180);
      Y(1) = cos(92*pi/180);
      Z(1) = cos(90*pi/180);
   elseif (vector_num == 8)
      X(1) = cos(2*pi/180);
      Y(1) = cos(90*pi/180);
      Z(1) = cos(88*pi/180);
   elseif (vector_num == 9)
      X(1) = cos(2*pi/180);
      Y(1) = cos(90*pi/180);
      Z(1) = cos(92*pi/180);
   end
%*************************************************************************
```

```
%Tracing the ray through the lens
        x(1) = startpoint_y*tan(DMDangley)+startpoint_z*tan(DMDanglez);
        y(1) = startpoint_y;
        z(1) = startpoint_z;
        for (i = 2:1:number_of_thicknesses)
%Transfer equations
           e(i) = t(i-1)*X(i-1) - (x(i-1)*X(i-1)
                              + y(i-1)*Y(i-1) + z(i-1)*Z(i-1));
           Mx(i) = x(i-1) + e(i)*X(i-1) - t(i-1);
           Msquare(i) = x(i-1)^2 + y(i-1)^2 + z(i-1)^2
                          - e(i)^2 + t(i-1)^2 - 2*t(i-1)*x(i-1);
           E(i) = sqrt(X(i-1)^2 - c(i)*(c(i)*Msquare(i) - 2*Mx(i)));
           L(i) = e(i) + (c(i)*Msquare(i) - 2*Mx(i))/(X(i-1)+E(i));
           x(i) = x(i-1) + L(i)*X(i-1) - t(i-1);
           y(i) = y(i-1) + L(i)*Y(i-1);
           z(i) = z(i-1) + L(i)*Z(i-1);

%Refraction equations
           Edash(i) = sqrt(1- ((N(i-1)/N(i))^2) * (1-E(i)^2));
           g(i) = Edash(i) - ((N(i-1)/N(i)))*E(i);
           X(i) = (N(i-1)/N(i))*X(i-1) - g(i)*c(i)*x(i) + g(i);
           Y(i) = (N(i-1)/N(i))*Y(i-1) - g(i)*c(i)*y(i);
           Z(i) = (N(i-1)/N(i))*Z(i-1) - g(i)*c(i)*z(i);
        end

%Transfer equations from last lens surface to image plane
        for i = image_plane_tnumber;
           e(i) = t(i-1)*X(i-1) - (x(i-1)*X(i-1)
                              + y(i-1)*Y(i-1) + z(i-1)*Z(i-1));
           Mx(i) = x(i-1) + e(i)*X(i-1) - t(i-1);
           Msquare(i) = x(i-1)^2 + y(i-1)^2 + z(i-1)^2
                          - e(i)^2 + t(i-1)^2 - 2*t(i-1)*x(i-1);
           E(i) = sqrt(X(i-1)^2 - c(i)*(c(i)*Msquare(i) - 2*Mx(i)));
           L(i) = e(i) + (c(i)*Msquare(i) - 2*Mx(i))/(X(i-1)+E(i));
           x(i) = x(i-1) + L(i)*X(i-1) - t(i-1);
           y(i) = y(i-1) + L(i)*Y(i-1);
           z(i) = z(i-1) + L(i)*Z(i-1);
        end
%**************************************************************************
```

```
%Recording the position of the ray on the image plane
        xpos(raycount) = x(i);
        ypos(raycount) = y(i);
        zpos(raycount) = z(i);
        w(raycount) = 1-0.00086*p-0.00883*p*p;
                %exp(-(p*p)/10000);%; %1-0.0028*p-0.0005*p*p;
                %0.6921+0.0284*p-0.0007*p*p full beam profile
        raycount = raycount + 1;

%The points of intersection with the image plane are recorded as xpos, ypos,
%zpos;
      end
      count_zbitmap = count_zbitmap + 1;
   end
end
%Here ends the loops selecting the point on the bitmap.

%************************************************************************
%Plotting the points on the image plane
set(0,'DefaultFigureColor','w'); %change default figure background
plot(zpos,ypos,'.');                        % color to white
title('Plot of Points Traced to Resin Surface');
xlabel('Z-axis (mm)');
ylabel('Y-axis (mm)');
hold on;
axis equal;

%************************************************************************
%Measuring the irradiance
%Dividing the resin surface area into a x by x grid of areas
%Resin surface is considered square from -1 to +1 along both directions
%Creating the grid
x = Irradiance_map_resoltion;%x is bound by the y dimension. See next line.
%y = 800; Note: the MATLAB graphs don't work unless the grid is square
%Select the ray under consideration. Divide its ypos by 0.9. Round it
%off. From the rounding off, determine the value of ylocaton it lies in.
%Same for zpos

number_of_areas = zeros((x+1),(x+1));
%Initialize number_of_rays = 0;
```

```
for ytemp = (1:1:(x+1))
   for ztemp = (1:1:(x+1))
      number_of_areas(ytemp, ztemp) = 0;
   end
end
clear ytemp ztemp;
%Now, find the number of rays that land in each square of the mesh on the
%irradiance map. This is where the build_envelop variable is used.
num_of_rays1 = raycount-1;
for temp = (1:1:num_of_rays1)
   y_ray = ypos(temp);
   z_ray = zpos(temp);
   ynumber = y_ray+(build_envelope/2);
   znumber = z_ray+(build_envelope/2);
   ynumber1 = int16(0.5 + ynumber/(build_envelope/x)); %The number 0.5
   %if (ynumber1 > x+1);                          %affects the origin
   %    ynumber1 = 1;
   %end
   znumber1 = int16(0.5 + znumber/(build_envelope/x));
   number_of_areas(ynumber1, znumber1) =
                        number_of_areas(ynumber1,znumber1) + w(temp);
end
clear temp;

%Totalling the number of weights.
clear temp;
sigmaw = 0;
for temp = 1:1:raycount-1;
   sigmaw = sigmaw + w(temp);
end
clear temp;

irradiance = zeros((x+1),(x+1));
InvertedGrayscale = zeros((x+1),(x+1));
irradiance = 5*number_of_areas*x*x/(sigmaw);

%**************************************************************************
%Plot the irradiance map
figure;
[A,B] = meshgrid(-x/2:1:x/2, -x/2:1:x/2);%Creates a grid for the irradiance
```

```
surf(A,B,irradiance,'EdgeColor','none'); %data. Relates to x.
title('Irradiance Map at Resin Surface (mW/cm^2)');
xlabel('Z-mesh');
ylabel('Y-mesh');
view(2);

clear xpos ypos zpos w;

imwrite(irradiance,'irrad_map.bmp','bmp');

%************************************************************************
%Create the compensated bitmap.
%Convert the irradiance map into a grayscale bitmap.
ua = unique(irradiance); %returns irradiance but with no repetitions.
%The resulting vector is sorted in ascending order.
%Now find the min and max for grayscale scaling.
minIrr = ua(2);
maxIrr = max(ua);
%Mat2Gray treats minIrr as 0.0 = Black, maxIrr as 1.0 = white
CompensatedGrayscale = Mat2Gray(irradiance, [minIrr maxIrr]);
%imview(CompensatedGrayscale);
% Invert the grayscale colors, but need to keep background black.
for i=(1:1:x+1);
   for j=(1:1:x+1);
      if  (CompensatedGrayscale(i,j) == 1.00);
         CompensatedGrayscale(i,j) = 0.99; % Done to distinguish bright
                                  % areas from back when inverted.
      elseif (CompensatedGrayscale(i,j) == 0.00); %Here the black
                           % background 0.00 is changed to white so
         CompensatedGrayscale(i,j) = 1.00; %that it is black when it
      end                              %gets inverted.
   end
end

%Now invert the grayscale colors
InvertedGrayscale = 1 - CompensatedGrayscale;
%imview(InvertedGrayscale);
%For most cases, the profile needs to be brightened. So brighten by 0.50
for i=(1:1:x+1);
   for j=(1:1:x+1);
```

```
        if (InvertedGrayscale(i,j) > 0.00);
            InvertedGrayscale(i,j) = 0.50+InvertedGrayscale(i,j);
        end
    end
end
imview(InvertedGrayscale);
imwrite(InvertedGrayscale,'InvertedGrayscale_map.bmp','bmp');
for i=(1:1:x+1);
    for j=(1:1:x+1);
        if (InvertedGrayscale(i,j) > 0.00);
            InvertedGrayscale(i,j) = 1.00;
        end
    end
end
imview(InvertedGrayscale);
imwrite(InvertedGrayscale,'InvertedBW_map.bmp','bmp');

%*************************************************************************
%Now work out the cure depth for each row using the cure depth equation.
%Values for DSM Somos 10120 resin (Dp = 0.16mm and Ec = 9.7mJ/cm^2)
%Values for SL7545 resin (Dp = 0.16764mm and Ec = 9.6mJ/cm^2):
Dp = 0.16764; %mm NOTE: 1mils = 0.0254mm
Ec = 9.6;   %mJ/cm^2
TOE = 45;    %time of exposure for Bitmap in seconds.
Cd = Dp.*log(irradiance*TOE/Ec);
%Now because log(0) = -inf, where -inf is in the Cd matrix it must be
%changed to = 0. And -ve real numbers mean not enough irradiance to cure so
%must all so = 0. All other values are inverted so that the graph shows
%depth rather than height.
for i=(1:1:x+1);
    for j=(1:1:x+1);
        if (isinf(Cd(i,j))== 1 || Cd(i,j) < 0);
            Cd(i,j) = 0;
        elseif (Cd(i,j) > 0);
            Cd(i,j) = -Cd(i,j);
        end
    end
end
%Create a grid for the irradiance data. Relates to x
figure;
```

```
[A,B] = meshgrid(-x/2:1:x/2, -x/2:1:x/2);
surf(A,B,Cd,'EdgeColor','none');
title('3D View of Cure Depth (Cd)');
xlabel('Z-axis (mm)');
ylabel('Y-axis (mm)');
zlabel('Cd (mm)');
view(3);
%plot cross sections of the cure depth across the middle of the image.
figure;
subplot(2,1,1);
zaxis = [-build_envelope/2:build_envelope/x:build_envelope/2];
ydepth = Cd(x/2,:);
plot(zaxis,ydepth,'-');
title('Cross Section View of Cure Depth (Cd) Through Centre of Z-axis');
xlabel('Z-axis (mm)');
ylabel('Cure Depth (mm)');
subplot(2,1,2);
ydepth = Cd(:,x/2);
plot(zaxis,ydepth,'-');
title('Cross Section View of Cure Depth (Cd) Through Centre of Y-axis');
xlabel('Y-axis (mm)');
ylabel('Cure Depth (mm)');
```

15 Appendix C: SLA CAD Drawings

The following drawings were created using SolidWorks. Note that the drawings may not be to the scale written in the drawing due the page size constraints.

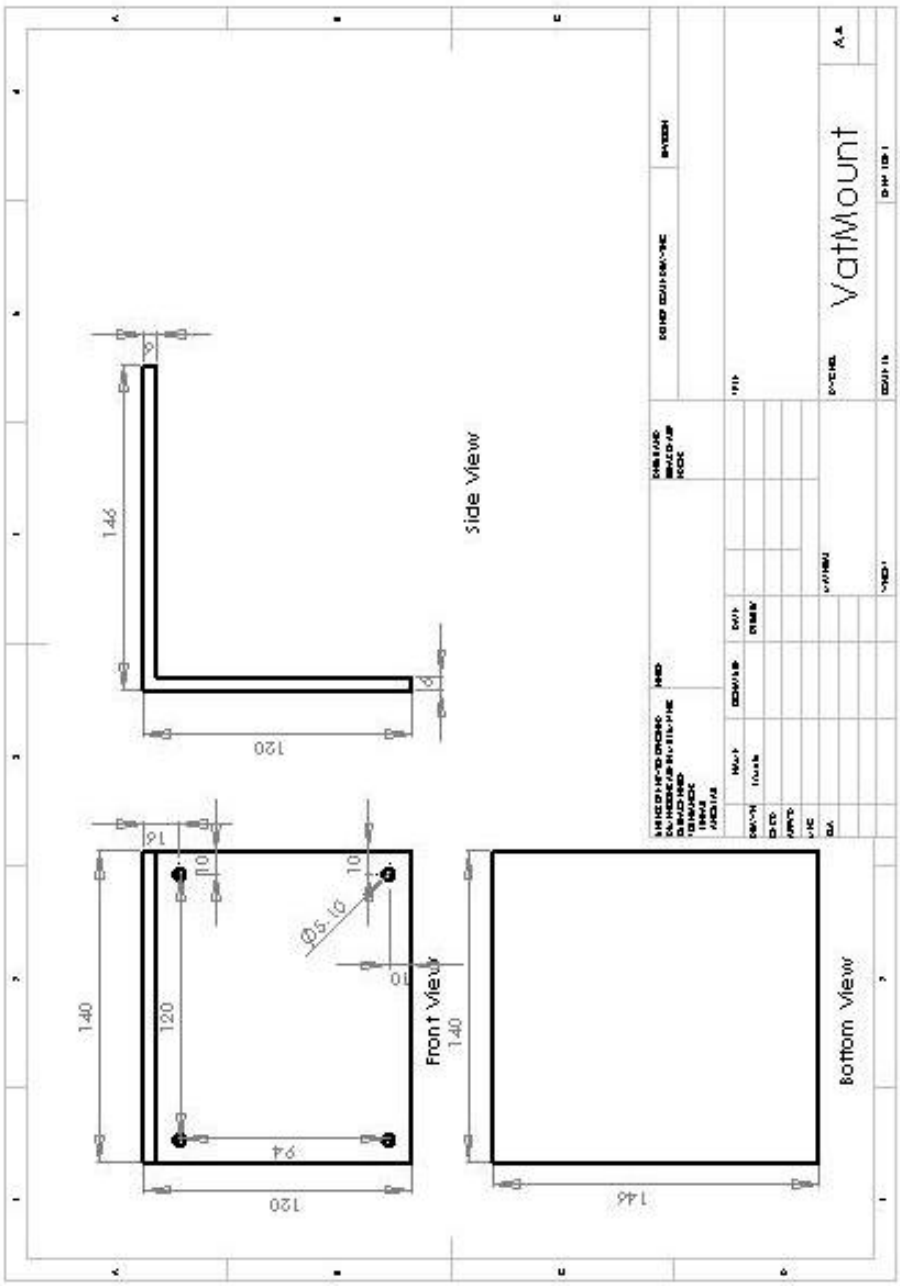

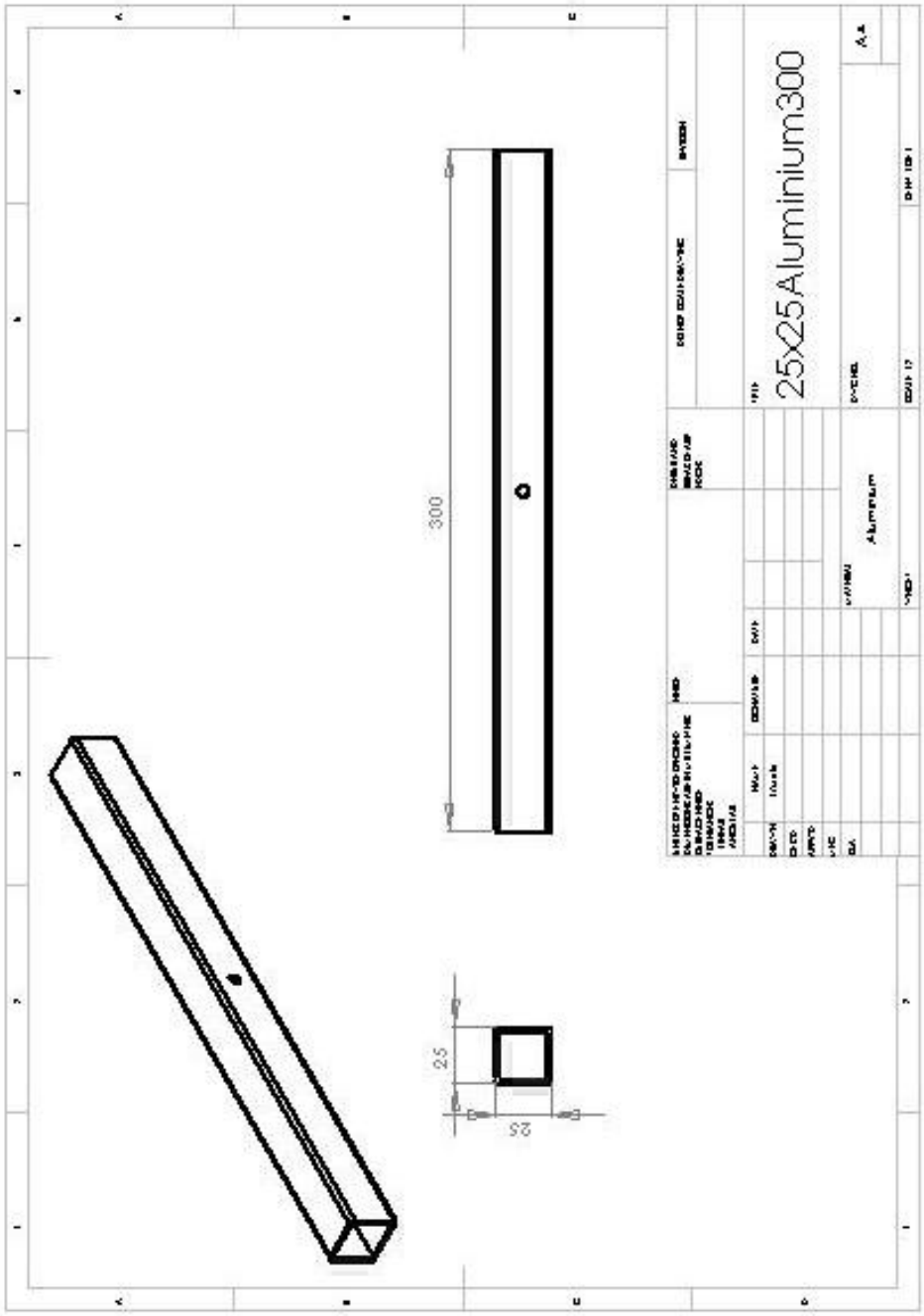
300
25
25
25x25Aluminium300
Aluminium
A4

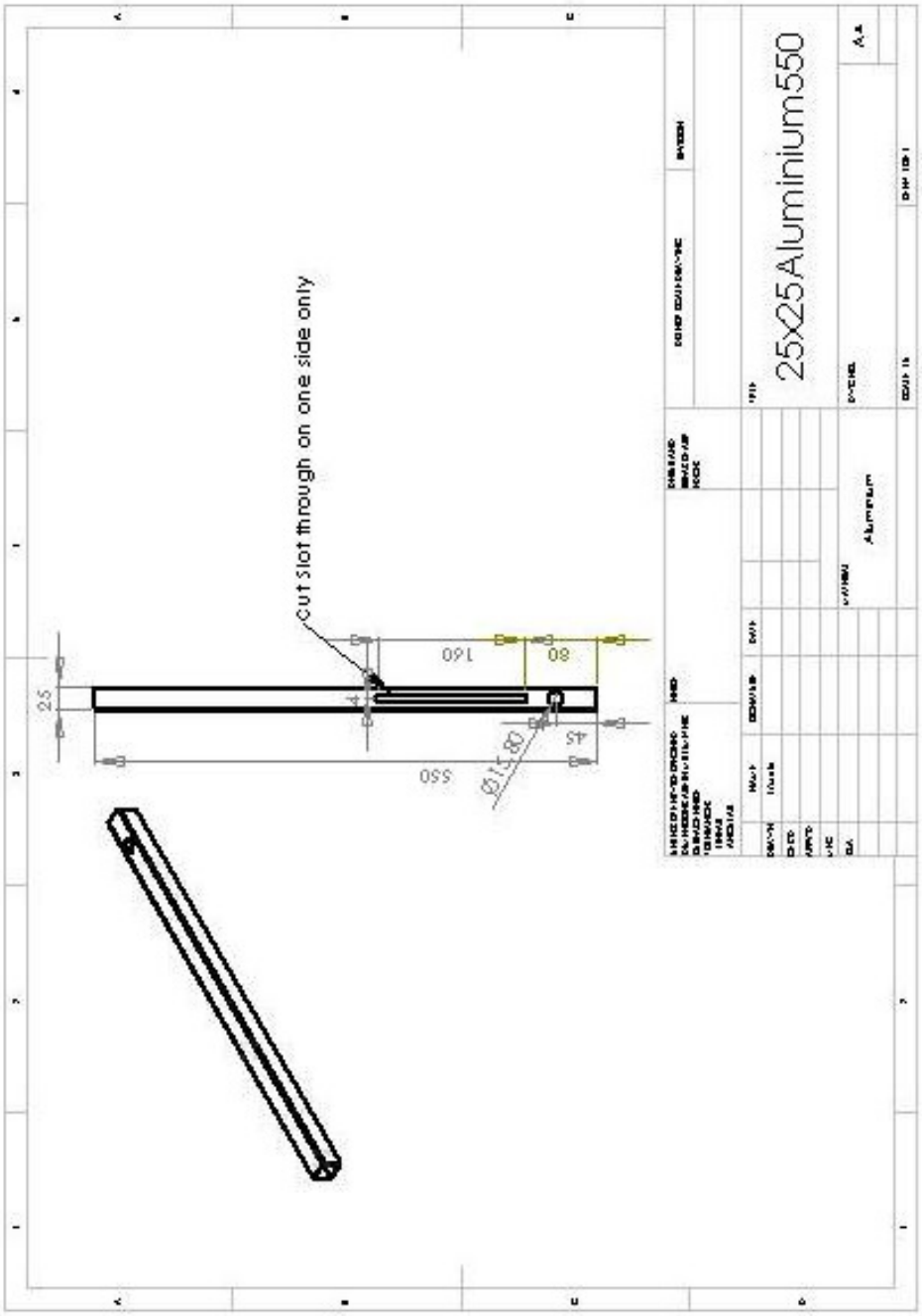
Cut Slot through on one side only
160
80
25
4
45
550
Ø13.80
25x25Aluminium550
Aluminium

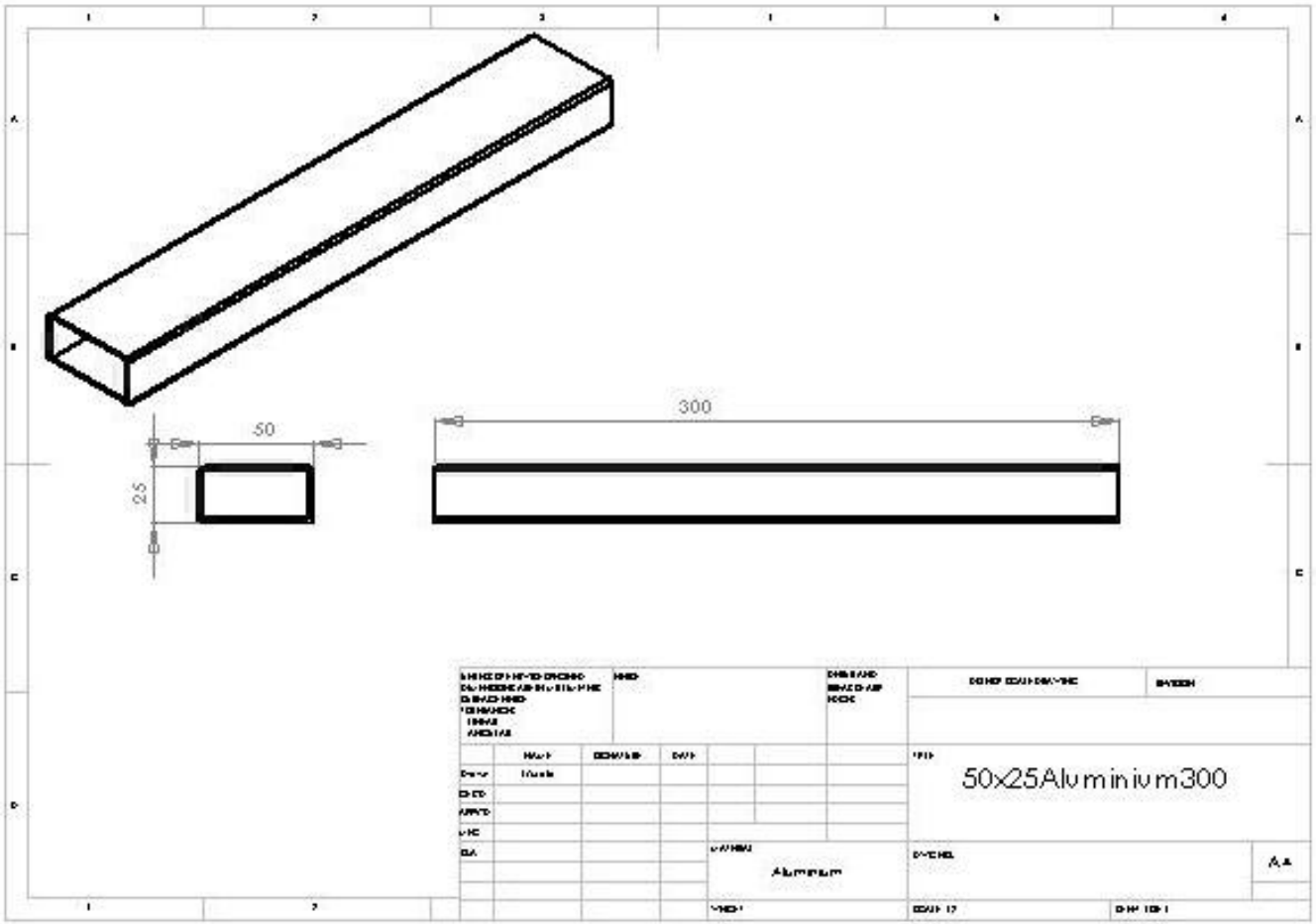
50
25
300
50x25Aluminium300
Aluminium

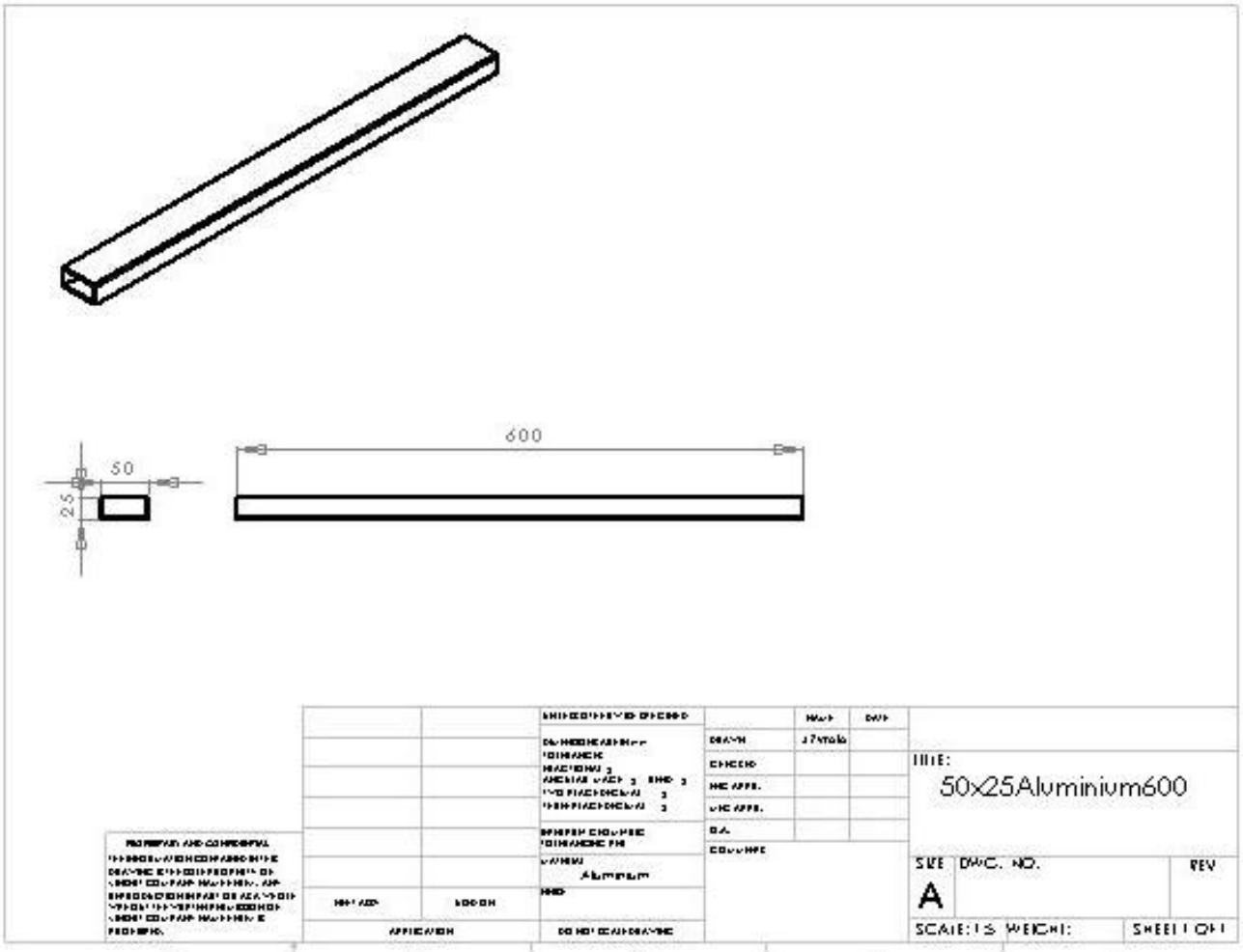
600
50
25
Aluminium
A
50x25Aluminium600

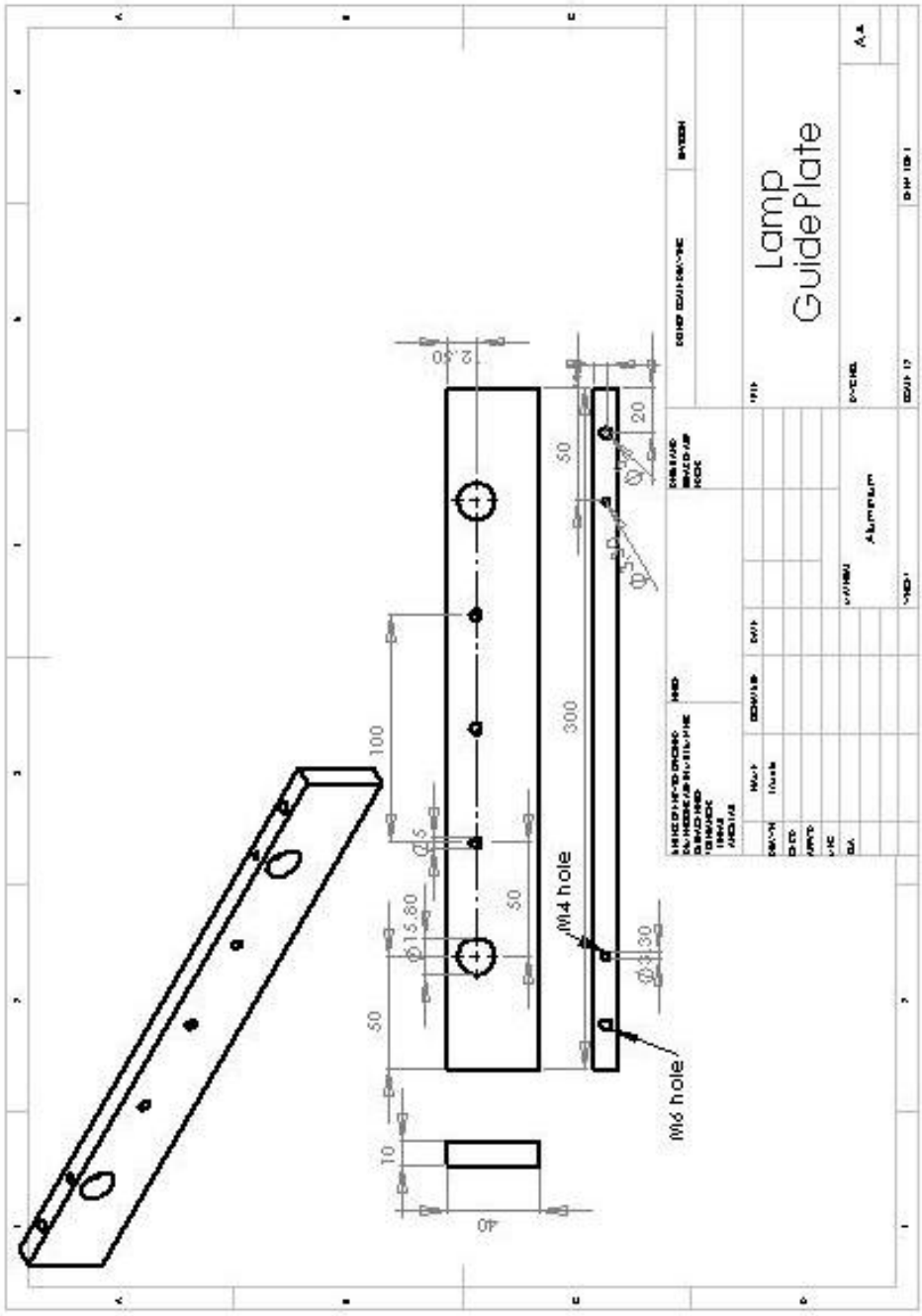
Lamp
GuidePlate
Aluminium
M4 hole
M6 hole
100
300
50
50
40
10
20
Ø5
Ø15.80
Ø13.30

Lid Required
Bottom View
150
150
Front View
80
80
70
20
Right Side View
Left Side View
20
15
20
60
70
5
R2.50
LampBox

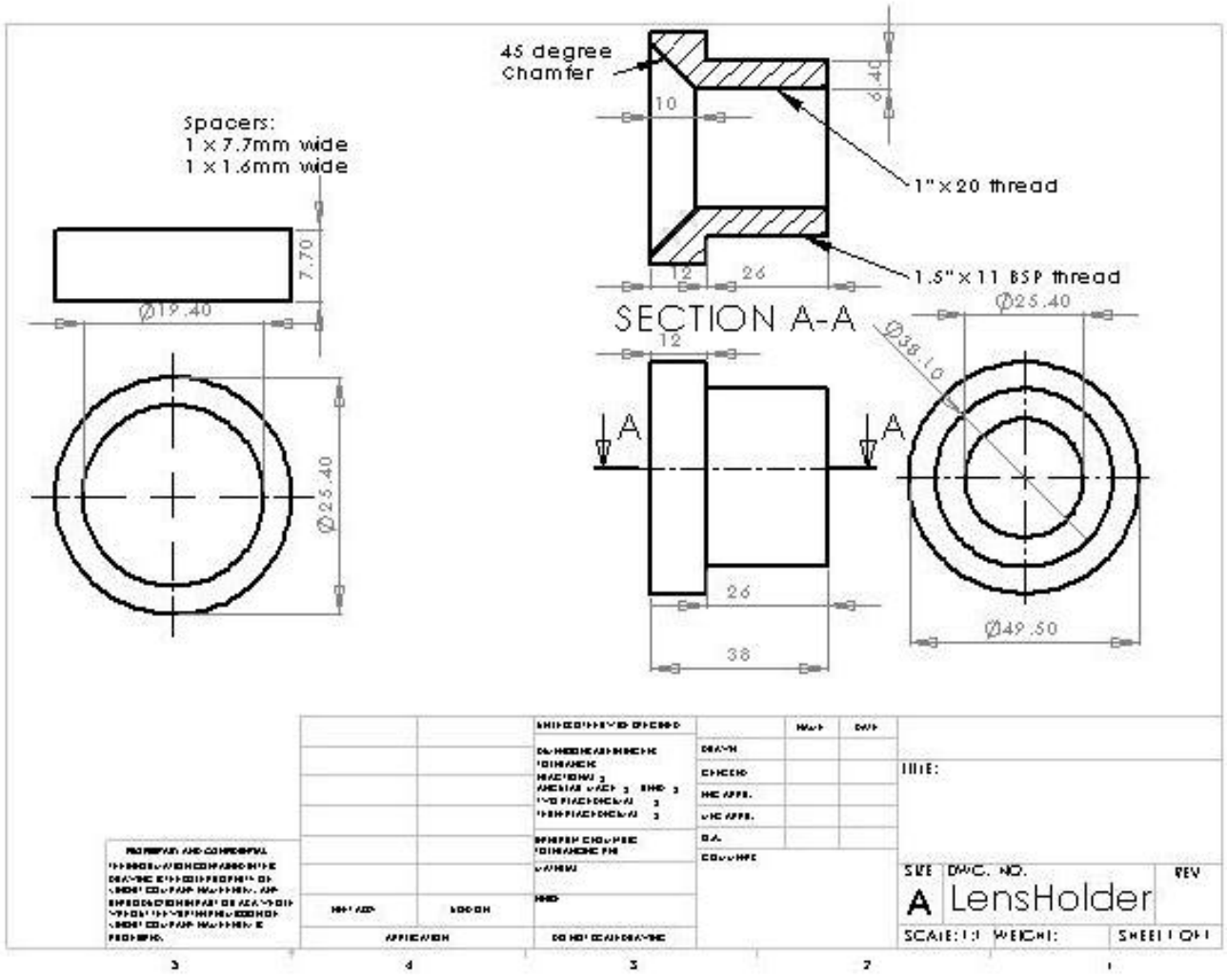
45 degree
Chamfer
10
6.40
1" x 20 thread
1.5" x 11 BSP thread
12
26
SECTION A-A
Ø25.40
Ø38.10
12
A
A
26
38
Ø49.50
Spacers:
1 x 7.7mm wide
1 x 1.6mm wide
7.70
Ø19.40
Ø25.40
SIZE
A
DWG. NO.
LensHolder
REV
SCALE: 1:1
WEIGHT:
SHEET 1 OF 1

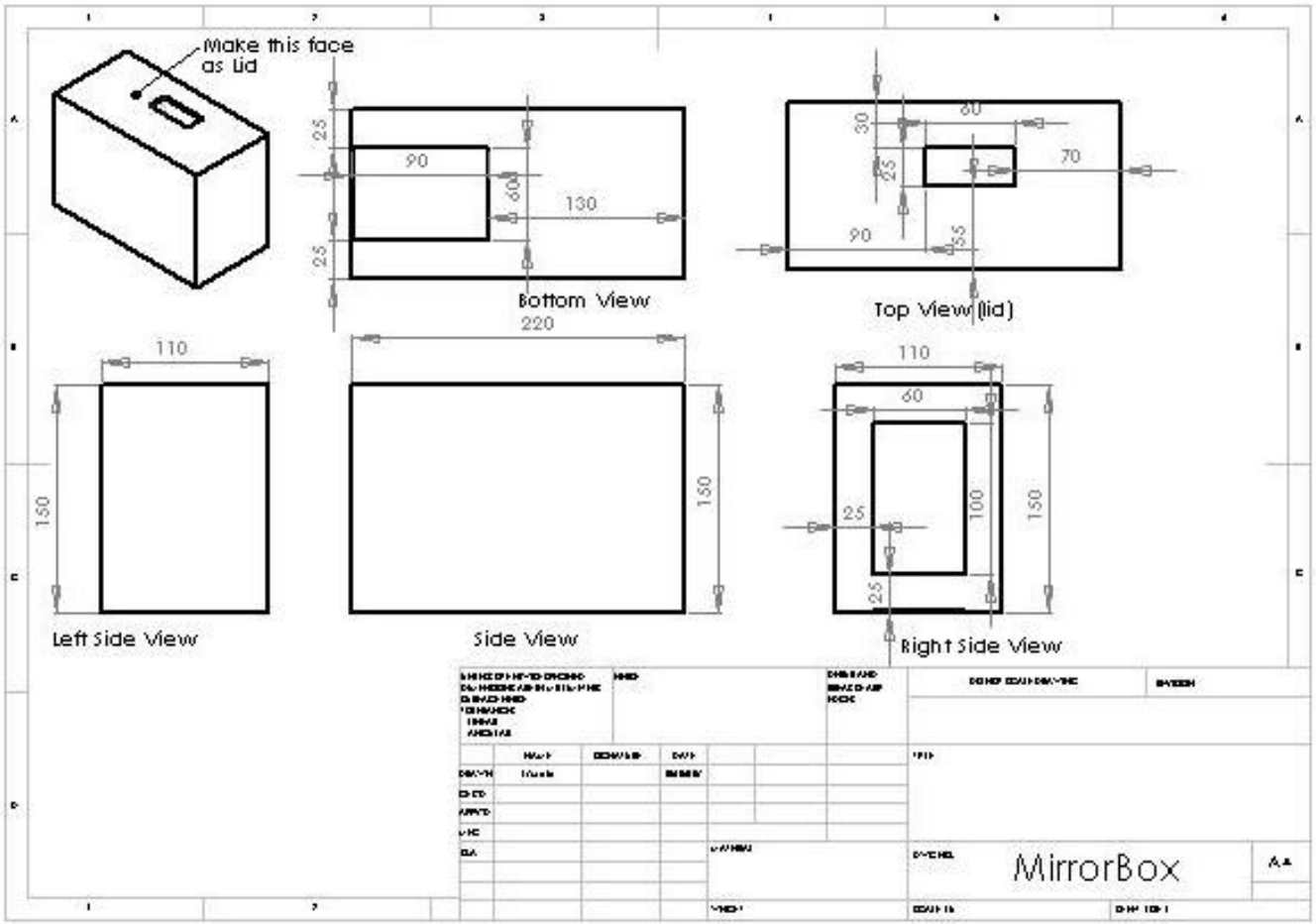
Make this face as Lid
25
90
60
130
25
Bottom View
30
60
25
70
90
55
Top View (lid)
110
150
Left Side View
220
150
Side View
110
60
25
100
150
25
Right Side View
MirrorBox
A4

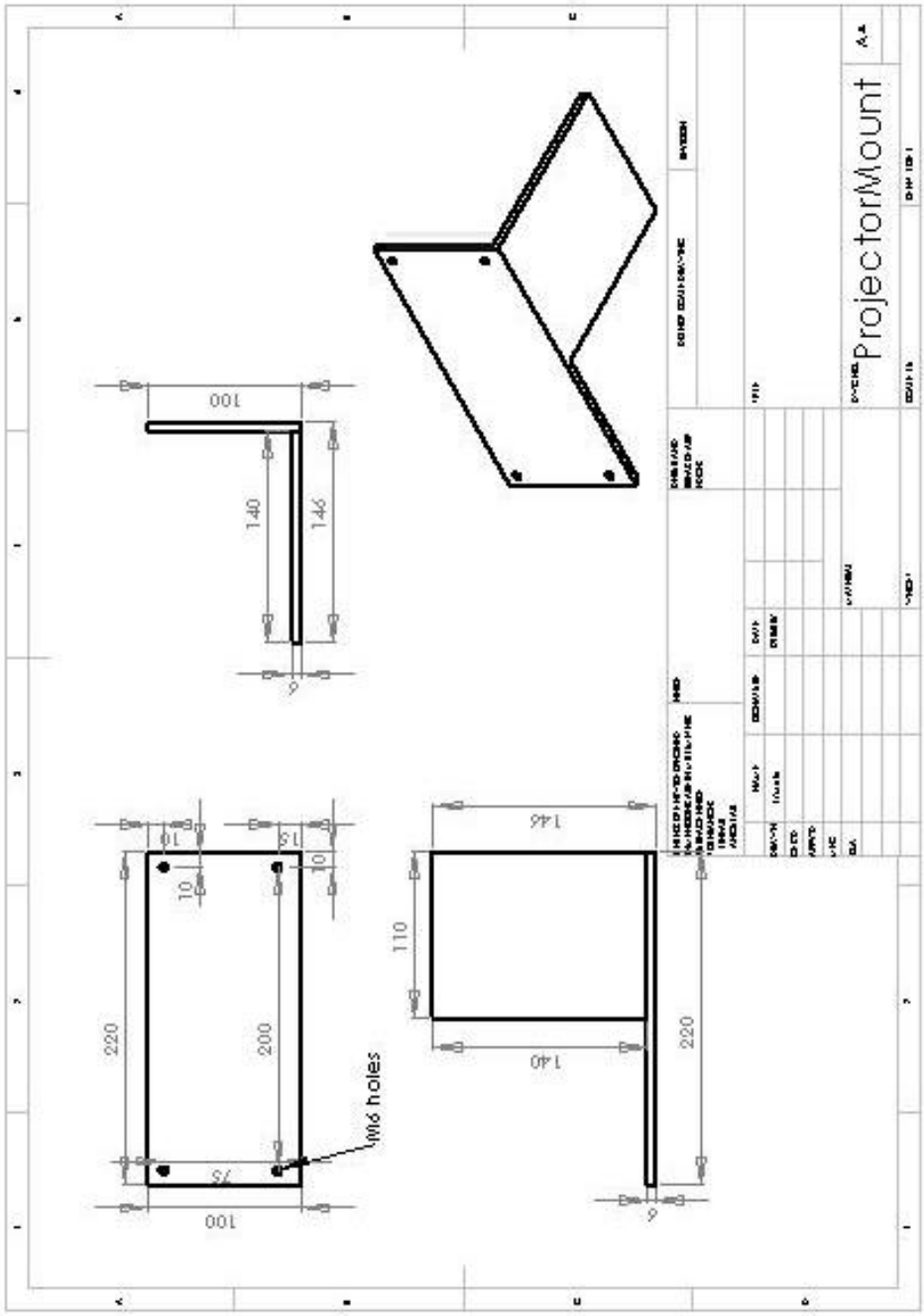
ProjectorMount
100
140
146
6
146
110
140
220
6
10
10
15
10
220
200
M6 holes
75
100

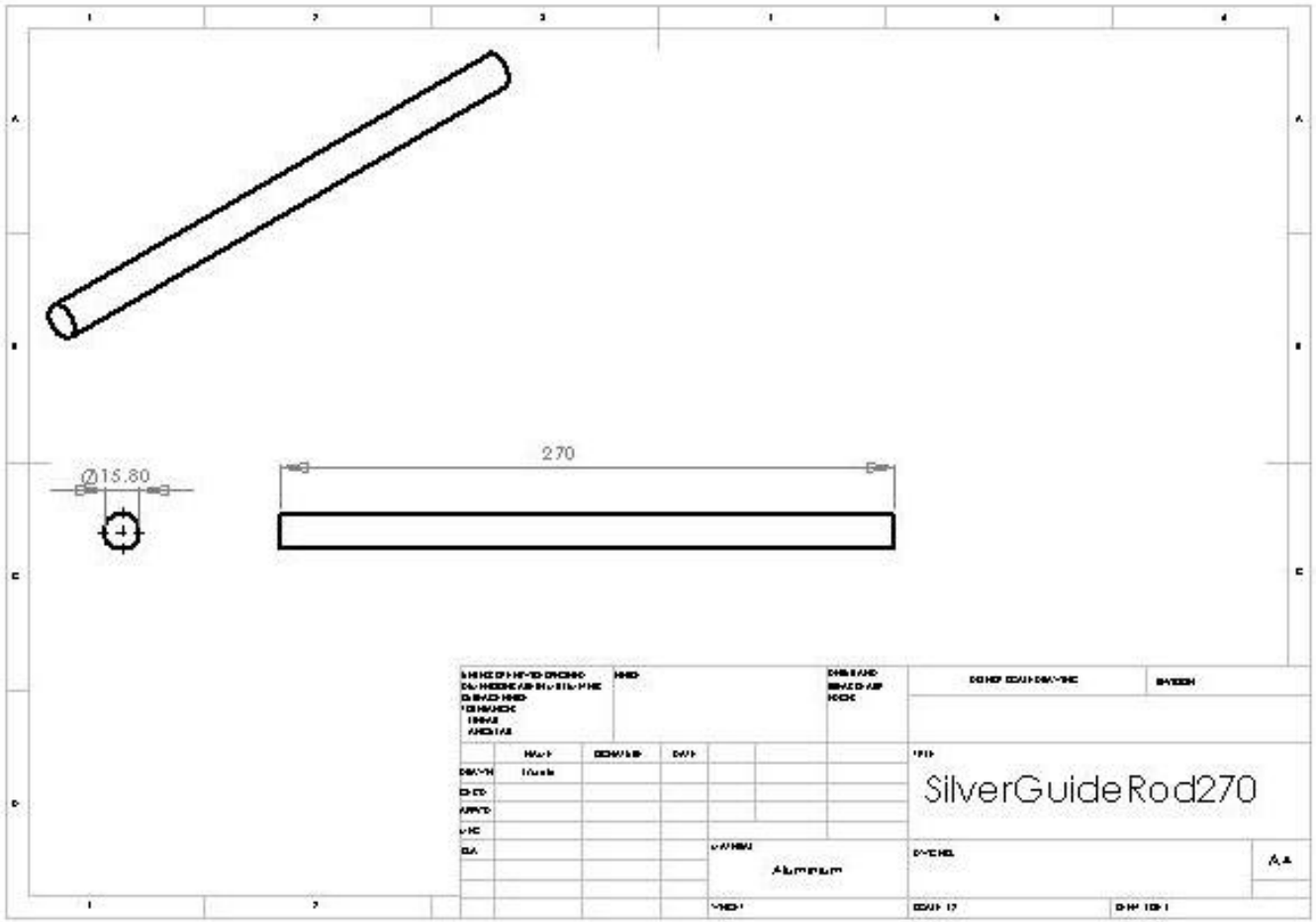
Ø15.80
270
Aluminum
SilverGuideRod270

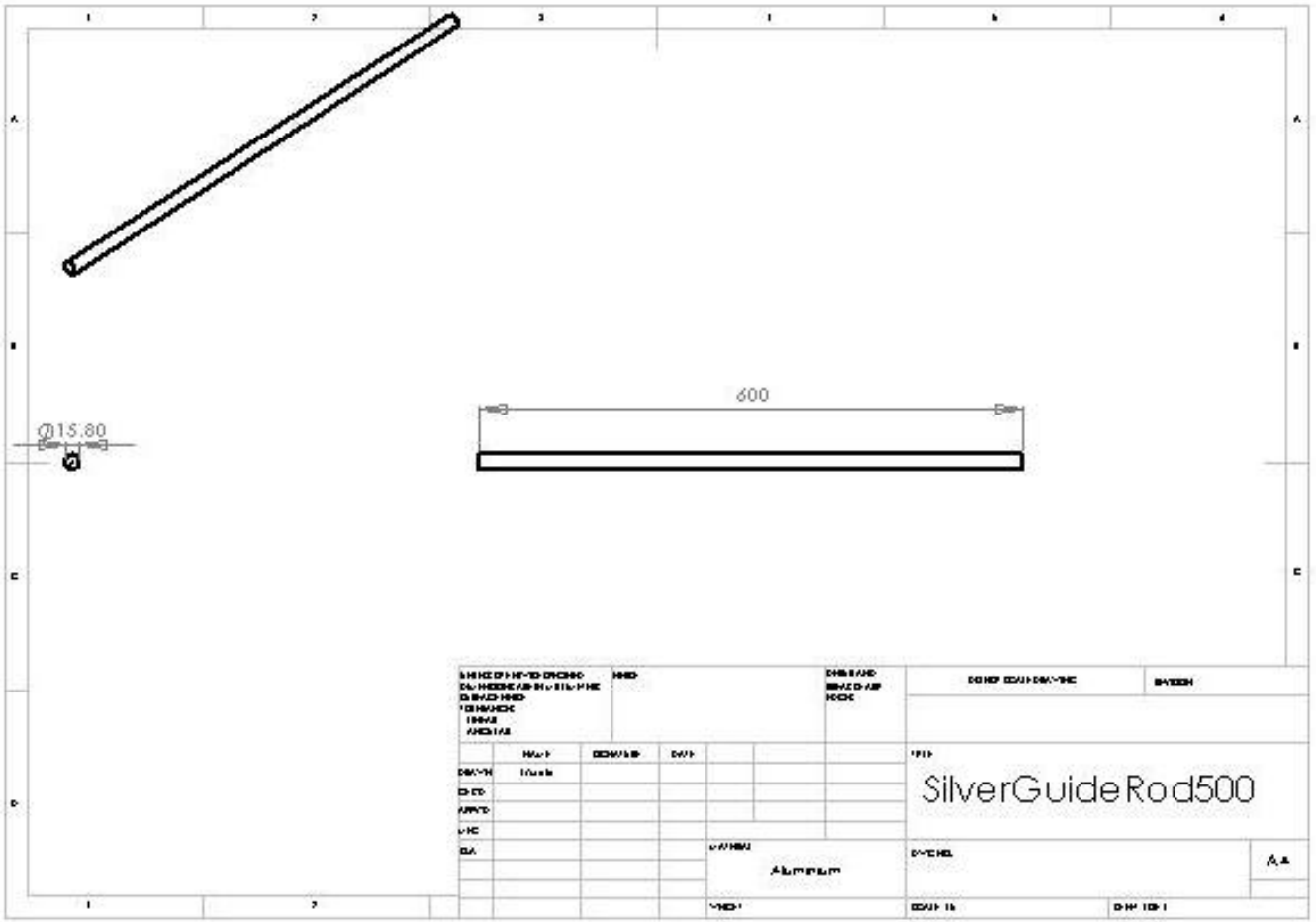
Ø15.80
600
Aluminum
SilverGuideRod500
A4

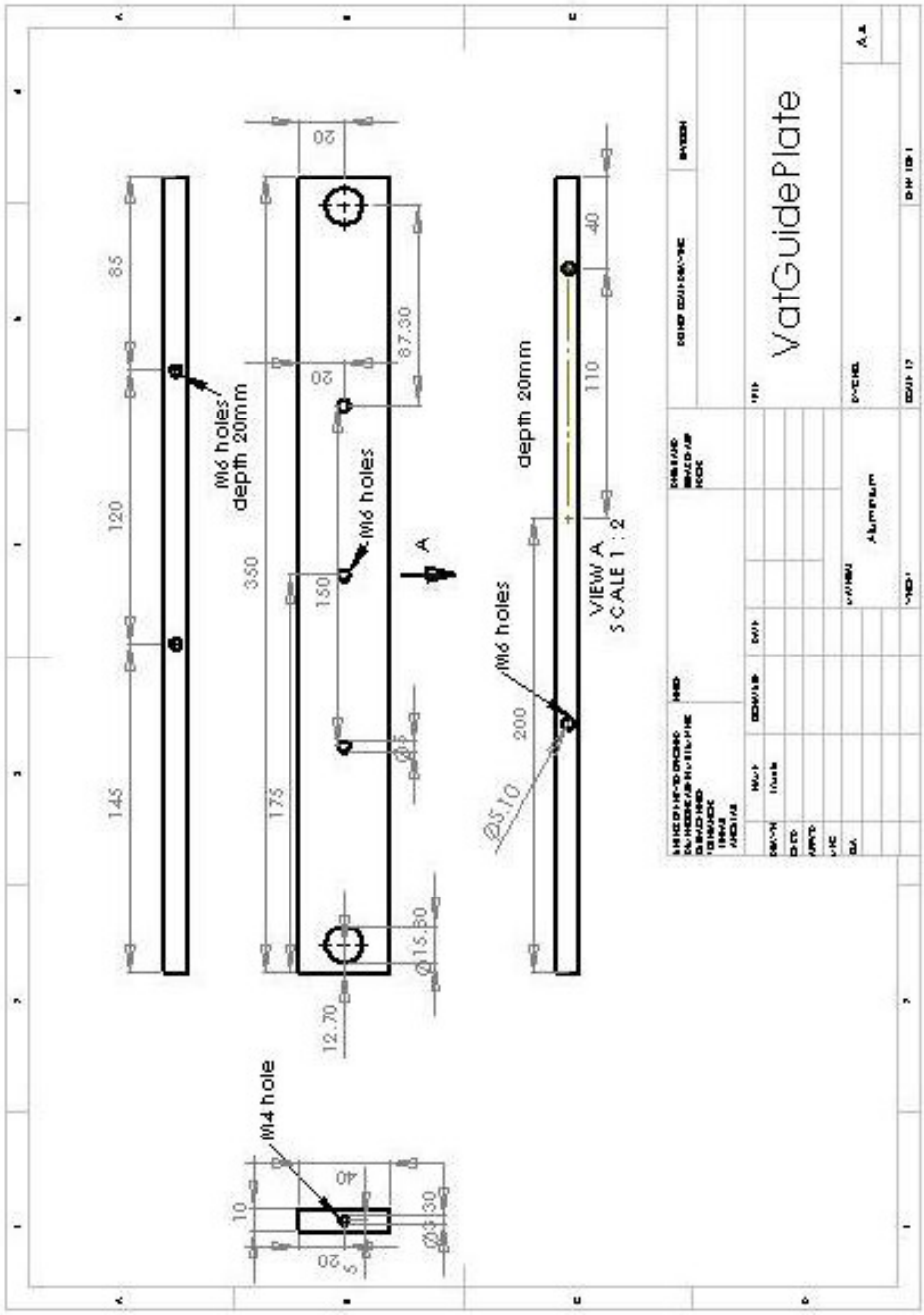
VatGuidePlate
M6 holes
depth 20mm
M6 holes
M6 holes
depth 20mm
M4 hole
VIEW A
SCALE 1 : 2
A
Aluminium
A4
85
120
145
175
350
150
87.30
20
40
110
200
12.70
10
30
Ø5.10
Ø15.80

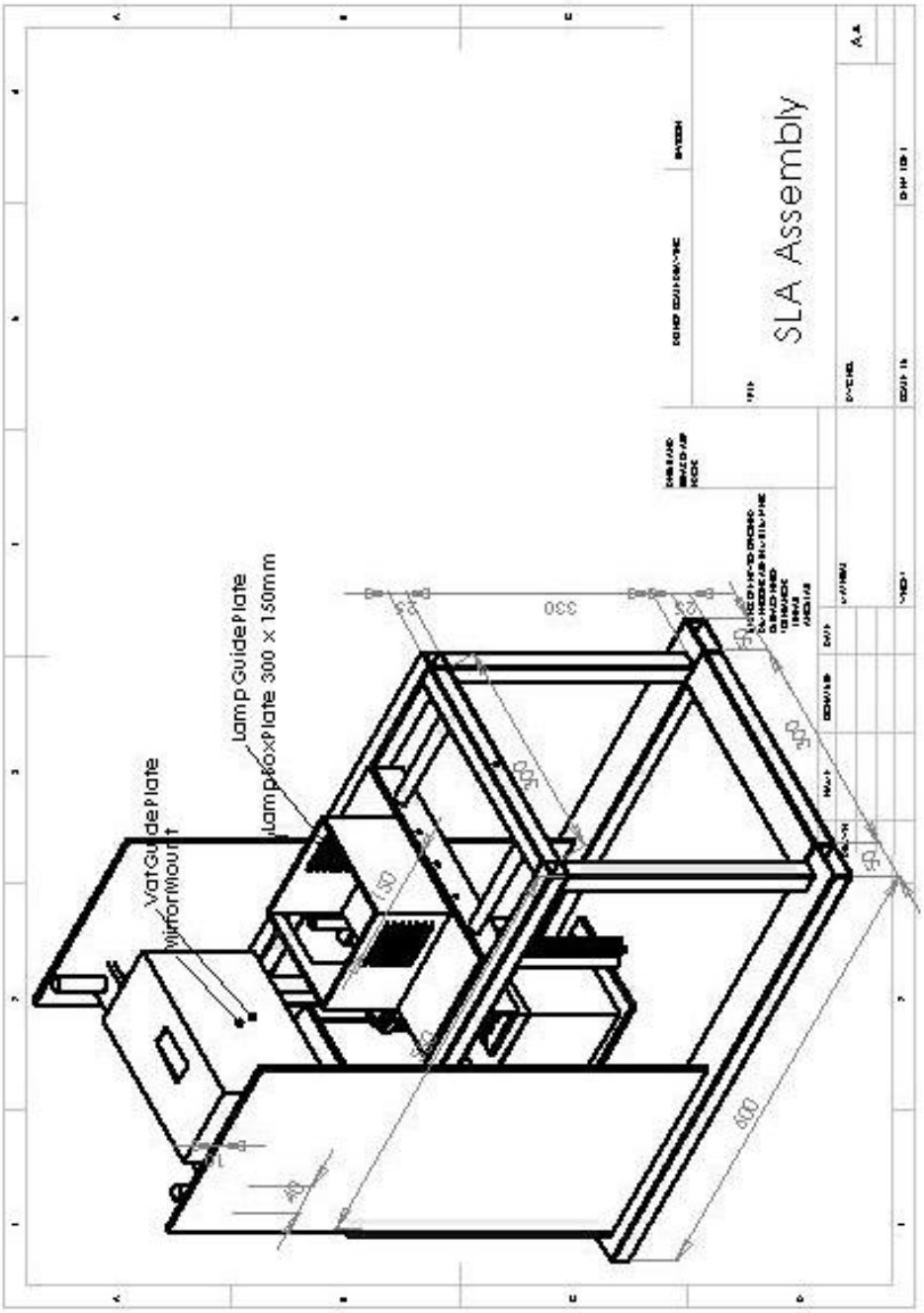
SLA Assembly
Lamp Guide Plate
Lamp Box Plate 300 x 150mm
Vat Guide Plate
Mirror Mount
330
600

16 Appendix D: Experimental Layers

The following images are photographs of the cross-section of the arrow shaped layer cut approximately across the base of the main triangle. The photo graphs were taken with a ZEISS Stemi 2000-C microscope with an attached Canon PowerShot A640 digital camera (10.0megaPixels) at F/3.5. Photos are taken with a ruler scale present. Measurements are taken by counting the number of pixels between two adjacent markings of the ruler in the photo. The distance between two marks indicates 0.5mm. The ratio of pixels per 0.5mm is used find a distance in the photo.

The figures are named according to the following convention:

1-2_45CN = set 1, second exposure, 45sec exposure time, photo of layer centre, Natural (all mirrors on) bitmap projected.

2-1_55LC = set 2, first exposure, 55sec exposure time, photo of layer left, Compensated bitmap projected.

So that's set number, exposure number, exposure time, centre right or left, Natural Compensated or Test (outer border lighter than interior).

16.1 Photos of Cross-sections

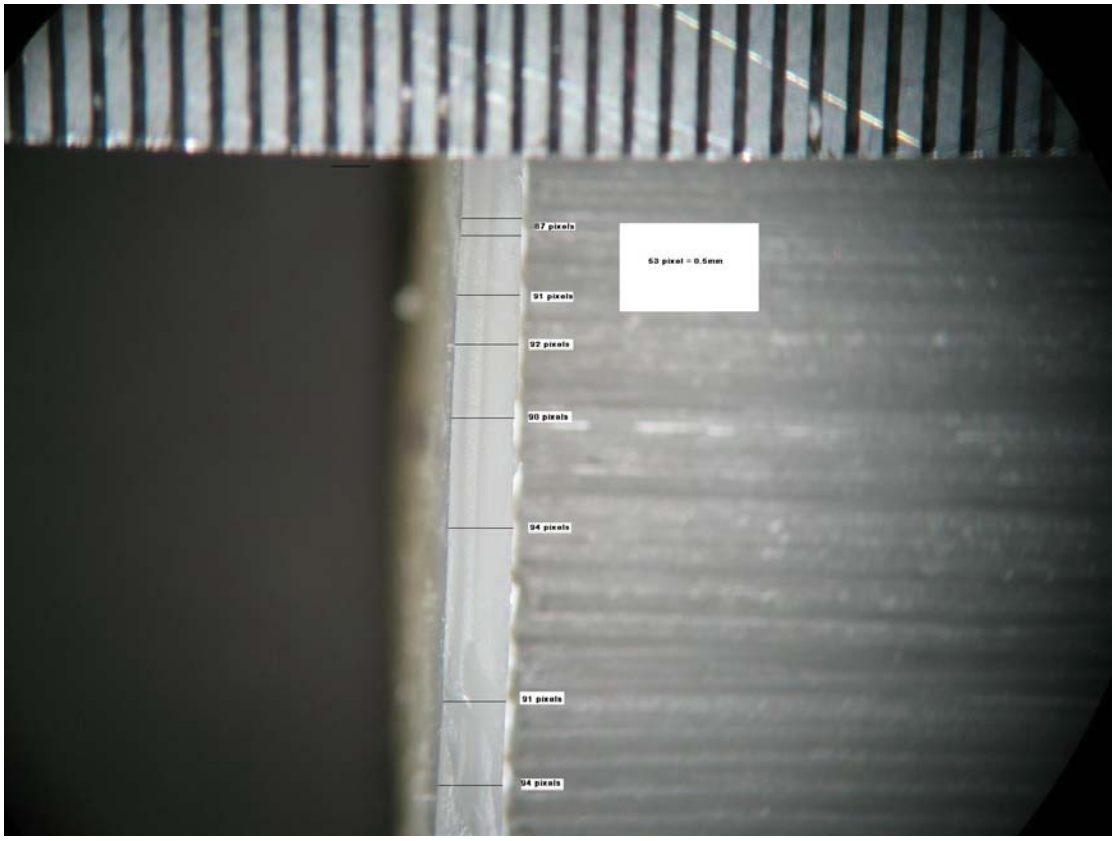

Figure 16.1 Sample 1-1_45CN

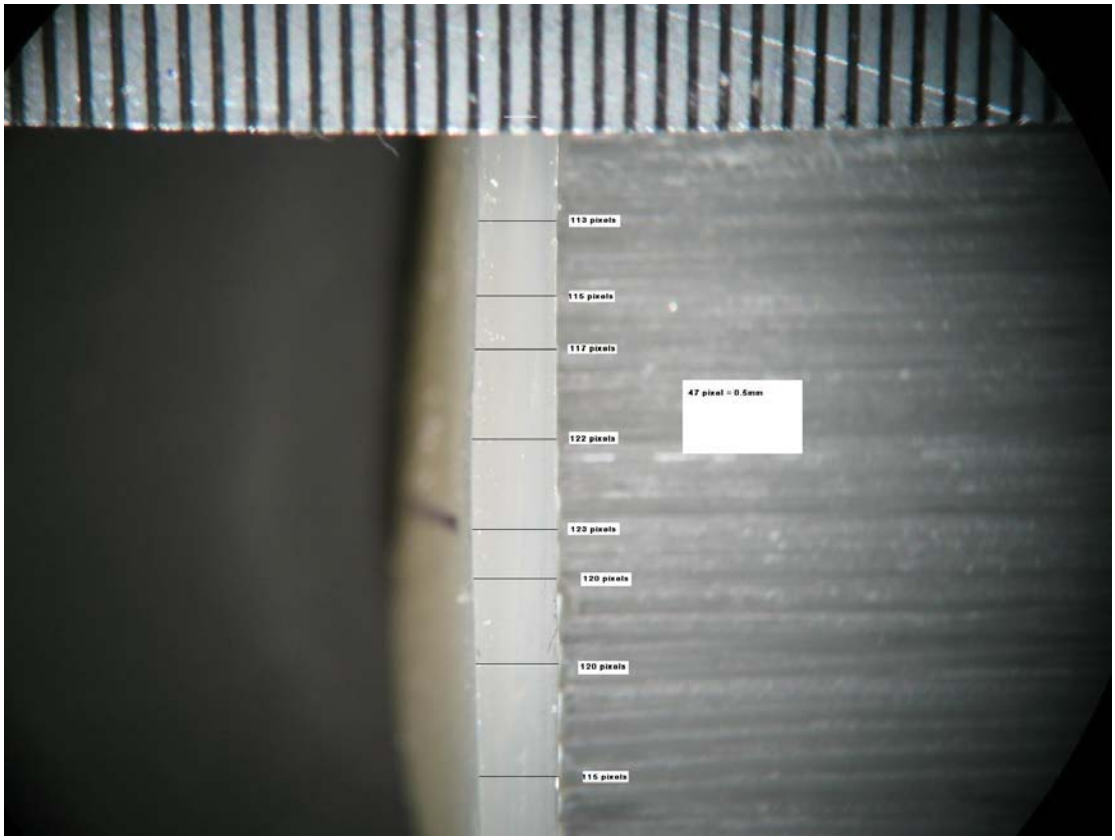

Figure 16.2 Sample 1-1_50CN

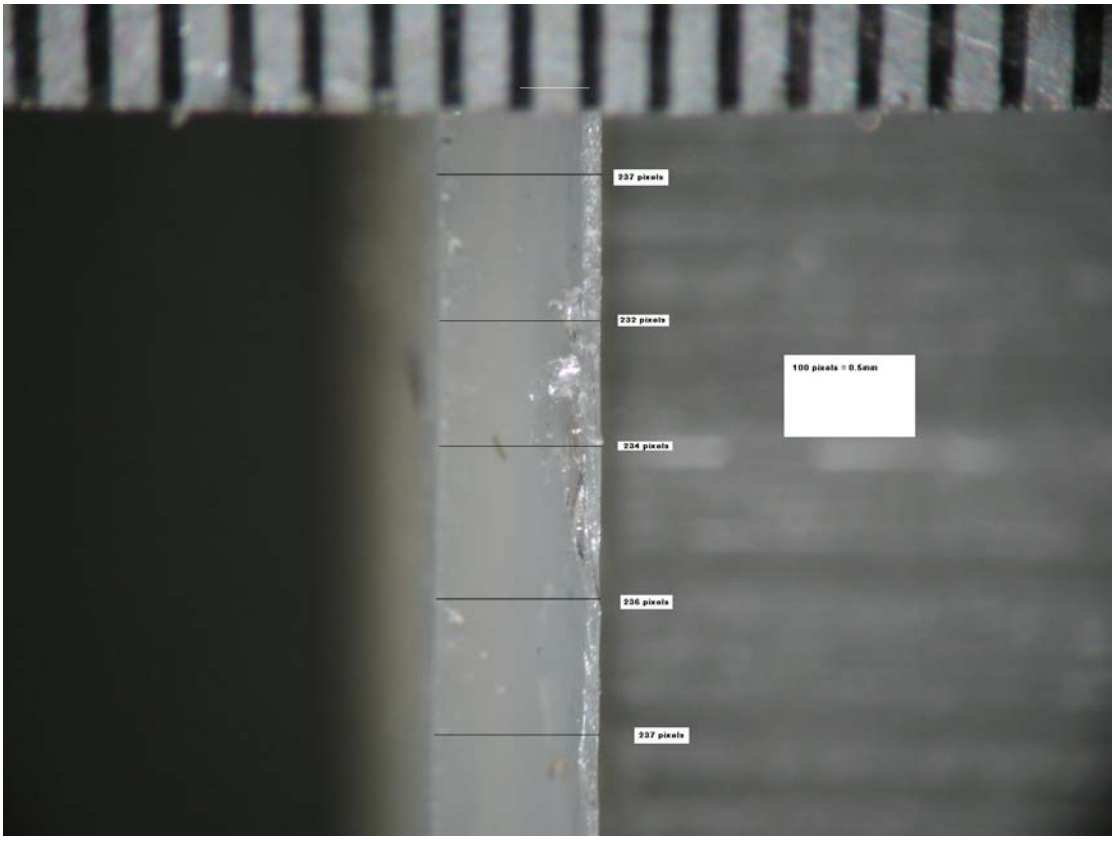

Figure 16.3 Sample 1-2_45CN

Figure 16.4 Sample 1-2_50CN

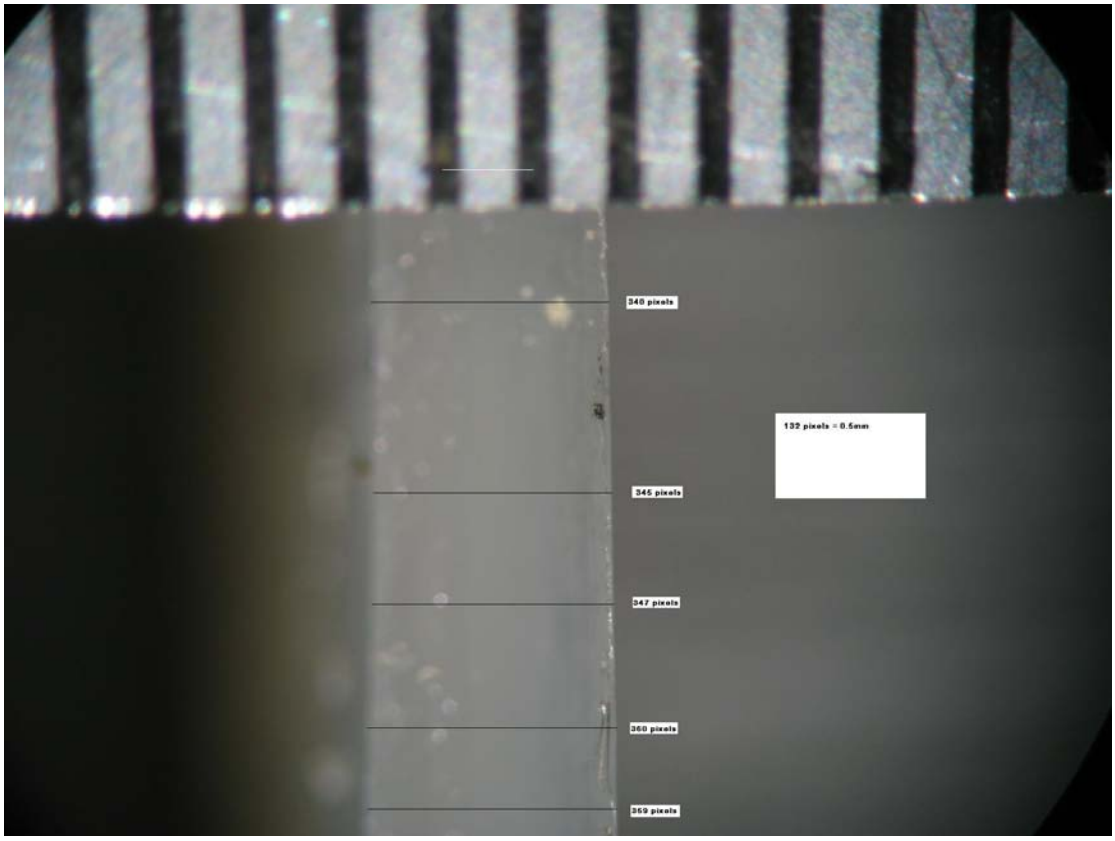

Figure 16.5 Sample 1-2_55CN

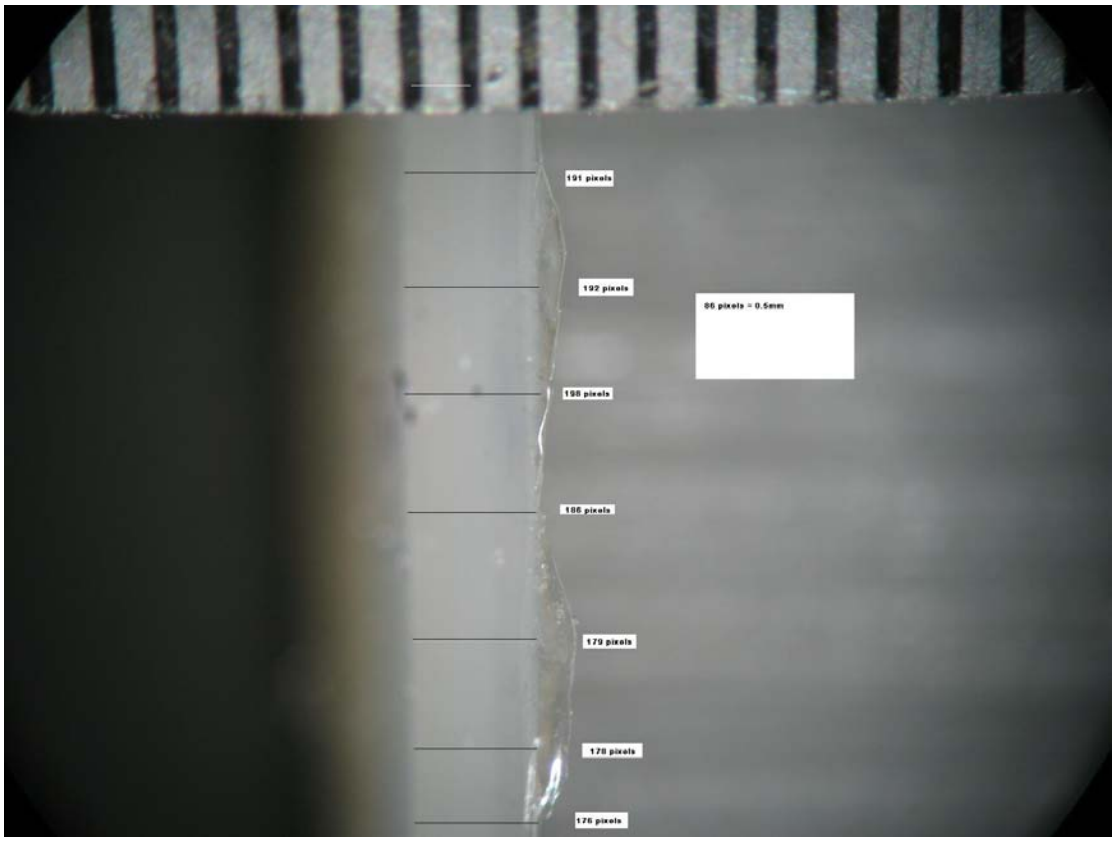

Figure 16.6 Sample 2-1_45CC

Figure 16.7 Sample 2-1_50CC

Figure 16.8 Sample 2-1_55CC

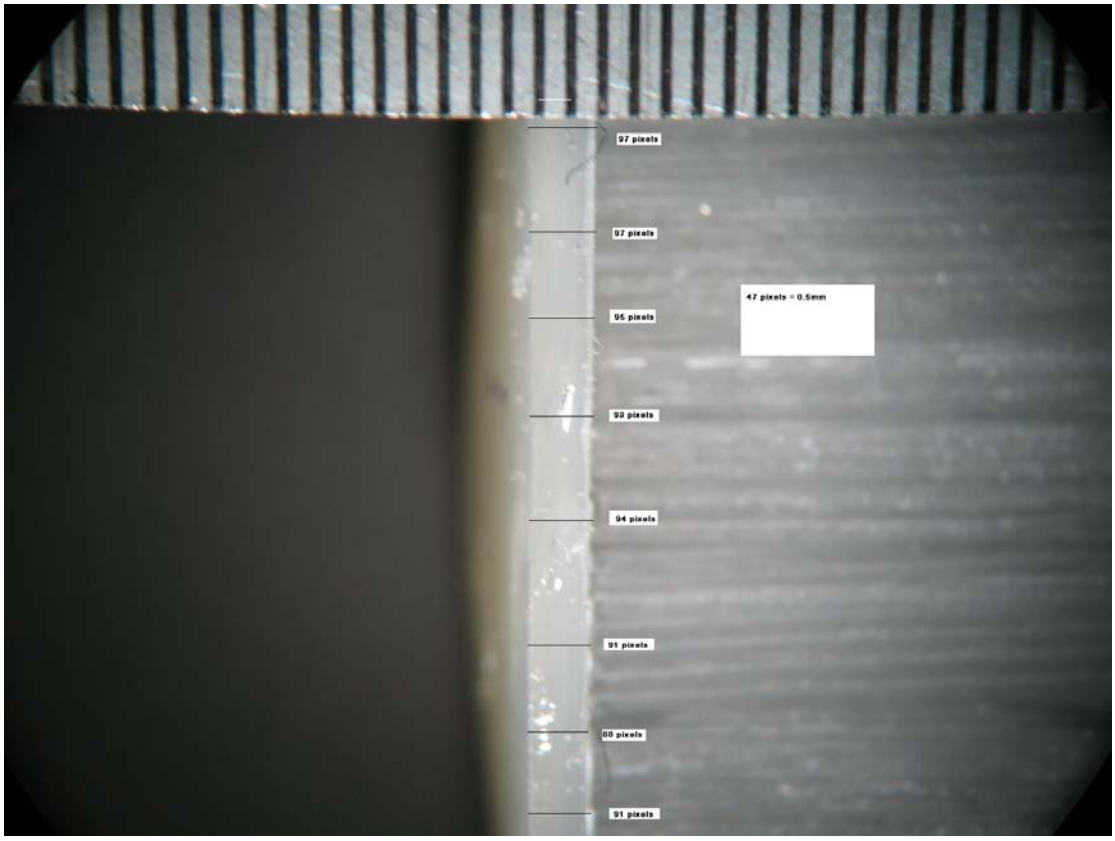

Figure 16.9 Sample 2-2_45CC

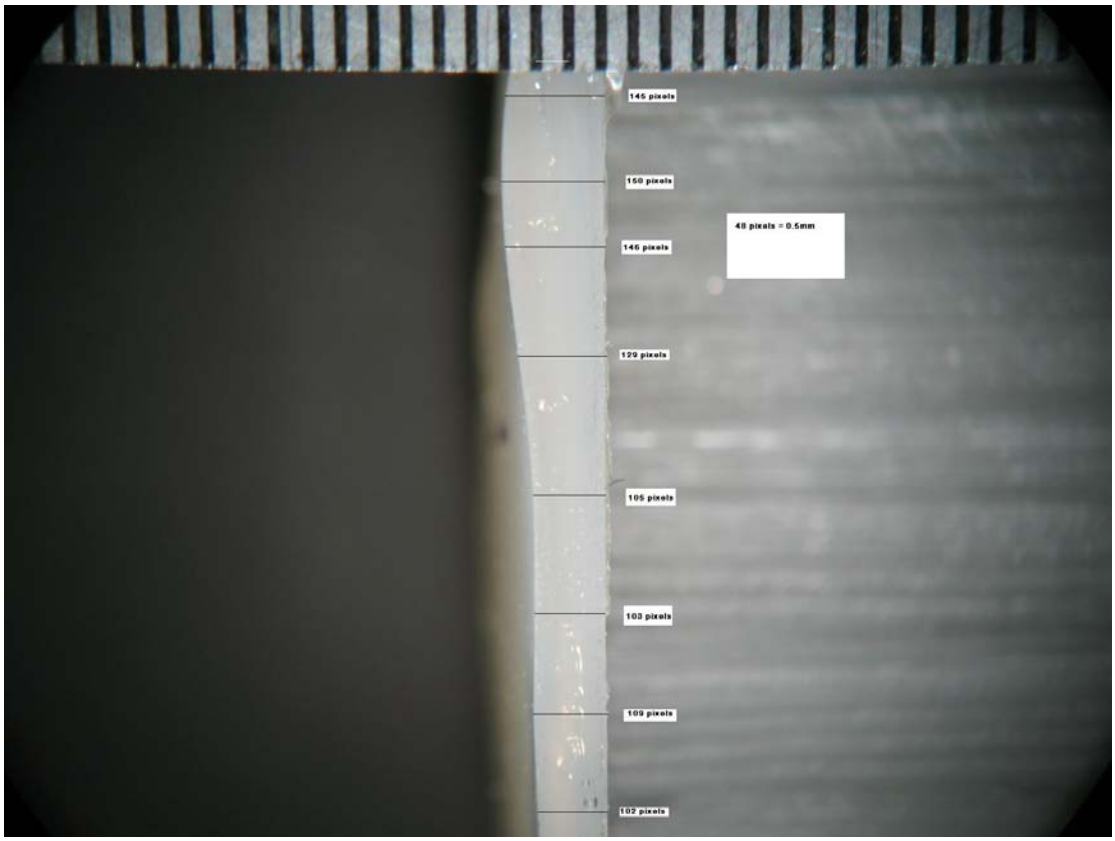

Figure 16.10 Sample 2-2_50CC

Figure 16.11 Sample 2-2_55CC

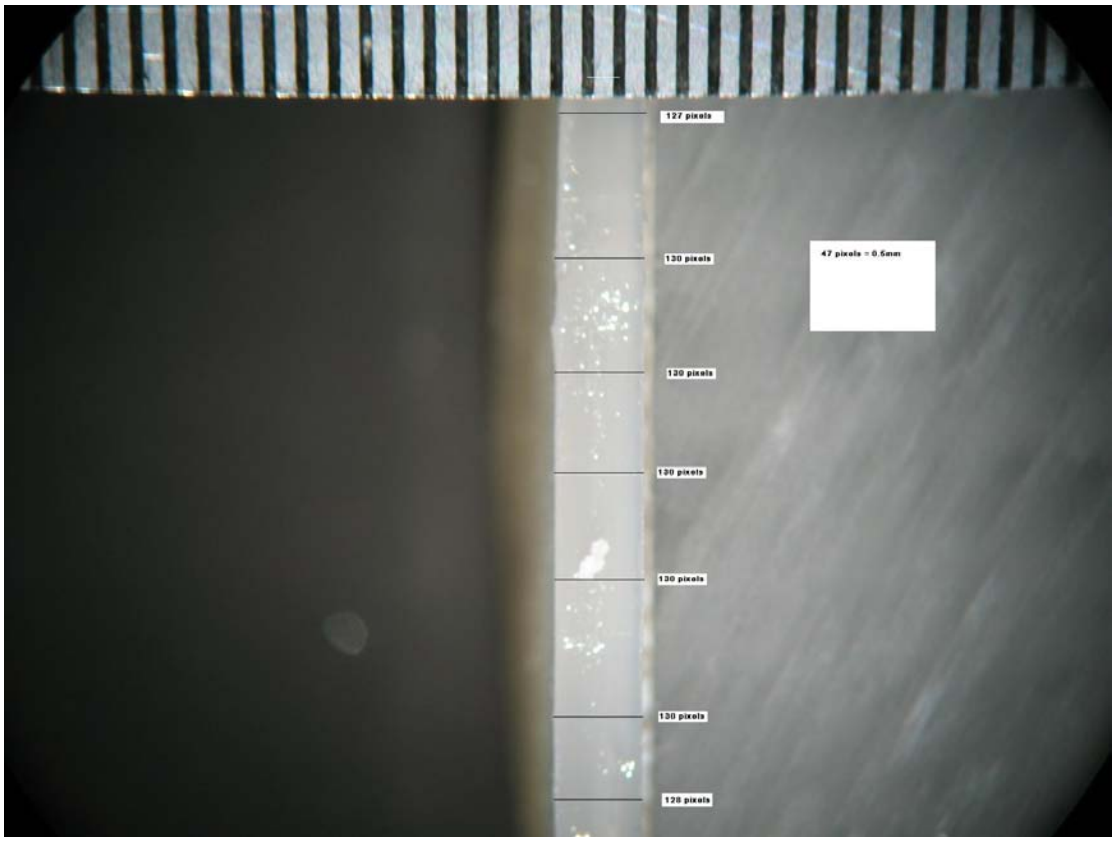

Figure 16.12 Sample 3-1_115CT

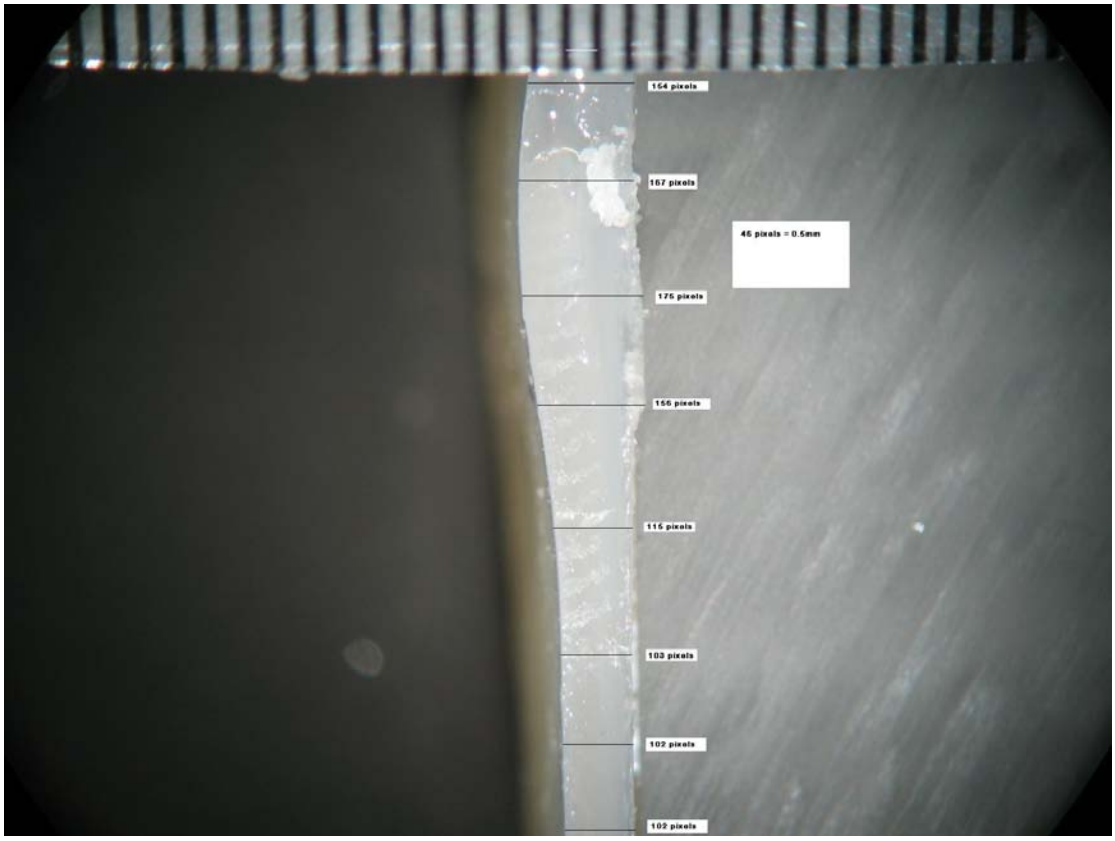

Figure 16.13 Sample 3-1_120bCT

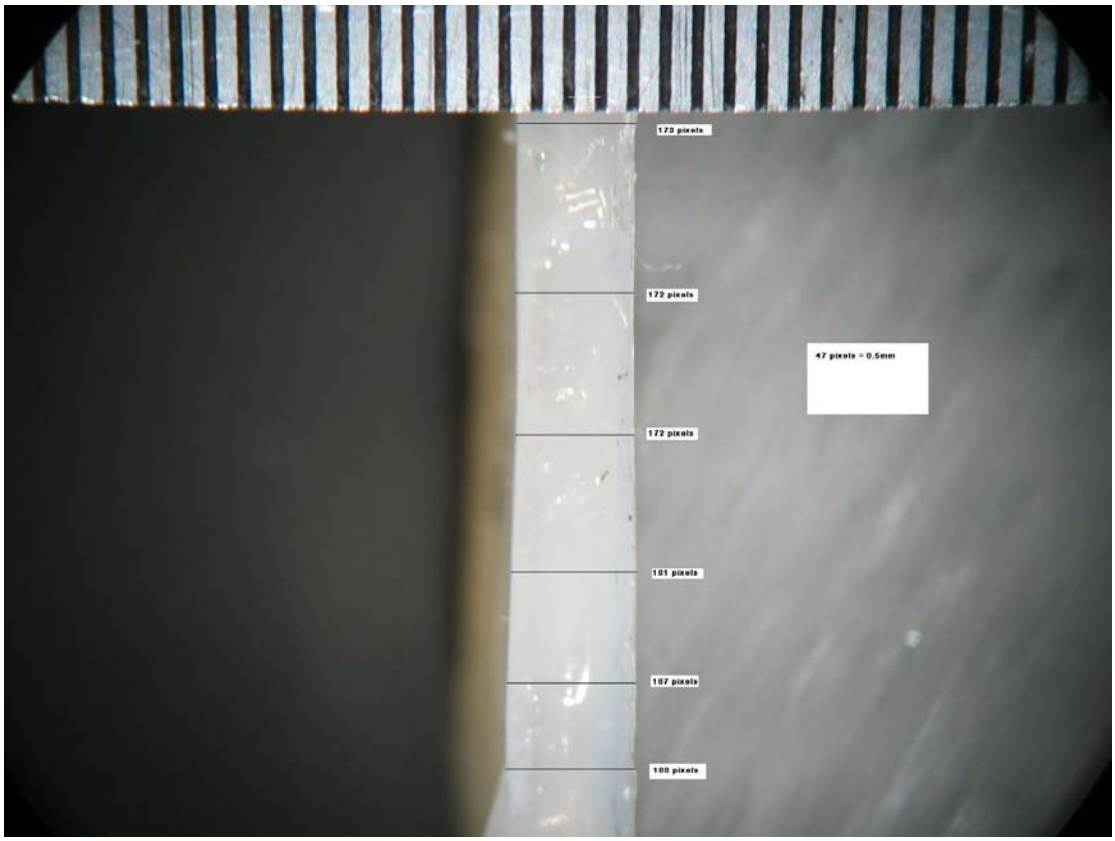

Figure 16.14 Sample 3-1a_120CT

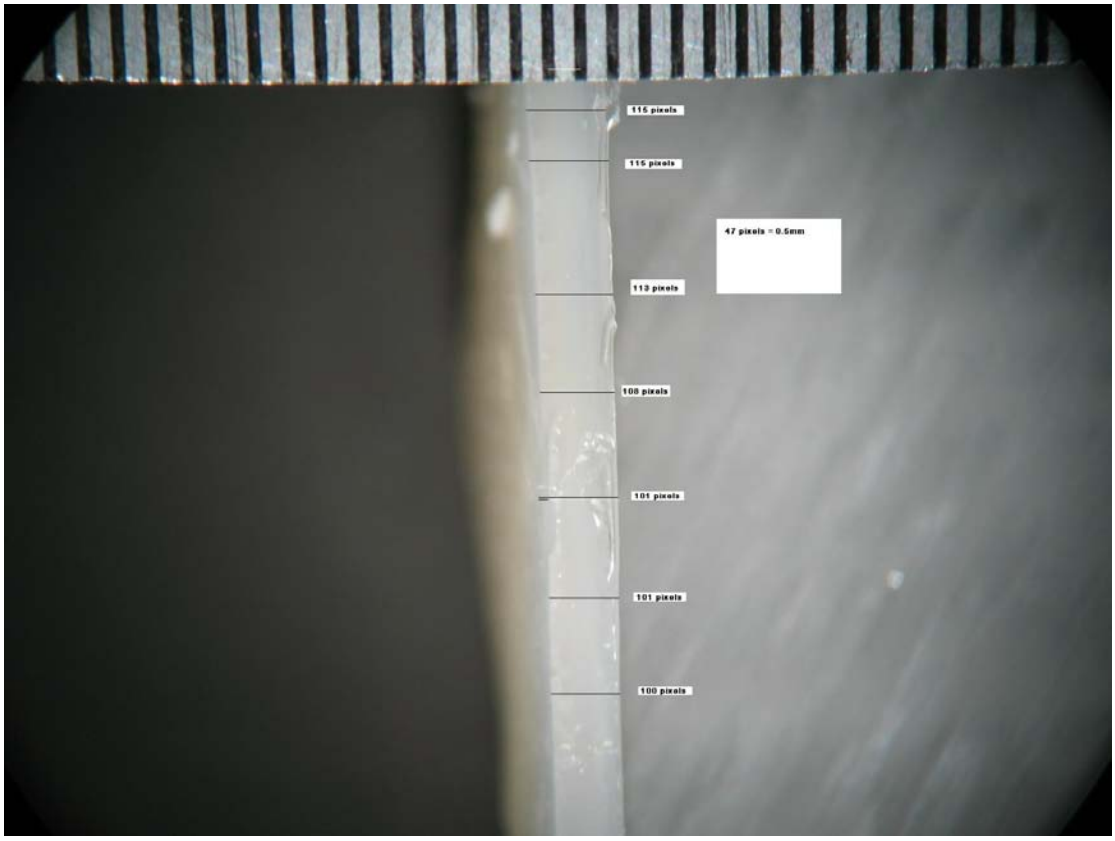

Figure 16.15 Sample 3-1b_551CT

16.2 Photos of the Cross-section at the Edges

The following photos are of the left edges of the layers. In these photos, the edge is measured to find the length of the Beer-Lambert Law occurring at the edges. The same naming convention is used that was explained at the start of this appendix.

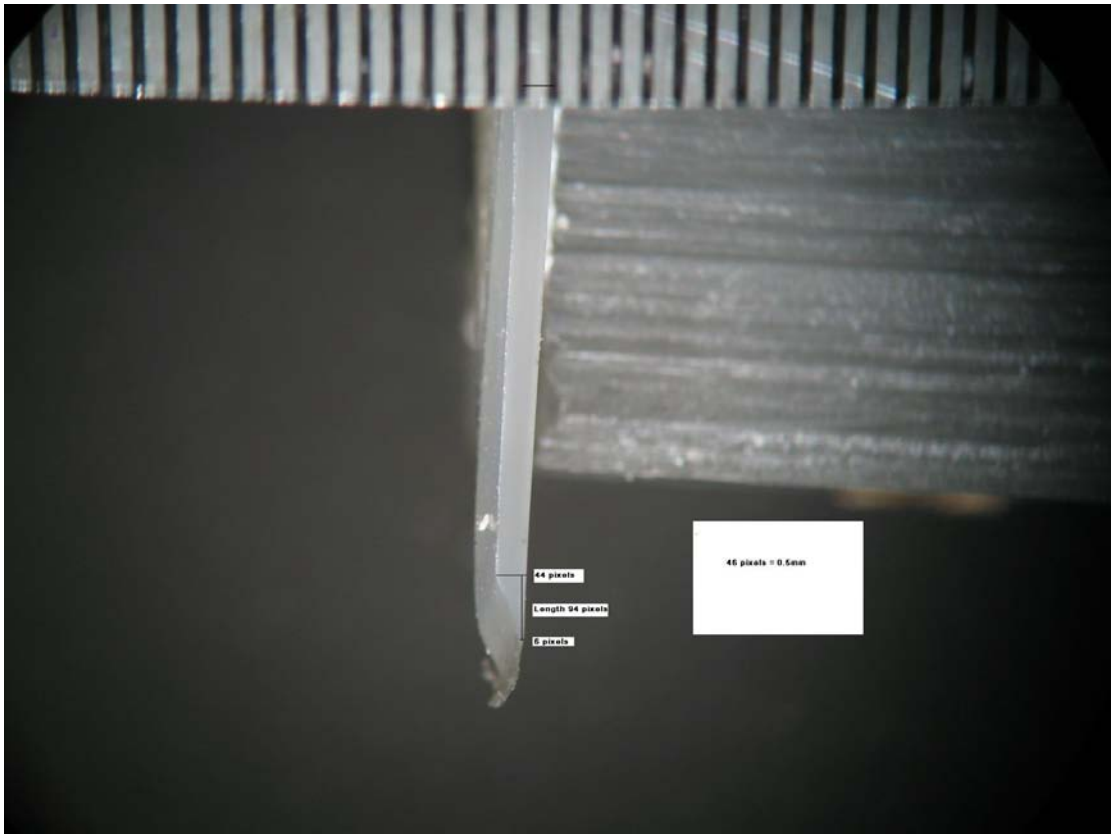

Figure 16.16 Sample 1-1_45LN

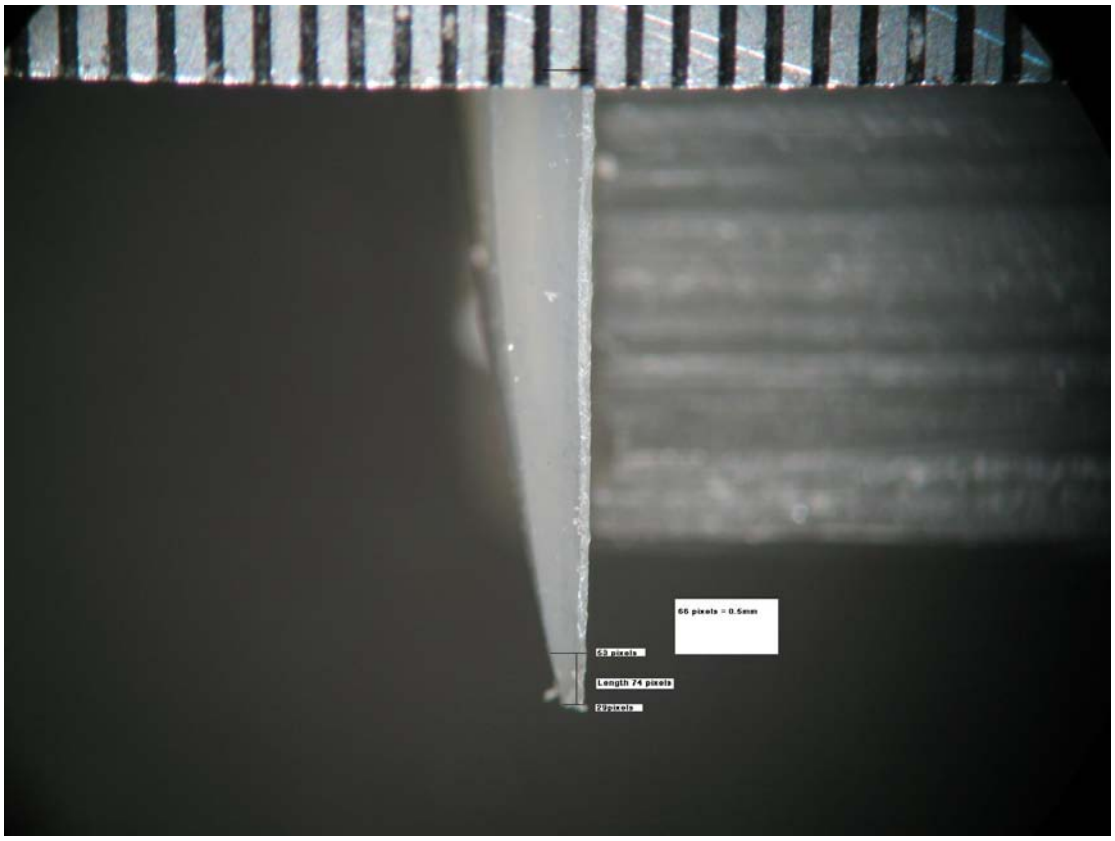

Figure 16.17 Sample 1-2_45LN

Figure 16.18 Sample 2-1_45LC

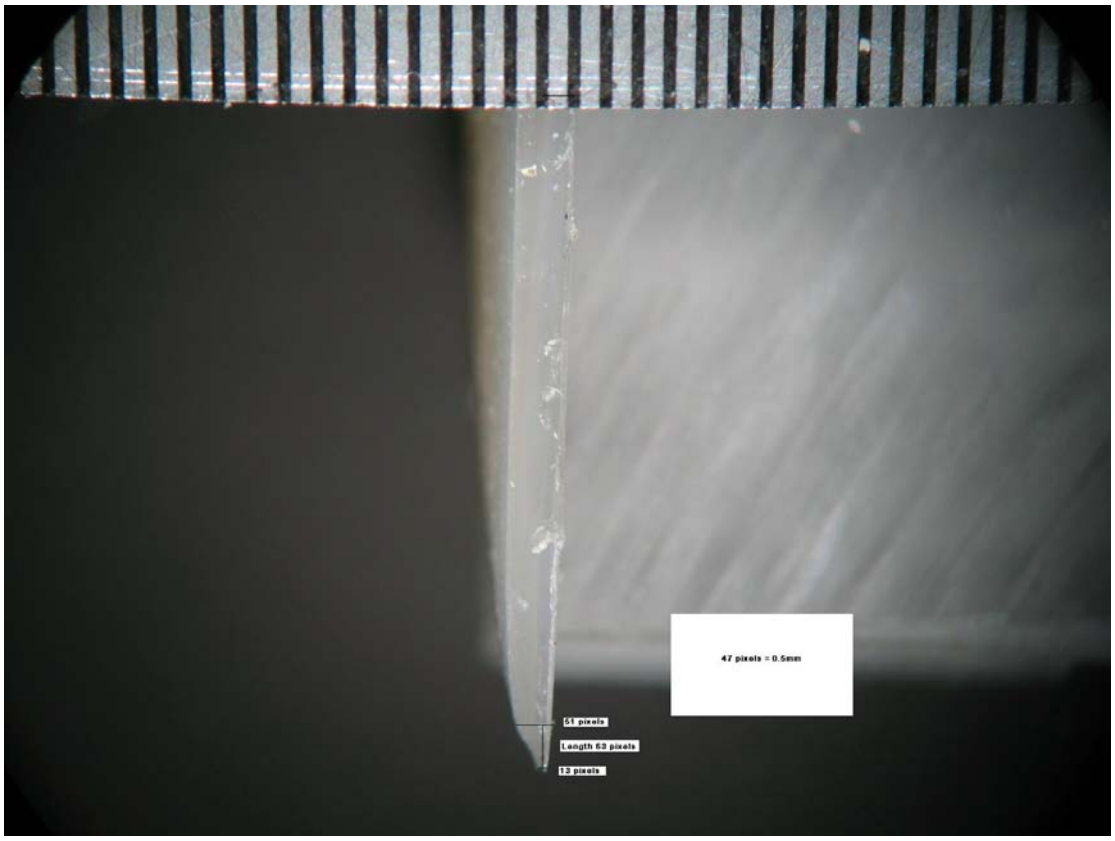

Figure 16.19 Sample 2-2_45LC

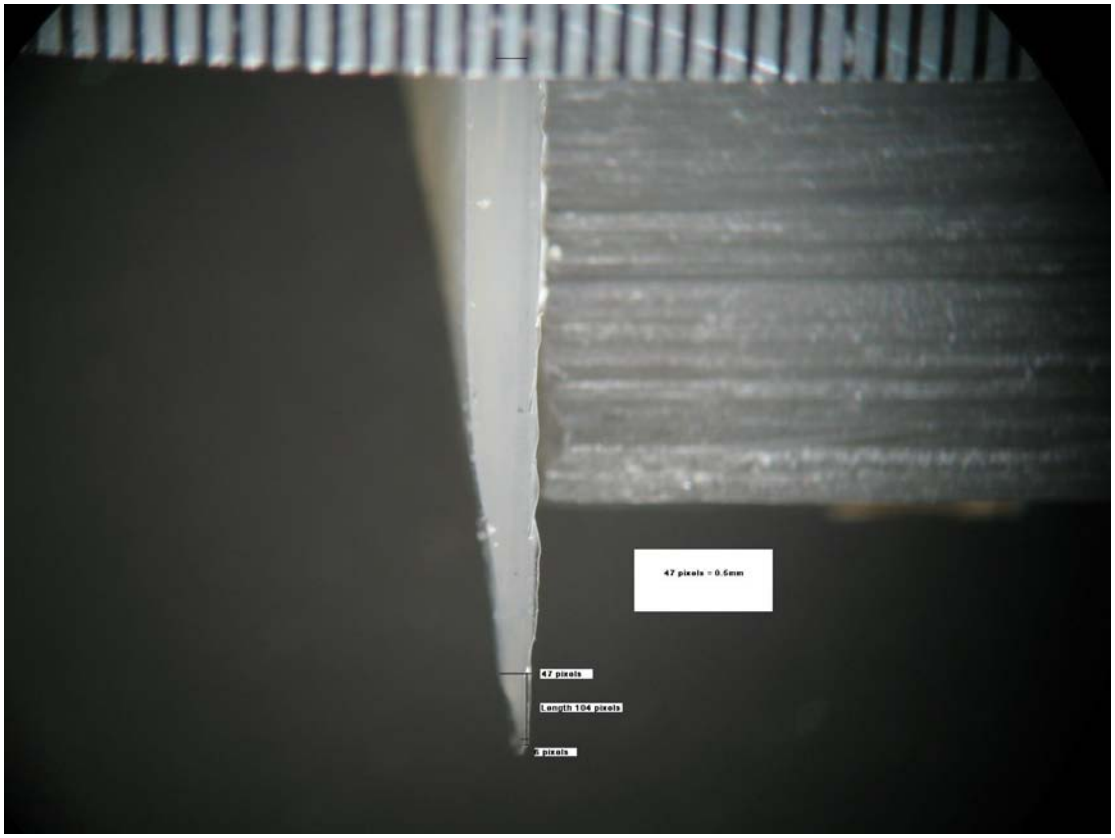

Figure 16.20 Sample 1-1_50LN

Figure 16.21 Sample 1-2_50LN

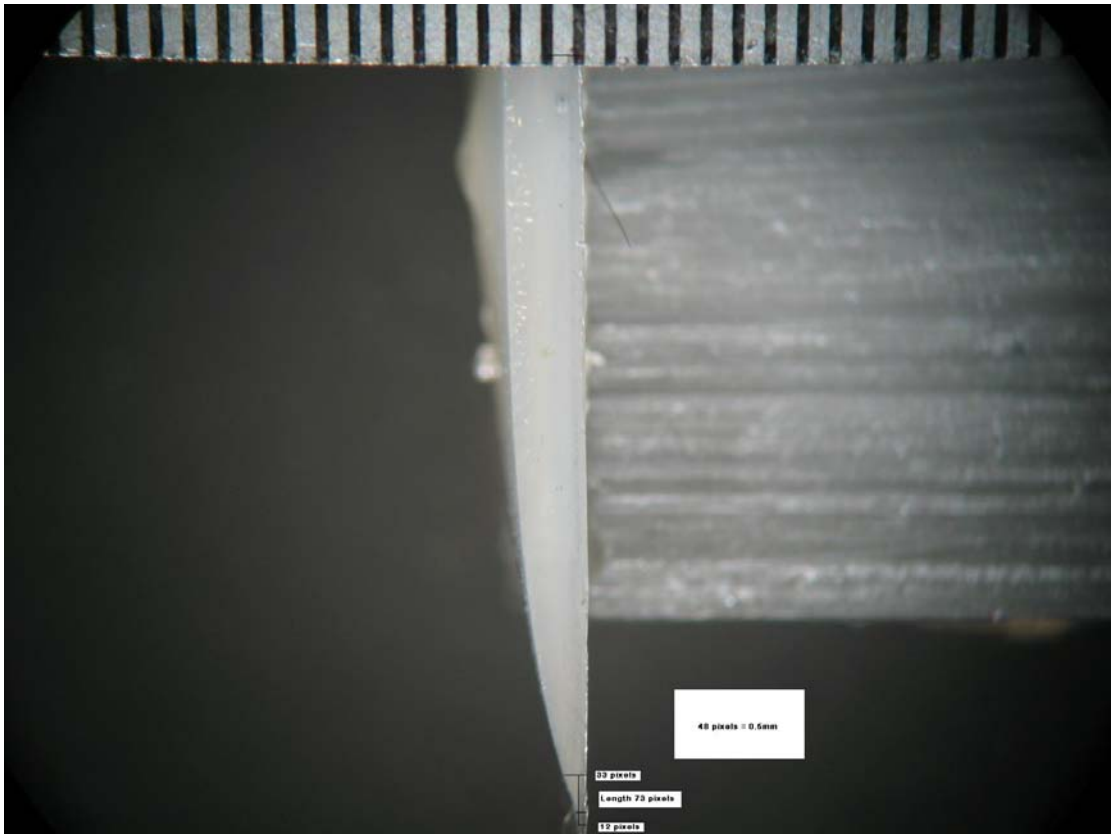

Figure 16.22 Sample 2-1_50LC

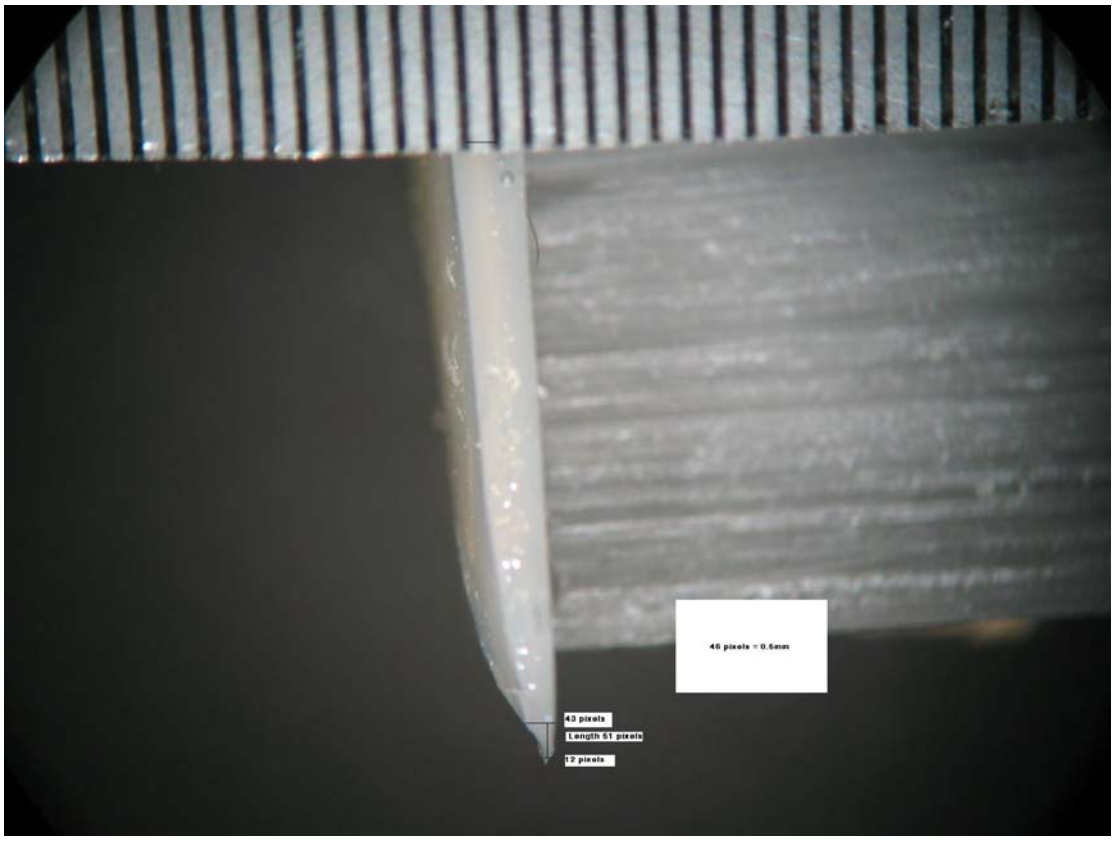

Figure 16.23 Sample 2-2_50LC

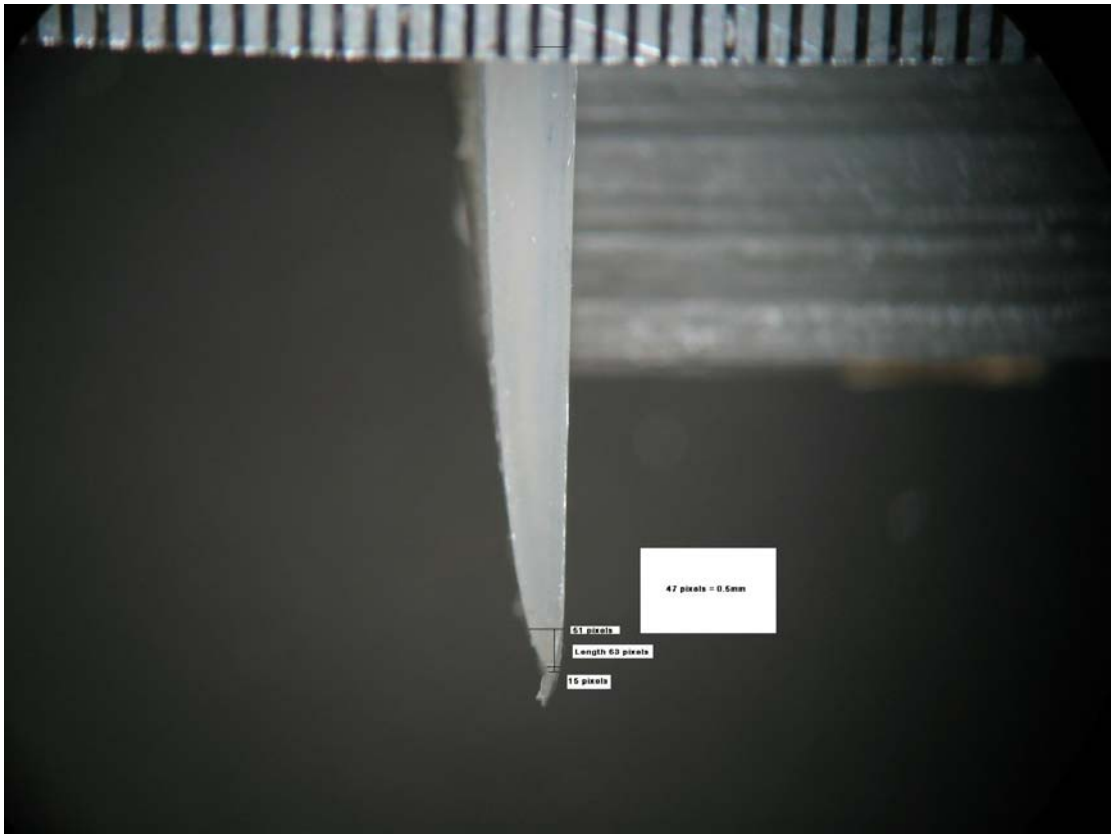

Figure 16.24 Sample 1-2_55LN

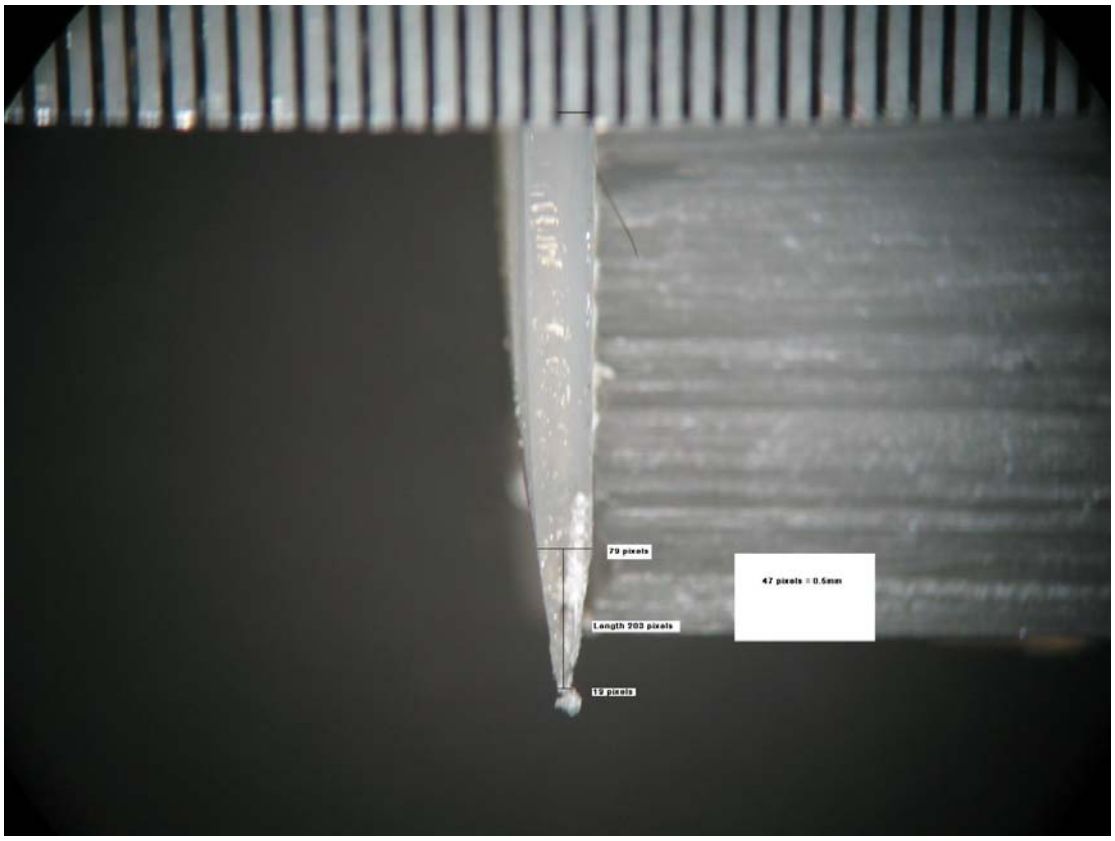

Figure 16.25 Sample 2-1_55LC

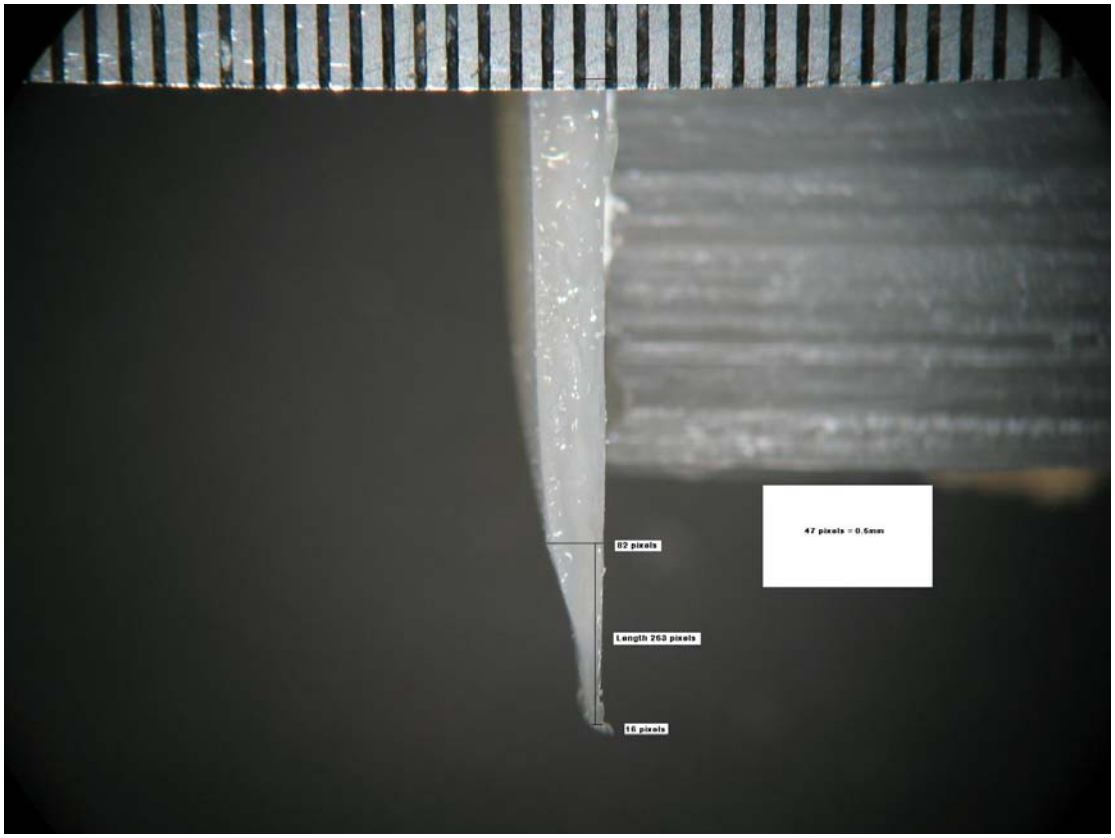

Figure 16.26 Sample 2-2_55LC

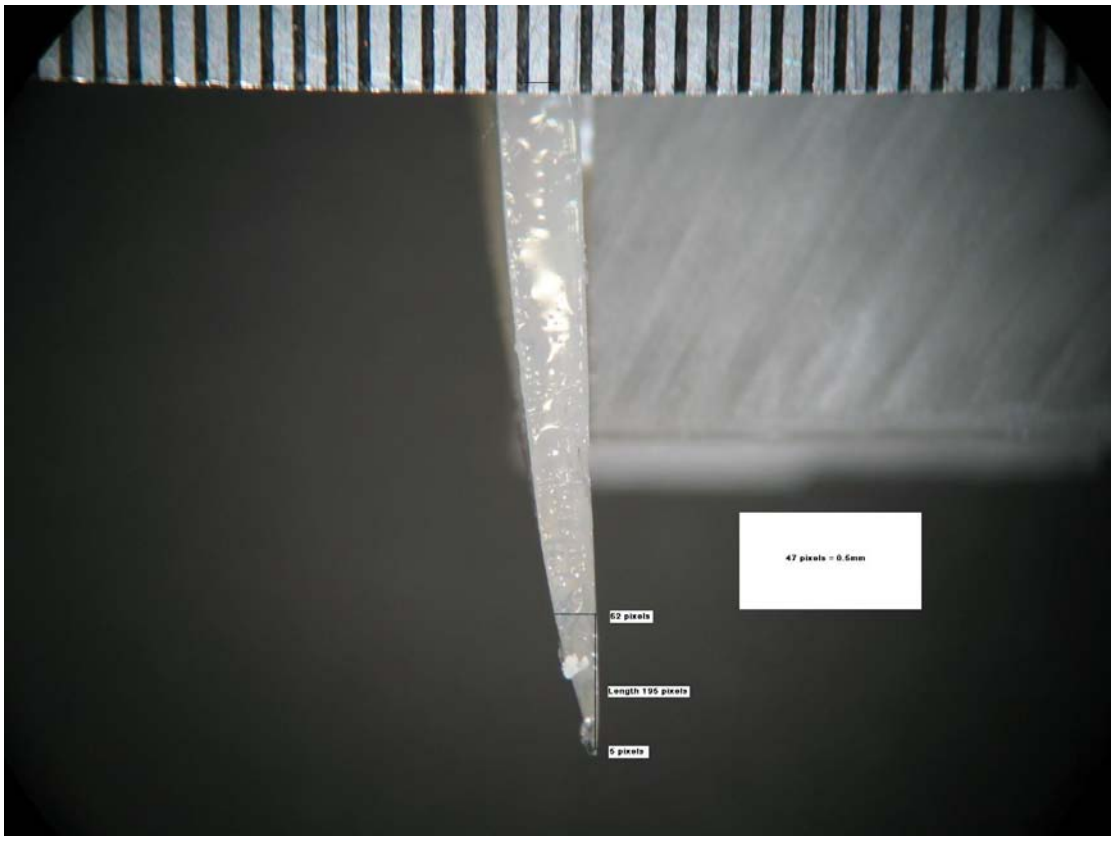

Figure 16.27 Sample 3-1_115LT

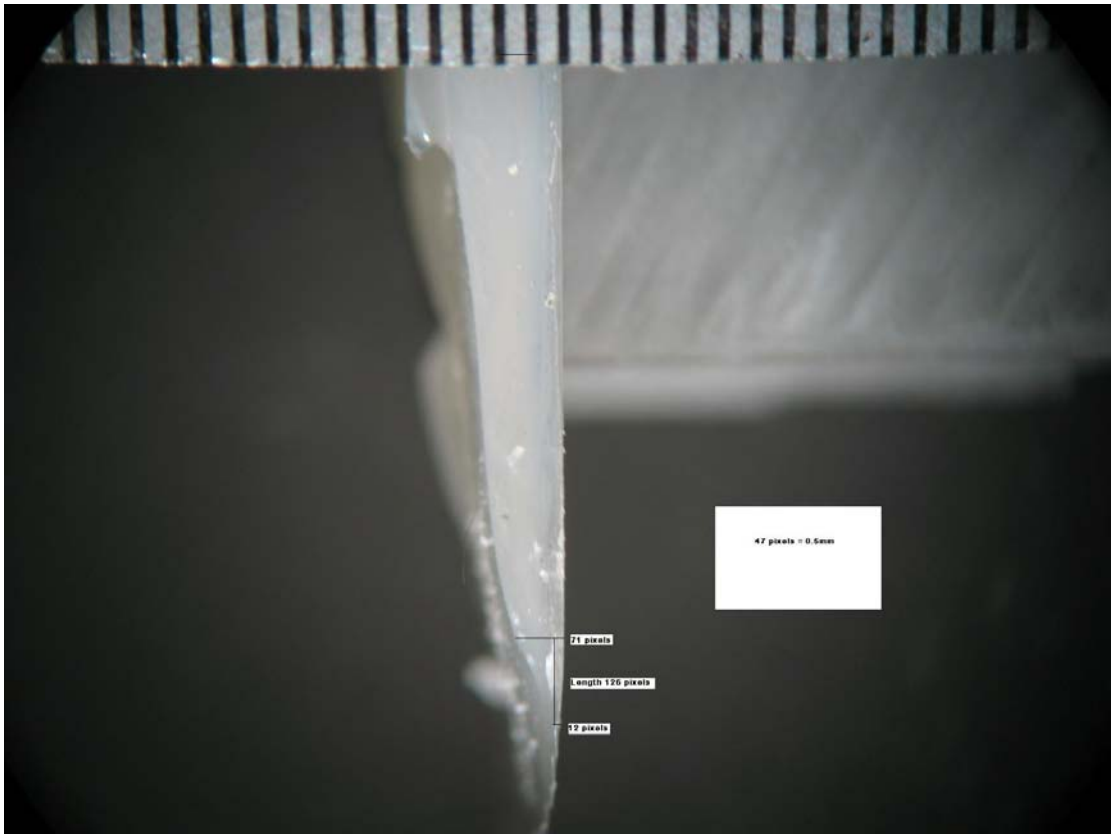

Figure 16.28 Sample 3-1a_120LT

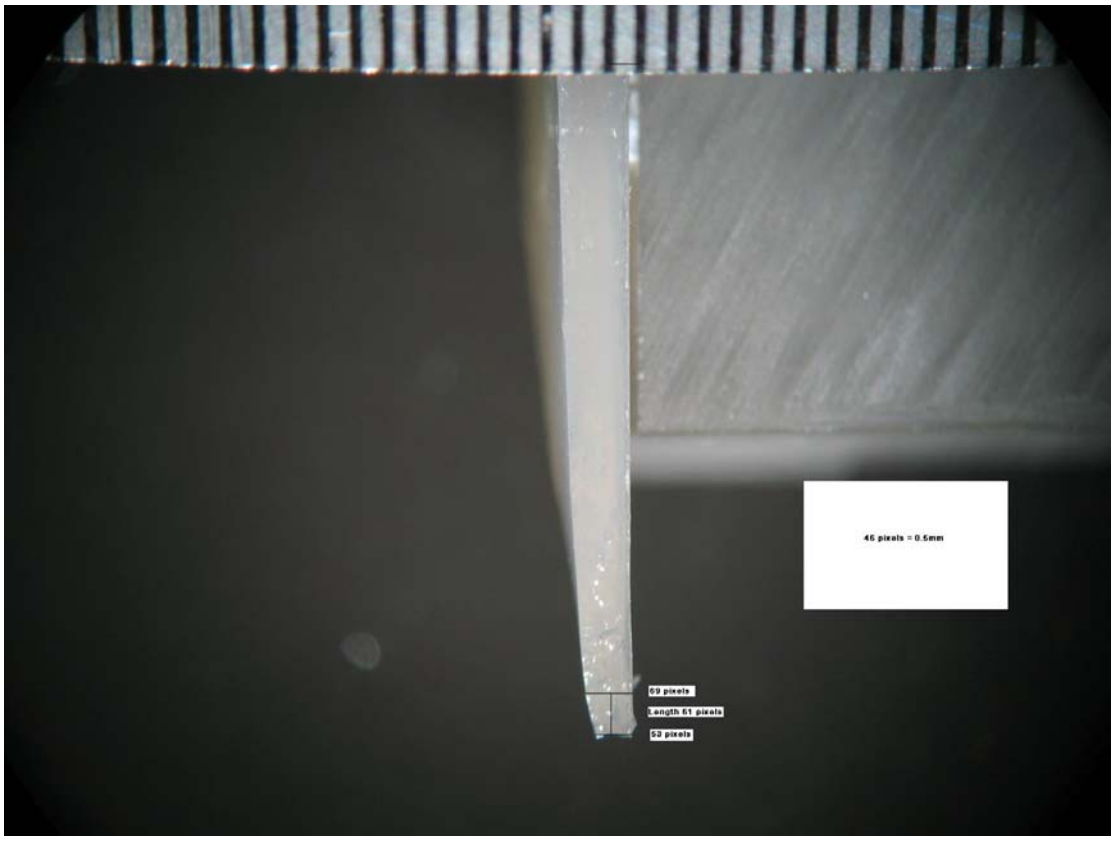

Figure 16.29 Sample 3-1b_120LT

17 Appendix E: Resin Data Sheets

17.1 RenShape SL7545 Photopolymer Resin

PROVISIONAL DATA SHEET

Stereolithography Materials

SL DIRECT

for use on

Solid State Laser SLA® systems

RenShape® SL 7545

Durable Stereolithography Material for Polypropylene-like Parts

- High green strength
- Accurate material with wide process latitude
- Excellent side walls and fine features
- High durability
- High elongation at break
- Suitable for snap-fit parts

Liquid Material

MEASUREMENT	CONDITION	VALUE
Appearance		Clear Amber
Density	@ 25°C (77°F)	1.15 g/cm³
Viscosity	@ 30°C (86°F)	350 cps
Penetration depth (Dp)		6.6 mils
Critical exposure (Ec)		9.6 mJ/cm²
Part building layer thickness*		0.10mm (0.004in) 0.15mm (0.006in)

*Dependent upon part geometry and build parameters.

Post-Cured Material

MEASUREMENT	TEST METHOD	VALUE	VALUE
		90-minute UV post-cure	90-minute UV + 2 hours @ 80° thermal post-cure
Hardness, Shore D	ASTM D 2240	79	81
Flexural modulus	ASTM D 790	1,390 - 1,560 MPa (200 - 225 KSI)	1,460- 1,600 MPa (210 - 230 KSI)
Flexural strength	ASTM D 790	50 - 55 MPa (7,300 - 8,000 PSI)	52 - 56 MPa (7,500 - 8,100 PSI)
Tensile modulus	ASTM D 638	1,400 - 1,900 MPa (200 - 275 KSI)	1,500 - 1,900 MPa (220 - 280 KSI)
Tensile strength	ASTM D 638	35 - 40 MPa (5,000 - 5,700 PSI)	35 - 40 MPa (5,000 - 5,700 PSI)
Elongation at break	ASTM D 638	12 - 21%	10 - 16%
Impact strength, notched Izod	ASTM D 256	28 - 39 J/m (0.5 - 0.7 ft - lbs/in)	22 - 33 J/m (0.4 - 0.6 ft - lbs/in)
Heat deflection temperature	ASTM D 648 @ 66 PSI @ 264 PSI	48-50°C 43-48°C	58-60°C 48-50°C
Glass transition, Tg	DMA, E" peak	55°C (131°F)	58°C (136°F)
Density		1.19 g/cm³	

For SL Technical Support: Tel: 866-288-3554 (Toll Free), Fax: 517-324-1416. Email: slmaterials@vantico.com
www.tooling.vantico.com
Vantico A&T US, Inc. 4917 Dawn Ave, E. Lansing, MI 48823 USA Tel: 800-285-4784 Fax: 517-351-6255

RenShape solutions

17.2 Vantico SL5170 Photopolymer Resin

SL 5170 Typical Properties

for the SLA 190/250 systems

3 SYSTEMS

Liquid Material

Measurement	Condition	Value
Appearance		Clear amber
Density	@ 25°C (77°F)	1.14g/cc
Viscosity	@ 30°C (86°F)	165 - 195 cps
Penetration depth (Dp)		4.8mils
Critical exposure (Ec)		13.5mJ/cm²
Part building layer thickness*		0.10 mm (0.004 in)
		0.15 mm (0.006 in)

*Dependent upon part geometry and build parameters.

Post-Cured Material

Measurement	Test Method	Value 90-minute UV post-cure
Tensile strength	ASTM D 638	59 - 60 MPa (8,600 - 8,800 PSI)
Tensile modulus	ASTM D 638	3,737 - 4,158 MPa (542 - 603 KSI)
Elongation at break	ASTM D 638	8%
Flexural strength	ASTM D 790	107 - 108 MPa (15,500 - 15,700 PSI)
Flexural modulus	ASTM D 790	2,920 - 3,006 MPa (423 - 436 KSI)**
Impact strength, notched Izod	ASTM D 256 DIN 53455/ISO R 527	27 - 37 J/m (0.5 - 0.7 ft - lbs/in)
Heat deflection temperature	@ 66 PSI @ 264 PSI	55°C (131°F) 49°C (120°F)
Glass transition, Tg	DMA	65 - 90°C (149 - 184°F)
Coefficient of thermal expansion	TMA (T<Tg)	90ppm/°C (184°F)
Thermal conductivity		0.200 W/m.°K (4.78 x 10^{-4}Cal/sec.cm.°C)
Hardness, Shore D	DIN 53505	85
Density		1.22 g/cm³

MATERIAL UPGRADE PROGRAM Upgrade your existing material and take advantage of a substantial discount off the regular purchase price with 3D Systems Material Upgrade Program. To place an order, contact your local sales office or in the US call toll free 800.889.2964.

Like all our stereolithography materials, SL 5170 is developed and manufactured by Vantico (formerly Ciba Specialty Chemicals, Performance Polymers Division), for exclusive distribution by 3D Systems. Vantico and 3D Systems collaborate continually to develop faster, more durable, and more accurate materials for all our SLA solid imaging systems, and for your solid imaging applications.

vantico

3D Systems
26081 Avenue Hall
Valencia, CA 91355 USA
telephone 661.295.5600 ext. 2882
fax 661.294.8406
toll-free 888.337.9786
email moreinfo@3dsystems.com

www.3dsystems.com
Nasdaq: TDSC

FRANCE
telephone +33 1 69 35 17 17

GERMANY
telephone +49 6151 357 303

HONG KONG
telephone +852 2923 5077

ITALY
telephone +39 039 68 904 00

SPAIN
telephone +34 93 754 04 00

UK
telephone +44 1442 282600

P/N 70158 Rev 03/01

18 Appendix F: Cooke Triplet simulations

Three Cooke triplets were analysed using lens design software by OSLO-EDU 6.4.3 by Lambda Research Corporation. The lenses in each Cooke triplet were selected from the Edmond Optics Catalogue. All have a diameter of 25.4mm except the negative element in Cooke Triplet 2 which has a diameter of 12.7mm. The following images are screen shots of the lens data (surface data), the optical layout (autodraw), the ray diagram (ray analysis), distortion plots, and radial energy distribution plot for each triplet.

18.1 Cooke Triplet 1: Effective focal length = 26.43mm

Surface Data

Gen | Setup | Wavelength | Variables | Draw On | Surfs | Notes

Lens: Cooke Triplet Efl 26.456721

Ent beam radius 10.000000 Field angle 50.000000 Primary wavln 0.354000

SRF	RADIUS		THICKNESS		APERTURE RADIUS		GLASS		SPECIAL
OBJ	7.500000		80.000000	V	95.340287		AIR		
AST	0.000000		9.300000		9.600000	A	AIR		
2	17.420000		7.250000		12.700000		SILICA	C	F
3	0.000000		0.880000	V	12.700000		AIR		
4	-92.080000		2.500000		12.700000		SILICA	C	
5	92.080000		0.880000	V	12.700000		AIR		
6	0.000000		7.250000		12.700000		SILICA	C	
7	-17.420000		0.000000	V	12.700000		AIR		
IMS	0.000000		210.000000		200.000000				F

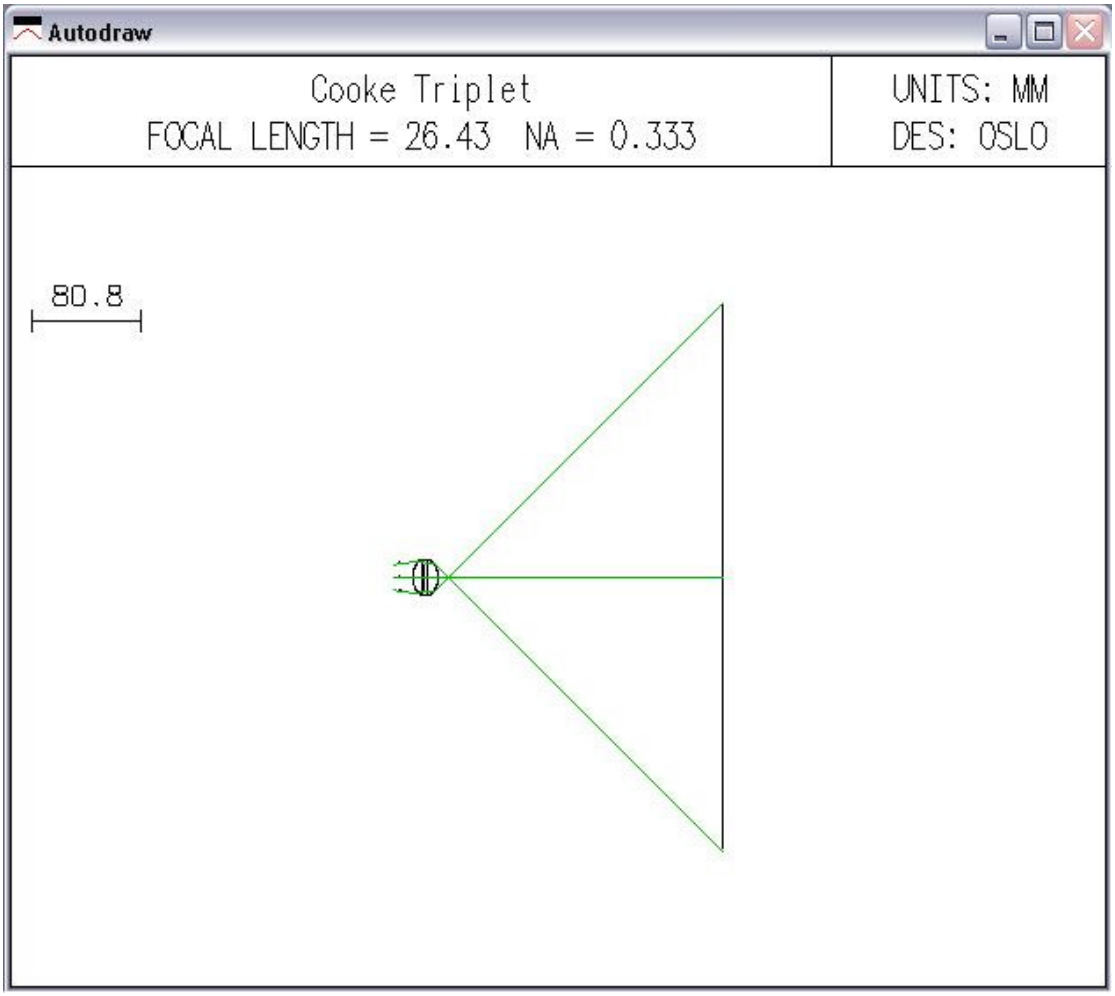
Autodraw
Cooke Triplet
FOCAL LENGTH = 26.43 NA = 0.333
UNITS: MM
DES: OSLO
80.8

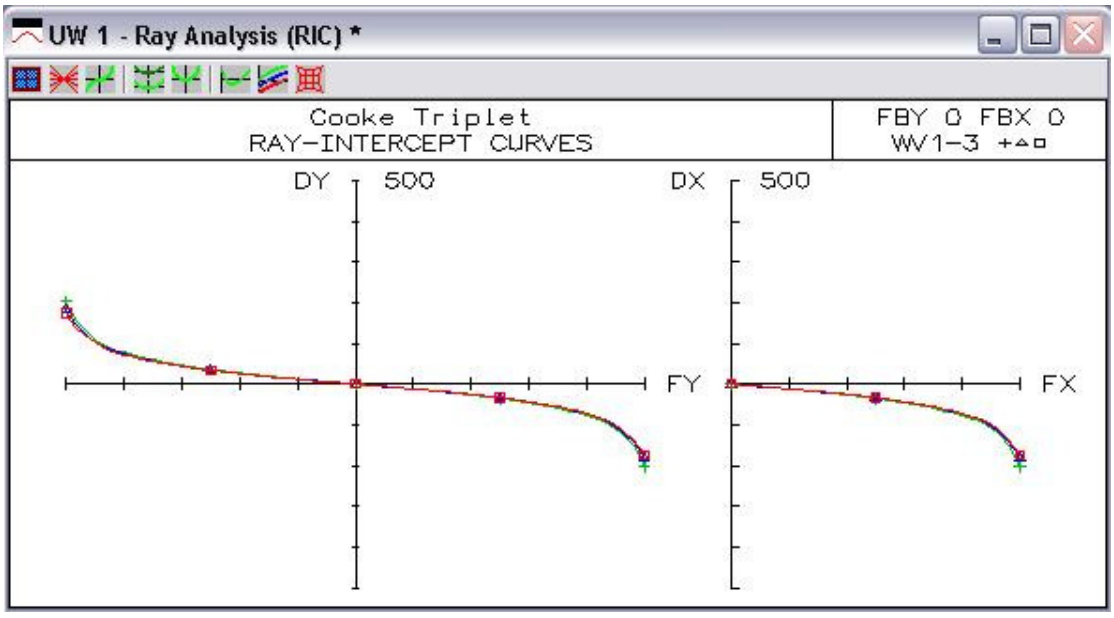
UW 1 - Ray Analysis (RIC) *
Cooke Triplet
RAY-INTERCEPT CURVES
FBY 0 FBX 0
WV1-3
DY
500
FY
DX
500
FX

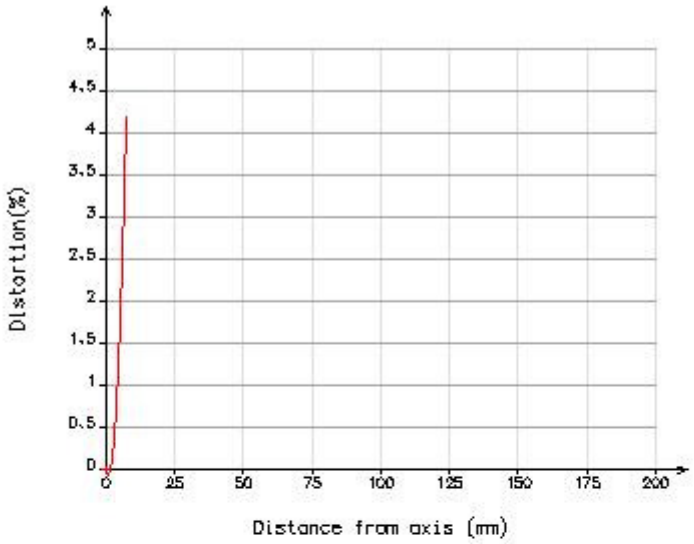
Distortion(%)
5
4.5
4
3.5
3
2.5
2
1.5
1
0.5
0
0
25
50
75
100
125
150
175
200
Distance from axis (mm)

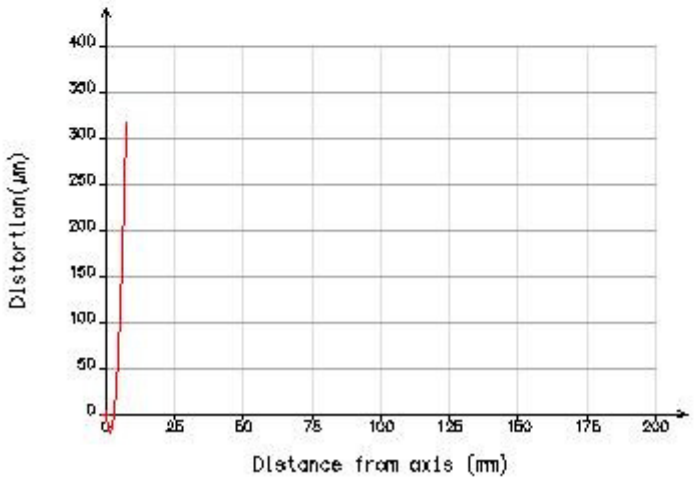
Distortion(µm)
400
350
300
250
200
150
100
50
0
0
25
50
75
100
125
150
175
200
Distance from axis (mm)

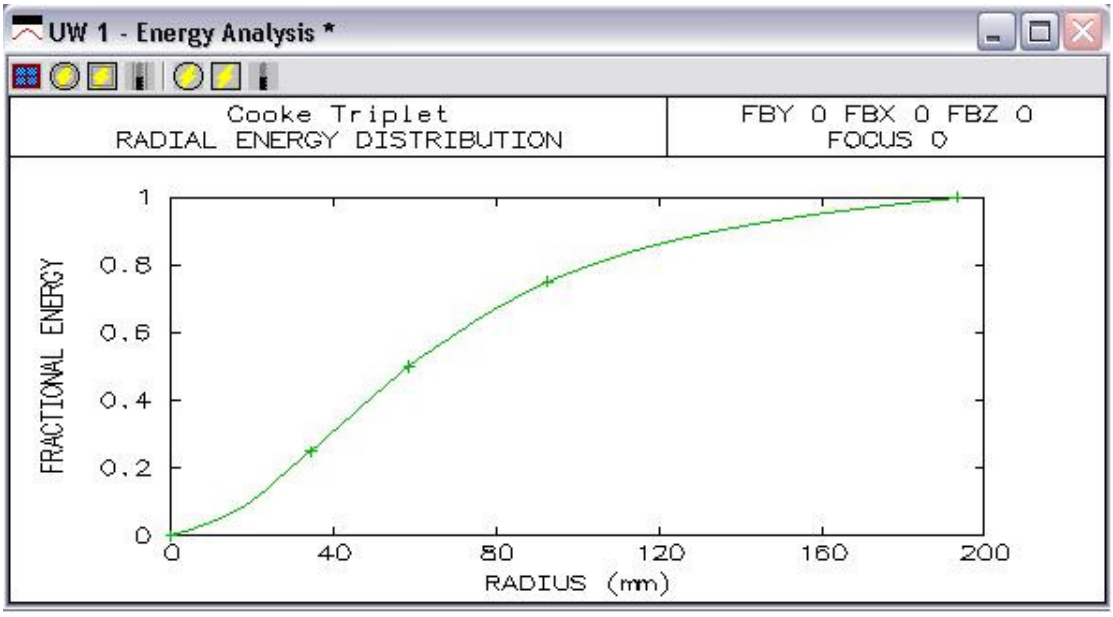
UW 1 - Energy Analysis *
Cooke Triplet
RADIAL ENERGY DISTRIBUTION
FBY 0 FBX 0 FBZ 0
FOCUS 0
FRACTIONAL ENERGY
1
0.8
0.6
0.4
0.2
0
0
40
80
120
160
200
RADIUS (mm)

18.2 Cooke Triplet 3: Effective focal length = 49.13mm

Surface Data

Command:

Gen | Setup | Wavelength | Variables | Draw On | Surfs | Notes

Lens: Cooke Triplet Efl 49.132533

Ent beam radius 10.000000 Field angle 5.770103 Primary wavln 0.354000

SRF	RADIUS		THICKNESS		APERTURE RADIUS		GLASS		SPECIAL
OBJ	7.500000		80.000000	V	28.243314		AIR		
1	17.420000		7.250000		12.700000		SILICA	C	F
2	0.000000		26.000000	V	12.700000		AIR		
AST	-18.640000		2.000000		6.350000	A	SILICA	C	
4	18.640000		0.960000	V	6.350000		AIR		
5	0.000000		7.250000		12.700000		SILICA	C	
6	-17.420000		0.000000	V	12.700000		AIR		
IMS	0.000000		210.000000		23.000000				F

Autodraw

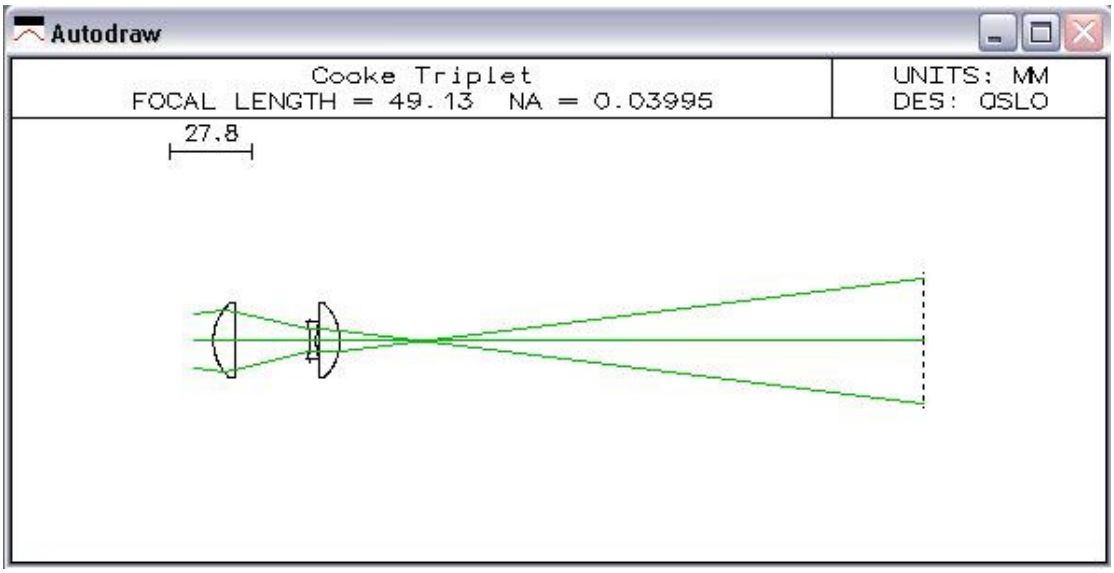

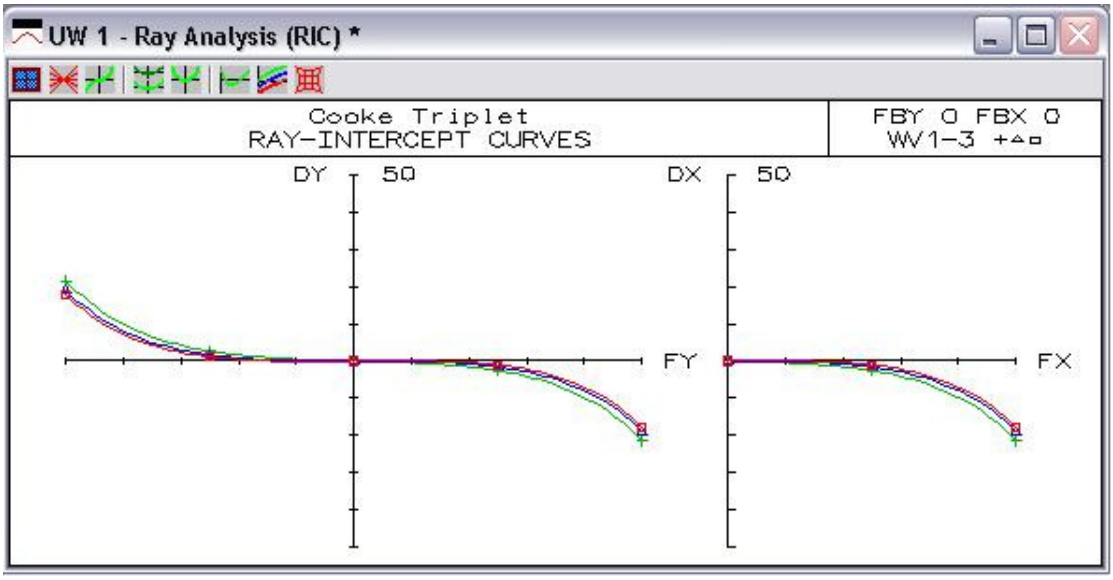
UW 1 - Ray Analysis (RIC) *
Cooke Triplet
RAY-INTERCEPT CURVES
FBY 0 FBX 0
WV1-3
DY
50
FY
DX
50
FX

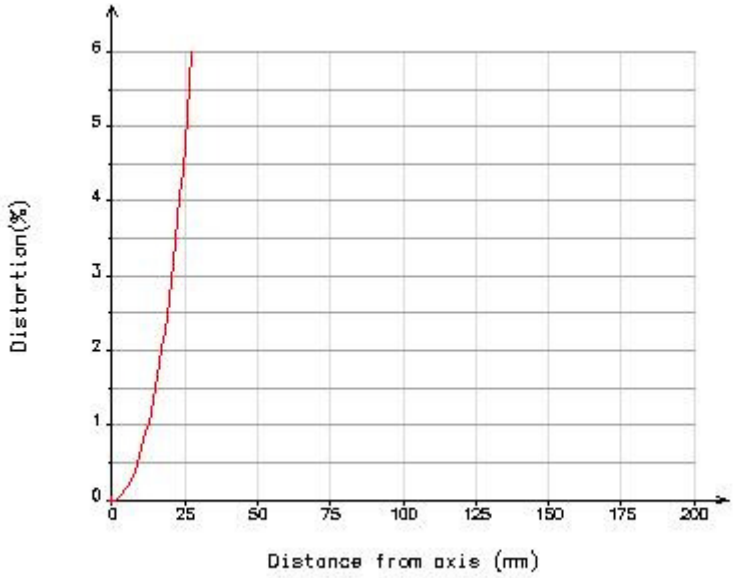
Distortion(%)
0
1
2
3
4
5
6
0
25
50
75
100
125
150
175
200
Distance from axis (mm)

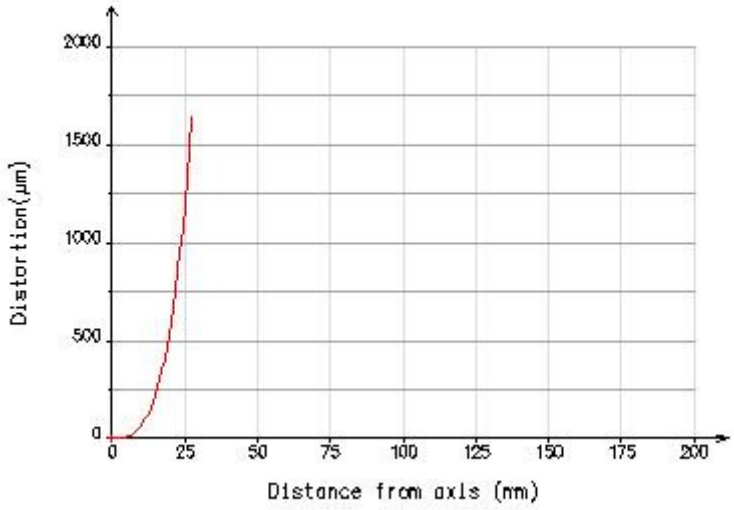
Distortion(µm)
0
500
1000
1500
2000
0
25
50
75
100
125
150
175
200
Distance from axis (mm)

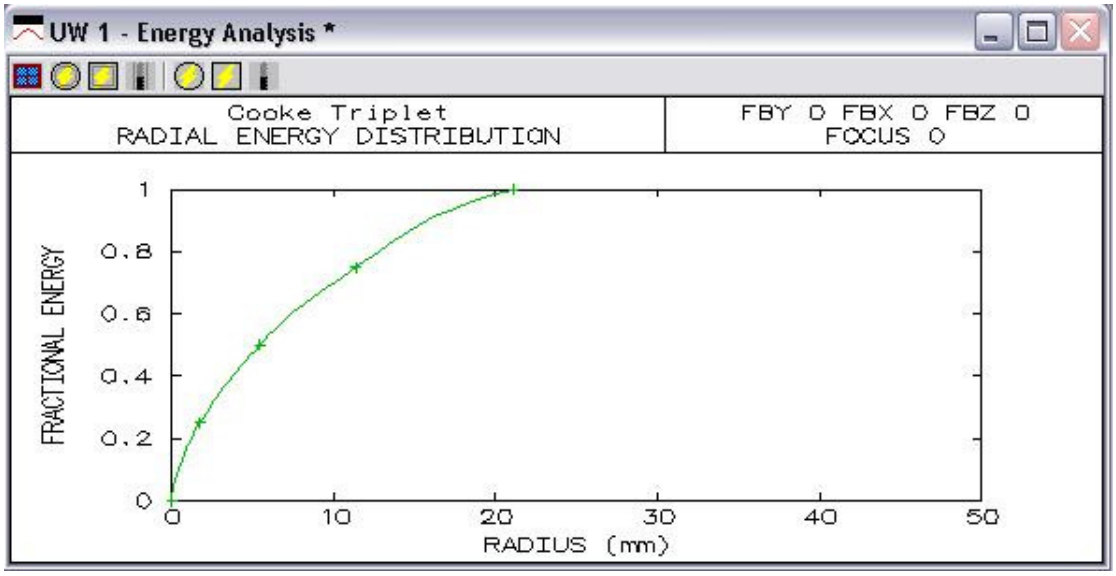

18.3 Cooke Triplet 3: Effective focal length = 29.53mm

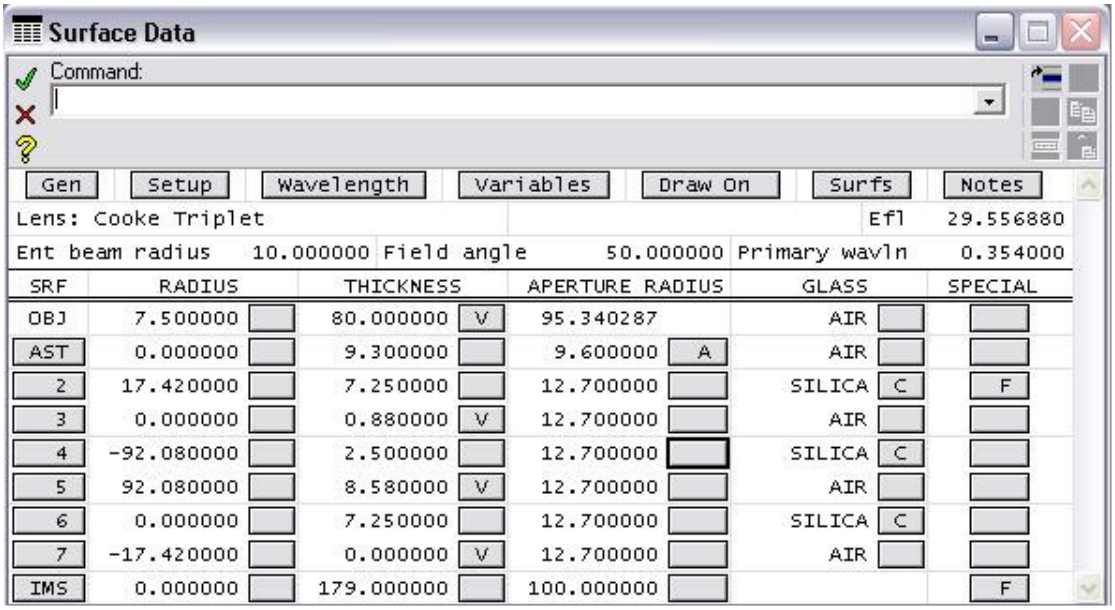

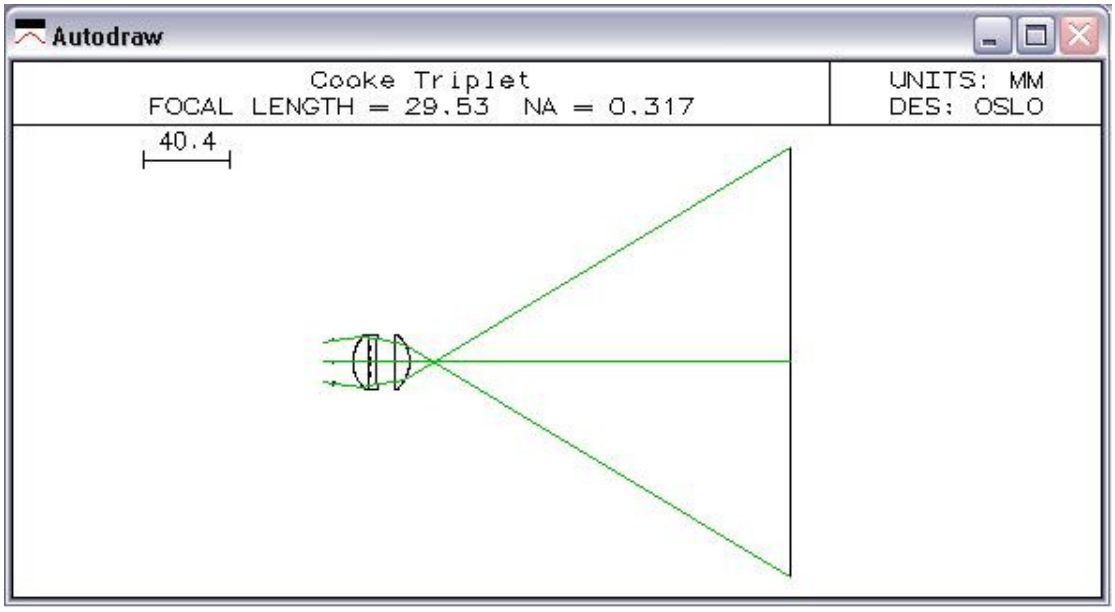
Autodraw
Cooke Triplet
FOCAL LENGTH = 29.53 NA = 0.317
UNITS: MM
DES: OSLO
40.4

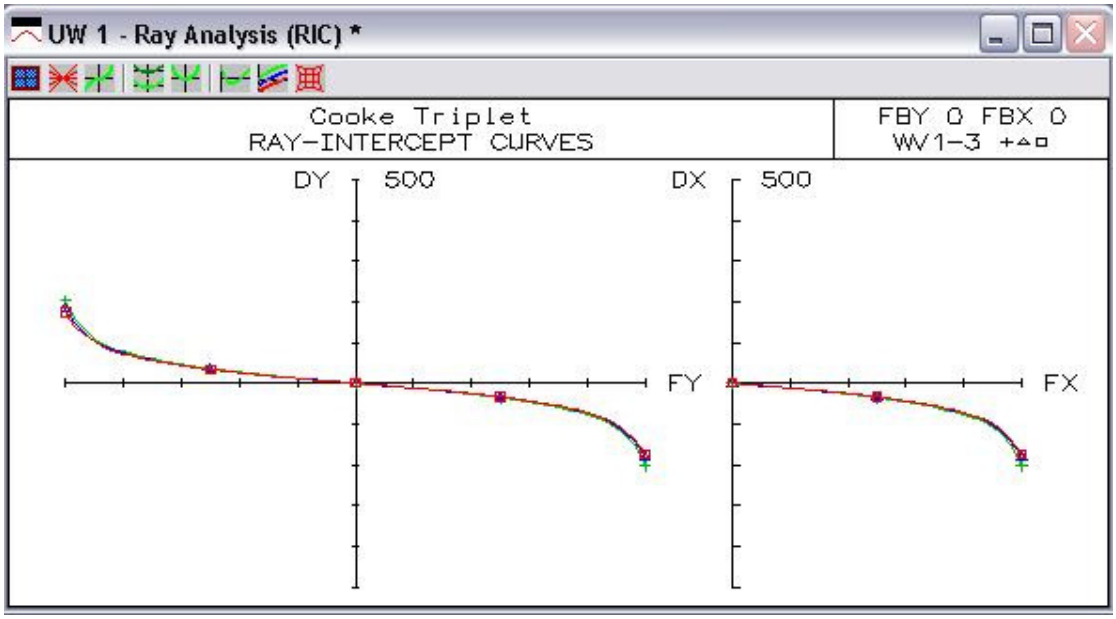
UW 1 - Ray Analysis (RIC) *
Cooke Triplet
RAY-INTERCEPT CURVES
FBY 0 FBX 0
WV1-3
DY
500
FY
DX
500
FX

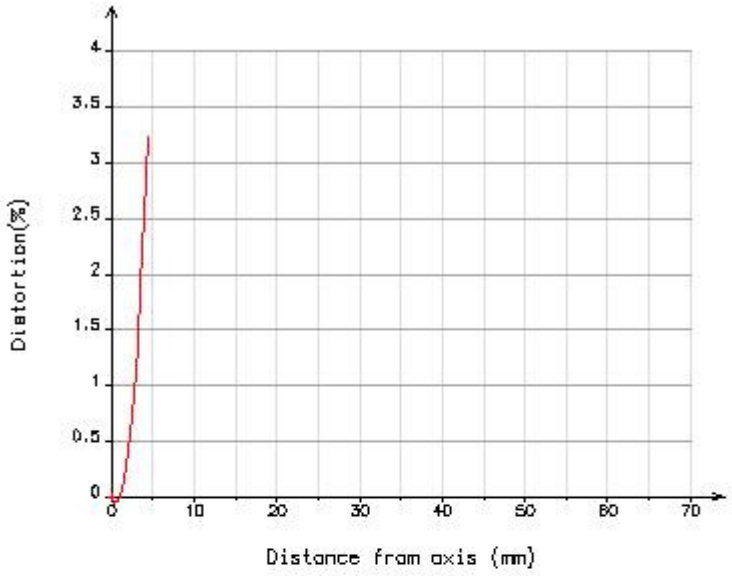
Distortion(%)
4
3.5
3
2.5
2
1.5
1
0.5
0
0
10
20
30
40
50
60
70
Distance from axis (mm)

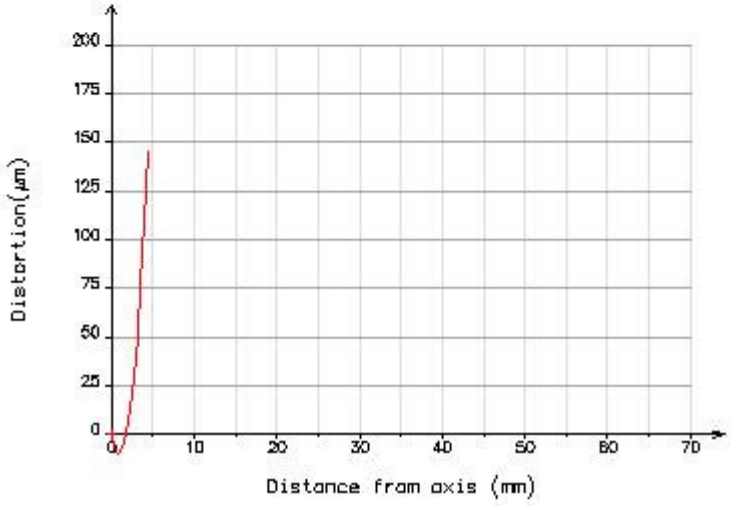
Distortion(µm)
200
175
150
125
100
75
50
25
0
0
10
20
30
40
50
60
70
Distance from axis (mm)

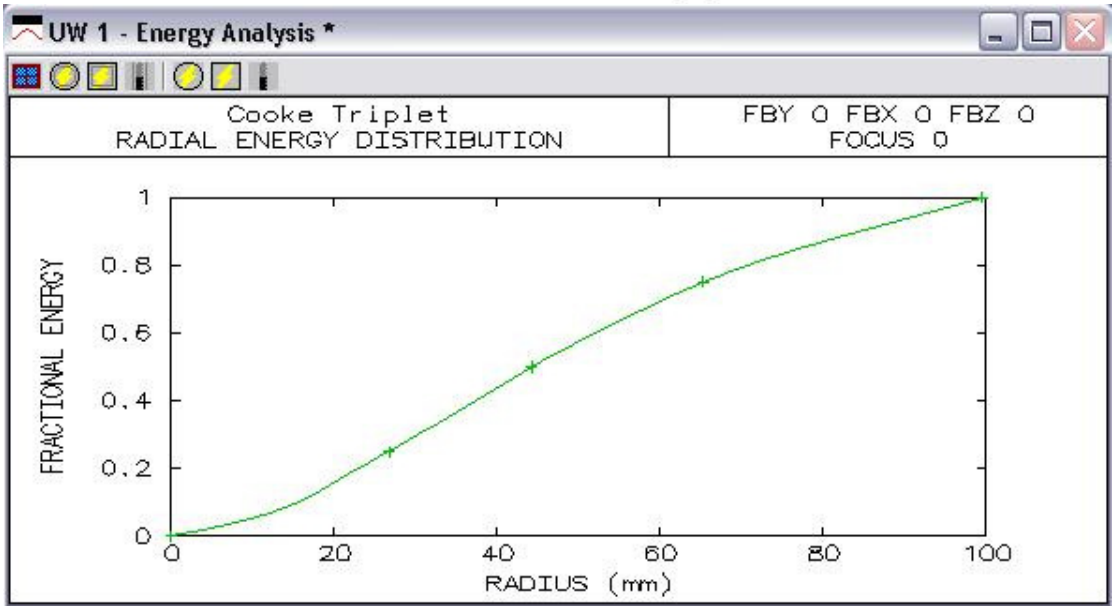
UW 1 - Energy Analysis *
Cooke Triplet
RADIAL ENERGY DISTRIBUTION
FBY 0 FBX 0 FBZ 0
FOCUS 0
FRACTIONAL ENERGY
1
0.8
0.6
0.4
0.2
0
0
20
40
60
80
100
RADIUS (mm)